Sheffield Hallam University

A Sheffield Hallam University thesis

Analysis of three dimensional cell cultures using mass spectrometry imaging

Ieva Palubeckaitė

Centre for Mass Spectrometry Imaging,
Biomolecular Sciences Research Centre

Sheffield Hallam University

A thesis submitted in partial fulfilment of the requirements of Sheffield Hallam University for the degree of *Doctor of Philosophy*

September 2018

i. Abstract

In order to better replicate disease and response to therapeutics 3D cell culture methods have been increasingly developed for use in research and industry. Two key areas where 3D cell cultures are being used as alternative models to animals are the study of prevalent diseases such as cancer and therapeutic toxicity testing in key metabolising organs such as the liver. Matrix-assisted Laser Desorption Ionisation Mass Spectrometry Imaging (MALDI-MSI) is an untargeted molecular imaging technique capable of imaging multiple molecules within a single experiment. This can be utilised for the investigation of molecular mechanisms of biological function or treatment response within 3D cell cultures, however, optimised methods are required for the analysis of these models.

In this thesis, a novel 3D cell culture model of osteosarcoma was developed. Sample preparation and MALDI-MSI workflows were optimised initially for small molecule analysis. Following this, doxorubicin responses in the 3D osteosarcoma model were assessed. Detection of doxorubicin-induced changes to lipids and metabolites in 3D cell culture were subsequently detected, and Principle Component Analysis (PCA) used to identify metabolite signatures associated with doxorubicin treatment.

Methods were then adapted for MALDI-MSI of proteotypic peptides within the model and a novel method for peptide quantitative mass spectrometry imaging (QMSI) was developed. MALDI-MSI successfully allowed the identification and quantification of 25 proteotypic peptides, using a 120-peptide standard array, demonstrating, for the first time, that QMSI is possible for proteomic quantification in 3D cell cultures.

Development of, and preliminary MSI analysis of, a novel 3D cell culture model of liver toxicity is reported. The L-pNIPAM scaffold and HepG2 cell lines used demonstrates hepatocyte differentiation and is potentially suitable for monitoring of hepatic metabolism and adverse drug reaction. Taken together, these studies represent a considerable development in simultaneous quantification of metabolites, lipids and proteins in 3D cell cultures.

Table of Contents

ii. Candidates statement

I declare that no part of this thesis has been submitted in support of any other degree or qualification at this university or any other institute of learning.

All the work presented in this thesis was undertaken by myself, Ieva Palubeckaite, with the exception of the fluorescent imaging of doxorubicin penetration into spheroid aggregates (Figure 3.5), which was carried out by Dr Neil Cross. The in-depth statistics in chapter 3 was performed with help from Dr Lucy Crooks. Confirmation of the absence of binding of ALP antibody in the L-pNIPAM model was performed by Dr Rasha Dosh. The second grader of the ALP IHC was Christine Le Maitre.

The FT-ICR-MSI work presented in chapter 4 was done in collaboration with Assoc. Prof. Liam McDonnell at the Centre for Proteomics and Metabolomics at Leiden University Medical Centre.

iii. Acknowledgements

"Therefore, he understood, there is in truth no past, only a memory of the past. Blink your eyes, and the world you see next did not exist when you closed them. Therefore, he said, the only appropriate state of the mind is surprise. The only appropriate state of the heart is joy. The sky you see now, you have never seen before. The perfect moment is now. Be glad of it."

— Terry Pratchett, Thief of Time

I would also like to thank our collaborators in Leiden, specifically Dr. Bram Heijs, for being so helpful and lovely during my visit there. Also, a big thank you to my current boss Prof. Judith Bovée for being understanding about me writing up during my post-doc and giving me the opportunity to not just continue further research in this field but to take it to the next level.

Norėčiau nuoširdžiai padėkoti savo šeimai, kuri manimi pasitikėjo ir mane palaikė visais ilgų studijų metais. Be tėvų pavyzdžio ir paramos, aš tikrai nebūčiau pasiekusi šio tikslo. Esu dėkinga už auklėjimą, suteiktas galimybes, meilę ir paramą. Dėkoju seneliams už rūpestį ir begalinę meilę. Nuoširdų ačiū tariu sesei kuri yra mano guodėja, ginėja ir linksmintoja.

And finally, last but nowhere near least, I would like to thank Andy from the bottom of my heart. You were my source of strength throughout and shared each good and bad experience. We've finally made it through to the other end. Thank you for being there always and your love and support. To you, my other half, I am eternally grateful. You definitely deserve it this time.

iv. List of Tables

v. List of Figures

vi. Abbreviations

1, 5-DAN- 1, 5-Diaminonaphthalene

2D- Two dimensional

3D- Three-dimensional

3Rs- Replacement, Reduction, Refinement

9-AA- 9-aminoacridine

ABC- ATP-Binding Cassette

ABC- ATP-binding cassette

ADME- Absorption, Distribution, Metabolism and Excretion

AIBN- Azobisisobutyronitrile

ALP- Alkaline Phosphatase

AmBic- Ammonium Bicarbonate

AMP- Adenosine 5′-monophosphate

ANOVA- Analysis of Variance

AOP- Adverse Outcome Pathway

APAP- N-acetyl-p-aminophenol (Acetaminophen)

ATCC- American Type Culture Collection

ATP- Adenosine 5′-triphosphate

BLM- Bleomycin

BME- Basement Membrane Extract

BSA- Bovine Serum Albumin

CAF- Cancer Associated Fibroblast

α-CHCA- α-Cyano-4-hydroxycinnamic acid

CLSM- Confocal Laser Scanning Microscopy

CMBT- 5-chloro-2-mercaptobenzothiazole

CMC- CarboxyMethyl Cellulose

CMP- Cytidine 5′-monophosphate

CSC- Cancer Stem Cell

CTP- Cytidine 5′-triphosphate

CYP- Cytochrome P450

DA- Discriminant Analysis

DHB- 2,5-Dihydroxybenzoic acid

DILI- Drug-induced Liver Injury

DMSO- Dimethyl sulfoxide

DNA- Deoxyribonucleic acid

ECM- Extra-Cellular Matrix

ELISA- Enzyme-Linked Immunosorbent Assay

EU- European Union

FA- Formic acid

FBS- Foetal Bovine Serum

FDA- Food and Drug Administration

FF- Fresh Frozen

FFPE- Formalin-Fixed Paraffin Embedded

FT-ICR- Fourier-Transform Ion Cyclotron Resonance

GAGs- Glycosaminoglycans

GSNO- S-nitrosoglutathione

GSTP- 1glutathione S-transferase P1

H+E- Haematoxylin and Eosin

HA- Hyaluronic acid

HIF-1- Hypoxia-inducible Factor 1

IC50- Half maximal inhibitory concentration

IHC- Immunohistochemistry

IMS- Ion Mobility Spectroscopy

iPSCs- induced Pluripotent Stem Cells

IR- Infrared

ITO- Indium-Tin Oxide

LA-ICP- Laser Ablation- Inductively Coupled Plasma

LC- Liquid Chromatography

LCST- Lower critical solution temperature

LDH- Lactate Dehydrogenase

LESA- Liquid Extraction Surface Analysis

LMS- Leiomyosarcoma

LOA- Likelihood of Approval

LOD- Limit of Detection

LOQ- Limit of Quantification

LSE- Living Skin Equivalent

LSFM- Light-Sheet-based Fluorescence Microscopy

m/z- Mass-to-charge ratio

MALDI- Matrix-Assisted Laser Desorption Ionisation

MAPK- Mitogen-Activated Protein Kinase

MCTS- Multicellular tumour spheroids

MFS- Myxofibrosarcoma

MRP2- Multidrug Resistance Protein 2

MS- Mass Spectrometry

MS/MS- Tandem Mass Spectrometry

MSCs- Mesenchymal stem cells

MSI- Mass Spectrometry Imaging

MTT- 3-(4,5-dimethylthiazol-2-yl)-2,5-diphenyltetrazolium bromide

NAPQI- N-acetyl-p-benzoquinone imine

NEDC- N-(1-Naphthyl) ethylendiaminedihydrochloride

NF-κB- Nuclear Factor-κB

NIPAM- N-Isopropylacrylamide

NO- Nitric oxide

OS- Osteosarcoma

PARP- Poly(ADP-ribose) Polymerase-1

PBS- Phosphate-Buffered Saline

PCA- Principal Component Analysis

PCA-DA- Principal Component Analysis- Discriminant Analysis

PCR- Polymerase Chain Reaction

PEG- Polyethylene glycol

Pgp- P-glycoprotein protein

PHHs- Primary human hepatocytes

PI- Propidium Iodide

QMSI- Quantitative Mass Spectrometry Imaging

Q-TOF- Quadrupole- Time Of Flight

RMS- Root Mean Square

ROI- Region of Interest

SPIM- Single (or selective) Plane Illumination Microscopy

SubX- Xylene Substitute

TBS- Tris-buffered saline

TFA- Trifluoroacetic acid

TIC- Total Ion Count

TPM/MPM- Two-Photon Microscopy/ Multi-Photon Microscopy

TRACER- Tissue Roll for the Analysis of Cellular Environment and Response

UMP- Uridine 5′-monophosphate

UPS- Undifferentiated pleomorphic sarcoma

UV- Ultraviolet

VCN- Vincristine

Chapter 1: Introduction

1.1 Introduction

Study using two-dimensional (2D) cell cultures and animal models has contributed greatly to current knowledge of disease mechanisms and development of treatment options. It has provided a large amount of information about biological mechanisms within the human body and interactions with pharmaceuticals; however, none of the current models provide a reliable translation of the complex human environment. Two-dimensional cell culture has been utilised for many years as it is a cost-effective option which provides a relatively homogenous, highly reproducible environment for experimental purposes. Nonetheless, there is agreement in the scientific community that 2D cell culture is far from a perfect model of the *in vivo* human environment in regards to limited cell type, lack of physiochemical gradients and a lack of conditional heterogeneity. Differences in gene expression, compared to the *in vivo* environment, alter central, significant cell functions, changes in morphology contribute to vast differences in drug-interactions, and there are also differences in cell-cell interactions and cell-matrix interactions. All these fundamental changes lead to large differences between limited 2D cell cultures and the *in vivo* human patient responses they are attempting to predict (Horvath *et al.*, 2016). Conversely, the animal model is highly complex, consisting of hundreds of cell types with varying local cell environments, cell-cell and cell-extracellular matrix interactions, stem cell populations, difficulties in drug delivery, and hepatic drug metabolism. The animal model, for a long period of time has been considered the 'gold standard' for models of human disease. It is the most representative, as it contains not only all the complexity of tissues but also interactions between multi-organ systems which cannot be simply predicted *in vitro*. On the other hand, the animal model has also received considerable criticism, particularly in industry, where many pharmaceuticals pass through the time-intensive and expensive animal testing stage only to be retracted at the human trial stage. These do not get approved or have to be discontinued due to a late discovered side effect or ineffectiveness (Ledford, 2011; Hutchinson & Kirk, 2011; Arrowsmith, 2011).

The predictive power of animal models and their possible replacement and reduction has been a focal point of discussion and was already mentioned in the first ever UK large scale survey where Russell and Burch's 3R (replacement,

reduction and refinement) principles were first introduced (Russell WMS, 1992). One of the arguments made in this original publication was the need to validate the ability of animal models to represent human processes and keep focus on laboratory efficiency so that the least amount possible of an animal species is used, which is defined as representative of humans for the application. The inter-species and intra-species variability have been heavily studied since then and significant differences in results have been found based on the species used. For example, when assessing pharmacokinetic variability in the testing of new compounds, one major risk factor was found to be higher variability in dogs compared to mouse, rat and monkey, particularly at high dose treatments (Daublain *et al.*, 2017). This was mainly attributed to the major variability of dog gastric pH and gastric residence time (Sagawa *et al.*, 2009). In the field of cancer biology, mouse models predominate, however these tend to display a number of limitations due to large biological variations such as lack of human lifespan compensating antineoplastic mechanisms, differing levels of DNA damage and vastly differing metabolic conversion mechanisms which disable their predictive behaviour for humans (Rangarajan & Weinberg, 2003). Genetic modification has been used to improve these limitations, however it is still difficult to recapitulate the complexity of cancer in an animal model (Heyer *et al.*, 2010). Some mouse strains that are naturally cancer-prone are well characterised, e.g the min mouse model , and may represent a good model for hereditary cancers such as *adenomatous polyposis coli* (Moser *et al.*, 1995). However hereditary cancers might not represent the genetic landscape of sporadic cancers. Syngeneic tumour models, e.g. myeloma 5T33 model, are propagated in genetically identical littermates and represent tumours that may be 'passaged' between animals (Manning *et al.,* 1992). However these models often represent a single cancer in multiple different animals and may be artificially homogeneous vs. spontaneous cancers. Finally, xenograft models, typically growing human cancers in immunocompromised mice, are gaining widespread use. Initial limitations of growing established cell lines in mice have been super-ceded by patient-derived xenograft models, whereby sporadic human cancers are grown in athymic mice. These models suffer from a lack of endogenous tumour immunity, however drug responses in mouse models predicts patient responses well (Poh, 2016). Naturally occurring cancer in dogs has been suggested as a more predictive

chemotherapeutic model in this field, however further knowledge of the comparative oncology between dogs and humans would be required (Sultan & Ganaie, 2018; Lawrence *et al.*, 2015). Overall, it is very difficult to select an animal model which is representative of the human disease situation and considerable time and funding is lost due to false positive and false negative results.

Recent focus of disease modelling has been dedicated to alternative *in vitro* models such as three-dimensional (3D) cultures and microfluidic systems. 3D constructs employ the same cell lines, primary cells or stem-cell derived cultures as are used in 2D cell culture models (Ravi *et al.*, 2017). However, 3D constructs produce cultures with different cell-cell interactions to 2D cell culture, and an altered environment, towards better mimicking of the *in vivo* environment (Wang *et al.*, 2018). 3D culture has been shown to alter cell signalling to produce a more representative environment using altered adhesive, mechanical, topographical, soluble and extracellular matrix (ECM)-bound cues to aid cell processes such as migration, proliferation repolarization and matrix remodelling (Baker & Chen, 2012). These cultures have shown similar gene expression and morphology to cells *in vivo* for biomedical applications and translational medicine (Ravi *et al.*, 2017; Duval *et al.*, 2017; Dutta *et al.*, 2017). Additionally, microfluidic systems may contain 2D or 3D cultures; however, the structure is designed to improve functionality similar to *in vivo* by introducing a more representative nutrient input and waste output, as well as dynamic therapeutic dosing (Trietsch *et al.*, 2017).

On the other hand, there are some drawbacks of switching to 3D cell culture workflows. Drawbacks of 3D cell culture vs. 2D cell culture include increased complexity of experimental design, and lack of standard methods of analysis, resulting in potentially different results depending on 3D methods employed (Hilton *et al.*, 2019; Nunes *et al.*, 2019; Shieh *et al.*, 2017; Stock *et al.*, 2016) (Table 1.1). Furthermore, cell lines grown in 3D cell culture in different scaffolds may exhibit markedly different drug responses, whereas responses on plastic in 2D cell culture may be more reproducible, if not representative of the *in vivo* situation (Hongisto *et al.*, 2013). Cost should also be considered, as some of the currently available *in vivo*-like culture methods involve the use of expensive medium components, such as R-spondin, or scaffolds or scaffold formation

techniques, such as electrospinning, which are not available in all laboratories (Shin *et al.*, 2018; Sachs *et al.*, 2018).

1.1.1 3D cell culture methods

There are several commonly used types of 3D culture method (Table 1.1) (Figure 1.1). These differ greatly in production and culture approach and each method possesses advantages and disadvantages for a chosen application.
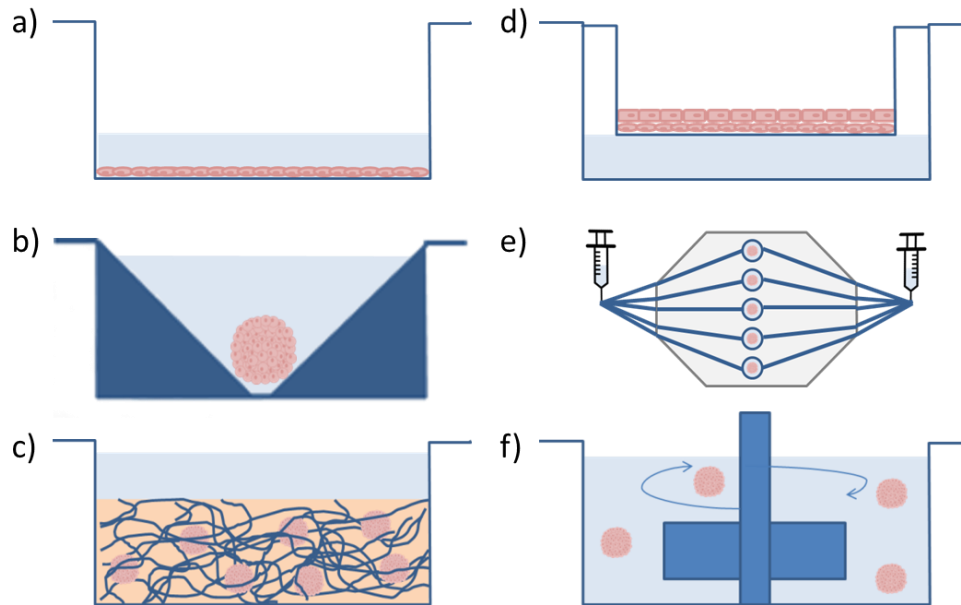
Figure 1.1 Types of cell culture. a) 2D cell culture. Cells grown in monolayer directly on plastic or glass surfaces. b) Attachment prevention culture. Cells are cultured on top of a non-adherent surface and form spheroids. c) Embedded culture. Cells are cultured inside a natural/synthetic scaffold e.g. hydrogel. d) Interface culture. Cultures where air-liquid interface is required e.g. skin constructs. e) Microfluidic culture. Cells are cultured in specially designed microchips, with a flow present. These can be either embedded in a scaffold or flow trapped by preventing cell flow through a channel. f) Bioreactors. Cells are cultured in rotating vessels which promote aggregation.

Type of culture	Cost	Variability	Complexity	Throughput	Ease of culture	Extended incubation
2D cell culture	Low	Low	Low	High	Easy	X
Attachment prevention	Low - Medium	Low	Medium	High	Easy-Moderate	✓
Embedded	Medium - High	Medium - High	High	Low - Medium	Easy – Moderate	✓
Interface	High	Medium - High	High	Medium	Easy – Moderate	✓
Microfluidics	Medium - High	Low - Medium	Medium - High	Medium - High	Moderate - Difficult	✓
Bioreactor	Low - Medium	Low	Medium	Medium	Easy - Moderate	✓

Table 1.1 Comparison of culture types

1.1.1.1 Attachment prevention

The attachment prevention technique (Figure 1.1b) is one of the simplest and low-cost 3D techniques available, often used for cancer modelling. It consists of the use of ultra-low attachment surfaces, such as commercial ultra-low attachment plates or agarose coated plates, or suspension of cells within an environment which prevents cell adhesion to a surface, such as the hanging drop model (Thomsen *et al.*, 2018; Close *et al.*, 2018; Shri *et al.*, 2017; Costa *et al.*, 2014). These are commonly used to produce multicellular tumour spheroids (MCTS) (Feng *et al.*, 2017). An additional benefit of this type of culture is that the spheroids can be cultured separately and are often highly reproducible, which allows for individual monitoring and ease of handling. However, this method is not ideal for all cultures, and in some cases cells will not form spheroids or display higher functional behaviour, as could be observed in other types of 3D cultures due to a lack of environmental factors (Nagelkerke *et al.*, 2013).

1.1.1.2 Scaffolds

Scaffold models are based on a suspension of cells within a construct, either of natural or synthetic origin (Figure 1.1c). Natural scaffolds, such as laminin-based basement membrane extract (e.g. Matrigel), collagen or hyaluronic acid based hydrogels are biocompatible as they are made up of ECM components (Gillette *et al.*, 2008). In the case of single component scaffolds, there may be a lack of ECM complexity, which may lead to a lack of functional differentiation for cell types which are more dependent on the stroma. On the other hand, use of a complex cell-derived basement membrane extract (BME) would provide more ECM complexity, but would introduce high inter-batch variability and a higher possibility of unknown factor effects. Most of the BMEs available are derived from the basement membrane of the Engelbreth-Holm-Swarm (EHS) sarcoma the composition of which may have unwanted effects, due to the presence of growth factors and other ECM components which influence cell behaviour (Vukicevic *et al.*, 1992; Kleinman *et al.*, 1986). Other natural scaffolds, such as alginate, agarose and cellulose, are biologically derived however contain no animal derived ECM components for the cells to recognise, as they are plant-based (Moffat *et al.*, 2018; Aurich *et al.*, 2018; Modulevsky *et al.*, 2016). Synthetic scaffolds, such as poly-ethylene glycol (PEG) or other polymer hydrogels can be

tailored mechanically to the application requirements, are known to be reproducible and can be sterilised prior to use. The synthetic scaffolds can also be enhanced with specific ECM binding motifs to improve differentiation and growth (Gentile *et al.*, 2017).

To achieve a complex environment, such as that of tissues and organs, some research has focused on the use of decellularised organs as matrices. In these cases an organ is decellularised, commonly by perfusion, and the native macro and micro-architecture remains intact. These scaffolds potentially contain all the necessary infrastructure, signalling cues for cell differentiation, attachment and function required for a highly efficient, complex model (Lorvellec *et al.*, 2017; Tapias *et al.*, 2015). However, these scaffolds are very time consuming and costly to produce for all applications. Additionally, the methods used to decellularize tissue may not remove all cells, leading to safety concerns for *in vivo* applications and concerns of cellular contamination for *in vitro* purposes (Saldin *et al.*, 2017).

1.1.1.3 Interface models

Mechanically-supported 3D models are commonly used for skin constructs but have also been used for other tissue such as lung and GI tract cancers (Elbadawy *et al.*, 2018; Hiemstra *et al.*, 2018; Kim *et al.*, 2017) (Figure 1.1d). This type of culture allows for presence of an air-liquid interface which aids cell differentiation over time. In the case of skin equivalent models a co-culture of keratinocytes and fibroblasts is deposited on top of a wire mesh or well inserts. For cancer models, epithelial cancer cells are typically grown on a fibroblast layer which acts as stroma and excretes important factors for continued growth (Emura & Aufderheide, 2016). These models have shown to have very high correlation to *in vivo* yet they are relatively expensive, and there is a significant difference in organisation complexity between different model types (Zscheppang *et al.*, 2018; Lee *et al.*, 2014).

1.1.1.4 Microfluidics

Microfluidic methods are of much higher complexity, yet there are many benefits (Figure 1.1e). The cells are cultured in micron-sized fluidic chambers, with either a continuous or transient media exchange. These models allow easy integration into automation, high throughput, drug studies and simultaneous imaging. Recent

technological advancements make production of chips easier, more affordable and the materials chosen more amenable to analysis (Knowlton *et al.*, 2016). For example, dependant on the material used for the microfluidic construct, rapid evaporation may occur (Mehling & Tay, 2014). Microfluidic constructs have been combined with scaffold cultures to produce complex cultures. For example, a commercially available Mimetas microfluidic plate was used in combination with a collagen scaffold to mimic vascular permeability *in vivo* (van Duinen *et al.*, 2017).

1.1.1.5 Bioreactors

Bioreactor models consist of either free flowing or bead-attached cells in a constant flow environment (Figure 1.1f). This model type encourages proliferation and cell-cell attachment by increased contact and produces reproducible, large spheroids at high-throughput whilst still maintaining nutrient and waste flow. Bioreactors have been used for enhanced hepatogenic, osteogenic, chondrogenic stem cell differentiation (Khurshid *et al.*, 2018; Egger *et al.*, 2017; Cipriano *et al.*, 2017). Perfusion systems have also shown use in long-term organotypic, specifically tumour, cultures by maintaining their physiological state (Wan *et al.*, 2017). Scaffolds can also be combined with bioreactors in order to improve the culture perfusion to O_2, nutrients and release of waste products like CO_2 and lactate which would usually have a varied distribution (Schmid *et al.*, 2018; Yi *et al.*, 2018).

1.1.2 Cell culture origin

An important decision in choice of 3D culture is the cell source required for a functional construct. The cell viability, phenotypic functionality and activity in the construct must be at sufficient levels to predict the reactions of its target tissue.

In the cases of all 3D constructs, similarly to 2D cultures, primary cells are most often incorporated due to their high equivalence to *in vivo* cells in human subjects. There are, however, disadvantages to the use of primary cells such as their phenotypic instability during culture, scarce and irregular availability, inter-donor variability and their poor plating efficiency. Phenotypic instability of primary cells, leading to loss of key functions, has been shown to occur less in 3D models (Lee *et al.*, 2013). This expansion and self-organisation, with exhibition of correct

morphology and behaviour, was observed in primary human breast epithelial cells grown within hydrogel scaffolds (Sokol *et al.*, 2016).

Use of immortalised cell lines for 3D culture has been common over the past few years, not solely for the study of cancer. The main disadvantage of the use of immortalised cell lines is the loss of cell type function-specific activity compared to primary cultures. On the other hand, benefits of immortalisation include robustness, reproducibility and unlimited availability, which simplifies the culture process. With use of 3D models, research has also partially overcome the loss of functional activity of cell lines (Gago-Fuentes *et al.*, 2014).

Over the years, stem-cell derived cultures were developed as an attractive option for pharmacodynamic and pharmacokinetic models. However, these differentiated cells, until recently, possessed very low phenotypic function and the differentiation methods were too complex and time consuming. By incorporating the use of 3D scaffolds, several recently produced models show an improvement in functional activity and highly optimised differentiation protocols (Khetan *et al.*, 2013). The use of stem cells in 3D cell culture was improved greatly by the Clevers group (2016), who developed a method of growing organoids from a patient derived stem-cell population, using a mixture of Wnt/R-Spondin and Noggin conditioned medium and specific growth factors combined with a BME gel matrix, and are now able to use this method for a variety of tissue types (Clevers, 2016; Jung *et al.*, 2011).

An increasing amount of 3D models include stromal, supporting cell types in co-culture with parenchymal, tissue function defining cells. Cell-cell interactions are highly relevant to all tissues as they have a dramatic influence on the tissue environment. An increased amount of cancer 3D models are incorporating cancer-associated fibroblasts with the tumour culture, as these have been shown to play a supporting role in cancer. For example, a recent 3D cell culture platform, Tissue Roll for the Analysis of Cellular Environment and Response (TRACER), probed cell-cell interactions by incorporating cancer associated fibroblasts (CAFs) in head and neck tumour cultures (Young *et al.*, 2018). In other cases, co-culture shows that changes in drug interaction may not always be due to signalling but may be physical. A triple co-culture model made up of epithelial

cells, monocyte-derived macrophages, and dendritic cells, demonstrated barrier ability. Polyelectrolyte microcapsules were not able to pass through the triple co-culture, though in previous studies the passing of small nanoparticles was observed between macrophages and dendritic cells (Kuhn *et al.*, 2015).

1.1.3 3D culture of cancer cells

3D models have been introduced over the last few decades to improve predictability of pre-clinical oncological drug studies (Ibarrola-Villava *et al.*, 2018). This has been achieved with 3D modelling using cell lines, differentiated stem cells and primary tumour cells.

Use of cell lines is a cost effective and simple method, however confirmation of its validity and representability is required for these models to be used for chemotherapeutic testing and biological studies. In several cases, cell signalling pathways has been thoroughly analysed to determine tumour cell changes in 3D compared to monolayer culture. Altered signalling has been observed in the Mitogen-activated protein kinase (MAPK) pathway and a general reduction in cell cycle progression (Stadler *et al.*, 2016). An evaluation of 3D cultured breast cancer cell lines showed a higher resistance to classical chemotherapy drugs and increased expression of cell survival and drug resistance proteins, such as Akt and p-glycoprotein (Pgp), compared to 2D cultures, suggesting a higher representability of *in vivo* chemotherapy resistance (Breslin & O'Driscoll, 2016).

A recent innovation created by the Clevers (2016) lab is patient derived tumour organoids. These can be produced from patient derived epithelial tumour material and form *in vivo* like structures which are representative of the original tumour (Clevers, 2016). These have the potential for long term propagation and the creation of disease representative biobanks (Sachs *et al.*, 2018; Van De Wetering *et al.*, 2015). As the method used forms clonal organoids, the intra-tumour diversification in cancers can be observed by examination of differences between individual clones derived from a single patient (Roerink *et al.*, 2018).

It is widely agreed that the tumour associated ECM contributes towards cancer behaviour, including its influence on the hallmarks of cancer (Pickup *et al.*, 2014).

The hallmarks of cancer are defined as essential acquired capabilities for the development, growth and dissemination of all human cancers (Hanahan & Weinberg, 2011). The hallmarks of cancer include maintenance of proliferative signalling, evasion of growth suppressors, resistance to cell death, replicative immortality, promotion of angiogenesis, as well as activation of invasion and metastasis. By influencing each of the different hallmarks of cancer using biophysical and biochemical cues the ECM can have a significant effect on cancer behaviour and malignancy (Pickup *et al.*, 2014). Even sarcomas, which arise from mesenchymal origin and are part of the stroma, should benefit from 3D cell culture. In these tumours, however, the presence of ECM components, such as collagen, laminin, or glycosaminoglycans (GAGs), within the scaffold and mechanical characteristics may be of importance for differentiation and maintenance (Gao *et al.*, 2017; Teicher, 2012). Several 3D models of sarcoma have been developed using cell lines, which demonstrated restoration of chemo sensitivity in chondrosarcoma and vascular-like formation in a co-culture model of osteosarcoma and endothelial cells (Chaddad *et al.*, 2017; Van oosterwijk *et al.*, 2012).

As increased culture time period and high-throughput capabilities are required to integrate these models into industry workflows, more focus has been concentrated on microfluidic constructs. A microfluidic platform has been created recently for the study of chemotherapeutic drug efficacy, employing U251 human glioma cell lines to form spheroids by physical trapping during flow. Physical trapping consisted of creating a microfluidic design which sequestered cells in designated areas in order to create aggregates. They observed long-term (over one month) culture stability and increased apoptotic response as well as decrease in spheroid size due to treatment with clinical chemotherapeutic drugs Vincristine (VCN) and Bleomycin (BLM) (Liu *et al.*, 2015). Another highly versatile microfluidic system was developed to try and overcome some challenges posed by typical microfluidic models, such as nutrient availability (McMillan *et al.*, 2016). These systems overcome the 'static' nature of *in vitro* cultures, which do not represent the *in vivo* situation of vasculature-based nutrient and metabolite delivery. The model could maintain spheroid cultures for long time periods whether they were in medium or within a scaffold (McMillan *et al.*, 2016).

1.1.4 3D cell culture strategies for models of hepatoxicity

Idiosyncratic drug hepatoxicity is an adverse reaction to drugs occurring in a minority of patients, which cannot be predicted using usual animal tests. This is a major cause for concern during drug discovery and development and the highest contributor to post-clinical trial withdrawal of pharmaceuticals (Kaplowitz, 2005). The liver is an exceptionally important organ for drug development studies, as it is the major site of drug metabolism elimination and toxicity. Presently, pharmaceutical absorption, distribution, metabolism and excretion (ADME) studies include extensive testing of drug hepatotoxicity and metabolism on firstly 2D cultured primary hepatocytes, microsomes or cell lines then moving onto animal studies for more complex tests such as metabolite profiling in order to identify the full adverse outcome pathway (AOP) of a therapeutic candidate, as illustrated in figure 1.3.
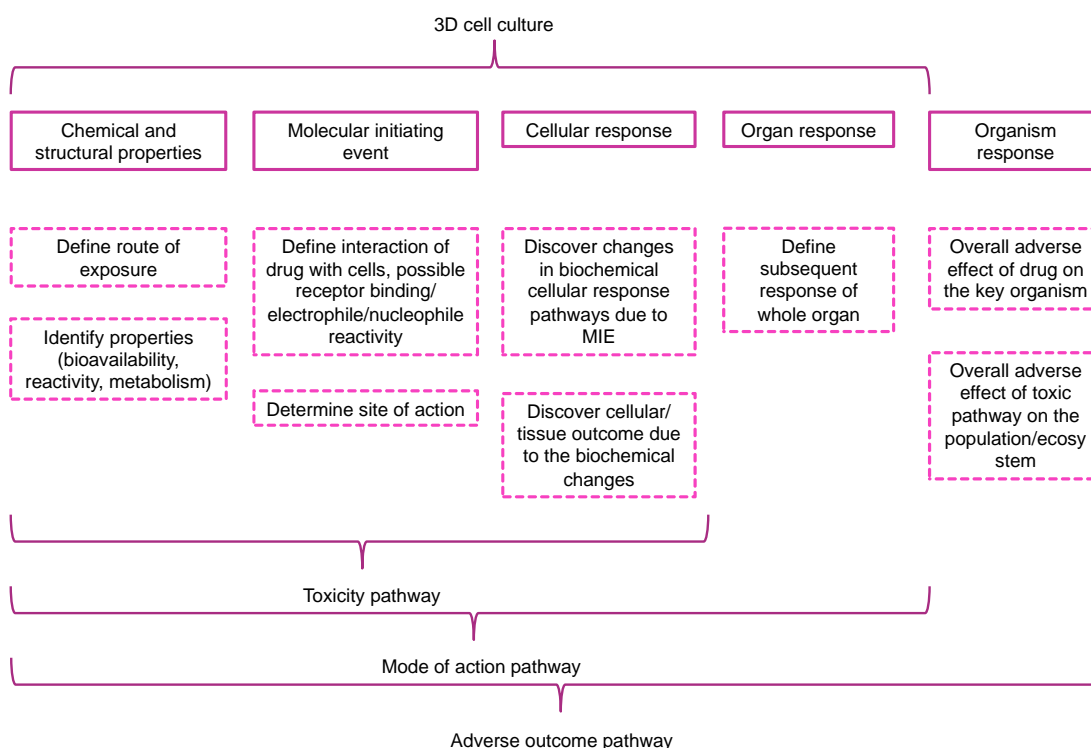
Figure 1.3 3D cell culture applications for identification of an adverse outcome pathway for a chemical of interest (adapted from the OECD AOP handbook).

There have been many 3D cell culture models based on cell lines due to their robustness, reproducibility and unlimited availability. In 2D cell culture, cell lines such as HepG2 have undergone criticism as these lack the basal gene expression profile that hepatocytes possess, therefore they lack the metabolic activity required from a pharmaceutical study model (Zeilinger *et al.*, 2016; Godoy *et al.*, 2013). However, in an extracellular matrix-based hydrogel (Matrigel) 3D culture the HepG2 cell line has been shown to recover hepatic function, increased Cytochrome P450 (CYP) enzyme activity and form hepatic culture associated structures, such as bile canaliculi (Ramaiahgari *et al.*, 2014). Several other immortalised lines, such as HepG2/C3A and HepaRG have been used more recently due to a more hepatic differentiated phenotype (Nelson *et al.*, 2017). These have also been employed in 3D cell culture, showing promising results. For example, the HepaRG cell line hepatic differentiation relies on high concentrations of dimethyl sulfoxide (DMSO) in the cell media in 2D cultures, which may interfere with many pharmaceutical studies (Anthérieu *et al.*, 2012). By suspending this cell line in an alginate-based 3D scaffold Rebelo and colleagues could culture the cells in DMSO-free media, whilst still obtaining comparable phase I drug metabolism enzyme activity, formation of phenotypic structures and excretory functionality, assessed by specific activity of multidrug resistance-associated protein 2 (MRP2) (Rebelo *et al.*, 2014). 3D cell line models are being utilized in drug adverse outcome studies. For example, a recent 3D model study has emerged, using an *in vitro* HepG2/C3A microfluidic model, in combination with *in silico* pharmacokinetic mathematical simulations, to investigate N-acetyl-p-aminophenol (APAP), otherwise known as acetaminophen, toxicity in detail. Levels of reactive oxygen species were shown to increase after APAP treatment, metabolism was determined by monitoring biotransformation products APAP-sulphate and APAP-GSH and growth inhibition due to treatment was also measured. Using the experimental information and combining it with other information in the literature, predictions could be made of the intracellular concentration of APAP and N-acetyl-p-benzoquinone imine (NAPQI) accumulation in a cell (Leclerc *et al.*, 2015).

Even with the progress made with immortalised cell line cultures, primary hepatocytes still possess a higher basic hepatic functionality, and these are also

commonly incorporated into 3D cultures. By using 3D cell culture techniques, the dedifferentiation that primary cells undergo in 2D cultures are slowed or reversed and these cells have been observed to regain function. A bioprinted human liver tissue mimetic, comprised of patient-derived hepatocytes and non-parenchymal cells in a defined architecture, maintained adenosine 5′-triphosphate (ATP), albumin and CYP450 enzyme activity over 4 weeks in culture (Nguyen *et al.*, 2016).

Development of stem-cell derived hepatic 3D cultures has also increased in the past few years. Broutier and colleagues utilised a basement membrane extract matrix and defined medium for the propagation of stem-cell derived human and mouse adult liver organoids and demonstrated their differentiation into functional cells which were genetically stable (Broutier *et al.*, 2016). Further work has focused on adapting these culture protocols for drug screening purposes by increasing throughput and generation of robust, simple conditions (Sgodda *et al.*, 2017; Carpentier *et al.*, 2016).

1.1.5 Molecular analysis of alternative models

Alternative models can be defined as *ex vivo* or *in vitro* models of disease or tissue function, which have been designed to represent their *in vivo* human equivalent tissue. These models are developed as an alternative to experiments involving patients, which are limited to clinical trial studies and cannot be invasive, and animal models, which are also limited and not always representative of human function and response to therapeutics. The majority of alternative models are analysed by methods such as commercial biochemical activity assays, immunohistochemistry (IHC), enzyme-linked immunosorbent assay (ELISA), fluorescent probes and colorimetric assays in order to observe specific cell activity or determine abundance of molecules involved in pathways of interest. This type of analysis is typically moderate/low-throughput and relatively costly. Additionally, not all methods can retain spatial information, i.e. western blotting and biochemical assays, and others are not capable of detecting high levels of multiple analytes within a single experiment i.e. fluorescent microscopy. To integrate use of these models in research and the higher-throughput required by

industry, high content analytical methods, such as mass spectrometry imaging, should be applied to this field. Using mass spectrometric tools allows for the simultaneous detection, and even quantification, of multiple molecular species, minimizing sample required and increasing experimental efficiency.

1.1.5.1 Mass Spectrometry of alternative models

Mass spectrometry is an analytical method which involves ionization of chemical species within a sample of interest and subsequent sorting of the ions formed based on their mass-to-charge ratio (*m/z*). This enables the specific and sensitive determination of the molecular make-up in the sample of interest. In a typical MS experiment a sample may be solid, liquid or gas and each type of instrument can handle different forms of sample. For example, Liquid-chromatography mass spectrometry (LC-MS), which is the most commonly used mass spectrometric method, is capable of liquid sample analysis. However, samples can be manipulated and prepared for analysis, whilst maintaining the original levels of analyte. In the case of some solid samples, for example biopsies, homogenisation and extraction can be used in order to obtain a suitable form for analysis. The data, consisting of *m/z* values and abundances of each chemical species present, is displayed as a spectrum. Tandem MS (MS/MS) could be further used to confirm identities of the molecules by selected collisional dissociation inside the instrument and analysis of the fragment ions produced.

A large number of *ex vivo* and *in vitro* models are commonly investigated using mass spectrometry methods for characterisation of the model and its translatability to *in vivo* results. LC-MS has been applied to analysis the metabolome of 3D constructed cultures in order to study the metabolic reprogramming that occurs in cancer (Rodenhizer *et al.*, 2016). The 3D cancer model was developed specifically to rapidly unroll after culture, exposing different biocomposite layers for hypoxic gradient investigation. The design limits metabolomic changes by reducing the time between culture and analysis. Using this unique TRACER system and mass spectrometry they could observe changes in the metabolome consistent with known hypoxia mechanisms, such as the glycolytic switch and decreased levels of glutathione (Rodenhizer *et al.*, 2015). LC-MS was also used to characterise the processed human cardiac extracellular matrix protein composition, to improve a decellularised human cardiac tissue

model. The method allowed detection of residual protein material 'contamination' which was not previously apparent with conventional assays for residual DNA and ECM proteins (Kappler *et al.*, 2016). Recently, a microfluidic culture method was used to maintain the metabolic functionality of primary hepatocytes for modelling of Hepatitis B virus infection. In this study, mass spectrometry was used to indirectly quantify the increased activities of P450 drug metabolism enzymes by quantification of their metabolites; tacrine (CYP1A2), diclofenac (CYP2C9), and midazolam (CYP3A4) (Ortega-Prieto *et al.*, 2018). In a different study, an increased complexity immune-competent co-culture liver model was established and characterised in order to capture human toxicities, which arise from immune responses. Here, LC-MS/MS was used to analyse the acute phase response to diclofenac and demonstrate the applicability of the model in the drug discovery workflow (Sarkar *et al.*, 2017).

1.1.5.2 Mass spectrometry imaging of alternative disease models

Mass Spectrometry Imaging (MSI) is a novel molecular imaging method which, due to its many applications, is increasingly popular in many fields (Doerr, 2018). The use of MSI for the analysis of alternative disease models has several advantages. The main two advantages are the potential for untargeted *de novo* discovery, and the capability to observe multiple analytes of interest in a single experiment. Unlike LC-MS, the mass spectrometry-based method mostly used in the analysis of alternative models, MSI is also able to preserve spatial information, requiring no homogenisation of the sample. Furthermore, less sample preparation is involved. Many MSI methods are also non-destructive, which may lead to the sample being used again, commonly for a histological stain. Considering these advantages, MSI will become a powerful, regularly used technique for the investigation of alternative, *in vitro* disease models.

Several MSI methods are suitable for the analysis of alternative disease models. When looking for a high spatial resolution method to observe the alternate model microenvironment in detail, Secondary Ion Mass Spectrometry (SIMS) imaging must be considered due to its high spatial resolution imaging capabilities. The technique was demonstrated recently to detect the subcellular distribution of cardiolipin and a multitude of phospholipids and instrumental developments were carried out in order to increase the mass range capabilities of SIMS (Tian *et al.*,

2019). SIMS is a mass spectrometry method based on pulsed sputtering of a sample surface using a primary ion beam and analysing the generated secondary ions (Vanbellingen *et al.*, 2015). A static SIMS instrument is capable of imaging a wide range of samples or a dynamic SIMS instrument could be chosen which possesses the ability to depth profile to create three-dimensional images, with some loss of range. SIMS is an imaging method currently capable of single-cell and even sub-cellular imaging, as shown by Passareli and colleagues who observed the cellular uptake of a pharmaceutical compound in a single macrophage cell (Passarelli *et al.*, 2015). As of yet, this methodology hasn't been used for the analysis of 3D cell cultures, however it would provide extremely detailed information of the composition and interaction of cells and the heterogeneity within a model. This ability was demonstrated by Barnes and colleagues, who were able to distinguish between two different cell types within a culture using SIMS (Barnes *et al.*, 2012).

Laser Ablation Inductively Coupled Plasma Mass Spectrometry (LA-ICP-MS) is a molecular imaging method commonly used for trace elemental imaging in tissue sections, as it can provide elemental information and, with the use of matrix matched standards, or more recently isotope dilution, is capable of quantitative imaging (Moraleja *et al.*, 2018). LA-ICP-MS has been used in its imaging modality in order to examine the cellular uptake of a second generation photosensitizer into a tumour spheroid, with and without the assistance of a nanoparticle delivery system. A more homogenous distribution of nanoparticle delivered photosensitizer was determined using imaging, compared to freely dissolved drug (Niehoff *et al.*, 2014). In order to achieve high sensitivity with this system, the drug was tagged with palladium. Having to tag the analyte of interest is a significant disadvantage as, since a target has to be known, it means that the technique is not suitable for de novo discoveries. However, as shown in a more recent study using LA-ICP-MSI, tagging is not always required as long as the analyte of interest has a suitable metal component. Niehoff and colleagues developed a methodology for the imaging of platinum group containing drugs, such as cisplatin, in tumour spheroids, as well as the previously imaged palladium tagged photosensitizer. Quantitation of all the imaged drugs was also achieved by using different matrix-matched standards (Niehoff *et al.*, 2016) . In both cases

of using LA-ICP-MSI, high spatial resolution was used (<10µm), which is an advantage of the technique, as well as the need for very little sample preparation. Nevertheless, this method can only be used for *de novo* discovery when looking at changes in metal groups.

Another commonly used imaging method, Desorption Electrospray Ionisation (DESI), is also potentially capable of alternative model imaging. DESI requires minimal sample preparation compared to other methods, is set up at ambient conditions (no high-pressure vacuum) and can analyse many different sample types, though it is presently used mainly for small molecule and lipid analysis. Although in the past it was limited by spatial resolution capabilities and robustness, recent improvements have led to >20µm consistent spatial resolution (Tillner *et al.*, 2017).

1.1.5.2.1 *Matrix Assisted Laser Desorption Ionisation Mass Spectrometry Imaging*

Matrix Assisted Laser Desorption Ionisation Mass Spectrometry Imaging (MALDI-MSI) is an imaging method which was introduced by Spengler (1994) and developed primarily by Richard Caprioli and colleagues in 1990 and is currently the most popular ionisation source used for mass imaging worldwide for biological applications (Caprioli *et al.*, 1997; Spengler, 1994). The approach consists of coating a sample with a suitable energy absorbing material (matrix) that is then fired upon with an ultraviolet/infrared (UV/IR) laser. Most commonly, a highly focused laser is fired on a large array of two-dimensional positions on a sample plate, which creates a set of sample mass spectra with corresponding x and y coordinates. This then allows for reconstruction of the results into an image made up of spatial information and abundance of ions at each ionisation point (Francese & Clench, 2010). Reducing the raster distance increases the number of ionisation points on the sample and number of subsequent pixels on the image, leading to a higher spatial resolution. This can either be done by oversampling, where the laser diameter is slightly smaller than the step size and the raster points overlap slightly, or by reducing the laser diameter and therefore reducing the ablation area.
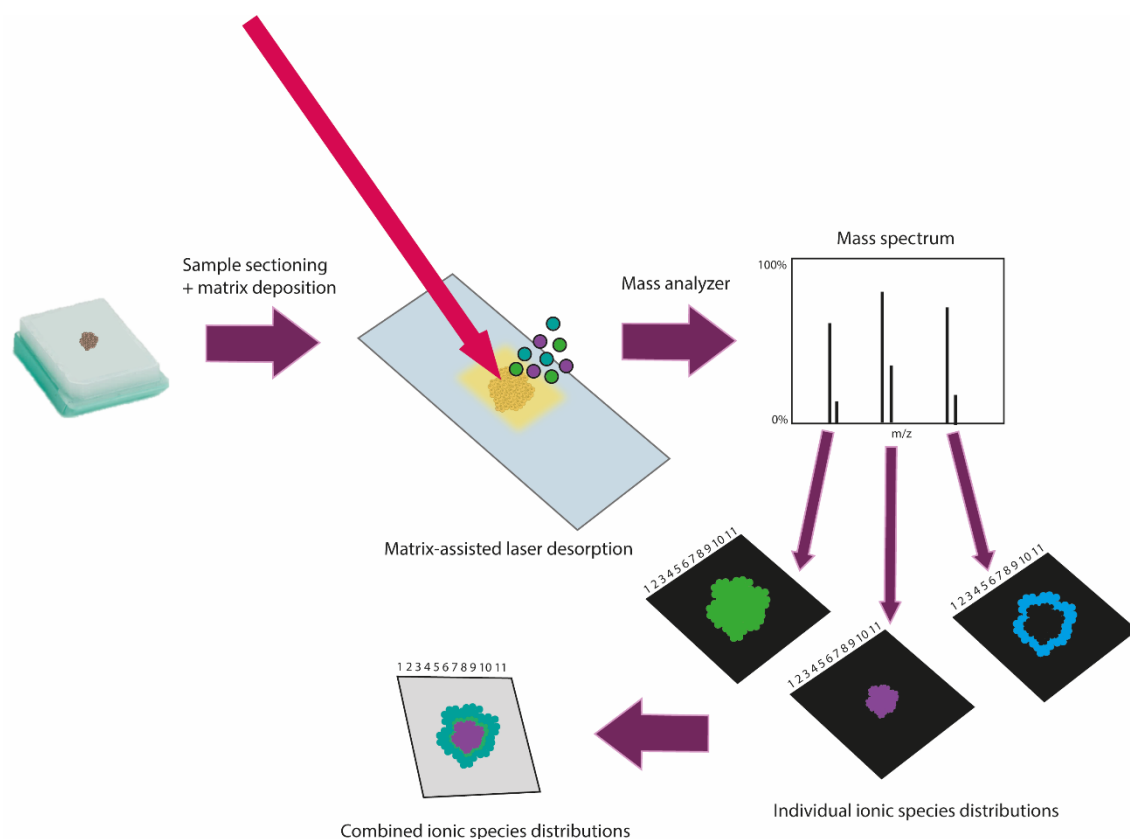
Figure 1.2 A typical MALDI-MSI workflow

There are several advantages to using MALDI as an ionisation instrument for the imaging of biological substances (Aichler & Walch, 2015). The main advantage is its ability to produce highly resolved mass spectral data without damaging the sample, which could then be used for other experiments such as histological stains and data can be combined for an enhanced understanding of the substance involved. This is particularly useful in situations where samples are limited or differences between serial sections are too large for comparison. Because it is regarded a 'soft' ionisation technique it can analyse a very wide mass range of analytes compared to other ionisation techniques, typically from 100 Da to over 100kDa, as the ionisation process does not degrade certain molecular groups as much as other methods. In addition, the MALDI mode of ionisation produces mostly singly charged ions, which makes data analysis of complex mixtures more straightforward (Cornett *et al.*, 2007). Because the ionisation of analyte is performed using a UV/IR, laser the irradiation area size and location can be controlled very precisely. The irradiation area can vary from around 5µm to over a 100µm and can be simply manually controlled (Francese

& Clench, 2010). The instrumentation for MALDI-MSI instruments has also improved greatly in recent years leading to greater resolution, high sensitivity and, most importantly, higher throughput. These features are key for making these instruments efficient to use in every day research in pharmaceutical research and development and oncology fields (Schulz *et al.*, 2019; Baker *et al.*, 2017; McDonnell *et al.*, 2017).

1.1.5.2.2 Drawbacks of MSI

However, use of MSI for the analysis of biological samples also has some drawbacks. As mass spectrometers are highly complicated instruments the cost of a suitable instrument, particularly one capable of MSI, is much higher than the cost of more common benchtop analytical techniques. Therefore, currently these instruments are only present in MSI focused research group institutes and in analytical departments within industry. Additionally, in order to obtain and interpret MSI results at least some knowledge of the methods and software is required, as the methods are far more complicated and less user friendly than commercialised standardised assays. Although methods for specific molecular groups can be created, these often require optimisation in terms of sample preparation and changes in instrumental methods for optimal analysis of a new sample. As most mass spectrometric methods are often lab-developed these can be substantially different from one another. Standardisation is principally an issue in the MSI field as many different sample preparation techniques and instrumental set-ups are currently used all over the world to achieve similar goals. This leads to a discrepancy between different labs and an inability to create reference intervals when detecting specific analytes, which have potential for clinical impact (Addie *et al.*, 2015). For a method where results differ by a significant level with different sample preparation, standardisation is important to note for any experiment. Some effort within the field has been made towards standardisation primarily under the support of the European network COST Action BM1104. When considering shortcomings of MSI, the fact that some molecules are more readily ionisable than others should be mentioned. The technique is dependent on ionisation efficiency of molecules of interest which, for example in the case of hormones, is not always high. This is partially being overcome with derivatization methods in order to add charges to otherwise neutral molecules (Barré *et al.*,

2016; Beasley *et al.*, 2016; Holst *et al.*, 2016). Additionally, once a molecule of interest is identified using MSI, it is often difficult to fully confirm its identity. This is often done in the form of tandem MS techniques, however due to poor peak separation, low molecular abundance or inability to narrow the mass selection window, peak identifications are not always easily confirmed through MS/MS.

1.1.5.2.3 Laser types commonly used with MALDI-MSI

The MALDI technique involves the use of a laser as the energy source which triggers the desorption ionisation process by irradiation of the sample surface. There are several types of lasers currently used for MALDI-MSI. Since the matrix is the energy absorbing molecule within the reaction, the laser wavelength doesn't need to be matched to a specific analyte but to the matrix absorption frequency, which makes MALDI more universal compared to other laser techniques (Robinson *et al.*, 2018). Among the selection of lasers, UV lasers are the most commonly in use due to their ease of operation and affordability. Frequently, N2 ($\lambda = 337$nm) or Nd:YAG ($\lambda = 266$ or 355) lasers are used, although IR lasers such as Er:YAG ($2.94~\mu$m) could also be used, which may result in less fragmentation but lower sensitivity. In general, it is important to optimise the laser pulse energy in a given wavelength for a specific spot diameter in order to achieve the highest molecular signal without inducing a significant amount of fragmentation (Hoffmann & Stroobant, 2007).

1.1.5.2.4 Mass analysers commonly used with MALDI-MSI

A mass analyser is the part of a mass spectrometer in which the ions are separated based on their *m/z* values. Because MALDI is a pulsed ionisation technique and produces ions in bundles by an intermittent process it is well suited for analysis with the time-of-flight (TOF) analyser. A TOF analyser separates ions by their velocities which are determined by initially accelerating the ions with an electric field and letting them drift through a free-field region, called a flight tube and into a detector (Hoffmann & Stroobant, 2007). As all ions acquire the same kinetic energy, the time taken to drift through the flight tube is then directly correlated to mass and charge. Benefits of MALDI-TOF-MSI include their high upper mass range limit, which leads to imaging capabilities of very large molecules, and their high transmission efficiency, which leads to high sensitivity,

as well as their speed (Drake *et al.*, 2017). However, when higher mass resolution is required, the most common mass analyser in use for MALDI-MSI is Fourier Transform Ion Cyclotron Resonance (FT-ICR). This method is capable of much higher mass resolution than a TOF mass analyser, defined by the ability to resolve peaks at a much higher power, aiding distinction and identification of molecules (Piga *et al.*, 2019; M. Dilillo *et al.*, 2017). FT-ICR consists of trapping the ions within a magnetic field, called a cyclotron, and exciting all of them simultaneously by a rapid scan of a large frequency range. This induces a trajectory in each ion, which comes close to the detector wall perpendicular to the orbit. Transformation of the detected wave as a time-dependent function into a frequency dependent intensity function using a Fourier Transform (FT) is then done in order to retrieve data, which can be directly correlated to mass and charge (Hoffmann & Stroobant, 2007). There are downsides to this technique, such as the high cell vacuum necessary to achieve high resolution and the need for appropriate computers for the large amount of data flow, therefore a much higher cost, as well as it's limit of the number of ions in the cell.

1.1.5.2.5 Matrix application methods commonly used with MALDI-MSI

Matrix selection and application optimisation is an important part of MALDI-MSI analysis because it fundamentally determines the quality of results by altering the method sensitivity and spatial information quality. Selection of the matrix depends mainly on the type of molecule being analysed, the laser wavelength and whether positive or negative ions are being observed. In general, matrices tend to be small molecules, for easy sublimation, with highly conjugated structures, which therefore absorb strongly at the laser wavelength, are stable under vacuum, lack chemical reactivity and are soluble in analyte compatible solvents (Hoffmann & Stroobant, 2007). However, not only the matrix choice but also its application is important for analysis. Automatic spraying and sublimation are the two most common, reproducible techniques used for the application of matrix for MSI. Automatic spraying is a method developed to replace manual airbrush spraying and remove the variability observed due to inconsistencies in spraying distance and speed of application and therefore any negative effects, such as poor matrix coverage and analyte diffusion (Gemperline *et al.*, 2014). Using an automatic sprayer system generally improves the uniformity of matrix density and crystal

size, therefore increasing reproducibility, and has a good analyte extraction capability (Anderton *et al.*, 2016). However, in the case of some matrices this method is incapable of producing small regular crystals, which may be required for higher spatial resolution analyses. Sublimation is typically a solvent-free matrix application technique, which utilises the sublimation temperature of a matrix molecule to apply a defined amount of it onto a sample section, creating uniform, small matrix crystals. As it is a solvent-free method, analyte diffusion is reduced but this also comes with a reduction in extraction capability, particularly in proteins (Lin *et al.*, 2018). This may be overcome with recrystallization post-sublimation, however during this process the matrix crystals may once again become irregular (Lin *et al.*, 2018; Dueñas *et al.*, 2016). Use of binary matrices (a combination of two molecules) would also not be possible using this method, unless the matrices require similar sublimation conditions.

1.1.5.3 MALDI-MSI of alternative models

Compared to the amount of research conducted every year on *ex vivo* and 3D cell culture models, only a few research groups have utilised MALDI-MSI as a method of validating and facilitating the study of disease in alternative models. A number of research groups have begun work regarding this.

1.1.5.3.1 MALDI-MSI of 3D models of cancer

There is currently a vast amount of interest in analysis of 3D cultured cancer tumour spheroids, which are being used as *in vitro* models of cancer for characterisation and drug dynamics studies (Russo *et al.*, 2018). The first proof-of-principal publication on the use of MSI with these models, by Li *et al.* (2011) demonstrated that a MALDI-MSI workflow could be used to examine the changes in protein and peptide distributions within cancer spheroids in an unbiased fashion, suitable for *de novo* discovery (Li & Hummon, 2011). More recently, the same group produced a dynamic flow version of the cancer spheroid model, enabling the reconstruction of more representative conditions with the use of a fluidic device (LaBonia *et al.*, 2016). The platform was constructed to assess drug penetration and metabolism and allow dynamic dosing of the chemotherapeutic drug, irinotecan. Drug penetration into the spheroids was observed, as well as the distribution of its active metabolite SN-38 inside the spheroid core, necrotic region (LaBonia *et al.*, 2016). MALDI-MSI has also been used to evaluate

therapeutics in patient-derived colorectal tumour organoids, which are classed as a more representative model of the disease, by only two groups to date (Liu *et al.*, 2018; Hiraide *et al.*, 2016). Recently, MALDI-MSI was used to analyse a novel 3D model of high grade serous ovarian cancer (HGSOC) using a completely novel sample preparation method which did not require sectioning (Zink *et al.*, 2018). An ovarian explant was co-cultured fallopian-tube-epithelium-derived cells engineered to represent several stages of ovarian cancer in order to study metastasis of HGSOC to the ovaries. Using MALDI-TOF-MSI the key role of the molecule norepinephrine was demonstrated (Zink *et al.*, 2018).

1.1.5.3.2 MALDI-MSI of ex vivo models

Ex vivo models are also used to study human processes and some focus has gone towards development of methods to assess *ex vivo* models of disease. MSI of *ex vivo* cultured alternative samples is more straightforward to develop compared to 3D cell cultures, as the sample composition is identical to a human tissue sample, which is a common sample type analysed by mass spectrometry imaging techniques. The differing factor derives from the culture and treatment of the cells outside of the body. Explants of breast cancer cultured using a xenograft method have been imaged to visualise uptake of peptide drugs and probes. The benefit of using explants in this case was the control over the explant size and uniformity compared to spheroid culture (David *et al.*, 2018). The use of *ex vivo* human skin for the study of disease and treatment penetration has become more prevalent, possibly due to an increase in sample availability with an increasing popularity in cosmetic surgical solutions. MALDI-MSI has been recently used to generate quantitative skin distribution profiles of four different drug molecules (roflumilast, tofacitinib, ruxolitinib, and LEO 29102) applied topically to human skin explants (Bonnel *et al.*, 2018). Each of the drugs of interest had different physiochemical properties and therefore demonstrated the applicability of the method as a screening tool for topical drug products. Not only MALDI-MSI but also SIMS has been employed for the imaging of *ex vivo* skin. The aim of the study was to determine the fatty acid enhancing effect on drug penetration into human skin, yet using MSI it was discovered that all fatty acids used in the experiment penetrated the skin, however only oleic acid demonstrated significant enhanced penetration of the drug (Kezutyte *et al.*, 2013). However, the rapid

dedifferentiation and loss of viability of the explanted tissue is the main disadvantage of *ex vivo* models and these currently cannot be used in a majority of cases (Meijer *et al.*, 2017).

1.1.5.4 Challenges of MALDI-MSI analysis of 3D models

Several parameters would require consideration when analysing 3D cell models, as they are both similar to tissue and 2D cell culture models. These parameters will depend on the type of model used, its size, composition and sample preparation required. For instance, the majority of 3D cell culture models are relatively small (μm scale), which leads to many of these requiring an embedding step. This additional step also introduces more time to the sample preparation process, which should be considered particularly in the analysis of small molecules. The size of the sample will affect the spatial resolution and ionisation method to be used. As there are many alternative disease models available, sometimes the most appropriate model can be chosen to suit the method plan. MALDI-MSI does require a matrix application step and does not routinely provide spatial resolution in the very low µm range. In general, 3D cell culture models are not large in size. For instance, certain types of single clone tumour spheroids in the current literature are <300 µm in diameter, although use of macropellet spheroids of around 1-2mm is also common (Schultz *et al.*, 2016; Feist *et al.*, 2015). This does not result in issues for commonly used techniques such as fluorescent microscopy, however in order to observe small spheroid molecular microenvironment, higher spatial resolution is required for MSI. Attachment prevention methods can produce macropellet spheroids, which are currently the only spheroid type, excluding two organoid culture publications, analysed using MALDI-MSI (Liu *et al.*, 2018; Hiraide *et al.*, 2016; LaBonia *et al.*, 2016). However, this spheroid production method has been shown to be limited for the study of the tumour microenvironment as it does not always produce a representative model of a specific tumour type (Fennema *et al.*, 2013). Common use of attachment prevention methods in combination with MALDI-MSI is due to the ease and speed of production of these spheroids, compared to other methods involving growth inside scaffolds, as well as the benefit of the reproducible, large spheroid size that the method produces. The time required generating the engineered model and ease of production, as well as possibility for integration

into high throughput protocols, are all parameters which require consideration. However, there are many different alternative models available for study of disease, many of which are suitable for MSI. As interest in the investigation of these models grows, the emergence of more specialised, functional method workflows will emerge focused on the analysis of more complex types of 3D cell culture.

The two main issues which commonly arise during MALDI-MSI of 3D cell cultures are lack of spatial resolution and small sample size which leads to a low abundance of molecules and reduces the probability of confirmed identities of molecules of interest. Firstly, since the samples are usually much smaller in size than the commonly optimised tissues, spatial resolution of the instrument used must be improved to see differences between specific regions of interest. Mass spectrometric images can now be achieved by several mass spectrometer designs to a pixel size as low as 1μm, although these require further optimisation in order to achieve better result quality (Zavalin *et al.*, 2015). For example, decreased sensitivity at lower pixel sizes is a problem which could be solved with derivatization or post-ionization steps (Barré *et al.*, 2016; Soltwisch *et al.*, 2015). Recent work has indicated that spot size dependent thermodynamic conditions may need to be optimised for the ideal signal to be observed (Niehaus & Soltwisch, 2018). In order to increase the number of confirmed identities of molecules of interest, high mass accuracy (<5 ppm) and resolving power (>50,000) capabilities of orbital trapping (Orbitrap) and Fourier-transform ion cyclotron resonance (FT-ICR) are being used (Ly *et al.*, 2016; Sun *et al.*, 2016; Prideaux *et al.*, 2015). These detector systems are capable of producing much higher mass resolution spectra than the commonly used Q-TOF hybrids and identify more peaks which would be overlapping at a lower resolving power (Spraggins *et al.*, 2016).

In order to be representative of tissues, which are quite diverse in general, ideally the model design should involve as much detectable heterogeneity as possible. This would mean that, for example, in the case of a cancer model ideally physio chemically differing areas within the model should be large enough to be detectable, as well as clonal differences within the tumour spheroid. Currently, clonal spheroid formation methods are limited in size (<300μm) and therefore

clonal differences can only be detected with high spatial resolution. However, techniques such as MSI are not always capable of spatial resolution high enough to detect differences within low micron-scale samples. Creation of MSI compatible models, which still maintain the information provided by classical 3D cell culture models would be beneficial for the study of disease. Additionally, currently there is an insufficient amount of sample handling methodologies available for working with 3D cell culture models in an MSI setting. Most MSI has been performed on attachment prevention based models, which are not necessarily representative of all 3D cell cultures available and are not effective for culture of every cell type. MSI methodology should be developed for a variety of different 3D cell culture models in order to increase its utilisation within this field. Once optimised for this sample type, the technique will be capable of analysis of metabolites, lipids and proteomic changes in a spatial distribution in 3D cell cultures which will provide useful information for study of disease.

This thesis aimed to develop 3D cell culture models which are still representative of their human *in vivo* counterparts but are also compatible with MSI. Following this, sample preparation and analysis methods were developed and optimised to gain useful molecular insights into disease and treatment.

1.2 Aims

1. To create more representative 3D cell culture models of their *in vivo* cell counterparts, working towards the 3R principles.
2. To develop methods using MSI tools applicable to 3D cell culture analysis.
3. To demonstrate the use of these methods to gain insights into disease and treatment.

1.3 Objectives

1. To create a 3D cell culture model of osteosarcoma for the study of potential therapeutic options for the tumour (Chapter 2).

2. To develop MSI methods for the small molecule and lipid analysis of osteosarcoma spheroid aggregates (Chapter 2).

3. To demonstrate the use of these methods to assess osteosarcoma drug response (Chapter 3).

4. To develop MSI methods for the proteotypic peptide analysis of 3D cell cultures (Chapter 4).

5. To develop an MSI method for quantification of proteotypic peptides within a spheroid aggregate (Chapter 4).

6. To create a 3D cell culture model of liver for the study of ADME responses to therapeutics (Chapter 5).

7. To assess the use of the small molecule MSI methods on a polymer scaffold-based model of liver for the evaluation of AOPs (Chapter 5).

Chapter 2: Optimisation of cancer spheroid culture and development of small molecule and lipid Mass Spectrometry Imaging

2.1 Introduction

In the field of cancer research, typically *in vitro* two -dimensional cell cultures are employed to investigate mechanisms involved in metabolism, metastasis and drug resistance. However, it has been shown that 2D cultured cells are not necessarily representative of *in vivo* mechanisms and environment (Rodrigues *et al.*, 2018; Seo *et al.*, 2018; Lhuissier *et al.*, 2017; Shamir & Ewald, 2014). 2D cell cultures display differences in cell-cell interactions and a lack of interactions with the extracellular matrix. Gene expression profiles of 2D cells are considerably altered from their *in vivo* counterparts (Senkowski *et al.*, 2016). Deviations in gene expression lead to modified cell function, changes in morphology, and contribute to vast differences in drug-interactions. All these fundamental changes lead to large differences in responses between 2D cell cultures and the *in vivo* human response, which they are attempting to replicate. 3D cell culture is a method developed to overcome some of the limitations of 2D cell culture (Ravi *et al.*, 2015; Pampaloni *et al.*, 2007; Birgersdotter *et al.*, 2005).

2.1.1 3D cell culture of cancer

There are many methods to generate 3D cancer models, dependant on the experiment application and different cell sources can be used (Sections 1.1.1 and 1.1.3). Choice of model is dependent on the application. For example, cancer heterogeneity is well known to contribute to chemotherapeutic and immune resistance (Alizadeh *et al.*, 2015). Cell heterogeneity as well as the hypoxic gradients within a tumour lead to different behaviour between cell populations within a tumour (Rankin & Giaccia, 2016), therefore these features have to be considered when developing a cell culture model to study drug response. There is also communication observed between tumour and its surrounding stroma, immune cells, blood vessels and extracellular matrix components. This promotes specific cancer related behaviours leading to a more complex tumour microenvironment. Several tumour models aim to replicate these complex features within an *in vitro* culture(Yang & Lin, 2017; Rimann *et al.*, 2014).

2.1.2 3D cell culture scaffold models

Scaffold models are widely used in order to replicate the native environment to a larger extent and maintain more *in vivo* like behaviour in culture (Sitarski *et al.*,

2018; Bäcker *et al.*, 2017; Caliari & Burdick, 2016). Naturally derived scaffolds of non-animal origin are extensively used for 3D cell culture of mammalian cells due to biocompatibility, homogeneity, reproducibility and the mild gelation. Dependant on the type of experiment an exact replication of the *in vivo* extracellular framework is not always required. Close mimics of the native environment are sometimes sufficient (Magin *et al.*, 2016). Biocompatibility of animal-derived scaffolds is sufficient and basement membrane extracts such as Matrigel® or Cultrex® are used successfully for many applications (Cavo *et al.*, 2018; Sachs *et al.*, 2018). However, these are susceptible to batch to batch variations due to the extraction and solubilisation processes (Saldin *et al.*, 2017; Nath & Devi, 2016; Sharma *et al.*, 2010). Homogeneity and reproducibility of synthetic scaffolds is much better than naturally derived scaffolds as the composition is designed avoiding this variability. The benefit of these types of scaffolds, is their mechanical stability, controllable degradation and structure, which are important factors in both *in vitro* modelling and regenerative medicine (Annabi *et al.*, 2014). An increased number of highly biocompatible synthetic scaffolds are being utilized, including cell-degradable hydrogels (Sawicki *et al.*, 2018).

Alginate is a naturally derived polysaccharide extracted from brown algae (*Phaeophyceae*). The scaffold polymerises by an ionic cross-linking process. The process involves linking units of alginic acid with a cross-linking ion, commonly Ca^{2+} (Figure 2.1), but can be controlled by adjusting the composition and concentration (Augst *et al.*, 2006) as well as adjusting the rate of gelation (Growney Kalaf *et al.*, 2016) and combination with other biomaterials (Venkatesan *et al.*, 2015). The first instance of alginate use to culture cells was in the 1980s where it was used to encapsulate islet cells in order to culture and implant these into rats as a way to correct their diabetic state (Lim & Sun, 1980). Since then the use of alginate for tissue engineering and *in vitro* cell culture purposes has been extensively considered and some of its benefits include its non-toxicity, soft gelation, control over matrix stiffness and simple cell recovery (Diekjürgen & Grainger, 2017).
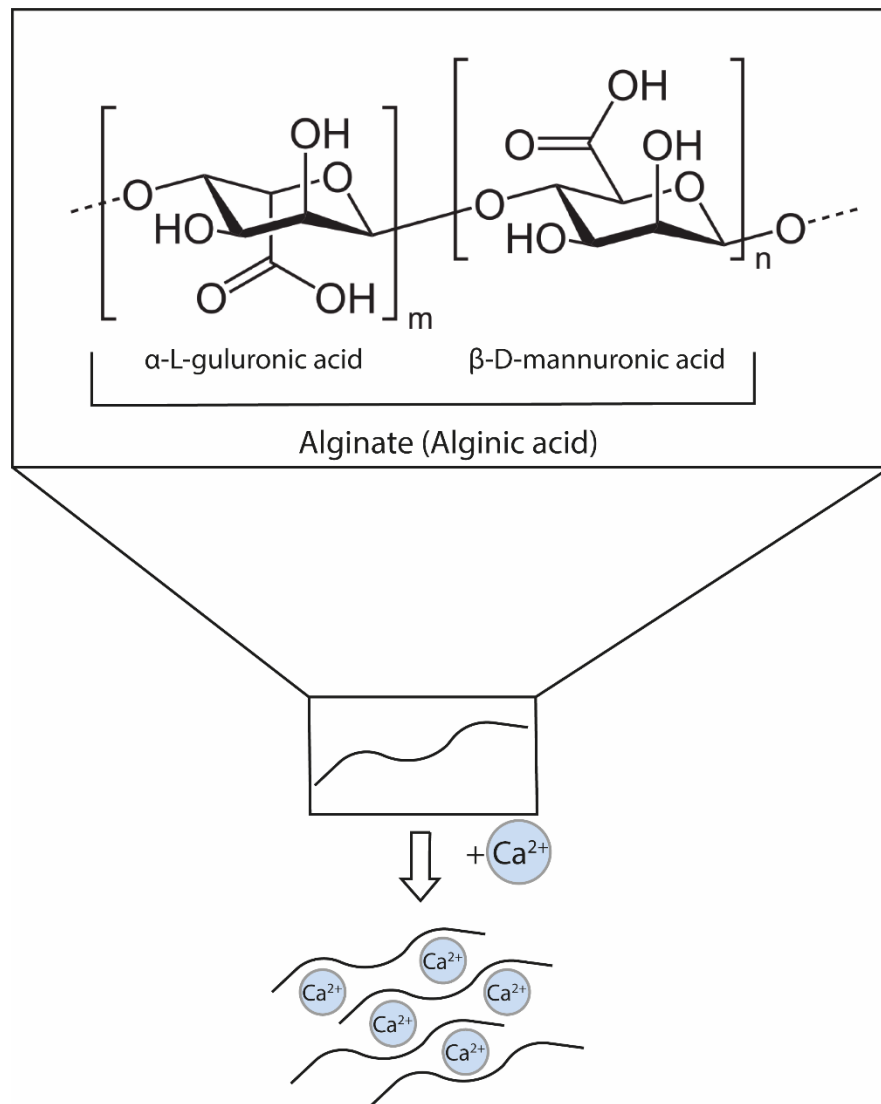
Figure 2.1 Alginate chains are composed of guluronic acid and mannuronic acid units. In the presence of cross-linking ions such as Ca2+ alginate polymerises reversibly.

2.1.3 The challenges of 3D cell culture analysis

Although the use of 3D cell culture models is more representative of the *in vivo* environment, it has also generated some analytical challenges. The 3D structure has resulted in a requirement to adapt or create new methods of analysis, as certain current methods are no longer suitable. For example, fluorescence microscopy is often used to characterise tumour spheroids without the need for sectioning, however sample thickness and difficulty of light penetration makes this technique more difficult to use than with conventional cultures (Graf & Boppart, 2010). Confocal microscopy variants are now commonly used, such as

confocal laser scanning microscopy (CLSMO); light-sheet-based fluorescence microscopy (LSFM); Single (or selective) plane illumination microscopy (SPIM) and Two-photon microscopy (TPM)/multi-photon microscopy (MPM); however even these are limited by sample thickness due to light scattering and 3D cell culture samples in some cases still have to be sectioned to solve this (Costa *et al.*, 2016). Auto-fluorescence of some scaffolds is also an concern preventing the use of fluorescence microscopy for analysis, although methods are in development to try and overcome this such as pre-culture in autofluorescence suppressing agents like Sudan Black B (Qi *et al.*, 2017).

Another common method of cell analysis which requires an adjusted methodology to study tumour spheroids is flow cytometry. In order to analyse cells using flow cytometry, these have to be completely separated to a single suspension. This means the spheroids cannot be observed in their native state and have to be disaggregated using non-enzymatic cell dissociation reagents such as Versene (Florczyk *et al.*, 2016) or cellular detachment promoting enzymes such as trypsin (Tung *et al.*, 2016). Recently, Sart and colleagues presented a microfluidic platform which could be combined with cytometry methods at population, spheroid as well as single cell scale capable of analysing small spheroids (<200μm) (Sart *et al.*, 2017). In some cases, if a fluorescent stain is added before dissociation of the tumour spheroid, penetration time has to be considered, especially with larger spheroids. Alternatively, the slow spheroid penetration time of the Hoechst 33342 dye may be utilised to the experimenters advantage as an indicator of which spheroid layer they are observing (Beaumont *et al.*, 2015).

Commonly used colorimetric cell viability assays, such as the 3-(4,5-dimethylthiazol-2-yl)-2,5-diphenyltetrazolium bromide (MTT) and lactate dehydrogenase (LDH) assays, have also required optimisation for use in the study of 3D cell cultures. In particular concerning tumour spheroid model analysis, assays such as MTT work in some cases without protocol adjustment, some with adjustment and in some cases the assay does not produce reliable results (Pereira *et al.*, 2017; Galateanu *et al.*, 2016; Ho *et al.*, 2012). This may be due to difference in cell density and spheroid size in each model design, which could affect assay penetration. As the penetration is not complete the correct amount

of product is not created, and the value given by the test becomes inaccurate. Cells in the proliferating region would produce a relatively higher signal throughout due to higher cell activity, therefore smaller sized spheroids would produce a higher signal than large spheroids. As long as the reagent is non-toxic, which is the case of the Resazurin assay, which is also a redox indicator, the incubation time of the assay can be increased to long enough to penetrate most 3D cultures (Uzarski *et al.,* 2017; Riss *et al.,* 2004). However, in the case of many biochemical endpoint assays, long incubations are not possible due to toxicity to the cells and alternatively fluorescence and luminescence assays are developed specifically for 3D cell culture use. Special software is required for the analysis of growth when techniques such as nuclei counting are not feasible. For example, AnaSP, a software analysing morphological parameters was developed in order to determine the role sphericity and volume variance play in reproducibility of results (Zanoni *et al.,* 2016). Volume increase in these cases was used as a measure of spheroid growth. In the same study, the ability of several viability assays to measure correctly and reproducibly the viability of spheroids of up to 850µm diameter was assessed. Pre-selecting spheroids for homogenous volume and shape and observing the overall morphological changes during treatment, as well as noting variability within data, allowed the researchers to assess the accuracy of each viability test. Results showed that the conventional Trypan blue method was not sufficiently reproducible and accurate at predicting cell viability in spheroids. The CellTiter-Glo® 3D Cell Viability Assay, which is based on a luminescence reaction and designed specifically for 3D cell culture analysis, provided the best and most reproducible results however was still hindered at spheroid sizes of >650µm diameter (Zanoni *et al.,* 2016). This could have been either due to the penetration limit of the assay, light scattering or the presence of a necrotic core at this size.

In the case of tumour spheroids, size may contribute greatly when trying to recapitulate pathophysiological conditions including hypoxic and necrotic areas and proliferation gradients. Smaller spheroid cultures can be used to represent certain cell-cell, cell- matrix interactions but are not always representative of the whole microenvironment, therefore this is a consideration for culture of each specific tumour type (Friedrich *et al.,* 2009). In fact, sarcomas are known to be

least dependent upon endothelial-cell proliferation and have very little vasculature compared to other lesions, therefore in these cases hypoxic and necrotic areas in a model may be of high relevance (Azam *et al.*, 2010). It is known that the initial foci of neoplastic cells receive their nutrients and oxygen by diffusion from a host blood vessel up to a distance of 100-200µm, therefore in order to represent tumour areas further away than this gradient, larger spheroid models are required (Baronzio *et al.*, 2008).

Frequently used methods such as western blotting, quantitative PCR and immunohistochemistry all require different levels of adaptation for 3D cell culture analysis. These detect important molecules of interest within the cultures, however all the methods mentioned thus far have been targeted analysis methods. Additionally, out of all the methods previously mentioned only IHC is capable of maintaining spatial biochemical information.

2.1.4 MSI of cancer 3D cell cultures

Mass spectrometry imaging (MSI), has been adapted towards the analysis of 3D cell culture of cancer. MSI of spheroids was first initiated by the Hummon group in 2011. The group published the first proof-of-principal publication on the use of MSI with these models and proved that a MALDI-MSI workflow could be used to examine the changes in protein and peptide distributions within cancer spheroids in an unbiased fashion, suitable for *de novo* discovery (Li & Hummon, 2011). Although MALDI-MSI is the most commonly type of MSI technique used for this purpose, other techniques have also been used for MSI of 3D cell cultures. Secondary Ion Mass Spectrometry (SIMS) imaging was used as a tool for the metabolic profiling of small molecules in squamous cell carcinoma MCTS. The MCTS in this study were treated with Doxorubicin and multivariate statistics was used to reveal a metabolite pattern, which indicated hypoxia-induced chemoresistance (Kotze *et al.*, 2013). Using Laser ablation Inductively Coupled Plasma Mass Spectrometry (LA-ICP-MS) imaging, a technique capable of imaging elements rather than larger molecules, another research group developed a methodology for the imaging of platinum group-containing drugs, such as cisplatin, in tumour spheroids, as well as a palladium-tagged photosensitizer. Quantitation of all the imaged drugs was also achieved by using

different matrix-matched standards (Niehoff *et al.*, 2016). Use of mass spectrometry imaging in order to visualise molecules within 3D cancer cultures is increasing due to the numerous advantages of the method. The main two advantages are the potential for untargeted *de novo* discovery, and the capability to observe multiple analytes of interest in a single experiment. Unlike LC-MS, a method which has also been used in the analysis of 3D cell culture models, MSI is also able to preserve spatial information, requiring no homogenisation of the sample, and frequently less sample preparation is involved. Many MSI methods are also non-destructive which may lead to the sample being used again, commonly for a histological stain. In light of these advantages MSI is destined to become a powerful, regularly used technique for the investigation of 3D cell culture disease models. However, prior to widespread adoption of this technique, more optimisation of mass spectrometric imaging techniques of several types of 3D tumour spheroid models is required.

2.1.5 Chapter aims

In the following chapter the aim was to develop a suitable 3D cell culture model of cancer and determine whether MSI could be used to image the spatial distribution of small molecules within that model. Firstly, a small panel (PC-3, DU-145, MG-63 and SAOS-2) of prostate cancer and osteosarcoma cell lines were cultured using alginate-based cell culture. The SAOS-2 cell line was then selected for further spheroid aggregate culture for the production of larger spheroid aggregates. The aggregates were developed to sizes large enough for representative physiological gradients to lead to formation of hypoxic and necrotic regions and for easier determination of regions using MALDI-MS imaging. Once the 3D cell culture model was established, optimisation of sample preparation was performed for MALDI-MS imaging, including choice of best matrix, sample fixation and embedding techniques. Finally, the samples were imaged, using three different mass spectrometers capable of imaging, in order to assess the compatibility of different sample types, preparations and to assess the effect of spatial resolution, small molecule and lipid signal in positive and negative modes.

2.2 Materials and Methods

2.2.1 Chemicals and materials

α-Cyano-4-hydroxycinnamic acid (α-CHCA), 2,5-Dihydroxybenzoic acid (DHB), 9-aminoacridine (9-AA), 1, 5-Diaminonaphthalene (1, 5-DAN), N-(1-Naphthyl) ethylendiaminedihydrochloride (NEDC), 5-chloro-2-mercaptobenzothiazole (CMBT), Glycine, Pyruvic acid, Putrescine, Alanine, Lactic acid, Serine, Proline, Fumaric acid, Valine, Threonine, Cysteine, Leucine, Isoleucine, Oxaloacetic acid, Asparagine, Aspartic acid, Malic acid, Glutamine, Lysine, Glutamic acid, Methionine, Histidine, Phenylalanine, Arginine, Glucose, Tyrosine, Citric acid, Tryptophan, Glucose-6-phosphate, Cytidine 5'-monophosphate (CMP), Uridine 5'-monophosphate (UMP), Fructose-1,6-bisphosphate, Adenosine 5'-monophosphate (AMP), Cytidine 5'-triphosphate (CTP), Adenosine 5'-triphosphate (ATP), alginic acid, ethanol (EtOH), methanol (MeOH), acetonitrile (ACN), chloroform ($CHCl_3$), Xylene Substitute (SubX), Acetone, trifluoroactic acid (TFA), formic acid (FA), Paraformaldehyde, Hoechst 33342, propidium iodide (PI), gelatin, carboxymethyl cellulose (CMC), sodium chloride (NaCl) and calcium chloride ($CaCl_2$) were purchased from Sigma–Aldrich (Poole, UK). Industrial methylated solvent (IMS) was obtained from Fisher Scientific (Loughborough, UK). X-tra® slides, Mayer's Haematoxylin, Eosin and Pertex were purchased from Leica Biosystems (Milton Keynes, UK). NucView™ 488 Caspase-3 substrate was obtained from Cambridge Bioscience (Cambridge, UK). ITO-coated slides were obtained from Visiontek Systems Ltd (Cheshire, UK).

2.2.2 2D cell culture

PC-3, DU-145 (prostate adenocarcinoma) and MG-63 (osteosarcoma) were obtained from the American Type Culture Collection and cultured in Dulbecco's Modified Eagle Medium (DMEM) supplemented with 10% foetal bovine serum (FBS) and 10 U/ml penicillin and 10 µg/mL streptomycin (Thermo Scientific, USA) and SAOS-2 cell line was obtained from American Type Culture Collection (ATCC) and cultured in MEMα (Lonza Ltd, Switzerland) containing 10% foetal bovine serum (FBS) and 10 U/ml penicillin and 10 µg/mL streptomycin (Thermo Scientific, USA). All cell lines were maintained in a humidified atmosphere containing 5% CO_2 at 37ºC. These were cultured until they reached

approximately 80% confluency before transfer to 3D culture. Once confluent, the cell lines were passaged by trypsinisation, subsequent centrifugation, resuspension in fresh medium and seeded in new flasks. The cells were used for up to 15 passages from frozen stocks for experiments.

2.2.3 3D cell culture

2.2.3.1 Alginate culture

Following expansion in monolayer, cell lines were suspended in 1.2% w/v medium viscosity alginic acid in 0.15M NaCl. The initial seeding densities of all cell lines were between 1x 10^5 cells/mL for the 4-6 week cultures and and 1x 10^6 cells/mL for up to 2 week cultures of alginate. The cell concentrations were determined with the Countess® Automated Cell Counter and Trypan blue stain. Alginate beads were formed via dropping 2mL of cells in 1.2% (w/v) alginate/ 0.15M NaCl through a 19-gauge needle into 20mL 0.2M CaCl$_2$. After incubation at 37°C for 12 minutes beads were washed twice with 0.15M NaCl and washed twice in complete media before being placed in the appropriate culture media. All cell lines were cultured up to 2 weeks and the SAOS-2 cell line was cultured up to 6 weeks to observe potential further growth. In order for the spheroids not to merge in the longer-term cultures, the seeding density used was 1x10^5 cells/mL.

2.2.3.2 Releasing tumour spheroids from alginate matrix

Alginate beads were dissolved in 500µL alginate dissolving buffer (55mM sodium citrate, 30mM EDTA, 0.15M NaCl) per bead for 10 minutes at 37°C on a shaker after pipetting up and down in order to break up the bead. The solution was then centrifuged at 1,000g for 5 minutes at room temperature. Supernatant was removed and the spheroids were washed in media twice, each time centrifuging the spheroids according to the same protocol, then they were incubated in the appropriate culture media for 24 hours in order to equilibrate.

2.2.3.3 Formation of spheroid aggregates

In order to obtain spheroid aggregates, alginate grown spheroids were released from alginate using the alginate dissolving buffer and after two media washes, each followed by centrifugation (1,000g, 5 mins), they were immediately placed in 1% agarose coated 96 well plates. The tumour spheroids from half of one

alginate bead were added to each agarose-coated well and these were cultured for a further 7 days in the appropriate medium (Figure 2.2).
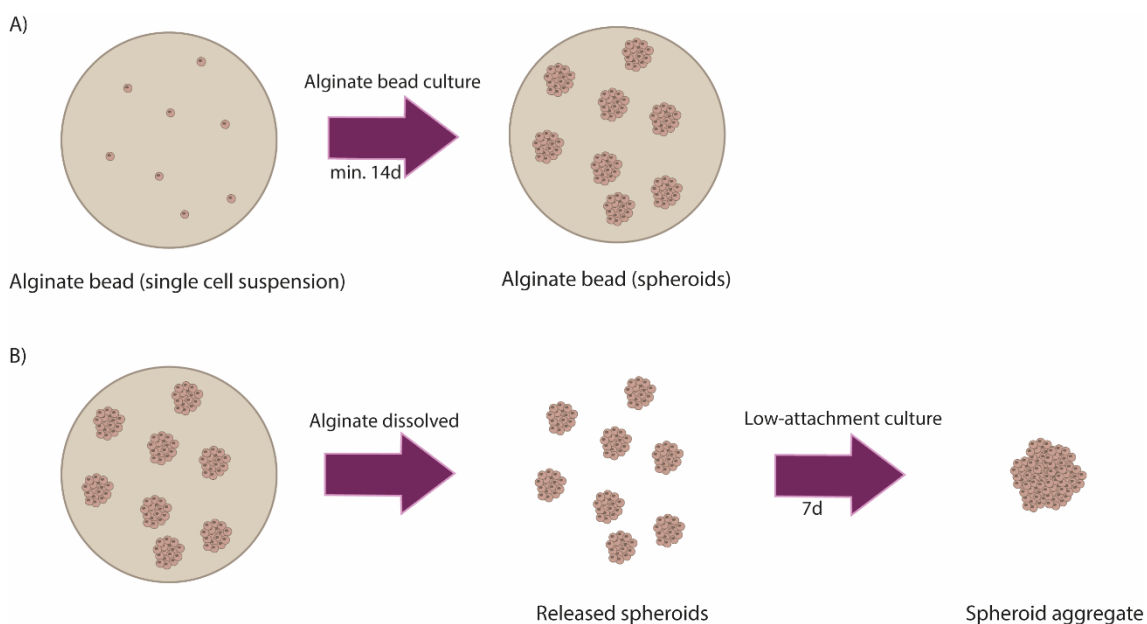
Figure 2.2 Three-dimensional cell culture methods used for formation of cancer spheroid models. A) Alginate bead spheroid formation. The cells are seeded as a single cell suspension within an alginate bead and grow into clonal spheroids. B) Two-step spheroid aggregate formation. After culture of cells in alginate beads, spheroids are released from alginate and collected into a spheroid aggregate within low-attachment wells.

2.2.4 Assessment of viability, apoptosis and necrosis

The cells were visualised by utilising three different stains; Hoechst 33342 (10µg/mL), Propidium Iodide (PI) (1µg/mL) and NucView™ 488 Caspase-3 substrate (20µM). Since PI has a broad emission peak, separate spheroid and spheroid aggregate samples were used for Hoechst 33342/PI and Hoechst 33342/Caspase-3 combinations in order to prevent green and red emission overlap within the same fluorescent image. Hoechst 33342/PI stained samples were incubated with Hoechst 33342 and PI for 25 minutes in a humidified atmosphere containing 5% CO_2 at 37°C. Hoechst 33342/Caspase-3 stained samples were first incubated in Caspase-3 stain for 15 minutes at room temperature after which Hoechst 33342 was added and another incubation of 25 minutes was carried out in a humidified atmosphere containing 5% CO_2 at 37°C. All incubations were performed in a dark environment to prevent photobleaching.

After the incubations the samples were washed twicewith phosphate-buffered saline (PBS) and stored in PBS during fluorescent visualisation.

Sample well plates were visualised on an Olympus IX81 microscope at 100x and 200x magnification under blue, green, red, and merged channels.. Images were captured using Cell^F software.

2.2.5 Sample preparation

2.2.5.1 Preparation of spheroids for histological and molecular analysis

Fresh frozen samples of 3D cell cultures were prepared several ways for comparison (Figure 2.3). The samples were all embedded in 5% gelatin + 2.5% carboxymethylcellulose (CMC) inside a silicone mould and immediately frozen using liquid nitrogen. The embedding medium was chosen by adapting the medium to a consistency similar to that of the sample for optimal sectioning. A similar mixture of gelatin and CMC was published as acceptable for whole-body zebrafish MALDI-MSI experiments in terms of its physical property, stability and lack of ion suppression and this slight variation was also found to be sufficient for sectioning of 3D cultures (Nelson *et al.*, 2013). The fixed frozen sample set was fixed by washing twice in PBS followed by immediate immersion in 4% paraformaldehyde at 4°C for 15 mins. These were then processed the same as the fresh frozen samples. The spheroids which had been released from alginate beads using dissociation buffer were incubated in media for a 24-hour equilibration then embedded in 5% gelatin 2.5% CMC inside a silicone mould and immediately flash frozen using liquid nitrogen. All samples were stored inside sealed containers at -80°C.
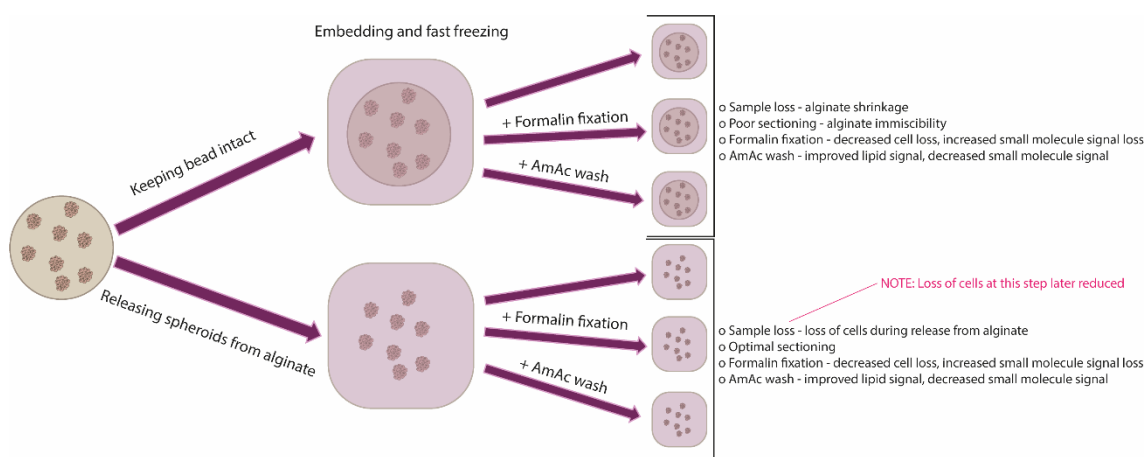
Figure 2.3 Schematic of sample preparation methods tested of fresh frozen spheroid cultures.

Sample sections were cut using the Leica 1850 UV cryostat (Leica Biosystems, UK), set to -30°C, at a 10 μm thickness, thaw mounted on a positively charged X-tra® adhesive slide (Leica Biosystems, UK) or on an Indium-Tin oxide (ITO)-coated slide (Visiontek Systems Ltd, UK) dependant on the analysis. The sample thickness chosen was the lowest consistent thickness achieved with the sample and equipment available, as published previously (Lewis *et al.*, 2018). The samples were then stored at -80°C in an air tight container.

2.2.5.2 Preparation of spheroid aggregates

The samples were processed by embedding the spheroid aggregates in 10% gelatin 2% carboxymethylcellulose (CMC) inside a silicone mould and immediately frozen using liquid nitrogen. The spheroid aggregates were moved from wells to embedding medium using a 200μL pipette tip with a cut-off end in order to better preserve the aggregate integrity. Care was taken to not damage the spheroid aggregate and to minimise the amount of media deposited alongside the sample. Any excess media was removed to the extent possible using a pipette. All samples were stored inside sealed containers at -80°C.

These samples were sectioned according to the same method as alginate cultures.

2.2.6 Optimisation of Mass Spectrometry Imaging

2.2.6.1 Production of small molecule standard mix

A small molecule standard mix was made by dissolving 35 small molecule standards at 50pmol/µL in 70% EtOH. The standard list is presented in Table 2.1. This was then aliquoted and stored at -80ºC in sealed containers.

Small molecule	Negative mode m/z
Glycine	74.0248
Pyruvic acid	87.0088
Putrescine	87.0928
Alanine	88.0404
Lactic acid	89.0244
Serine	104.0353
Proline	114.0561
Fumaric acid	115.0037
Valine	116.0717
Threonine	118.051
Cysteine	120.0125
Leucine	130.0874
Isoleucine	130.0874
Oxaloacetic acid	130.9986
Asparagine	131.0462
Aspartic acid	132.0302
Malic acid	133.0142
Glutamine	145.0619
Lysine	145.0983
Glutamic acid	146.0459
Methionine	148.0438
Histidine	154.0622
Phenylalanine	164.0717
Arginine	173.1044
Glucose	179.0561
Tyrosine	180.0666
Citric acid	191.0197
Tryptophan	203.0826
Glucose-6-phosphate	259.0224
CMP	322.0446
UMP	323.0286
Fructose-1,6-bisphosphate	338.9888
AMP	346.0558
CTP	481.9772
ATP	505.9885

Table 2.1 List of small molecule standards (50pmol/µL) included in the standard mixture and their m/z values in negative mode.

2.2.6.2 Mass Spectrometric Profiling of standards

A comparison of the use of four matrices for negative mode MALDI-MS was undertaken. The four matrices were 9-amino acridine (9-AA), 1, 5-Diaminonaphthalene (1, 5-DAN), N-(1-Naphthyl) ethylendiaminedihydrochloride (NEDC) and 5-chloro-2-mercaptobenzothiazole (CMBT). MALDI-MS profiles of spotted small molecule standard mix were compared against a direct injection of the standard using a Finnigan LCQ (Thermo Scientific, UK). The four matrices were first prepared; 9-AA (10mg/mL, 100% acetone), 1,5-DAN (10mg/mL, 100% MeOH), NEDC (10mg/mL, 70% EtOH), CMBT(20mg/mL (4:4:1 chloroform:MeOH:dH$_2$O (v/v/v))). The 50pmol/μL standard mix was spotted onto target plates (0.5μL) and matrix was deposited on top of each spot once dry (0.5μL).

Mass spectra were manually acquired on an Autoflex III (Bruker Daltonik GmbH, Germany) equipped with a 200-Hz smart-beam laser. Negative ion mass spectra were acquired from 50 *m/z* – 1000 *m/z* in reflectron mode. Six hundred laser shots were acquired for each spectrum at a random walk setting. This instrument was initially chosen for comparison of matrices due to its nitrogen laser beam profile, which comprises of several intense spots in order to generate a quazi-Gaussian profile and subsequently maximise ion yield, therefore it was most likely to yield results from the matrix panel (Zavalin *et al.*, 2014). External mass calibration was achieved using a phosphorus red standard of approximately 200 parts per million (ppm). Data was acquired using FlexControl (Bruker Daltonics, Germany), converted to .txt file format using FlexAnalysis (Bruker Daltonics, Germany) and analysed using Mmass v5 open source software (Strohalm *et al.*, 2010).

A further comparison of NEDC and 9-AA profiles was later made using a Synapt G2 operated with a 1 KHz Nd:YAG laser (355 nm) (Waters Corporation, UK) to achieve higher accuracy and reliability in the results. The standard was spotted onto a target plate (0.5μL) and 9-AA (10mg/mL, 100% acetone), and NEDC (7mg/mL, 50% MeOH) were prepared and deposited on top of the standard (0.5μL). Negative spectra were acquired from 50 *m/z* – 1000 *m/z* using an automated spiral raster pattern set to 60s raster for increased reliability. The ion mobility function was also used in order to improve separation of peaks. External

mass calibration was achieved using a phosphorus red standard to achieve 95% confidence of <3 parts per million (ppm). Data was acquired, converted to .txt file format using MassLynx™ software (Waters Corporation, UK) and analysed using Mmass.

2.2.6.3 Statistical analysis

The data was identified as non-parametric by the Shapiro Wilkes test of normality. Therefore, the Kruskal-Wallis test was used to determine if there were any significant differences between the treatments for each ionic species. This analysis was combined with Conover-Inman post-hoc test when a significant difference was seen between treatment groups. Statistical analysis was performed using StatsDirect software (StatsDirect Ltd, UK).

2.2.6.4 Mass Spectrometric Imaging of spheroids and spheroid aggregates

2.2.6.4.1 Matrix deposition

All sample sections were taken straight after cryosectioning or from -80°C storage and immediately placed in a vacuum desiccator for ~15 minutes prior to matrix application. In cases where samples were washed with ammonium acetate (pH 6.7) the slide sections were dipped in 50mM ammonium acetate for 15 seconds and dried in a vacuum desiccator again for ~5 minutes before matrix application. X-tra® slide mounted sections were used for Synapt G2 and Q-Star Pulsar-i™ analysis and ITO-coated slide mounted sections were used for Autoflex III analysis, where conductive slides were required due to the sample stage setup to prevent surface charging.

For positive mode imaging α-CHCA (5 mg/mL, 70:30 ACN:dH$_2$O, 0.1% TFA) was prepared as a matrix solution. The matrix was applied to the sample section using the SunCollect™ automated sprayer. Five layers of matrix were applied at 3.5 μL/min for the first layer and 3 μL/min for the remaining four layers (speed x: low 7, speed y: medium 1, Z position: 35).

For negative mode imaging, initially 9-AA was used (10mg/mL, 100% acetone) as a matrix solution. 9-AA was sprayed manually, giving 1 minute of drying time in between layers, until the sample was fully covered (~30 layers). In later

experiments, negative mode imaging was performed with NEDC (7mg/mL, 50% MeOH) prepared as a matrix solution. The matrix was applied to the sample section using the SunCollect™ automated sprayer. Fifteen layers of matrix were applied, at 4µL/min for the first layer and 3.5µL/min for the remaining layers (speed x: low 7, speed y: medium 1, Z position: 35).

2.2.6.4.2 Mass Spectrometric Imaging

Three separate MALDI-MS instruments were utilised for the imaging of spheroids and spheroid aggregates.

Initially, sample preparation methods were compared using a low spatial and mass resolution capability but high throughput instrument. For the evaluation of sample preparation methods a modified MALDI-Q-TOF, a Q-Star Pulsar-i™ (Applied Biosystems/MDS Sciex, Concord Ontario, Canada) was used. These modifications have been reported elsewhere (Trim *et al.*, 2010). Data were acquired in positive mode using an NdYVO4 laser (Elforlight "SPOT", Daventry, UK). Images of 150µm pixel size were acquired over the embedded culture area. Data was acquired over an *m/z* range of 50-1,200.

Several images of the spheroids and spheroid aggregates were obtained using a Synapt G2 for higher mass resolution imaging. Images of 60µm and 30µm pixel size were acquired. Data were acquired over an *m/z* range of 50–1,000 in negative mode and 50-1,200 in positive mode analysis. The ion mobility function was used in order to improve separation of peaks by addition of molecule separation by shape as well as mass and charge.

A study of the regional differences within a spheroid aggregate was executed using an Autoflex III due to its high spatial resolution capabilities because the laser could be focused to a smaller diameter (~20-30). Negative ion mass spectra were acquired at a pixel size of 30µm from 50 *m/z* – 1000 *m/z* in reflectron mode. The laser was focused to around ~50µm diameter. Four hundred laser shots were acquired for each spectrum at a random walk setting.

2.2.6.4.3 Data Processing

Images acquired on the Q-Star Pulsar-i™ were processed using Biomap Software 3.7.5.5 (Novartis, Basel, Switzerland). Images generated using the

Synapt G2 were processed using the Waters High Definition Imaging (HDI v 1.4) software package. Images generated using the Autoflex III were processed using FlexImaging 2.0 software. Images generated were all normalised through the division of the analyte image by that of the total ion count (TIC).

2.2.7 Histological analysis

2.2.7.1 Haematoxylin and Eosin staining

Haematoxylin and Eosin (H+E) staining was used to visualise sample morphology. Sections (10μm) were initially simultaneously dehydrated and fixed in 95% (v/v) MeOH for 5 minutes followed by ≥99.9% (v/v) acetone for 5 minutes. These two steps also removed any presence of matrix if sections were processed after MALDI-MS imaging. Sections were put through further dehydration in 99% (v/v) IMS for 5 minutes 3x then immersed in Mayer's Haematoxylin for 10 minutes, before being 'blued' in running tap water for a further 5 minutes. This step was followed by 2 more incubations in 99% (v/v) IMS for 5 minutes and immersed in Eosin for 1 minute. Sections were then immersed in 99% (v/v) IMS for 5 minutes 3x followed by immersion in SubX for 5 minutes 3x. Finally, sections were mounted using 2 drops of Pertex (Leica Biosystems, UK) per slide and coverslips applied.

2.3 Results

2.3.1 Optimisation of cancer cell line growth in alginate 3D culture

Two prostate cancer cell lines and two osteosarcoma cell lines were chosen for 3D cell culture. 3D cell culture was initially only alginate bead culture. At 14 days the PC-3 cell line proliferated into masses with diameters of ~200μm, with the larger spheroids presenting a potentially more hypoxic core (Figure 2.4). The DU-145 cell line proliferated to form ~50μm diameter masses, the spheroids showing no significant sign of nutrient or oxygen starvation in the core. After 14 days incubation in alginate MG-63 spheroids grew to a diameter of ~200μm and SAOS-2 cell line spheroids grew to a diameter of ~50μm (Figure 2.5), however during longer 4-week cultures SAOS-2 spheroids reached ~300μm diameters,

with significant red PI staining in the middle of the spheroids contrasting the blue outer layers (Figure 2.6).
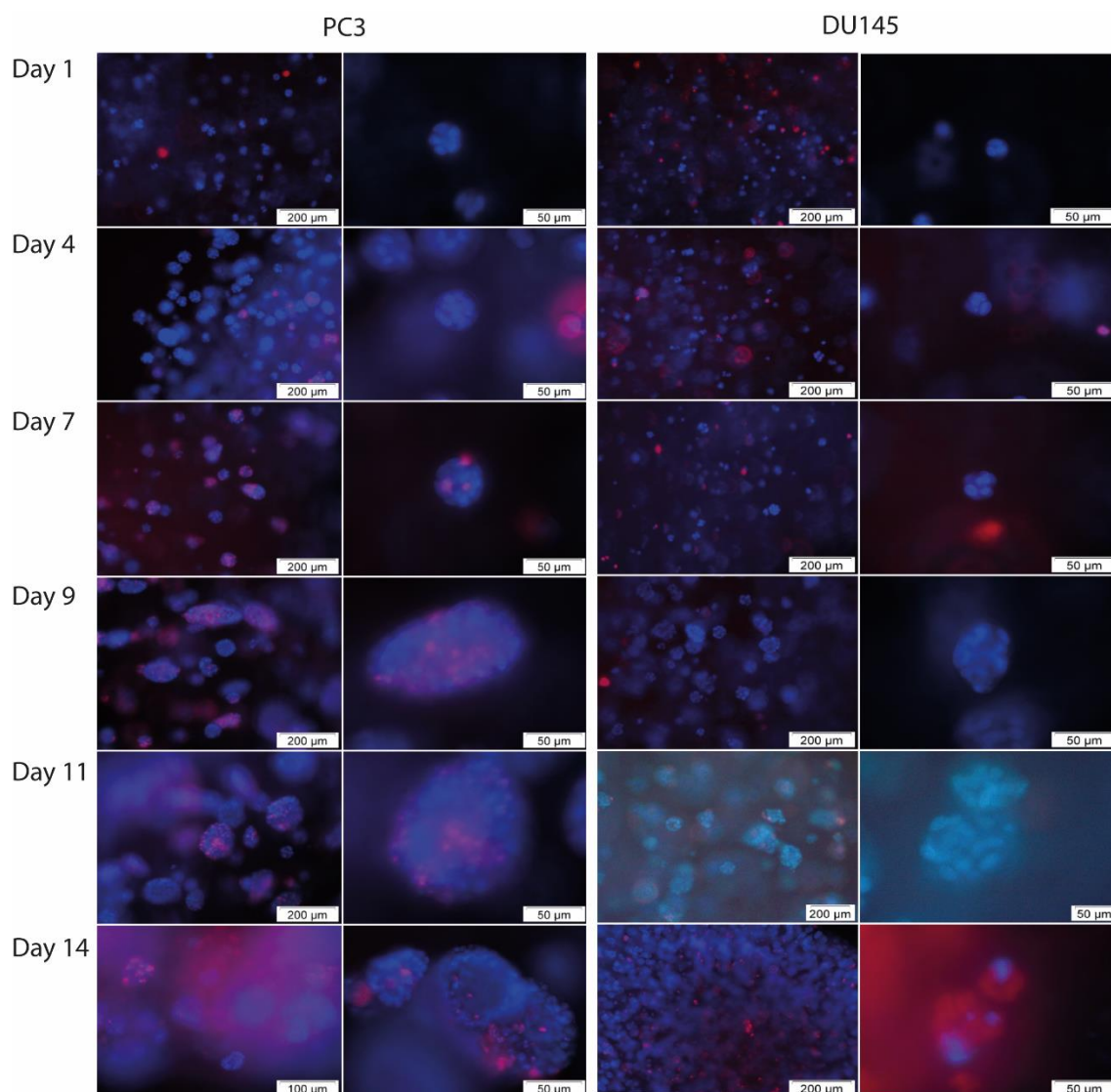
Figure 2.4 Fluorescent images obtained by Hoechst/PI stain of live cells inside intact alginate beads up to 14 days in vitro a) PC3 and b) DU145. Blue signal represents Hoechst staining of nuclei (viable cells) and red signal represents PI staining of dead/dying cells.
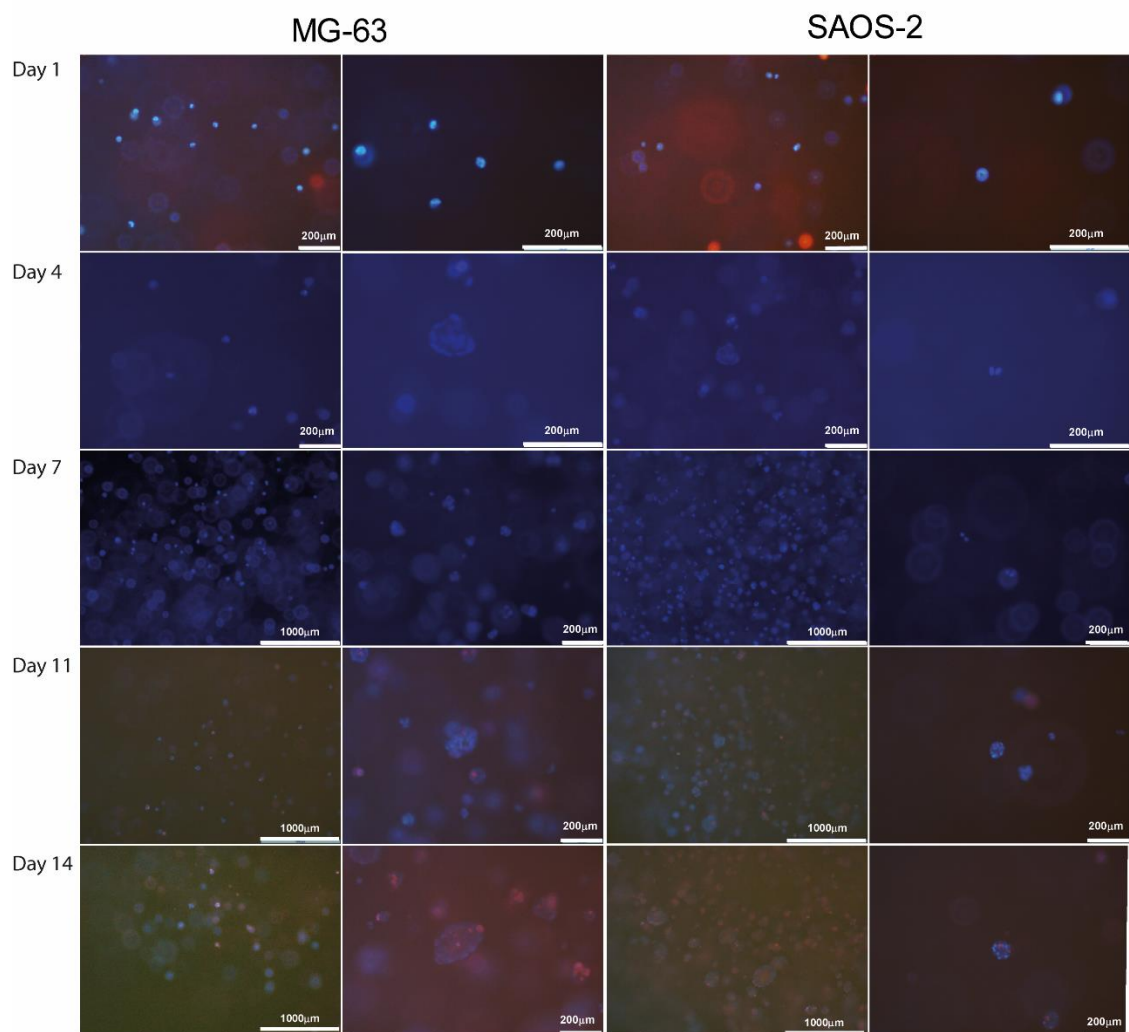
Figure 2.5 Fluorescent images obtained by Hoechst/PI stain of live cells inside intact alginate beads up to 14 days a) MG-63 and b) SAOS-2. Blue signal represents Hoechst staining of nuclei (viable cells) and red signal represents PI staining of dead/dying cells.
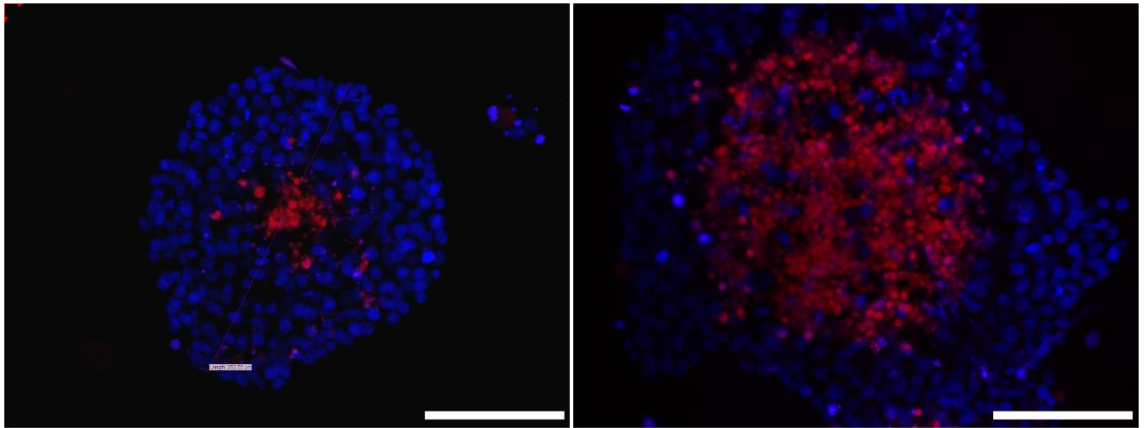
Figure 2.6 Fluorescent images obtained by Hoechst/PI stain of live cell spheroids released from alginate beads. SAOS-2 cell line spheroids were imaged after 4 weeks culture. Scale bar = 100 μm.

Differences were also observed within a bead, particularly in the later growth stages (Figure 2.7). The spheroids formed in the core of the beads displayed more PI positive dead cells than the spheroids on the outside of the beads, according to live cell staining with Hoechst 33342/PI.
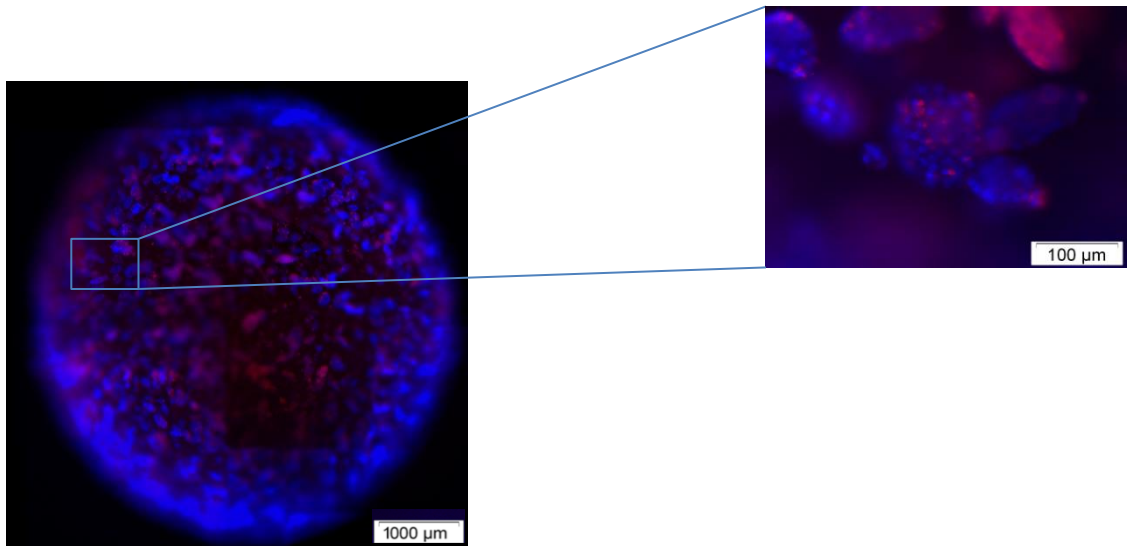
Figure 2.7 *Fluorescent images obtained by Hoechst/PI stain of a whole intact alginate bead containing PC-3 cells (day 11).*

2.3.2 Mass spectrometry imaging of spheroids

2.3.2.1 Comparison of negative mode matrices

In order to be able to compare different types of sample preparation a small molecule standard mixture was produced consisting of 35 small molecules including amino acids, organic acids associated with primary metabolism and glucose made up to a 50pmol/μL concentration (Table 2.1). This standard was first analysed on the LCQ instrument by direct injection and an average of 32 of the 35 metabolite standard signals were observed in negative mode from three separate injections. Then the standard was analysed using MALDI-MS profiling with four different matrices, 9-AA, 1,5-DAN, NEDC and CMBT. Both NEDC and 9-AA matrices presented the highest amounts of detected peaks on average (Figure 2.8), however 9-AA crystals were more homogenous whilst spotting, which lead to it being initially selected for negative mode mass spectrometric imaging. Matrix crystallisation patterns and inconsistencies contribute greatly to signal 'hot spots' and may influence profiling results.
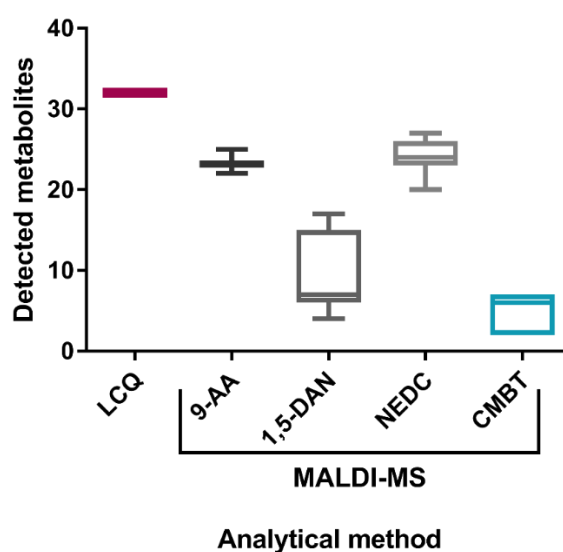
Figure 2.8 Comparison of direct injection MS analysis on LCQ instrument and MALDI-MS profiling using the Bruker Autoflex III with four matrices. Four negative mode matrices were used; 9-AA, 1, 5-DAN, NEDC and CMBT showing the average number of putatively identified metabolites (from a 35-metabolite standard mix) for each method. Three technical repeats were performed on the LCQ and 9 technical repeats were performed for each matrix (n=2).

In later experiments a higher mass accuracy instrument Synapt G2 was used and the two optimal matrices, 9-AA with an average of 23 metabolites and NEDC with an average of 24 metabolites detected, from the previous experiment were compared again by MALDI-MS profiling (Figure 2.9). The standards were analysed using an automated spiral raster pattern, which enabled ablation of a consistent amount of matrix in the case of both matrices. In this more controlled experiment, aiming to negate any low signals due to matrix crystal heterogeneity, 27 of the metabolite standards were observed using NEDC, compared to 24 using 9-AA (p= 0.0213), therefore NEDC was used in later experiments.
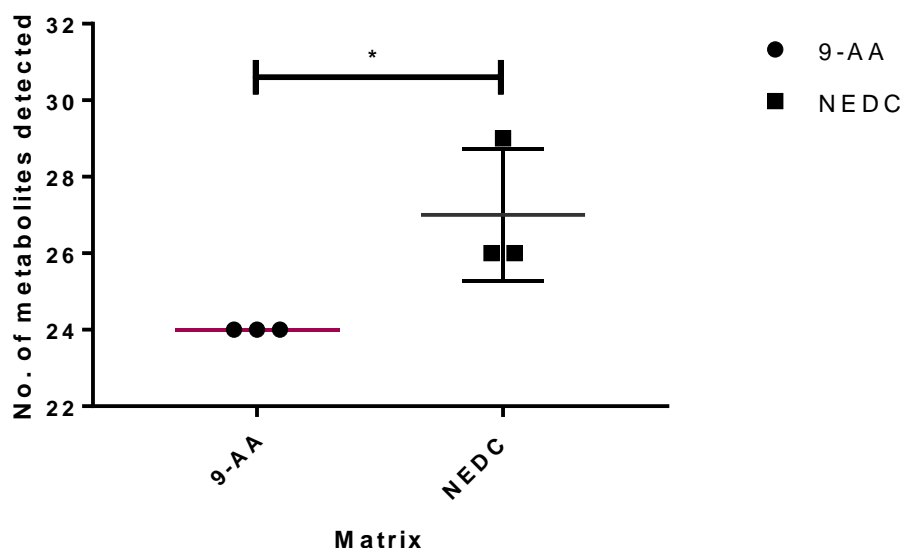
Figure 2.9 Comparison of optimal matrices. High accuracy MALDI-MS profiling using the Synapt G2. The matrices analysed were 9-aminoacridine (9-AA) and N-(1-Naphthyl) ethylendiaminedihydrochloride (NEDC) showing the average number of putatively identified metabolites (from the 35-metabolite standard mix) for each method. P<0.05 determined by Conover-Inman test (n=3).

2.3.2.2 Comparison of sample preparation methods

Comparison of the effect of different sample preparation methods was performed (Figure 2.3). As the alginate beads were 3mm in diameter these were too small to section without embedding. The beads could be directly embedded, or the

alginate could also be dissolved using a specific dissociation buffer and the intact spheroids then embedded. Initially, these two methods were compared to observe which one would be optimal. The FFPE method was dismissed immediately because this study focuses on metabolite analysis and the FFPE workflow solvents washed away soluble metabolites of interest, therefore would interfere with the analysis. In some cases of metabolite analysis formalin fixation can preserve metabolites of interest within the sample, however this was not found to be the case in these experiments (Ly *et al.,* 2016).

Analysis of the H+E stained comparisons of the two embedding methods (Figure 2.10) showed that the spheroids retained their structure better when released from alginate and directly embedded inside the embedding medium. This is possibly due to shrinking of the alginate bead during the embedding in the warm gelatin/CMC medium or inconsistency of resistance to the microtome blade during sectioning.
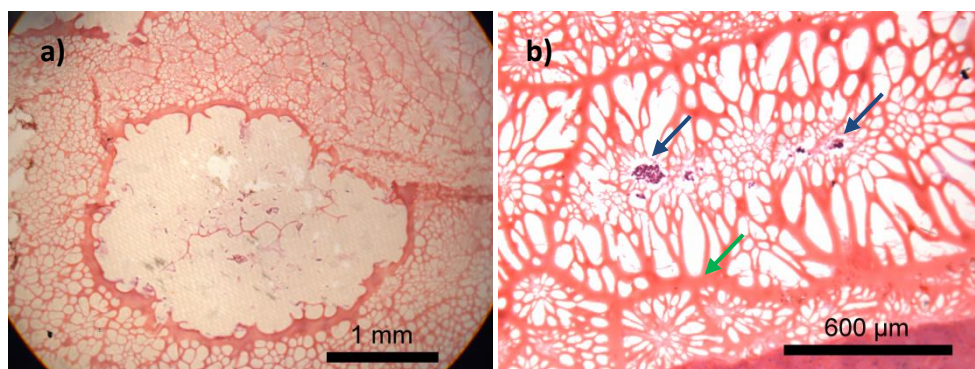
Figure 2.10 Haematoxylin and eosin stained spheroids displaying sample integrity. a) H+E of spheroids inside intact alginate bead embedded in a gelatin and CMC medium. b) H+E of spheroids released from an alginate bead embedded in a gelatin and CMC medium. The green arrow is indicating alginate and the blue arrows are indicating cell spheroids.

There was a significant loss of spheroids during the embedding process of the alginate released sample set, though this was reduced by formalin fixing before embedding (Figure 2.11F). In general, similar small molecule and lipid signals were observed in alginate and released samples. Secondly, the effect of fixing the cells with formalin was observed as well as the effect of washing the sections with ammonium acetate buffer. It was determined that fixing the samples did

improve sample integrity but reduced the amount of several small molecules detected in the sample. The buffer wash was useful in improving the lipid signal but reduced the small molecule signal as expected. The wash also resulted in slight sample loss.
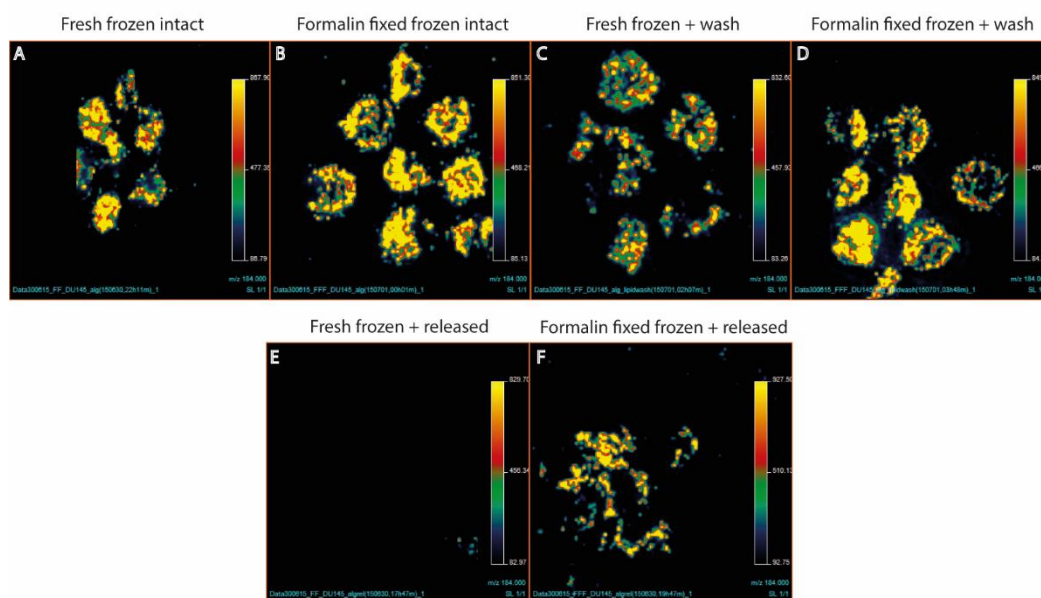
Figure 2.11 MSI of phosphocholine (m/z= 184.0736) as a cell marker inside spheroids. Comparison of different sample preparation methods on lipid signal and sample integrity; A) Alginate intact fresh frozen/ B) intact formalin fixed frozen, C) alginate intact and buffer washed fresh frozen/ D) formalin fixed frozen, E) released from alginate using dissolving buffer fresh frozen/ F) formalin fixed frozen.

Due to the least sample loss, highest small molecule signal and best embedded spheroid integrity, the fresh frozen and released spheroid method was chosen. The overall signal in alginate and released fresh frozen samples was found to be optimal and sample integrity was improved in released samples. This cannot be seen in the MSI data (Figure 2.11E) since spheroid loss was mostly observed during the embedding step. However, this was reduced by improving sample preparation in further experiments.

The SAOS-2 cell line cultured for a 4-week period was selected for further studies as it produced highly intact spheroids of <300µm diameter. However, the spatial resolution of the MALDI-MS instruments was not sufficient to observe the intra-spheroid environment. At a routine pixel size of 60µm only a maximum of 5 pixels could be attained across a spheroid. This is not sufficient in order to see molecular differences within the spheroids (Figure 2.12a).

In order to increase the size of the 3D model, longer term alginate culture of the SAOS-2 cell line was performed up to 8 weeks, however the spheroids did not develop past their maximum 300µm diameter and increased cell death was observed with longer culture periods (data not shown).
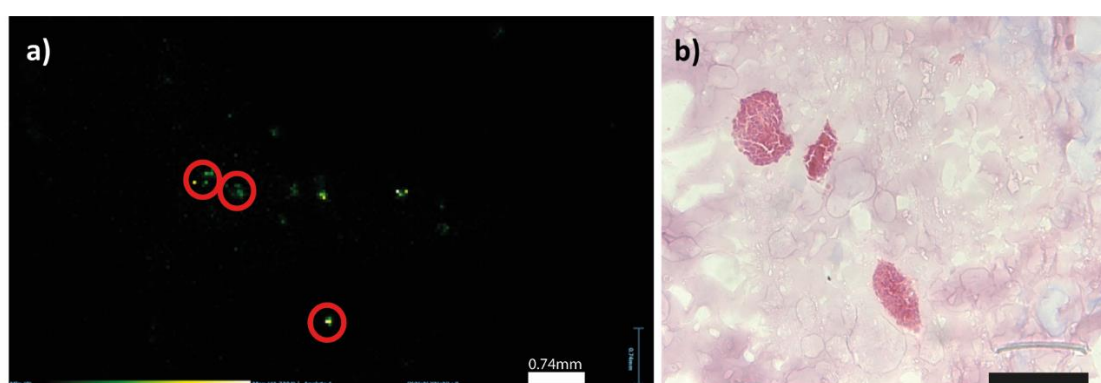
Figure 2.12 *a) MSI of phosphocholine (m/z= 184.0736) inside spheroids (circled in red) demonstrating the number of pixels (<4) achieved within individual spheroids and b) the corresponding H+E stained spheroids showing diameters of ≤300µm. Black scale bar = 200µm.*

2.3.3 Optimisation of spheroid aggregate growth

In order to create a larger 3D cancer model, 4-week SAOS-2 spheroids were released from the alginate beads using dissolving buffer. These spheroids were then aggregated by culture in 1% agarose well plates over a period of 7 days (Figure 2.2). This two-step method created large ' spheroid aggregates' of ~1mm. These spheroid aggregates consist of several clonal spheroids, which have combined into a single mass. Therefore, the spheroid aggregates are still capable of displaying observable clonal differences whilst also containing larger proliferating, apoptotic and hypoxic regions.

The aggregation of the spheroids could be observed using live fluorescence staining (Figure 2.13). At day 5 the clonal spheroid shapes are still observable by their apoptotic regions however by 7 days aggregation there is a singular apoptotic and greater cell death region. Despite the size of the spheroids a proliferating, viable cell region is still present around the edge of the mass.
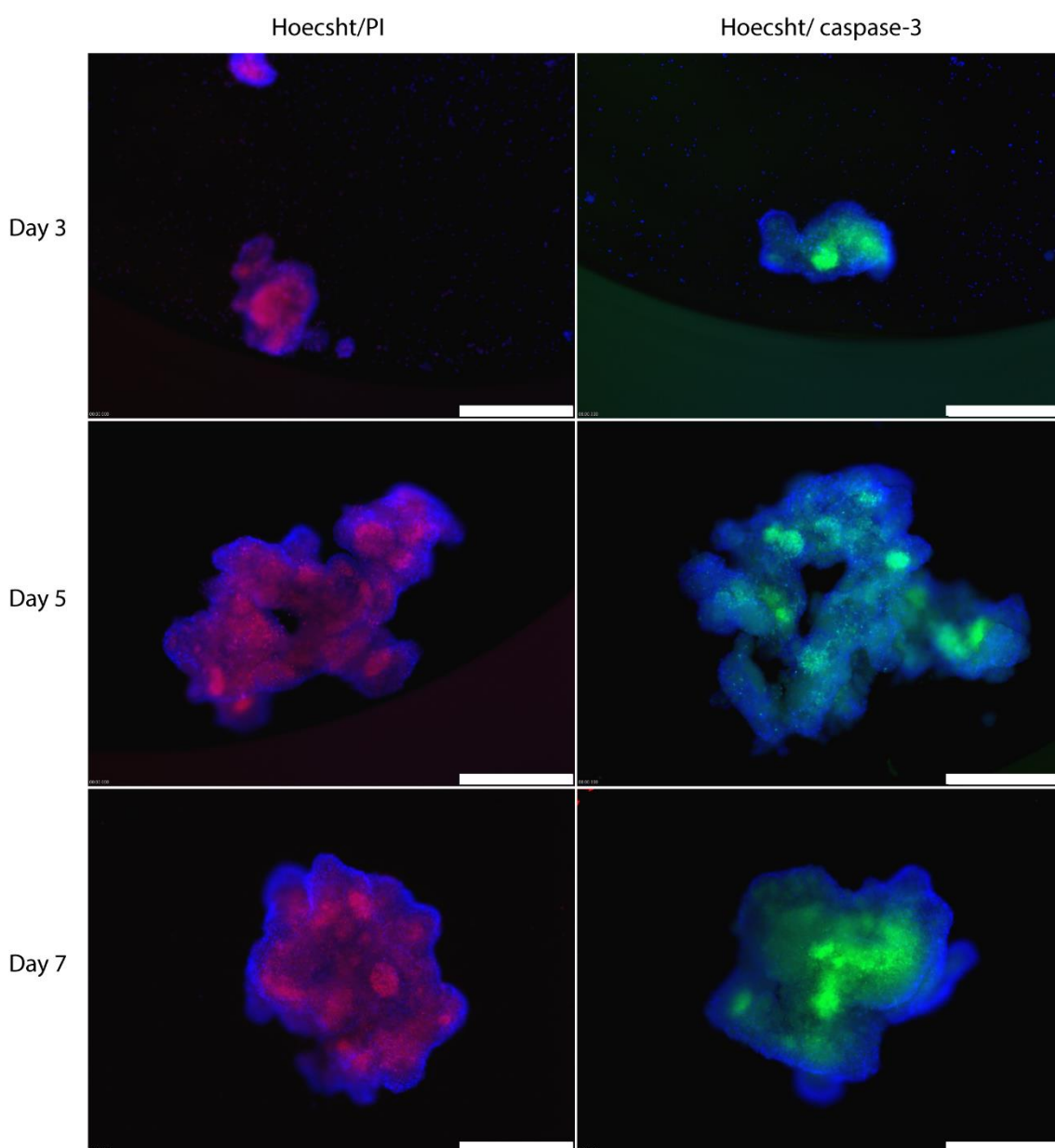
Figure 2.13 Live cell fluorescent imaging showing the aggregation of SAOS-2 spheroids into full size spheroid aggregates at 7 days culture on 1% agarose well plates. Staining was performed using Hoechst 33342 (blue), PI (red) and Caspase-3 (green) stains. Scale bar = 500μm.

77

2.3.4 Mass spectrometry imaging of spheroid aggregates

Two-step (alginate and agarose) 3D cell culture produced spheroid aggregates of ~1mm diameter, which led to MALDI-MS imaging with a higher pixel number within a spheroid. At a typical pixel size of 60μm, the method allowed for around 16 pixels across a spheroid aggregate, which was deemed sufficient to differentiate potential regional differences. Pixel sizes as low as 30μm can be achieved by oversampling in order to increase spatial resolution, however this can lead to a loss of sensitivity (Figure 2.14).
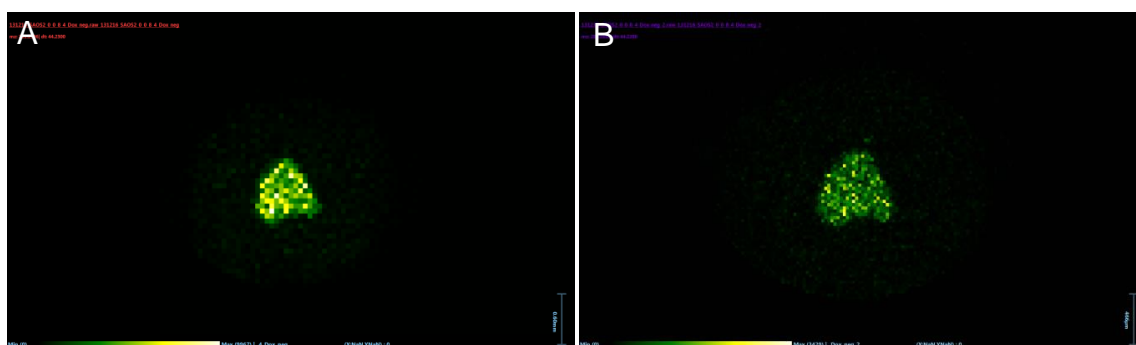
Figure 2.14 *MSI of peak m/z= 281.2596 distributed throughout a SAOS-2 spheroid aggregate at a) 60μm pixel size and b) 30μm pixel showing the difference in spatial resolution and signal.*

Regional differences can be observed in many different small molecule and lipid species (Figure 2.15). There are species distributed within the inner and outer regions within the spheroid aggregate. This provides evidence for the capability of this technique to distinguish between the different regions within the mass for future metabolomic and lipidomic studies. There were also ionic species identified which localised only within certain regions of the spheroid aggregate, which could potentially be showing the clonal differences between the different spheroids the spheroid aggregate consists of.
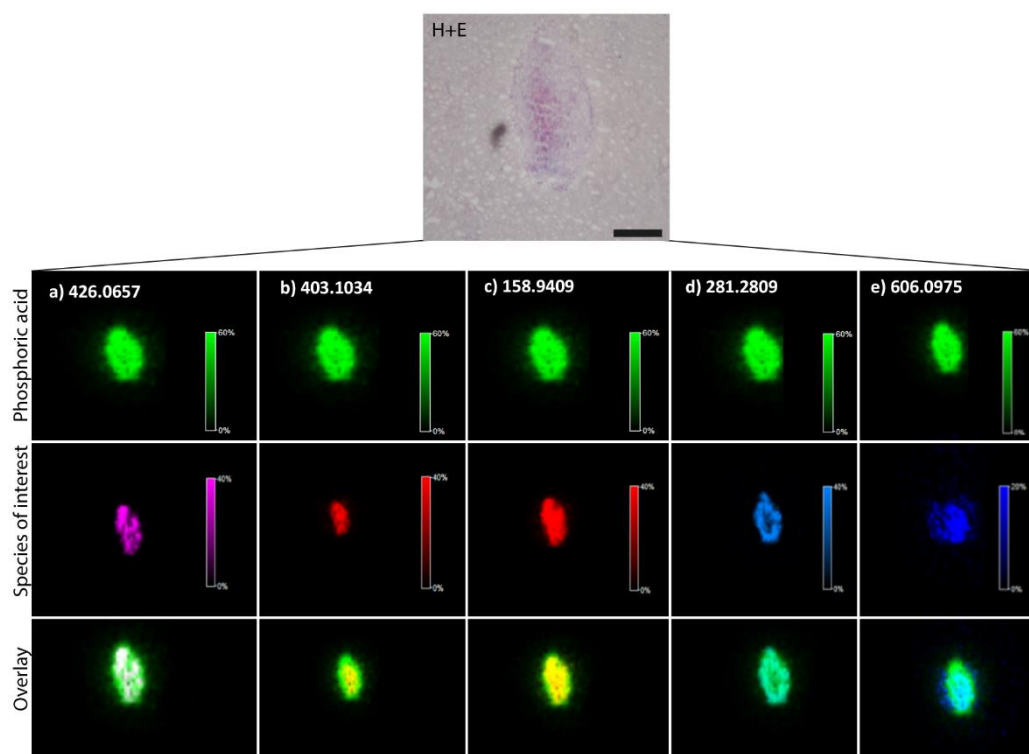
Figure 2.15 Combined MSI of SAOS-2 spheroid aggregate. Above the panel is the haematoxylin and eosin stained sample post-MSI. Several ionic species localised in specific spheroid regions. Species 78.9493 phosphoric acid (green) was used to identify the whole spheroid. This was overlaid with a) putative fatty acid species 426.0657 (pink) localised heterogeneously throughout, b) unknown species 403.1034 (red) localised in the necrotic region, c) putative pyrophosphate species 158.9409 localised in the apoptotic region, d) putative fatty acid species 281.2809 (light blue) localised in the viable region and e) putative UDP-N-acetyl glucosamine (606.0975, dark blue) localised in the apoptotic region. H+E scale bar = 500μm.

2.4 Discussion

The aims of the study were to design a cancer 3D cell culture model and workflow which was compatible with molecular imaging using MALDI-MSI. A method for the growth of spheroids and larger spheroid aggregates was demonstrated. The sample preparation workflow was optimised for improved histological and molecular analysis. Several aspects of the MALDI-MSI workflow were addressed including the culture size requirements, comparison of different matrices using a small molecule standard mix, effect of sample preparation steps on positive and negative mode molecular signal and the effect of spatial resolution. The method developed can be used to analyse small molecules and lipids to observe inter-aggregate as well as intra-aggregate molecular differences.

2.4.1 Development and analysis of alginate cultures

2.4.1.1 Alginate 3D culture selection

The spheroid forming potential of four different cancer cell lines within alginate culture was assessed. The four cell lines selected have been previously cultured using the alginate bead method within the research group and in previous studies the prostate and osteosarcoma cells formed and maintained spheroids during culture in alginate (Stock *et al.*, 2016; Akeda *et al.*, 2009). The size of spheroids obtained using the alginate method varied in this study between different cell lines as well as within the same cell line. The formation of spheroids by this method is clonal, where each spheroid is a clonal colony of a single cell, therefore each spheroid may behave differently. This may lead to inconsistency in size of spheroid and higher variance, however this could be advantageous in the study of cancer stem cell (CSC) populations and other research studies interested in clonal differentiation (Vermeulen *et al.*, 2008). In general, clonal spheroids tend to be more compact and routinely spherical but take longer to form compared to aggregation method formed spheroids. In a recent comparison, MCTS formation methods, although MCTS were of similar size, the expression of cell contact genes between the spheroids varied significantly (Gencoglu *et al.*, 2018). The MCTS formation method affected the cell line drug response, therefore the difference in gene expression could contribute to how representative the model is of the *in vivo* drug response. Additionally, differences in Hoechst 33342/PI

80

staining were observed within each individual bead. The PI stain became more intense towards the core of the bead, indicating an increase in cells with a disrupted membrane, such as dead, apoptotic and hypoxic cells. This may be due to the creation of a nutrient and oxygen starvation gradient towards the middle of a bead as a result of interference from the spheroids in the outer regions. As the cell number increases over culture time and the beads becomes more full of proliferating spheroids, diffusion of nutrients and oxygen into the core may become increasingly difficult. The proliferation rate and spheroid dimension limit, differed between cell lines and is something to consider when growing 3D cultures. The aim was to select an alginate culture which would create the largest intact spheroids, as it would be easiest to observe zonal variances within these, characteristic of spheroids. This was particularly important in order to develop these cultures for analysis using a technique such as MALDI-MS imaging, which is not capable of spatial resolution as high as microscopy techniques (Chapter 1.1.5.7).

An attempted solution to the spheroid size problem was longer period culture in order to give spheroids more time to grow in size. However, attempts to grow the spheroids for longer did not yield larger spheroids. Spheroids cultured using scaffold 3D cell culture techniques tend to be more limited in size, including alginate beads. Commonly, non-scaffold methods are used in order to achieve larger size diameters, such as liquid overlay techniques and bioreactors (Lu *et al.*, 2017). These methods usually involve aggregation of single cell suspensions to form heterogeneous multicellular masses. The spheroids formed by scaffold-based methods, in comparison, are each derived from a single cell and are therefore clonal spheroids. Easily discernible clonal colonies would be beneficial in analyses aiming to observe the effect clonal heterogeneity has on, for example, tumour drug resistance and angiogenesis (Katt *et al.*, 2016). It could be argued that scaffold-based techniques also provide a more *in vivo* like environment for tissue cancer cell types as the spheroid surroundings have a stable mechanical structure, resembling tissues, unlike non-scaffold methods. Cells must produce and organize their own matrix in scaffold-free systems as there is no physical support system. In scaffold-based models the cells are provided with an immediate structure where they can surround themselves with extracellular

matrix components and communicate with other stationary cell populations (Diekjürgen & Grainger, 2017).

Additionally, alginate is commonly cross-linked using Ca^{2+} which could potentially promote important biological pathways (Chan & Mooney, 2013). Scaffolds containing Ca^{2+} have been utilised in the past for differentiation of stem cells and bone regeneration, due to increased mimic of bone minerals, therefore it could be potentially beneficial to osteosarcoma model development (Tang *et al.*, 2013).

During the sample preparation process, leaving the spheroids inside alginate beads and embedding these whole proved an inferior method due to structural loss inside the alginate bead, leading to fracture of the spheroids and poor sections. This was possibly due to the fact that alginate is greatly hydrophilic, and its structure was compromised during the sample preparation process or due to the difference in composition between the alginate and embedding medium. In fact, alginate is a relatively stiff scaffold commonly used for embedding small formalin fixed samples before paraffin embedding, due to its compatibility with paraffin composition. Its compatibility with paraffin embedding is confirmed by the fact that it is the active ingredient in the Cytoblock™ sample preparation system which is commonly used for routine small sample embedding for paraffin blocks (Dagg *et al.*, 1992). However, the composition may be too hard when frozen, for the fresh frozen sample embedding media available, leading to poor sectioning. Washing the sections with ammonium acetate in order to remove salt contamination resulted in a large loss of small molecule signal and not a significant gain in lipid peak intensity, therefore this step was discarded. This was attempted as a desalting step which has been shown in the literature to increase lipid signal ten-fold (Angel *et al.*, 2012). Lastly, the formalin fixing step was useful in protecting cell loss due to washin and during embedding released cells, however it was already determined that the wash step was not useful and the extent of formalin fixing benefit for released samples was not high enough to make up for signal loss of small molecules caused by the 15-minute-long incubation. The idea of using a formalin fixing step without putting the sample through paraffin embedding has been mentioned in the literature as an alternative protocol for both lipid and peptide imaging (Pietrowska *et al.*, 2016). Mass spectrometry imaging of small molecules within FFPE samples has been

achieved in the past, however in this case the signal loss of molecules of interest solely from the fixing step was too high (Ly *et al.*, 2016). The cell loss experienced during spheroid release and embedding was later reduced by improvements to technique.

Nevertheless, there were still disadvantages to the chosen sample preparation method. There was cell loss due to steps involved during the alginate dissolving procedure and during cell embedding. As well as cell loss there was the issue of the dissolving process disturbing normal cell behaviour. In order to make sure there is no effect of the alginate dissolving process on the spheroids there was an additional 24-hour equilibration step in a culture environment. Although this step is required in order to make sure no effect of the releasing process is observed, in the case of future drug studies with this model it could be problematic. In these cases, the treated samples would have to be either treated after release from alginate or inside alginate culture and then released and equilibrated for 24 hours where the result seen may be altered due to incubation after treatment. The alginate dissolving buffer has a high salt concentration as well as EDTA, a chelating agent, therefore spheroids require an equilibration step in order to control for any effects on cell behaviour and sample composition. Protein and peptide studies may not have to involve an alginate dissolving step since these can be more easily applied to FFPE processed tissues and alginate is compatible with paraffin embedding (Patel, 2017). Comparison of the alginate culture sample preparation therefore led to a preparation sequence of releasing the spheroids from alginate, equilibrating these in culture media for 24 hours, directly embedding without fixation and fast freezing.

2.4.1.2 Alginate 3D culture MSI

The spheroid sizes achieved through alginate bead culture were not sufficient for observation by MALDI-MS imaging. As mentioned previously, only up to five pixels can be achieved across a spheroid of ~300μm diameter. This does not provide enough information to determine key components and discern between spheroid regions and MALDI-MSI analysis of these samples did not yield results. There are possible instrumental solutions to this, as certain MALDI-MS instruments are capable of high spatial resolution imaging (up to 5μm pixel size) for small samples or features, or a nanoSIMS instrument, which utilises a different

type of ionization and has higher spatial resolution capabilities, could be used (Dueñas *et al.*, 2017; Vanbellingen *et al.*, 2015).

2.4.2 Development and analysis of spheroid aggregates

2.4.2.1 Spheroid aggregate 3D culture selection

Taking into consideration previous discussion about insufficient spheroid diameter limiting MSI resolution, a modification of the alginate 3D culture model was developed in order to make larger spheroids with discernible and clear proliferating, apoptotic and hypoxic regions. The SAOS-2 cell line was chosen for these cultures as it produced the largest spheroids which were most consistent in size. In order to create the optimal 3D model, the alginate culture step remained in the protocol and an additional liquid overlay culture was added after release of spheroids. This decision was made in order to keep the benefits of scaffold-based culture and to potentially aid in aggregation of cells into larger compact masses. Therefore, a two-step 3D culture was designed, which could be potentially applied to many different cell types. Theoretically, because the cells are cultured in a scaffold culture initially they are given time to secrete ECM components which could aid in spheroid to spheroid adhesion during the aggregation process and longer-term culture. The spheroids were shown to aggregate into larger structured, termed 'spheroid aggregates', which displayed proliferating, apoptotic and necrotic regions and still remained aggregates of several clonal spheroids, which retained the potential of observing clonal differences within the structure.

Culturing the cells with this two-step culture method also removed a problematic equilibration step in the released alginate cultures. As the spheroids are cultured in liquid overlay culture for a further 7 days after release they are not compromised when harvesting occurs. Additionally, not only were the spheroid aggregates much easier to analyse due to their larger size there may be a benefit to a larger hypoxic and nutrient deprived region in the model, which more closely mimics the tumour micro-environment. The SAOS-2 cell line is derived from osteosarcoma, which commonly grows and survives in an oxygen low environment. Several reports of hypoxia related osteosarcoma drug resistance have been made (Zheng *et al.*, 2017; Roncuzzi *et al.*, 2014; Garofalo *et al.*, 2013). Additionally, larger spheroids are commonly used to study chemo and radio

therapeutic responses. The responses depend on oxygen depletion, compactness, apoptosis inhibition, damage repair, and permeability. All of these parameters feature at a greater extent in larger spheroid cultures (>500µm) (Zanoni *et al.*, 2016).

A possible disadvantage of the spheroid aggregate model is the irregular shaped masses it creates. A high variance in in spheroid aggregate morphology could lead to variance in results, as there is a difference in zone size and shape. Each zone will include cells of different proliferation statuses and therefore may alter results dependant on shape (Zanoni *et al.*, 2016). However, the spheroid aggregates have been shown to develop a single necrotic core and merged apoptotic and proliferating regions after the 7-day liquid overlay culture step. This indicates a lack of separated multi-regions within a mass, therefore the irregularity may not have as large a difference in the reproducibility of results. The extent of the potential variance needs to be evaluated and steps should be taken in order to improve the morphology of the spheroid aggregates. Methods, such as adjusting the composition of the growth medium, in order to improve compactness and spheroidal shape of masses have been widely studied and could be applied in this case (Leung *et al.*, 2015).

2.4.2.2 Spheroid aggregate 3D culture MSI

As the spheroid aggregates were significantly larger than the spheroids produced, MSI of samples could achieve up to 16 pixels across a spheroid aggregate. This increase in pixels per sample helped increase the amount of signal for each molecule of interest and aided in discerning localisation of ionic species within specific regions of the spheroid aggregate. By oversampling, using the Synapt G2 which has a laser diameter of around 70µm, the amount of pixels achieved across a sample could be increased but lead to loss of signal, as expected. Therefore, in order to observe localisation of small molecules within the spheroids the Autoflex III instrument was used, as it had an adjustable focus laser. Adjusting the focus of the laser to ~50µm led to less oversampling at 30µm pixel size and achieved improved spectra with higher overall molecular signal. Using this method, putative molecules which localised within specific regions of the spheroid aggregates were detected. The MS/MS capability of the instrument was not good enough to identify the molecules of interest. Localisation within specific nutrient

and oxygen dependant regions was observed as well as a potential localisation due to clonal heterogeneity. These results are promising for further studies of specific regional metabolomic and lipidomic differences as well as study of tumour heterogeneity and its association with drug resistance. This may be especially important as intra-tumour heterogeneity has been shown by several studies to predict cancer progression and response to therapy (Romero *et al.*, 2018; Rye *et al.*, 2012; Tixier *et al.*, 2011), even specifically for sarcoma types (Eary *et al.*, 2008). Observation of the clonal molecular responses to treatment within the spheroid aggregate model could be beneficial for study of intra-tumour heterogeneity and its effect.

However, to compare overall differences between spheroid aggregates the Synapt G2 was used to image at 60µm pixel size as this was found to be the most accurate and sensitive method. In cases where differences between spheroids are compared, spatial resolution was sacrificed for higher sensitivity and accuracy. MS/MS images were obtained in future experiments using the Synapt G2 due to its higher mass resolution capabilities. Due to the small size of the spheroid aggregates manual profiling was not possible.

2.5 Concluding remarks

Methods were developed for the creation of spheroid and spheroid aggregate 3D cell culture models. The models were examined using live cell imaging and histology to determine proliferating, apoptotic and necrotic regions. Observations of the two models using MALDI-MSI were made and methods for sample preparation and imaging were optimised. MALDI-MSI was not capable of extracting sufficient amounts of information from the spheroid model, due to lack of spatial resolution. Imaging of the larger spheroid aggregate model using MALDI-MSI was successful. The technique was capable of providing information on overall spheroid aggregate environment as well as specific regional localisation an abundance of small molecules and lipids.

Chapter 3: Quantitative Mass Spectrometric Imaging of doxorubicin in osteosarcoma spheroid aggregates and molecular analysis of response.

3.1 Introduction

3.1.1 Osteosarcoma

Rare cancers are defined by the RARECARE project as those with an annual incidence of less than 6 per 100,000 people in the European Union (EU) (Gatta *et al.*, 2011). Despite their individual low incidence rate these accounted for 24% of all cancers diagnosed during 2000-2007. There is a significant difference in the average 5-year relative survival of rare cancers (48.5%) compared to common cancers (63.4%) (Gatta *et al.*, 2017). This difference is likely due to the low numbers of cases which leads to a lack of knowledge, expertise and research.

Bone sarcomas are rare cancers, of estimated incidence of 4-5 per million population per year, most frequently affecting younger patients, with 60% of patients under the age of 25. Of all bone sarcomas, osteosarcoma is the most frequent primary malignant bone tumour (Fletcher *et al.*, 2013). 5-year survival of osteosarcoma has not improved significantly in Europe since the 1980s (Zhang *et al.*, 2018; Gatta *et al.*, 2011).The survival percentage for young patients in the UK on average is around 59%, which is slightly lower than most of Europe and is even lower (~20%) when considering advanced, metastatic stages (Eyre *et al.*, 2009). There is a clear need for better treatment programs, higher complexity models and increased knowledge of the disease in order to improve survival.

3.1.2 Osteosarcoma treatment

Management of osteosarcoma is complex and level of expertise in diagnostics and treatment is low, therefore the cases are usually dealt with by specialist reference centres to be able to provide the best care. The current therapeutic protocol for treatment of osteosarcoma is a multi-modal approach of surgery combined with chemotherapy. Surgery alone of high-grade osteosarcoma leads to a disease-free survival probability of only 10-20%, whilst combination with chemotherapy increases this probability to 60% (The ESMO/European Sarcoma Network Working Group, 2015). The chemotherapy regimen of doxorubicin, cisplatin and high-dose methotrexate is currently the most frequently used for osteosarcoma treatment (Ferrari & Serra, 2015). However, resistance to this combination is high and many studies and clinical trials are now focused on

finding novel drugs of differing mechanisms of action, some of which affect multiple targets or target the tumour environment (Heymann *et al.*, 2016).

3.1.3 Models of cancer

To understand the full effects of cancer treatment and drug resistance pharmaco-kinetic/dynamic modelling is required (Derendorf & Meibohm, 1999). By gaining in-depth knowledge on the path of a therapeutic once administered and the effect it then has on a tumour, we can improve design of treatment solutions. This would additionally help gain insight into the potential effect and potency of the therapeutic on a specific disease state. *In silico, in vitro* and *in vivo* models all play important roles within the pipeline and have improved greatly over the years (Harrison, 2016). The current process of drug discovery and development, based on 2D *in vitro* assays followed immediately by *in vivo*, has produced many effective drug candidates, however it is not efficient. This lack of efficiency is largely due to a drop in efficacy once in clinical trials, a lack of understanding of the disease biology and poor target selection (Harrison, 2016). Novel cancer drugs have been found to be one of the least likely to be approved by the FDA, with only a 6.7% likelihood of approval (LOA) of stage 1 to 2 clinical trials and a total LOA of 10.5% from stage 2 to 3 of trials. The major cause of this has been shown to be the high difference in efficacy of drugs between pre-clinical study models and clinical results (Hay *et al.*, 2014). The challenges in anti-cancer drug development have been identified as lack of understanding of the target downstream and off-target effects; lack of predictive models; the balance between drug safety and efficacy; lack of biomarkers and knowledge of population variance in response and cost of development (Hait, 2010). This especially affects the study of rare cancers as even less information and resources are available.

The issues caused by the lack of predictive models could be overcome with the introduction of 3D cell cultures into the pre-clinical workflow. These could be introduced to biomarker research workflows, chemotherapeutic efficacy and toxicity assays and reduce the overall cost of a drug discovery pathway due to a potential decrease in animal use as well as increased likelihood of approval due to a better understanding of the disease biology. 3D cell culture models are of an

advanced complexity compared to the conventional 2D cell culture models. Therefore, use of these would improve correlation between human *in vitro* and *in vivo* data. 3D cell culture would be particularly useful in the case of new osteosarcoma chemotherapeutics where a large inter-tumour and intra-tumour heterogeneity exists due to presence of different subtypes and many genomic rearrangements (Botter *et al.*, 2014).

Mass spectrometry imaging tools can be utilized to visualise the molecular changes within 3D cell culture models as a response to treatment. MALDI-MSI in particular has been used for drug response analysis in the past for other biological samples and is a suitable method for multiplex, untargeted analysis of cell culture models (Schulz *et al.*, 2019).

3.1.4 Chapter aims

Knowledge of tumour and novel treatment solutions could be discovered with the use of mass spectrometry imaging as a high content molecular tool. In chapter 2 methods were optimised for the small molecule MSI of spheroid aggregate 3D cultures. The aims of this chapter are to use the spheroid aggregate osteosarcoma model developed to investigate therapeutic response and utilise MALDI-MSI tools to elucidate molecules involved in this response. In this chapter, 2D monolayer and 3D spheroid aggregate osteosarcoma models were treated with several chemotherapeutics. Doxorubicin, an anthracycline which interferes with DNA transcription and replication through the stabilisation of topoisomerase II, which is one of the most widely used drugs for the treatment of high-grade osteosarcoma (Hattinger *et al.*, 2010). Paclitaxel, a taxane which binds to the β subunit of tubulin irreversibly, arrests microtubule function by hyper-stabilization of their structure and in turn arrests cell division. Paclitaxel has been used to treat a wide variety of cancer types, including soft tissue sarcoma (Horwitz, 1994). Paclitaxel has been found to induce apoptosis through binding to an apoptosis inhibitor called Bcl-2 (B-cell leukemia 2) and arrest its function (Jazirehi & Bonavida, 2004). A combination treatment of paclitaxel and doxorubicin was additionally performed as positive synergistic effects of combined treatment have been reported in the literature (Duong & Yung, 2013). Vinblastine, a vinca alkaloid, similarly to paclitaxel also arrests the cell cycle by binding to microtubules at

several sites (Himes, 1991). Vinblastine has been used as a chemotherapeutic in combination chemotherapy regimens for various cancer types, including sarcoma (Rowinsky, 2003). Following this, doxorubicin was chosen for detection by MALDI-MSI to observe drug distribution and identify the metabolomic and lipidomic response of the 3D cell culture model to treatment in order to elucidate novel significant response pathways.

3.2 Methods and Materials

3.2.1 Chemicals and Materials

Vinblastine sulphate, paclitaxel, doxorubicin hydrochloride, Dimethyl sulfoxide (DMSO) and Resazurin were purchased from Sigma–Aldrich (Poole, UK).

3.2.2 Cell culture

Initial cell culture conditions can be found in section 2.3.2. Once confluent, SAOS-2 osteosarcoma cells were trypsinised and seeded into 96-well plates at 5×10^4 cells per well. These were cultured for 24 hours before treatment.

SAOS-2 spheroid aggregates were cultured according to the method in section 2.2.3. These were kept in 96-well plates for treatment.

3.2.3 Cell viability tests

3.2.3.1 Sample preparation 2D
The SAOS-2 cell line cultured in 2D was used for testing the chemotherapeutic effect of vinblastine, paclitaxel, doxorubicin and a combination treatment with doxorubicin and paclitaxel.

SAOS-2 cells were treated with 200µL of each drug (Range of concentrations for vinblastine= 0-320 nM, paclitaxel= 0-2.56 µM, doxorubicin= 0-12.8 µM). Stocks of chemotherapeutics were dissolved in DMSO and serially diluted in culture media (vinblastine=11mM, paclitaxel=58.55mM, doxorubicin=40mM). The concentration of DMSO was kept under 0.1% for treatment. Fresh treatment media was added every 12 hours in the case of paclitaxel and doxorubicin and every 24 hours in the case of vinblastine. A combination treatment of paclitaxel and doxorubicin was also attempted in order to observe any possible synergistic

effect. The same ratios of the two drugs were combined as individual treatment e.g. 5nM paclitaxel was combined with 25nM doxorubicin as this was determined to be the optimal ratio for synergistic effect (Duong & Yung, 2013). Cell viability readings were taken at 0, 12 and 36hrs in the case of doxorubicin and paclitaxel and 24, 48 and 72hrs in the case of vinblastine to observe longer treatment effect. The doxorubicin and paclitaxel experiments were completed with 3 technical replicates performed within each set of experiments (n=3).

3.2.3.2 Sample preparation 3D

Doxorubicin treatment was selected for further analysis using SAOS-2 spheroid aggregates as it was the therapeutic found to be most effective in 2D experiments. The spheroid aggregates were treated with the range of doxorubicin concentrations chosen for study of drug effect (0, 0.16, 0.8, 4µM). Cell viability readings were taken at 0 and 48hrs and treatment media was refreshed at 24hrs. This experiment was completed in duplicate with six biological replicates per condition.

3.2.3.3 Cell activity/viability assay

To assess cell activity/survival during treatment a Resazurin assay was used. Resazurin stock was made at 3mg/mL in MEMα culture media. Resazurin (200µL of 0.3mg/mL) was added to each well and incubated for 1.5 hours (2D culture) or 3 hours (3D culture) at 37°C wrapped in foil to protect from light exposure. The fluorescence was recorded using a 530 nm excitation / 590 nm emission filter set using a CLARIOstar® plate reader (BMG LABTECH, Germany). After reading the plates, the cultures were washed twice with culture medium and cultured further until the last remaining time point. Resazurin has been shown to be relatively non-toxic with short incubation time and subsequent washes and therefore can be used for continuous studies (Riss *et al.*, 2004). In the case of SAOS-2 cultures, the Resazurin treatment did not have a significant effect on cell viability as can be seen from the control sets in each viability experiment (Figures 3.2 and 3.3). Additionally, Doxorubicin only controls at all concentrations used were tested in order to confirm the absence of fluorescent interference with the assay and differences were deemed insignificant (data not included).

3.2.3.4 Fluorescent imaging of doxorubicin in spheroid aggregates

The cells were visualised by utilising Hoechst 33342 (10µg/mL) and the spheroid aggregate sample was treated with doxorubicin (1µM) for 6 hours. The treated sample was then incubated with Hoechst 33342 for 25 minutes in a humidified atmosphere containing 5% CO_2 at 37°C. All incubations were performed in a dark environment to prevent photobleaching.

Sample well plates were visualised on an Olympus IX81 microscope. Images were captured using Cell^F software (Olympus, Germany).

3.2.3.5 Data processing and statistical analysis

The fluorescence readings were collected and media-only signal was subtracted from the sample set. Following this, all data was normalised to 0hr controls. The data was identified as non-parametric by the Shapiro-Wilk test of normality. Therefore, the Kruskal-Wallis test was used to determine if there were any significant differences between the treatments. This analysis was combined with Dwass-Steel-Chritchlow-Fligner post-hoc test when a significant difference was observed between treatment groups. Statistical analysis was performed using StatsDirect software (StatsDirect Ltd, UK). The Excess Over Bliss calculation was used to determine synergy of the paclitaxel and doxorubicin combination therapy (Borisy *et al.*, 2003).

IC_{50} graphs were produced by fitting a four parameter, variable slope non-linear regression curve using GraphPad Prism v7 software (GraphPad Software, USA). Data was transformed to a logarithmic plot for which 0nM control concentration value was changed to 1×10^{-10}nM to enable the data to be represented logarithmically. The bottom value was constrained to a constant value of 0.0 since the basal response was subtracted earlier. IC_{50} and R^2 (goodness of fit) was determined for each treatment.

3.2.4 Matrix optimisation

Several matrix combinations were compared in order to determine the optimal one to analyse doxorubicin. The selected matrix compositions are summarised in table 3.1.

Mode	Matrix solution	Final concentrations (mg/mL)	Solvent composition
Positive	5mg/mL CHCA	5	70:30 ACN:dH$_2$O+0.1%TFA
Positive	20mg/mL CHCA	20	70:30 ACN:dH$_2$O+0.1%TFA
Positive	20:20 CHCA:DHB	CHCA 15, DHB 5	70:30 ACN:dH$_2$O+0.025%TFA+3.75% FA
Positive	7:20 CHCA:DHB	CHCA 5.25, DHB 5	70:30 ACN:dH$_2$O+0.025%TFA+3.75% FA
Negative	NEDC	7	50:50 MeOH:dH$_2$O

Table 3.1 A summary of matrix compositions compared for the optimal analysis of doxorubicin by MALDI-MS.

Mass spectra were acquired using a Synapt G2 operated with a 1 KHz Nd:YAG laser (355 nm) (Waters Corporation, UK) as this instrument was accessible for the highest mass resolution at the time. A range of doxorubicin standards (0, 0.01, 0.1, 1, 10, 100μg/mL) were spotted onto a target plate (0.5μL) and the matrices were prepared and deposited on top of the standard (0.5μL). Positive spectra were acquired from 50-1200 *m/z*. Negative spectra were acquired from 50–1000 *m/z*. All matrices were analysed using an automated spiral raster pattern set to 60s raster for increased reliability. The ion mobility function was also used in order to improve separation of peaks. External mass calibration was achieved using a phosphorus red standard to achieve 95% confidence of <3 parts per million (ppm). Data was acquired and analysed using MassLynx™ software (Waters Corporation, UK). Linear regression was fitted using GraphPad Prism v7 software (GraphPad Software, USA). Additionally, the analyte standard limit of detection (LOD) and limit of quantification (LOQ) were determined. This was performed using Excel software to calculate standard error then divide this by slope of linear regression for each analyte. This value was then multiplied by 3.3 to determine LOD and by 10 to determine LOQ. These values define the limits of the analysis by taking into account the standard deviation and selecting values above the signal noise.

3.2.5 Production of doxorubicin spiked cell plug array

A doxorubicin standard spiked cell plug array was made to aid quantification of doxorubicin inside a spheroid using MALDI-MSI. The standards were spiked into the cell plug array in order to mimic the signal suppression effects in the samples. A gelatin block was made by pouring 20% gelatin into ice cube moulds, setting the moulds in the fridge for at least 4 hours and transferring to -80°C for freezing overnight and storage. The block was transferred from -80°C to a -30°C cryostat and the top of the block was cut to produce an even surface. Using a pillar drill, nine holes were then drilled into the frozen block at a drill diameter of 2.5mm and depth of 10mm. The block was placed back into -80°C storage before the loading process. During the loading process the cell plug was mounted in a cryostat set to -30°C.

SAOS-2 cells were cultured in 2D conditions as in section 2.2.2 until confluent. Cells were trypsinised, counted, centrifuged and the supernatant removed. Amount of cells required to make a full cell plug array were ≥70,000,000 cells (6-hole array), ≥11,000,000 cells (9-hole array). A range of doxorubicin concentrations were produced in culture medium (0, 0.09375, 0.1875, 0.375, 0.75, 1.5, 3, 6, 12µM). After removal of all medium the cells were mixed with drug standards 2:1 cell:doxorubicin v:v. The cell and drug mixture was made 2:1 to fill a total volume of 49.097mm^2 which was calculated using the diameter and depth of the drill hole. In order to pipette the viscous cells, the pipette tip was cut off. Immediately after mixing cells with drug standard, the mixture was deposited inside a 10mm depth and 2.5mm diameter cell plug hole. Once all the cell:drug mixtures were deposited inside the cell plug this was stored in a sealed container at -80°C. The resultant final concentrations of doxorubicin after mixing were lower by a factor of 3 (0, 0.031, 0.063, 0.125, 0.25, 0.5, 1, 2, 4µM) (Figure 3.1).
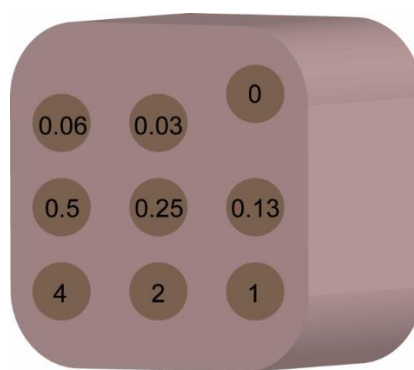
Dox array block

Figure 3.1 A schematic of the Doxorubicin spiked cell plug array.

3.2.6 MSI of doxorubicin

3.2.6.1 Sample preparation

Spheroid aggregates were treated with a range of doxorubicin concentrations chosen for study of drug effect (0, 0.16, 0.8, 4µM) and incubated in a humidified atmosphere containing 5% CO_2 at 37°C and harvested at 0, 24 and 48 hours. The sample preparation for the spheroid aggregates was identical to Chapter 2.2.4.2. Sectioning of the cell plug array and spheroids was performed as described in Chapter 2, however optimal sections were achieved when the cell plug array was sectioned immediately following transfer from -80°C.

All sample sections were taken straight after cryosectioning or from -80°C storage and immediately placed in a vacuum desiccator for ~15 minutes prior to matrix application. Negative mode imaging was performed with NEDC (7mg/mL, 50% MeOH) prepared as a matrix solution. The matrix was applied to the sample section using the SunCollect™ automated sprayer. Fifteen layers of matrix were applied, at 4µL/min for the first layer and 3.5µL/min for the remaining layers (speed x: low 7, speed y: medium 1, Z position: 35).

3.2.6.2 MALDI-MSI detection of doxorubicin in array and spheroid aggregates

Positive mode imaging of an array was conducted using a Synapt G2 for sufficient mass resolution data. Spectra were acquired at a pixel size of 100µm from 50-1200 *m/z* with the ion mobility function used to achieve better mass resolution. Data acquisition and analysis was performed using MassLynx v4.1 (Waters, UK)

and High Definition Imaging (HDI) Software (Waters, UK). This analysis did not detect doxorubicin inside the array, therefore negative mode analysis was attempted.

Imaging of the doxorubicin array and 4μM spheroid aggregate in negative mode was executed using an Autoflex III as in negative mode Doxorubicin is detectable at higher signals using this instrument. Negative ion mass spectra were acquired at a pixel size of 50μm from 50 *m/z* – 1000 *m/z* in reflectron mode. The laser was focused to around ~50μm diameter. Four hundred laser shots were acquired for each spectrum at a random walk setting. Data acquisition was performed using FlexControl (Bruker Daltonics, Germany), and visualizations were obtained from flexImaging4.0 (Bruker Daltonics, Germany).

MALDI-FTICR-MSI of 0, 0.8 and 4μM treated spheroid aggregates was performed on a 9.4T SolariX XR mass spectrometer (Bruker Daltonics, Germany) in negative-ion mode, using 200 laser shots per spot and 75 μm pixel size. This instrument was used because of its high mass resolution capabilities but was only available for a limited time, therefore use was limited. Data was acquired in a *m/z* range from 50 to 1000 Da. Data acquisition was performed using ftmsControl (Bruker Daltonics, Germany), and visualizations were obtained from flexImaging4.0 (Bruker Daltonics, Germany).

3.2.7 MSI of treated spheroid aggregates

3.2.7.1 Sample preparation
Treated spheroid aggregates (0, 0.8, 4μM) were sectioned as in section 2.2.4.1 at 10μm thickness, ensuring a section from the middle section of the spheroid aggregate was sampled. 3 sections were taken per sample, 3 samples were sectioned per treatment and the cultures were grown at n=3 which resulted in a total of 81 sections for MSI. The matrix deposition protocol used was identical to Section 3.2.6.1.

3.2.7.2 MALDI-MSI of small molecules and lipids
Imaging of spheroid aggregates was performed using a Synapt G2 because of its high sensitivity and substantial resolving power (10,000 in sensitivity mode). Images of 60μm pixel size were acquired. Data were acquired over an *m/z* range

of 50–1,000 in negative mode analysis. The ion mobility function was used to improve separation of peaks. Data acquisition and analysis was performed using MassLynx v4.1 (Waters, UK) and High Definition Imaging (HDI) Software (Waters, UK). Tandem MS fragmentation was performed using an isolation window of 0.3 Da.

3.2.7.3 Data processing

Regions of interest (ROIs) containing whole spheroid aggregates were selected in Waters HDI 1.4 imaging software and exported as average spectra into MassLynx software. They were then centroided and exported as .txt files. The data was imported into Marker View software 1.2 (Applied Biosystems/MDS Sciex, Canada), where it could be formatted into a table. An exclusion list to remove NEDC peaks was applied to the dataset, to remove the influence of the matrix signals when observing relationships of the treatment groups between spectra. The data was restricted to 5000 peaks and 0.1 minimum intensity and autoscaled. Principal Component Analysis- Discriminant Analysis (PCA-DA) was performed by informing the software which samples belonged to each treatment group. The software then selected two components optimal for separation of the treatment groups.

3.2.7.4 Statistical analysis

Reduced data generated by the DA-PCA was initially put through a screening by t-test comparison of each treatment group against each other. The top 50 p-values for ionic species of all comparison variants were chosen for statistical analysis. The data was identified as non-parametric by the Shapiro-Wilkes test of normality. Therefore, the Kruskal-Wallis test was used to determine if there were any significant differences between the treatments for each ionic species. This analysis was combined with Dwass-Steel-Chritchlow-Fligner post-hoc test when a significant difference was seen between treatment groups. Statistical analysis was performed using StatsDirect software (StatsDirectLtd, UK).

An alternative statistical method with a higher capability of dealing with large non-parametric data sets was also used in order to get more information from the data. Some significantly varying species may have been missed by using the t-test screening method to reduce the data size for Kruskal-Wallis analysis. The

compiled data in the form of a table was exported from MarkerView software into R Foundation for Statistical Computing Platform version 3.4.1 (R Core Team, 2017). A linear mixed effect statistical model package called nlme was used (Pinheiro & Bates, 2011) in order to compare groups in the full DA-PCA reduced data set, taking into account the fixed and random effects. This model uses an Analysis of Variance (ANOVA) model in order to determine significant values. The Bonferroni correction for multiple testing was applied to the significance threshold of 0.05, making the cut-off value 1×10^{-5} for the list of 5000 peaks. Twenty four significantly differing ionic species were identified, 6 of which were determined possible isotopes of existing hits and dismissed from the analysis. The 18 significantly differing ionic species were further tested in order to observe the t-values (representing difference between treatment values) and p-values (representing the degree of significance between treatment values). The test was run twice for each significant ionic species, once to compare treatment 0.8µM to control and 4µM and repeated to compare 4µM to control and 0.8µM treatments. Finally, the data was represented using the lattice package on R (Sarkar, 2008) by scatterplot attempting to show all random data variation due to batch, culture and fixed variation due to dose (Figure 3.2).
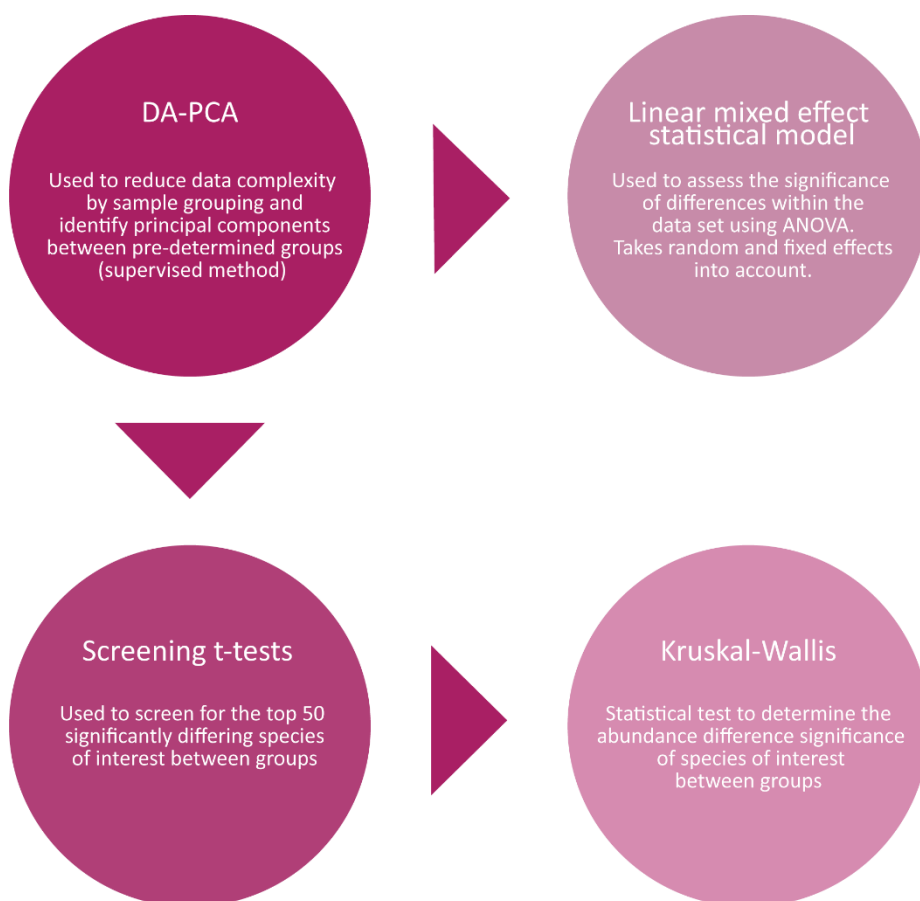
Figure 3.2 *Workflow diagram of the statistical tests used to determine significantly different ionic species.*

The significantly differing peaks discovered using either statistical approach were then given putative assignments based on a database search in the Human Metabolome, Metlin or LipidMaps search databases. The error allowance used was 30ppm for small molecules and 0.01 Da for lipid identifications which was acceptable for the data acquired. Following the database search biological relevance was investigated within the possible identities.

3.3 Results

3.3.1 Effect of drug treatment on cell viability

Initially several different chemotherapeutics relevant to osteosarcoma were chosen for treatment of 2D SAOS-2 cultures to observe their effect on cell viability using the resazurin assay. The resazurin assay consists or an in-cell reduction of resazurin, a REDOX indicator. This is then converted to resarufin which is

detectable using fluorescence. The cell activity, measured by increase in the fluorescent signal can be directly correlated to cell viability in most cell culture cases. It should be noted that this is not always the case and, ideally, a cell activity assay such as this one should be combined with a growth assay, such as cell counting or spheroid growth analysis. The cells were treated with a range of concentrations of doxorubicin, paclitaxel, vinblastine and a combination treatment of doxorubicin and paclitaxel. Doxorubicin had the most effect on cell viability of all the chemotherapeutics (Figure 3.3). Doxorubicin treatment displayed a dose-dependent and time-dependent decrease in cell viability. Cell viability was reduced at 36 hrs treatment compared to 12 hrs ($p < 0.0001$). A significant reduction in viability can be observed between 0nM and 3200nM treatments at 12 hrs ($p < 0.0001$) and at 400nM at 36 hrs ($p < 0.0001$). The IC_{50} of the doxorubicin and paclitaxel combination treatment (IC50= 0.9µM) is lower than doxorubicin alone (IC50= 1.09µM), however is most likely due to an additive effect rather than synergistic action as observed by the Excess Over Bliss values (<15%) (Table 3.2). Vinblastine treatment led to a significant drop in cell viability after 24 hrs of treatment at as low as 5nM (p= 0.0077). Vinblastine treatment was performed for a longer treatment period to observe longer term treatment effects of the chemotherapeutic on the SAOS-2 cultures. However, the overall effect at 72 hours was not significantly different from the effect at 24 hours of treatment (p= 0.2826). A similar effect was observed with paclitaxel treatment. The cell viability remained at a similar value between 12 and 36 hours of treatment (p= 0.2272).

Paclitaxel (nM)	Doxorubicin (nM)	Excess over bliss (%)
5	25	6.67
10	50	-1.66
20	100	-21.38
40	200	-31.30
80	400	-18.32
160	800	5.57
320	1600	8.78
640	3200	0.95
1280	6400	4.01
2560	12800	0.30

Table 3.2 Excess over bliss values for the combination chemotherapy of paclitaxel and doxorubicin on SAOS-2 cells cultured in 2D. Values <0= antagonistic, 0= additive, >0= synergistic (n=3).
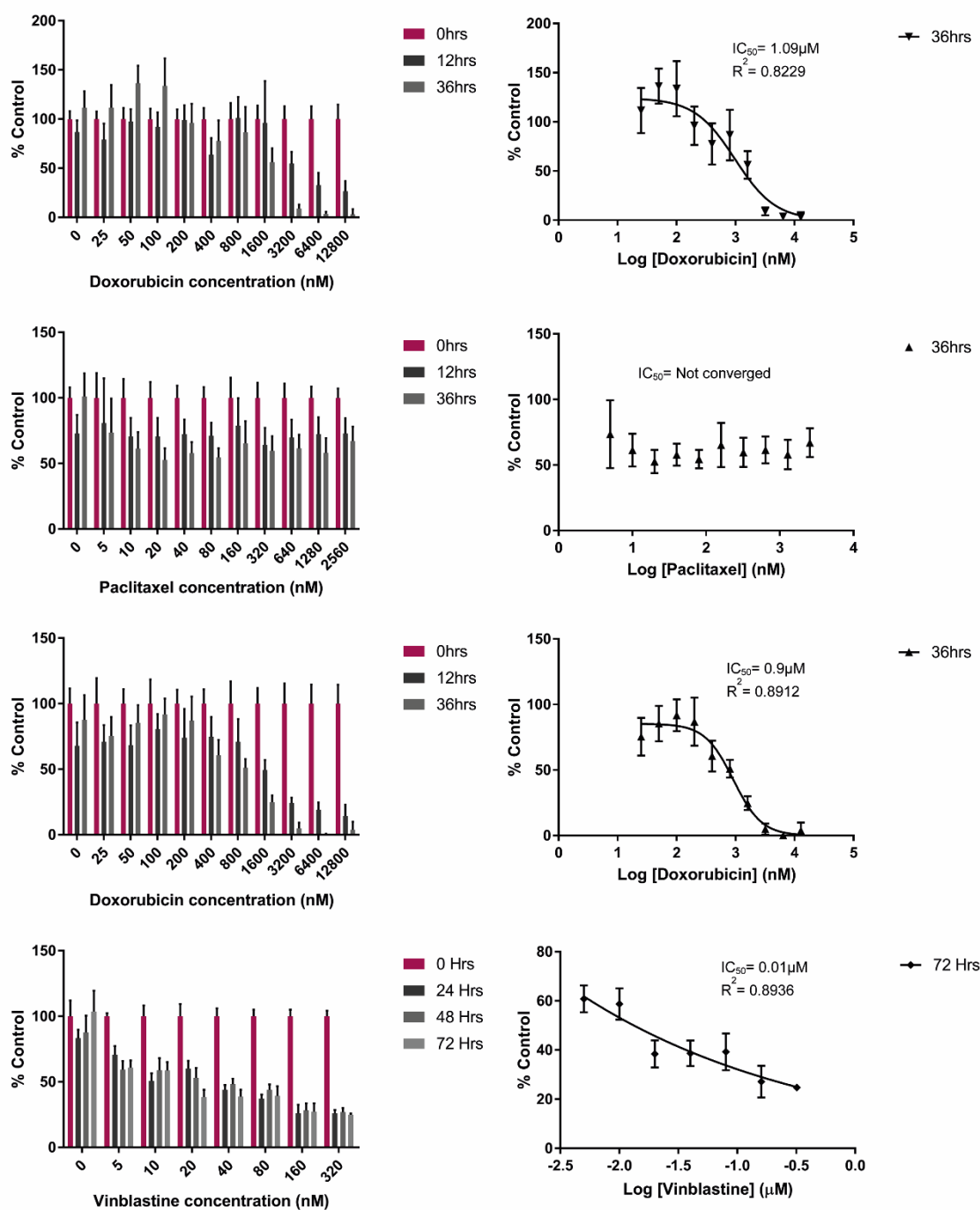
Figure 3.3 Percentage of cell viability compared to untreated control and a non-linear transform plot displaying amount of drug required to reduce cell viability by 50% (IC$_{50}$). For each treatment condition the IC$_{50}$ and R2 values are displayed. The treatments were performed on 2D cultured SAOS-2 cells. a) Doxorubicin treatment b) Paclitaxel treatment c) Doxorubicin and paclitaxel combination treatment of the corresponding concentrations to individual treatment combined (doxorubicin concentrations shown on scale) d) Vinblastine treatment. All experiments performed at n=3.

The 3D cell culture model results differed considerably to the 2D model (Figure 3.4). Doxorubicin was selected to pursue in further studies since its effect was the most profound in 2D cell cultures. In 3D culture there was a small but significant increase in cell viability between 0 and 4μM spheroid aggregates at 0 hrs treatment (p= 0.0101), possibly due to an immediate drug effect on cell viability. There was no significant change in the cell viability observed at treatment times of up to 48 hours at concentrations of up to 4μM, which is nearly five times the concentration of the IC_{50} in 2D cell cultures (Figure 3.3).
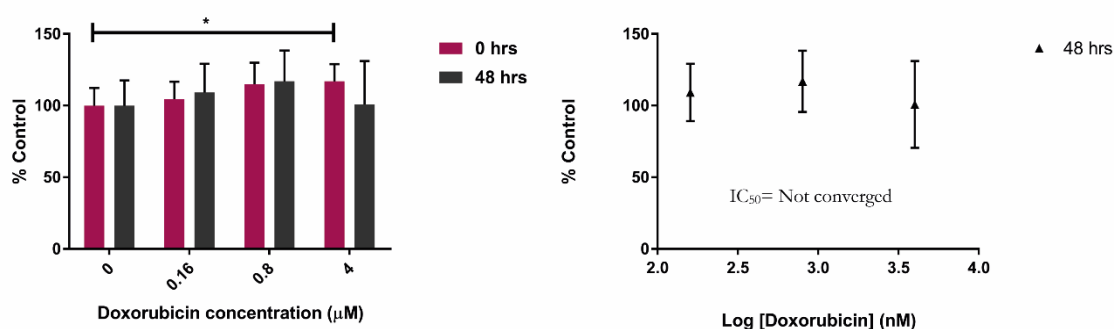
Figure 3.4 Percentage of 3D cell culture viability compared to untreated control and a non-linear transform plot displaying amount of drug required to reduce cell viability by 50% (IC50). 3D cell culture results show no significant effect on cell viability by doxorubicin at concentrations used after 48 hours treatment (n=2).

3.3.2 Detection of doxorubicin

3.3.2.1 Fluorescence microscopy detection of doxorubicin

As doxorubicin was found to be the most effective therapeutic treatment in 2D and not significantly effective in the 3D spheroid aggregate model it was important to determine whether the drug had fully penetrated the mass by the end of the 48-hour treatment period. After 6 hours, doxorubicin could be observed within all areas of the spheroid aggregate, indicating that it has diffused through the whole ~600μm mass (Figure 3.5).

Figure 3.5 *Fluorescence imaging (Hoechst (blue)/doxorubicin (red)) indicating full doxorubicin infiltration into spheroid aggregates. Scale bar = 500μm.*

3.3.2.2 Optimisation of matrices for detection of doxorubicin

Commonly utilised matrices in MALDI analyses, such as α-CHCA, do not always achieve the highest signals for a molecule of interest. Doxorubicin is a molecule which does ionise during the MALDI process but, due to close interfering lipid peaks in biological samples, is very difficult to detect at lower concentrations using conventional matrices. Thus a binary matrix combination of α-CHCA and DHB was tested for improved detection of doxorubicin. Mixtures of 20/20 (Final concentration α-CHCA= 15mg/mL, DHB= 5mg/mL) and 7/20 (final concentration α-CHCA=5.25mg/mL, DHB=5mg/mL) were used in order to determine if these were an improvement to the sole use of α-CHCA as a matrix. NEDC was also tested in negative mode in order to investigate whether doxorubicin detection produced a better limit of detection in negative mode. The lowest LOD (1.644μM) and LOQ (4.981μM) was achieved using the α-CHCA:DHB 7/20 matrix (Figure 3.6 and Table 3.3). This was not necessarily due to the signal to matrix peak ratio as this matrix did not produce the highest signal when normalised to a matrix peak (Figure 3.6). Interestingly, 5mg/mL α-CHCA which presented with the highest peak:matrix ratio resulted in the poorest LOD (18.5μM) and LOQ (56.1μM) (Figure 3.6 and Table 3.3). This is due to the way the limits are calculated. If the data values are less consistent and higher overall, the standard deviation will rise and therefore so will the LOD and LOQ values.
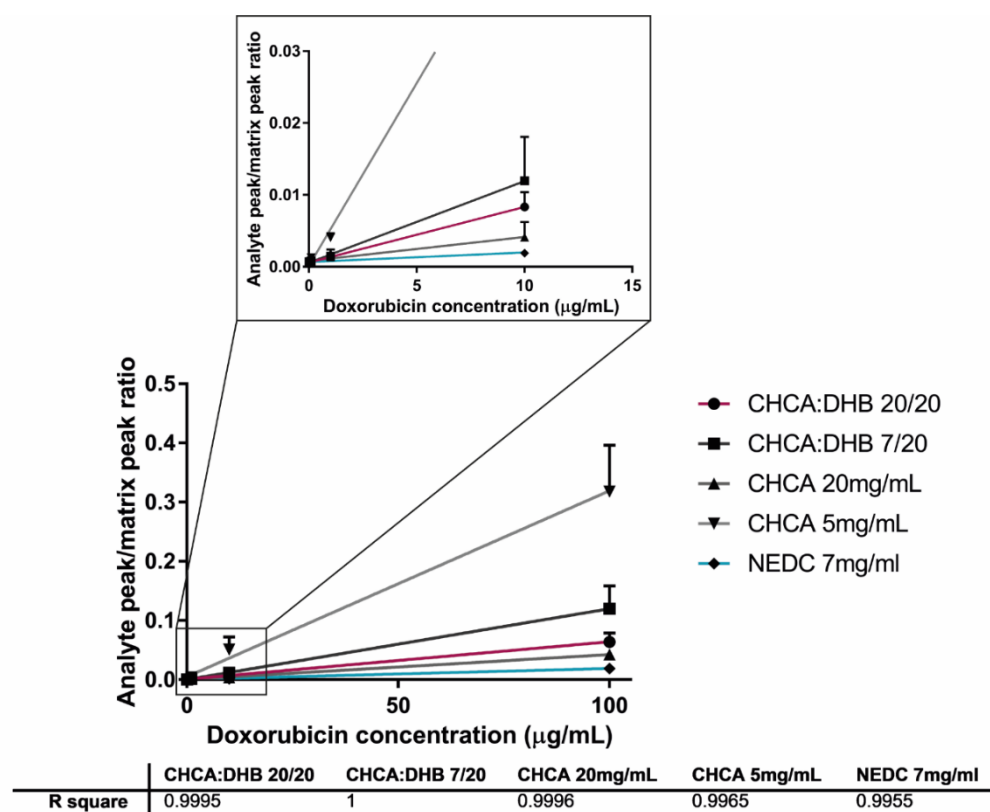
Figure 3.6 Detection and quantification limits of doxorubicin using MALDI-MS profiling in positive and negative mode. The signal was normalised by matrix peak and the data point distribution at lower concentrations is shown. Goodness of fit are displayed as R^2 values (n=3).

Matrix (positive)	LOD (mg/mL)	LOD (mM)	LOQ (mg/mL)	LOQ (mM)
CHCA:DHB 20/20	3.85	7.07	11.65	21.44
CHCA:DHB 7/20	0.9	1.64	2.71	4.98
CHCA 20mg/mL	3.67	6.74	11.11	20.43
CHCA 5mg/mL	10.06	18.5	30.47	56.07
Matrix (negative)	LOD (mg/mL)	LOD (mM)	LOQ (mg/mL)	LOQ (mM)
NEDC 7mg/mL	9.23	16.98	27.97	51.46

Table 3.3 *Comparison of matrices showing the limit of detection (LOD) and limit of quantification (LOQ) using each matrix.*

3.3.2.3 Detection of doxorubicin using cell plug arrays

Cell plug arrays were made to aid quantification of doxorubicin inside the spheroid aggregates. This was made by mixing SAOS-2 cells with doxorubicin standard and spiking these cells into a gelatin block. These could then be sectioned

alongside the sample of interest and used as an internal standard array to determine the concentration of doxorubicin within the sample.

Detection of doxorubicin within the cell plug arrays was not successful in positive mode by Q-TOF MS due to a close, interfering lipid peak. Other instrument types (FT-ICR) and negative mode were used to visualise the drug. Putative doxorubicin could be observed in negative mode showing a promising increase in signal with increase in doxorubicin concentration, however the TOF determined signal was not sufficient for absolute determination (Figure 3.7). Here a signal corresponding to the *m/z* of ATP was chosen not necessarily as a qualitative observation but simply to demonstrate that signal within the cell array was, in general, consistent throughout and this is not the effect seen for the Doxorubicin abundance.
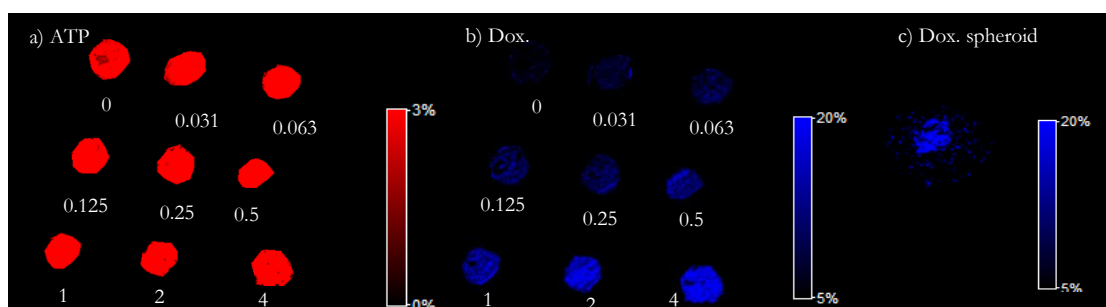
Figure 3.7 Negative mode MALDI-MSI of a cell plug doxorubicin array (0-4μM) and a 4μM treated spheroid aggregate. a) Distribution of ATP throughout the array to demonstrate even distribution of cells, b) Intensity of doxorubicin throughout the array (0-4μM doxorubicin), c) Intensity of doxorubicin inside a 4μM treated spheroid aggregate.

Treated spheroids were also compared using an FT-ICR instrument, which is known to obtain higher mass resolution and higher sensitivity data. Using this instrument the doxorubicin peak was well separated from any interfering peaks and could be easily identified (Figure 3.8). An increased doxorubicin signal could be observed with increased treatment concentration, whereas the signal for ADP is undetectable in 4μM treated spheroid aggregates (Figure 3.9). As before, the ADP signal was used to show that there isn't an overall increase with treatment within the model. Due to instability of the phosphate groups of ATP and ADP

during the desorption ionisation process levels of these molecules cannot be easily determined as you cannot be sure whether the molecule observed was fragmented. ADP and ATP peaks were used as references within this chapter as their structures could be confirmed using MS/MS.
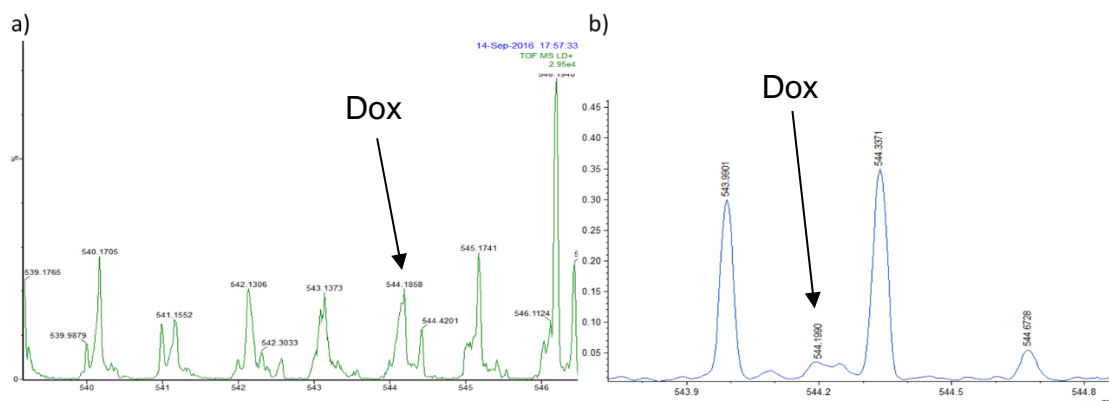
Figure 3.8 Positive mode MALDI-MSI a) Q-TOF of an average spectrum and b) FT-ICR-MS of a single spectrum of spheroid aggregates treated with doxorubicin (4µM).
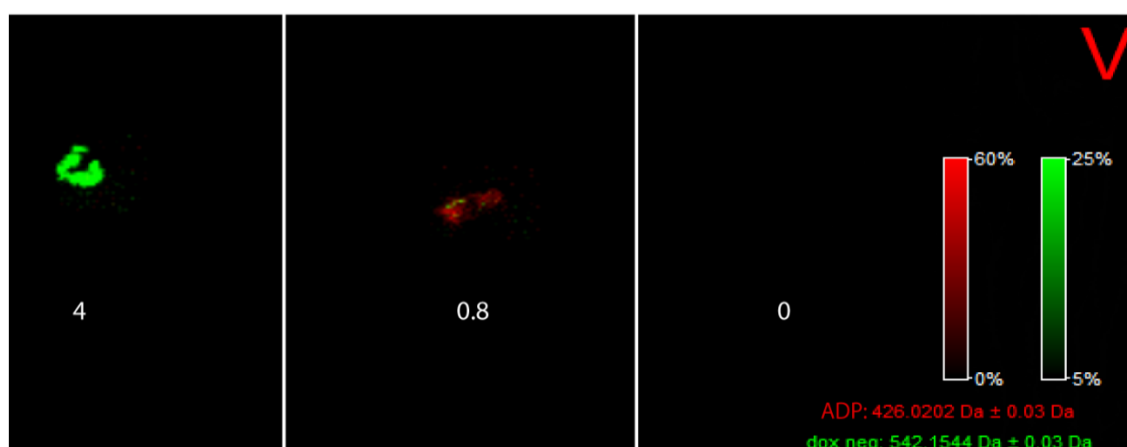
Figure 3.9 Negative mode MALDI-MSI (FT-ICR-MS) of spheroid aggregates treated with different concentrations of doxorubicin (0, 0.8, 4µM). Red signal represents ADP and the green signal represents doxorubicin.

3.3.2.4 Defining spheroid aggregate doxorubicin response using MSI

In order to define the metabolomic and lipidomic spheroid aggregate response to doxorubicin, treated and untreated 48-hour spheroid aggregate sections were

imaged in negative mode. The whole spheroid region was selected and average spectra were extracted for comparison between treatment groups. Comparison was performed using PCA-DA, a PCA which takes into account the group the samples belong to and finds the principal components which separate these groups. The control and treatment groups were well separated and several ionic species were separated out in the loading plot, in particular for the high treatment group (Figure 3.10).

The in-software t-test was used as a screening method and the top 50 significant variances were selected from the data. After removing high possibility isotope peaks, 42 species were left. Using the Kruskal-Wallis test of significance, several ionic species were found to be significantly higher with treatment such as *m/z* 335.0617 ($p<0.005$) and some were higher in control samples *m/z* 765.5488 ($p<0.005$) (Figure 3.11). The most significantly differing ionic species are displayed in figure 3.11 as determined by both statistical approaches used and remaining significant peaks are provided in the supplementary information (Appendix chapter 3 figures 1-9). Due to low abundance of these peaks, small sample size and interference of isobaric species, MS/MS analysis was not conclusive.
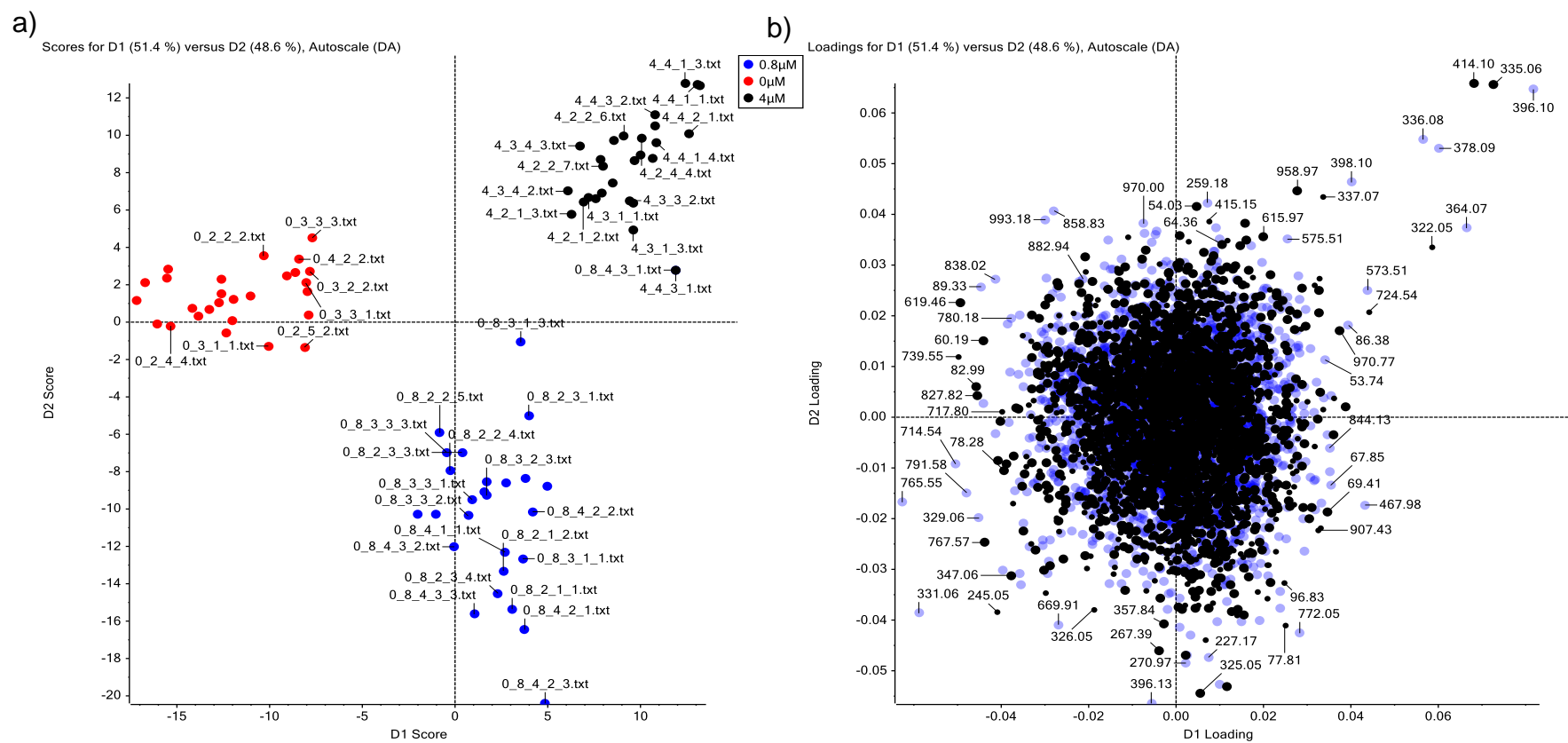
Figure 3.10 PCA-DA loading plots show a) a clear separation of treatment groups on the score chart and b) the weighting chart of all the ionic peaks. The significantly differing peaks of interest are found around the edges of the cluster and similar peaks are clustered around the middle. Principal component 1 = 51.4%, principal component 2 = 48.6% (n=3).
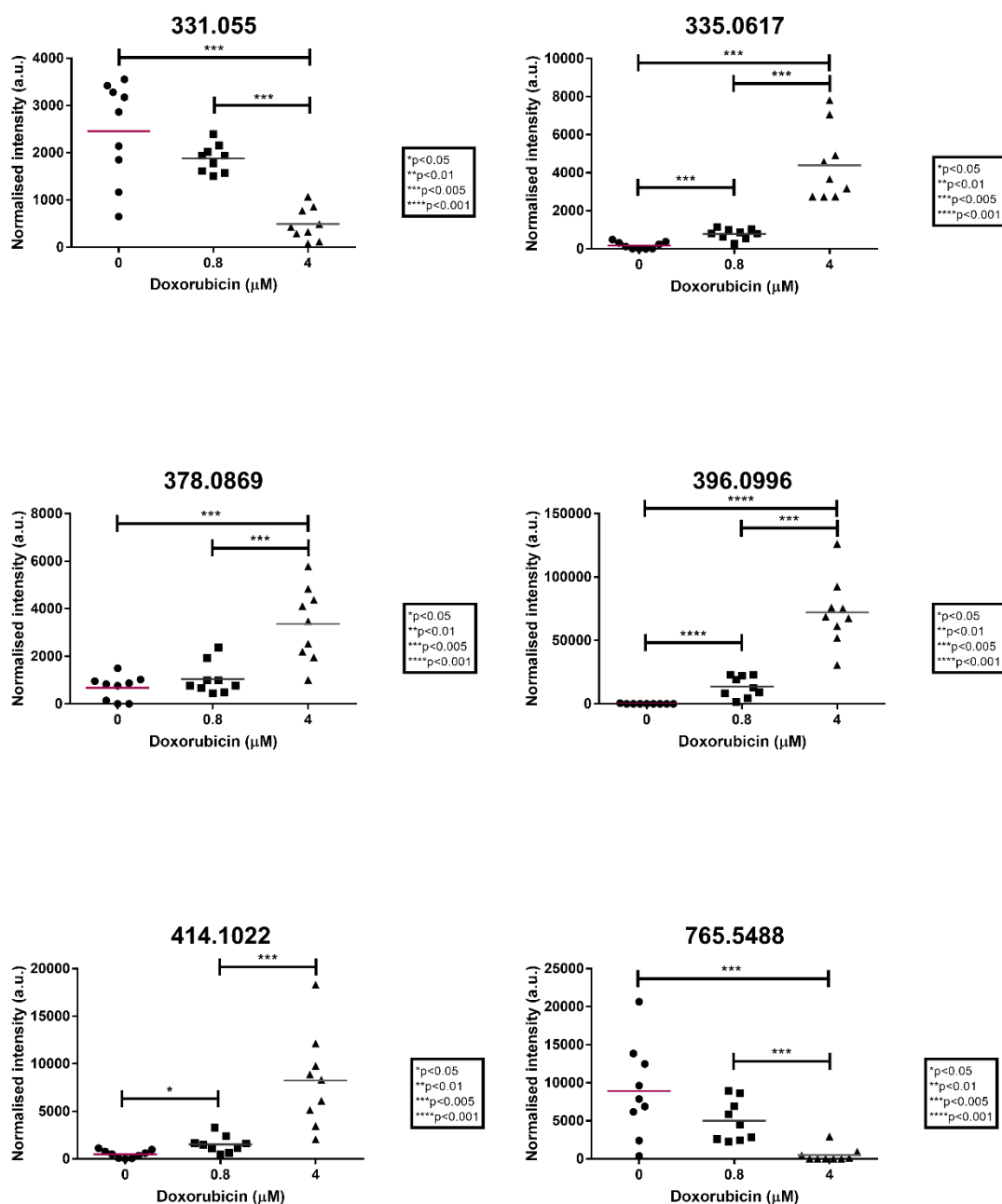
Figure 3.11 Comparison of normalised signal intensity of ionic peaks between control, 0.8 and 4 µM treatments. The species shown are the most significantly higher/lower between treatment groups as determined by both an in-software t-test and ANOVA (p<0.05) (n=3).

3.3.2.4.1 Linear mixed effects analysis

As well as the PCA-DA method discussed previously, a linear mixed effects model was also used to define the best statistical analysis method for this data. The resulting 18 ionic species and the corresponding F-values (overall

significance) are listed in Table 3.4. The data is also displayed in scatter graph form, sorted into random effects (batch and culture) and fixed effects (dose) in Appendix chapter 3 figures 10 and 11. The random effects were determined to not have a significance on the fixed effect variance. The data was displayed this way to show the high variability present and highlight the necessity for the three separate experiments with three biological and three technical replicates in this study in order to obtain significant data. The individual p-values of differences between treatment groups are given in appendix chapter 3 table 1. For the ionic species which were only discovered using the ANOVA method the individual p-values can only be found in appendix chapter 3 table 1 and not in appendix chapter 3 figures 1-9.

Ionic species (m/z)	F-value
180.4920	4.57×10^{-6}
245.0544	1.68×10^{-7}
253.2270	9.89×10^{-6}
331.0550	3.48×10^{-11}
335.0617	$<1.00 \times 10^{-12}$
347.0637	1.14×10^{-7}
364.0735	1.49×10^{-9}
378.0869	2.62×10^{-11}
396.0996	$<1.00 \times 10^{-12}$
404.0321	1.61×10^{-7}
414.1022	$<1.00 \times 10^{-12}$
464.0080	1.29×10^{-6}
565.9493	1.05×10^{-6}
583.9583	5.98×10^{-6}
589.9554	1.92×10^{-7}
714.5375	9.77×10^{-8}
765.5488	1.25×10^{-10}
791.5778	3.10×10^{-7}

Table 3.4 A list of doxorubicin treatment dose dependant significantly differing ionic species produced using an ANOVA test. Significance is represented by an F-value for which the significance threshold was 1×10^{-5}. 10 highlighted species (in pink) also appeared as significant in the in-software statistical test.

Ten ionic species (highlighted in Table 3.4) were detected as significant in both statistical tests (Figure 3.12), which may be indicative of the strong significance of these ionic species in drug response.
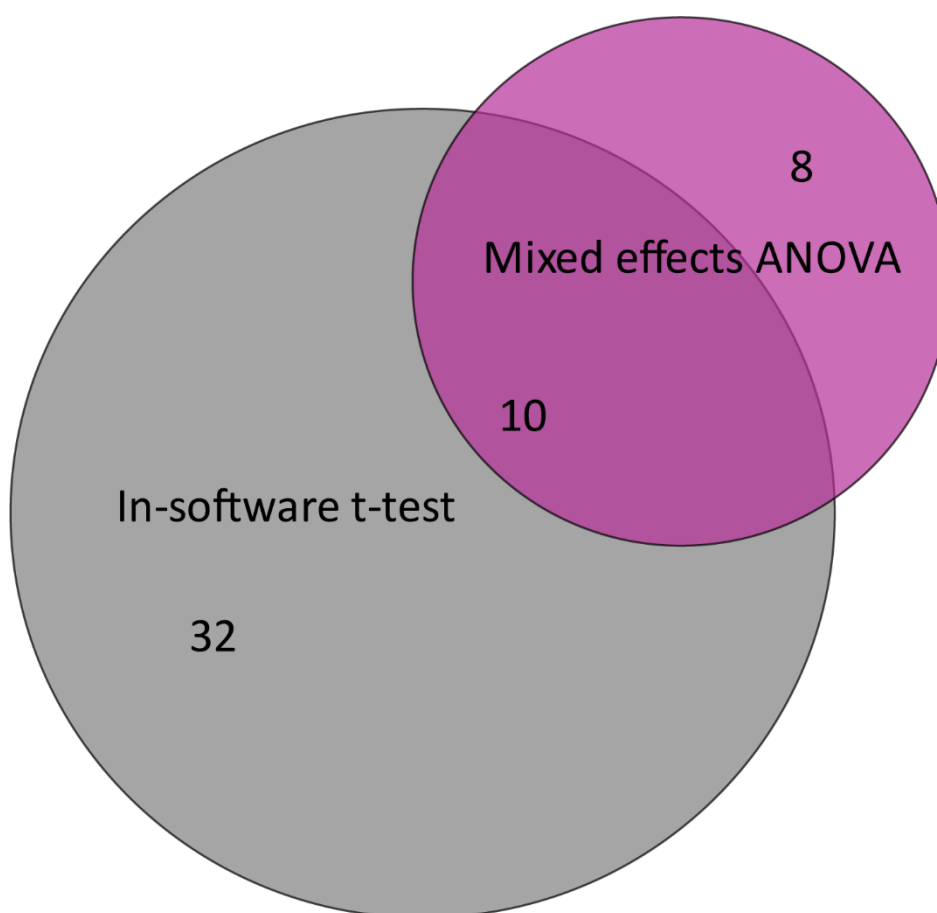
Figure 3.12 Venn diagram representing the difference between the statistical tests used. 10 of the ionic species 'hits' were matched between the two methods. The less stringent in-software test identified 32 unique ionic species and the mixed effects ANOVA identified 8 unique ionic species.

3.4 Discussion

The aim of this chapter was to determine the effect of chemotherapeutics on 2D and 3D models of osteosarcoma using mass spectrometry imaging. The dose response of SAOS-2 osteosarcoma monolayer cells to a small panel of chemotherapeutics was determined and doxorubicin was selected as a candidate for testing in 3D cell culture due to its effectiveness in 2D viability experiments. The metabolomic and lipidomic differences between the different treatment groups were then analysed using MALDI-MSI, including doxorubicin itself, in

order to identify novel molecules involved in drug response. Significantly differing ionic species were identified using DA-PCA and significance of these confirmed using an in-software statistical method as well as a more stringent mixed effects ANOVA model.

3.4.1 Effect of treatment on viability of 2D cell cultured SAOS-2 cells

Treatment of 2D SAOS-2 cells with paclitaxel, vinblastine, doxorubicin and a combination treatment of doxorubicin and paclitaxel all resulted in a decrease in cell viability. Paclitaxel induced a viability drop of nearly 50% compared to control at 10nM concentration, which did not increase significantly with higher concentrations of therapeutic. Because of this drop and a lack of further dose dependant response the IC_{50} could not be determined. This may be a result of the drugs mechanism of action, as paclitaxel blocks cells in the G2/M phase of the cell cycle which leads to an inability to form a mitotic apparatus (Horwitz, 1994). A further decrease in viability was seen at longer treatment times as this may allow more cells to enter the susceptible phase of the cell cycle (Straubinger, 1996). Vinblastine had a more significant effect on SAOS-2 cell viability. Vinblastine treatment showed a dose-dependent response, although this was not fully effective on all the cell viability within the culture. Even at longer treatment times (up to 72 hours) an unaffected cell population remained, either due to slow proliferation or cell cycle arrest. In the cases where there still remains a population of active cells after treatment the level of apoptosis should be assessed. The absence of a significant decrease in cell viability may also be due to osteosarcoma drug resistance mechanisms, such as overexpression of ATP-binding cassette (ABC) drug transporters which cause decreased drug uptake and increased drug efflux (Li *et al.*, 2016). To overcome these mechanisms research has been dedicated to the use of combination therapy to prevent drug resistance. The potential of combination therapy was demonstrated by Yang *et al.* who used a combination of a Pgp inhibitor NSC23925 and paclitaxel treatment on osteosarcoma cell lines aided in preserving their chemotherapeutic sensitivity (Yang *et al.*, 2014).

doxorubicin treatment reduced cell viability in 2D cultures with an IC_{50} of 1.09µM. The IC_{50} obtained with a combination treatment of paclitaxel and doxorubicin was lower (IC_{50}= 0.9µM) however this was not shown to be significantly higher than single dose experiments by Excess Over Bliss calculations, as the combined effect is not significantly higher (>15% cut-off value is commonly used) than the sum of the two treatments. As doxorubicin presented the largest dose dependent response out of the drug panel it was chosen for further testing on the 3D SAOS-2 model.

3.4.2 Effect of doxorubicin on 3D cell culture

A large difference in effect was observed in the 3D cell culture model compared to the 2D cell response. At a longer treatment time of 48 hours, compared to 36 hours, and nearly 4 times higher concentration (4uM compared to IC_{50} of 1.09µM) the cell viability was not significantly decreased in the 3D cell culture model. This difference could be due to the barrier-like environment of the spheroid structures preventing direct access of the drug to all cells within the culture. However, fluorescence microscopy and MSI results confirm that the drug penetrated the whole aggregate by the end of the 48-hour treatment period. Difference in response between 2D and 3D cell cultures could also be due to a decrease in proliferation or an increased expression of drug resistance mechanisms, such as ABC drug transporters. As doxorubicin-induced DNA damage predominantly occurs in the G2 phase of the cell-cycle reduction in cell proliferation is an important factor to increased resistance. A spheroid structure will consist of proliferating and quiescent regions which reduces the percentage of proliferating cells at a set time and reduces the number of cells entering the G2 phase of the cell cycle. An increase in resistance to doxorubicin in 3D cell cultures was also observed by Rimann *et al.* who observed higher resistance to treatment by the slower growing osteosarcoma HOS cell line (Rimann *et al.*, 2014). They also only observed a response to doxorubicin in the 3D model for chondroblastic osteosarcoma samples, which suggests changes in drug resistance mechanisms. ABC transporter-mediated drug efflux has been demonstrated as a relevant mechanism in doxorubicin resistance and inhibition of this mechanism lead to reduction in resistance (Fanelli *et al.*, 2016). There are several novel therapeutic treatments in development based on this knowledge including ABCB1 inhibitors,

protein kinase inhibitors, use of doxorubicin derivatives and nanodrug delivery systems (Hattinger *et al.*, 2017). The reduction in response could also be due to a change in drug inactivation pathways. For example, in osteosarcoma cell lines, xenografts and patients a higher expression of glutathione S-transferase P1 (GSTP1) was correlated to a poorer response. Additionally, inhibition of this enzyme in combination with treatment improved outcome (Pasello *et al.*, 2008; Bruheim *et al.*, 2004).

An increase in doxorubicin resistance within 3D cell culture compared to 2D is consistent with literature for the SAOS-2 cell line and other cell lines (Rimann *et al.*, 2014; Arai *et al.*, 2013), though the difference is more marked in this study. The IC_{50} values determined for 2D and 3D cultures of SAOS-2 cells vary as different treatment times, assay types and 3D cell culture methods have been used, but all observe an increase in resistance to doxorubicin in 3D cell cultures. Rimann and colleagues determined the 2D IC_{50} value for SAOS-2 of 0.12µM and 3D value of 0.3µM after 72 hour treatment (Rimann *et al.*, 2014). Baek and colleagues showed a 2D IC_{50} value of 0.1241µM and 3D value of 0.341µM after 24hrs of treatment with no further decrease in cell viability with longer treatments (Baek *et al.*, 2016). The Arai research group showed a 2D IC_{50} value of 0.19mM and 3D value of 0.47mM after 48 hours of treatment (Arai *et al.*, 2013). As all of these groups used different spheroid production techniques and different ways to treat and compare groups it is quite difficult to correlate the data. The lack of standardized and consistent 3D culturing systems thus far is a factor which affects reproducibility and reliability of drug screening (Verjans *et al.*, 2018).

2D IC_{50}	3D IC_{50}	Treatment time (hrs)	Reference
0.12mM	0.3µM	72	Rimann et al.
0.1241µM	0.341µM	24	Baek et al.
0.19mM	0.47mM	48	Arai et al.
1.09µM	>4µM	48	Current publication

Table 3.5 A summary of comparisons between 2D and 3D cultured SAOS-2 cell viability response to Doxorubicin.

3.4.3 Detection of doxorubicin by MALDI-MSI

The detection and quantification of doxorubicin and its metabolites by LC-MS in several biological matrices has been validated previously (Mazzucchelli *et al.*, 2017). However, MALDI-MS imaging capabilities to detect and quantify doxorubicin at lower concentrations (<25µM) are not as efficient due to lack of the LC separation modality. Detection is currently only possible at higher concentrations (~30µM) or with a high mass resolution instrument due to interference of abundant surrounding lipid peaks. Doxorubicin is a fluorescent molecule, therefore its distribution is commonly monitored using fluorescent imaging. However, there are well-known limitations associated with this method, such as variation in the fluorescent signal due to DNA, histone binding and its location in cell membranes, cytoplasm and nucleoplasm. It is often measured at early timepoints for this reason (Mohan & Rapoport, 2010). The potential benefit of mass spectrometry imaging is that the doxorubicin molecule itself is monitored and may be more accurate at detecting and quantifying doxorubicin but also that it can distinguish the drug and its metabolites, as has been demonstrated recently by the Hummon group (Lukowski *et al.*, 2017). However, a limit of detection (LOD) was not published for this method and the concentration used (30µM) was not necessarily treatment relevant. Doxorubicin treatment of osteosarcoma patients ranges from 40-60mg/m^2 which translates to a C$_{max}$ (maximum plasma concentration) of 3,660ng/ml which is equal to 6.73 µM/L (Liston & Davis, 2017). Considering that not all of the drug within patient serum will reach the osteosarcoma, the assumed concentration value would be much lower than 30µM. In fact little is published about the achievable LOD of doxorubicin, though the technical challenges have been noted (Baluya *et al.*, 2017). Use of a novel binary matrix in this chapter to observe doxorubicin by MALDI-MS led to a large improvement, of more than 10-fold, in LOD and LOQ, compared to the conventionally used 5mg/mL α-CHCA matrix (Table 3.3). A combination of α-CHCA and DHB has previously been used to improve performance for peptide glycan analysis. However, to our knowledge, nothing has been published on the use of the matrix combination on small molecules or its optimisation for an imaging modality (Laštovičková *et al.*, 2009; Laugesen & Roepstorff, 2003). However, even with the improved sensitivity, the limit of detection was slightly

higher than the predetermined IC_{50} of doxorubicin treatment in this study (1.64µM compared to 1.09µM) and the limit of quantification is higher than the highest treatment concentration used for 3D cell cultures in this study. However, the lower LOD will aid in future detection of the drug within models where higher concentrations of doxorubicin are used.

The LOD and LOQ of doxorubicin would also be improved by using a higher mass resolution instrument. The approach is demonstrated by using an FT-ICR instrument, where doxorubicin is identified more easily within the 4µM and 0.8µM treated spheroid aggregates (Figure 3.9).

3.4.4 Detection of the metabolomic and lipidomic doxorubicin response in SAOS-2 spheroid aggregates by MALDI-MSI

The metabolomic and lipidomic response of spheroid aggregates was analysed using a PCA-DA method, which separated the most significantly differing components between the three treatment groups (0, 0.8, 4µM) which were analysed using MALDI-MSI. Several masses were significantly up/down regulated and 10 of those were significant in both statistical analyses used. Interestingly ADP was found to be depleted to a level below detection in the 4µM doxorubicin treated samples (Figure 3.9). This reduction due to drug treatment is expected for ATP, however the fate of ADP during treatment of cancer is not as well described. Although this was not reported in the literature, it was shown in the spheroid aggregate imaging experiments where a dose dependant ADP concentration was observed even though the cell viability remained stable. The resazurin assay used to monitor cell viability in this study was based on reduction of resazurin by the electron transport system therefore arguably is less affected by the reduction in phosphate or irreversible binding of ADP. The reduction in signal observed could be due to apoptosis dependent changes of the glycolytic pathway (Pradelli *et al.*, 2014). Samples would require activated caspase-3 staining after treatment to specifically observe differences in apoptotic cell count rather than total cell viability. Reduction of ADP could be due to increased Poly(ADP-ribose) Polymerase-1 (PARP) expression. PARP is activated by DNA damage and PARP inhibitors combined with chemotherapeutics have shown a

significant effect in several osteosarcoma cell lines, therefore expression and activation of this should be investigated within the 3D model (Engert *et al.*, 2017). Reduction could also be due to a classic drug resistance response involving efflux of doxorubicin by ABC transporters. These efflux pumps require a constant supply of ATP which reduces the overall levels of the drug within the cell and decreases it's energy dependent activity (Tacar *et al.*, 2013; Gottesman *et al.*, 2002). On the other hand, there may be a more simple instrument related explanation. During the desorption ionisation process of MALDI phosphate group containing molecules may lose these groups and display reduced masses. As a reduction in ATP with treatment is expected it could be that a reduction in ATP signal would also reduce apparent ADP signal.

Several unknown ionic species were found to be significantly up/down-regulated with Doxorubicin treatment. These were putatively identified using database searching. Ionic species *m/z* 335.0617 was putatively identified in the Human Metabolome Database as S-nitrosoglutathione (GSNO) (15ppm), an endogenous nitric oxide (NO) carrier which plays a critical role in redox based NO signalling. This molecule has been shown to induce increased expression of stress response genes and proteins, such as hypoxia-inducible factor 1 (HIF-1) and nuclear factor-κB (NF-κB) and has been implicated as a contributor in various disease states (Broniowska *et al.*, 2013; Gaston, 2003). Ionic species *m/z* 364.0735 was identified as 2-S-glutathionyl acetate M-H (23ppm) which was recognised as a product of CYP2E1 metabolism and GSH conjugation of drugs such as 1,1-Dichloroethylene Epoxide and Vinylidene Chloride (Forkert, 1999; Liebler *et al.*, 1985). CYP2E1 is a drug metabolising enzyme with a broad substrate selectivity and a preference for low molecular weight substrates, therefore it is possible that it may also be involved in the breakdown pathway of Doxorubicin in osteosarcoma (Harrelson *et al.*, 2007). This may be an indicator of differential expression of cytochrome P450 enzymes in osteosarcoma as a chemoresistance response. Differential expression in P450 enzymes was previously reported in rhabdomyosarcoma where expression of CYP2E1, amongst other enzymes was expressed significantly higher in tumour tissue (Molina-Ortiz *et al.*, 2014). Another putative identification of potential interest to the study of osteosarcoma drug resistance was *m/z* 378.0869 which was

identified as S-Lactoylglutathione (28ppm). S-Lactoylglutathione is a known product of the Glyoxalase I (GLO1) enzyme. Elevated expression of GLO1 is significantly associated with many different cancer types, such as squamous cell carcinoma, gastric, high-grade breast, pancreatic, sarcoma, bladder and renal cancers. Additionally, high expression has been specifically associated with local invasion, metastasis, growth and progression (Zou *et al.*, 2015). A highly significant increase in ionic species *m/z* 396.0996 was also found. This was putatively identified as S-Adenosyl-4-methylthio-2-oxobutanoate (3ppm) which may be a factor in a modified methionine salvage pathway from 5'-methylthioadenosine (MTA) which could be of interest in cancer cases as a regulator of apoptosis and proliferation (Albers, 2009). Putative lipid identifications were also retrieved from the LipidMaps database for ionic species *m/z* 714.5375, identified as PE(O-35:2) (0.0068Da); *m/z* 758.4969, identified as PS(34:2) (0.0009Da); *m/z* 765.5488, identified as PA(41:4) (0.0048Da); *m/z* 791.5778, identified as PG(37:0) (0.0030Da); and *m/z* 858.8311, identified as 1-O-behenoyl-Cer(d34:1) (0.0027Da). Although the lipid identifications listed are not directly associated with any known osteosarcoma pathways, they are worth investigating as possible markers of drug response. Furthermore, many of the significantly differing small molecules were not identified in the database searches and further investigation into the identities of these should be done, as these could be novel or unique markers for osteosarcoma drug response.

Unfortunately, due to the small sample area (~1mm) and difficulty in obtaining MS/MS signal from these low abundance molecules due to interference from isobaric species, their identities were not confirmed. This issue could be circumvented by running LC-MS of pooled spheroid aggregate sections in order to increase detection of the peaks of interest and improve MS/MS signal, as reported previously (Acland *et al.*, 2018). Alternative methods could also be used to preserve some of the spatial localisation. For example, the Hummon group developed a method utilising serial trypsinisation to strip layers of cells from a spheroid and subsequent collection and extraction for LC-MS analysis (Feist *et al.*, 2017). Another alternative would be to use laser capture microdissection to dissect the spheroid aggregate regions and collect them for LC-MS analysis, which can be done after using the sample for imaging, as has been recently

demonstrated (Marialaura Dilillo *et al.*, 2017). Or methods such as Liquid Extraction Surface Analysis Mass Spectrometry (LESA-MS) could be used, as these have a higher extraction efficiency, though the spatial resolution (~1mm) of the analysis may not be sufficient (Eikel *et al.*, 2011).

3.5 Concluding remarks

In summary, a panel of 4 drugs was assessed on the SAOS-2 osteosarcoma cell line and doxorubicin was selected for further testing. A large difference in cell viability was observed between the 2D and 3D models of the tumour. Analysis of doxorubicin imaging inside a spheroid aggregate model of osteosarcoma was improved from a published concentration of $30\mu M$ to an LOD of $1.644\mu M$. The optimised sample preparation method could also be applied to tissue and in-solution in future experiments, as required. Quantification of the drug within the 3D cell culture sample set was not successful due to the limit of quantification remaining above the concentration range used. An untargeted MALDI-MSI analysis of treated spheroid aggregates was performed where a significant difference in the small molecule composition was observed between untreated and treated osteosarcoma spheroid aggregates as well as differences between treatment concentrations. These changes were observed despite no significant decrease in overall cell viability in the treated 3D model. Biologically significant putative identities, such as GSNO, 2-S-glutathionyl acetate and S-Lactoylglutathione, were assigned to several ionic species. The significantly varying species could not be identified using MS/MS due to sample size and interfering isobaric species. Therefore, the samples should be analysed additionally using a different method, such as LC-MS, to confirm the identities of the species of interest.

Chapter 4: Peptide and protein MS analysis of cancer spheroids and development of QMSI

4.1 Introduction

Conventional osteosarcoma (OS), the major subtype of OS, consists of complex karyotypes with the presence of multiple chromosomal abnormalities (Martin *et al.*, 2012; Hoogerwerf *et al.*, 1994). This atypically high level of chromosomal instability is thought to cause intra and inter-tumour heterogeneity, which complicates diagnosis and treatment (Kovac *et al.*, 2015). It has a broad spectrum of morphology and is currently sub-classified into 8 different histological subtypes. Additionally, osteosarcoma, primary or secondary, also has a broad immunoprofile which lacks diagnostic specificity (Fletcher *et al.*, 2013). A lack of specific diagnostic markers and full understanding of the molecular changes involved in the tumour subtypes in combination with the rarity of the disease contribute to difficulty in diagnosis and treatment of osteosarcoma (Zhong *et al.*, 2017; Kong & Hansen, 2009).

4.1.1 MSI of cancer heterogeneity

Mass spectrometry imaging is one of the analysis methods applied to enable the study of cancer heterogeneity (Bateman & Conrads, 2018). The technique is well suited for the analysis of heterogeneous samples as it can be used for untargeted, multiplex analysis of tissue or cell-based models and preserves spatial localisation of the molecules of interest. Therefore, within a single imaging experiment several molecular species can be visualised in order to elucidate differing areas of the sample (Balluff *et al.*, 2017). MSI has recently been used for discovery of high-grade sarcoma protein biomarkers (Lou *et al.*, 2016). Lou and colleagues additionally focused specifically on the identification of survival associated markers for high-grade OS, leiomyosarcoma (LMS), myxofibrosarcoma (MFS) and undifferentiated pleomorphic sarcoma (UPS) and found several proteins associated with poor and good responses to treatment within different sarcoma types (Lou *et al.,* 2016).

4.1.2 Quantification of proteins and peptides

Subsequent quantification of proteins and peptides within a tissue or culture model improve the analysis further. The current methods to do so are either tissue homogenisation dependent (e.g. LC-MS, western blot), which remove spatial information, or are limited in the amount of proteins that can be analysed in a

single experiment (e.g. IHC). MALDI-MS imaging is a multiplex method which is also able to preserve spatial information. A novel technique using this method produced a recombinant 'IMS-TAG' protein which could be trypsinised into several standard proteotypic peptides in order to validate the presence of specific proteins within tissue (Cole *et al.*, 2013).   Using this method a recombinant standard protein, made up of proteotypic (protein specific) peptide standards, could be trypsinised and prepared alongside the sample. Then appropriate isotopically labelled standards would be homogenously distributed across the sample and used as matched external standards for absolute quantification purposes. The standard would potentially be representative of the tissue as it would go through the same sample preparation process. This is similar to the QconCAT protein technique which has been adapted for quantification of peptides within cancer samples (Goddard *et al.*, 2016; Chen *et al.*, 2014; Beynon *et al.*, 2005). Development of a way to quantify proteins using MSI would aid investigations of the effect of treatment. Use of isotopically labelled standards may mitigate many of the heterogeneity, extraction, and suppression effects commonly encountered in MALDI MSI experiments. With the development of this technique, endogenous protein and biotherapeutics could be quantified within a culture model or tissue and the intensities localised to specific regions within the sample, providing accurate region-specific quantitative information.

4.1.3 Proteomic analysis of 3D osteosarcoma models

3D cell culture models of sarcoma have been shown to have different protein expression patterns compared to monolayers. These were largely found to correspond to a change toward a more stressful environment containing nutrient deficient and oxygen depleted areas as well as a decrease in proliferation (Gebhard *et al.*, 2018). However, it was determined that certain acutely localised protein species may have been 'buried' within the highly abundant peaks, as the whole spheroid was homogenised. MSI could be used to analyse proteins and peptides within osteosarcoma tissue and cell culture models in order to determine treatment dependent over/under expression. In the case of MSI, spatial distribution data would be preserved and species which are only present in a specific area of interest within the model may be easier to detect. This would aid

in the discovery of novel inhibitors of chemo-resistance due to increased understanding of sites of action and the mechanisms of resistance.

4.1.4 Chapter aims

To gain further knowledge of osteosarcoma and find solutions to chemo-resistance, spheroid aggregate peptide and protein changes in response to treatment should be observed. The aims of this chapter were to develop methods for the peptide analysis of the osteosarcoma spheroid aggregate model. Doxorubicin-treated osteosarcoma spheroid aggregates were analysed using MALDI-MSI and several putative peptides were identified. Proteotypic peptide standard arrays were produced using the osteosarcoma cell line SAOS-2 and the functionality and reproducibility of these were assessed for future MALDI-MSI peptide quantification experiments. These could potentially enable quantification of multiple peptides within a sample whilst maintaining spatial distribution information.

4.2 Materials and Methods

4.2.1 Materials

Peptide standards for heat shock protein 70 (VTHAVVTVPAYFNDAQR), heat shock protein 90 (GVVDSEDLPLNISR) and actin (AVFPSIVGRPR) and their ^{13}C, ^{14}N labelled versions were purchased from Cambridge Research Biochemicals (Billingham, UK). A custom SpikeMix mixture of peptide standards (Appendix chapter 4 table 1) and a SpikeMix 1000 labelled peptide mixture (Appendix chapter 4 table 2) were purchased from JPT Peptide Technologies (Berlin, Germany).

4.2.1.1 Production of 3 peptide standard

Peptide standards were dissolved in 1:4 ACN:0.1M ammonium bicarbonate solution in order to produce a solution of a mixture of the three containing 180pmol/µL of each peptide in solution. This standard mix was then used in the 3 peptide cell plug array (Section 4.2.3). The same stock mixture was produced with the three labelled standards for spraying on top of the sample.

4.2.2 Cell culture

Initial cell culture conditions were performed as stated in section 2.3.2. Once confluent, SAOS-2 cells were trypsinised then used for cell plug array production. SAOS-2 spheroid aggregates were cultured according to the method in section 2.2.3. These were treated and harvested as stated in chapter 2 with the addition of a PBS wash step before embedding.

4.2.3 Production of peptide arrays

As described in Chapter 3, gelatin blocks were made by pouring 20% (w/v in dH$_2$O) gelatin into ice cube moulds, setting the moulds in the fridge for at least 4 hours and transferring to -80°C for freezing overnight and storage. Each block was transferred from -80°C to a -30°C cryostat and the top of the block was cut to produce an even surface. Nine holes were then drilled into the frozen block at a drill diameter of 2.5mm and depth of 10mm using a pillar drill. The block was placed back into -80°C storage before the loading process. During the cell loading process the cell plug was mounted in a cryostat set to -30°C.

SAOS-2 cells were cultured in monolayer as in section 2.3.2 until confluent. Then they were trypsinised, counted, centrifuged and washed with 1:4 ACN:0.1M ammonium bicarbonate solution and the supernatant removed fully. The number of cells required to make a full cell plug array was ≥70,000,000 cells (6 hole array), ≥10,500,000 cells (9 hole array). A range of peptide mix concentrations were produced in 1:4 ACN:0.1M Ammonium bicarbonate solution (3 peptide array- 0, 1.5, 6, 15, 30, 45, 60, 90, 180 pmol/µL) (120 peptide array- 0, 1.5, 15, 30, 60, 90 pmol/µL). The cells were mixed with peptide standards 2:1 cell: peptide v:v. In order to pipette the viscous cells the pipette tip was cut off. Immediately after mixing cells with standard the mixture was deposited inside a cell plug hole. Once all the cell:peptide mixtures were deposited inside the cell plug this was stored in a sealed container in -80ºC. The resultant peptide concentrations after mixing were diluted by a factor of 3 (3 peptide array- 0, 0.5, 2, 5, 10, 15, 20, 30, 60 pmol/µL) (120 peptide array- 0, 0.5, 5, 10, 20, 30 pmol/µL).
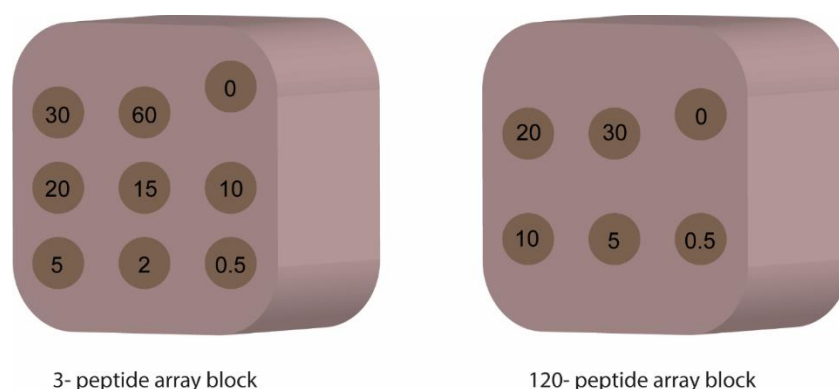
Figure 4.1 Peptide array block schematic. Blocks were made from frozen 20% (w:v) gelatin and 2.5mm diameter, 10mm depth holes were filled with a cell and peptide standard mixture (2:1 (v:v)). All final concentrations stated were at pmol/µL. The control cell plug was offset in order to aid coordination.

4.2.4 MSI of peptide arrays

4.2.4.1 Sample preparation

The sample preparation for the spheroid aggregates was identical to Chapter 2.2.4.2. Sectioning of the cell plug array and spheroids was performed as described in section 2.2.4.1, however optimal sections were achieved with the cell plug array when this was sectioned transferred directly from -80ºC.

All sample sections were taken straight after cryosectioning or from -80°C storage and immediately placed in a vacuum desiccator for ~15 minutes prior to wash steps. The sections were then washed 1min in 70% EtOH, 1min in 100% EtOH, dipped 10 times in dH$_2$0, 1min in 70% EtOH and 1min in 100% EtOH.

Labelled peptide standards were applied to sections using the SunCollect™ automated sprayer. The 3 peptide Q-TOF test array was coated with the corresponding labelled peptide mix (15pmol/µL, 1 layer) to produce a 0.75 pmol/mm^2 layer on top of the section. The 3 peptide standard arrays were coated with labelled peptide mix (0.94 pmol/µL, 2 layers) to produce a 92.6 (± 0.9) fmol/mm^2 layer on top of the sample. Due to a limited amount of the 1000 labelled peptide mixture (16.67 fmol/µL, 6 layers) the 120 peptide arrays were coated with a 2.48 (± 0.031) fmol/mm^2 layer which was not high enough to detect, therefore these samples could not be normalised using the labelled standards. All peptides were sprayed with the following settings- speed x: low 7, speed y: medium 1, Z position: 30.

Following the standard application, trypsin (20ng/µL, dH$_2$O) was applied using the SunCollect™ automated sprayer (15 layers, 10µL/min) (speed x: low 7, speed y: medium 1, Z position: 40) to produce approximately 3.35 µg/cm^2. Following overnight incubation at 37°C in a saturated environment (50% MeOH), matrix was applied to the section. The initial Q-TOF test 3 peptide array section was not trypsinised as the 3 peptides did not require trypsinisation in order to be seen on the spectrum. Three concentrations (20, 30 and 60 pmol/µL) of the labelled peptide mix were also spotted (1µL) on the initial Q-TOF test slide before matrix application.

The matrix was applied to the sample section using the SunCollect™ automated sprayer. For Q-TOF experiments α-CHCA (5mg/mL, 70:30 ACN:0.1% TFA) was used. Five layers of matrix were applied at 3.5 µL/min for the first layer and 3 µL/min for the remaining four layers. For the FT-ICR experiments DHB (25mg/mL, 50% ACN, 0.1% TFA) was used as a matrix. Three layers of DHB matrix were applied (at 10, 35 and 35 µL/min) (speed x: low 7, speed y: medium 1, Z position: 25).

4.2.4.2 Quadrupole-Time-of-flight MSI of 3 peptide array

For an initial evaluation of the array, a modified MALDI-Q-TOF; Q-Star Pulsar-i™ (Applied Biosystems/MDS Sciex, Concord Ontario, Canada) was used, as it is a high throughput instrument useful for preliminary testing. These modifications have been reported elsewhere (Trim *et al.*, 2010). Data was acquired in positive mode using an NdYVO4 laser (Elforlight "SPOT", Daventry, UK). Images of 150µm pixel size were acquired. Data was acquired over an *m/z* range of 700-2000.

4.2.4.3 Fourier-transform ion cyclotron resonance MSI of 3 and 120 peptide arrays

MALDI-FTICR-MSI of arrays was performed on a 9.4T SolariX XR mass spectrometer (Bruker Daltonics, Germany) in positive-ion mode, using 150 laser shots per spot and 75 µm pixel size. This instrument was used for the peptide quantification specifically because of its high resolving power (>100,000). Data was acquired in a *m/z* range from 700 to 2000 Da. Data acquisition was performed using FtmsControl (Bruker Daltonics, Germany), and visualizations were obtained from flexImaging 4.0 (Bruker Daltonics, Germany).

4.2.4.4 Data Analysis

After conversion of images to imzML format using FlexImaging 4.0 (Bruker Daltonics, Germany) MSIQuant software was used in order to visualise data and to extract average ROI signal for each of the spiked peptide standard areas. Different normalisation methods were used in order to analyse reproducibility (no normalisation, root mean square, label and combined). The data was visualised and linear regression was performed using GraphPad Prism v7 software (GraphPad Software, USA). The R^2 values were exported and the graphs were analysed visually to determine best fit. The LOD and LOQ were determined as described previously in chapter 3 (Section 3.2.4).

4.2.5 MSI of spheroid aggregates

4.2.5.1 Sample preparation

A 48 hour 4 µM doxorubicin treated spheroid aggregate was sectioned as in Chapter 2 at 10µm, making sure to sample a section in the middle region of the spheroid aggregate. The same H+E comparison was used for this section as in

chapter 2 as a serial section was used. The trypsin and matrix deposition protocol used was identical to Section 4.2.4.1. 48-hour 0, 0.8 and 4uM spheroid aggregates, with trypsin spotted (0.5μL) rather than sprayed, were also imaged.

4.2.5.2 MALDI-MSI of peptides

Imaging of spheroid aggregates was executed using a Synapt G2. Images of 60μm pixel size were acquired. Data were acquired over an *m/z* range of 700–2,000 in positive mode analysis. The ion mobility function was used in order to improve separation of peaks. Data acquisition and analysis was performed using MassLynx v4.1 (Waters, UK) and High Definition Imaging (HDI) Software (Waters, UK).

4.2.5.3 Data processing

For the spotted trypsin samples regions of interest (ROIs) containing whole spheroid aggregates were selected in HDI and exported as average spectra into MassLynx software. They were then exported as .txt files and peaks were selected using Mmass v5 open source software (Strohalm *et al.*, 2010). Peptide predictions were based on using the Mascot server. Up to two missed cleavages were allowed and methionine oxidation was set as a variable modification. Peptide assignments were made with a tolerance of 100ppm. As MS/MS was not performed the identities of these are still putative.

4.3 Results

4.3.1 MSI of abundant peptides within osteosarcoma spheroid aggregates

A trypsin digest of a spheroid aggregate was performed in order to observe protein intra-heterogeneity within the mass. The tryptic digest produced many proteotypic peptide peaks which were then used for putative protein identifications within the MASCOT database. Two peptide peaks in particular were localised within specific areas of the spheroid aggregate (Figure 4.2). Peptide species *m/z* 1032 was localised within the inner necrotic region of the spheroid aggregate and was putatively identified as Histone H3.1. Peptide

species *m/z* 1117 was localised within the perinecrotic region and was putatively identified as Hypoxia- Inducible Factor 1-alpha (HIF-1α).
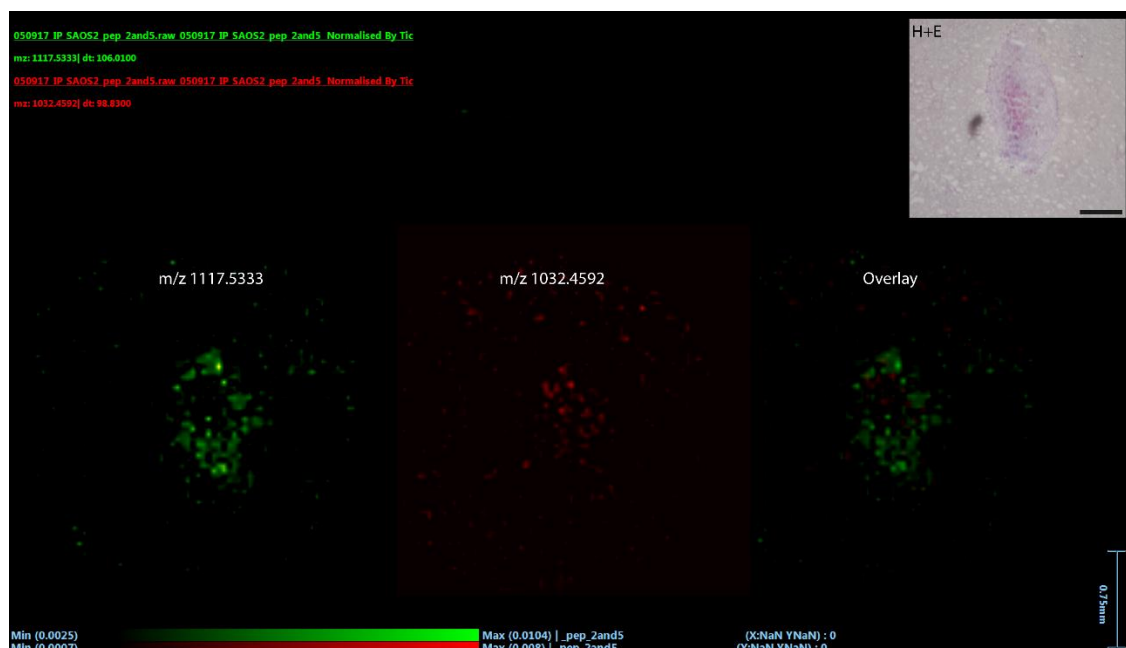
Figure 4.2 MSI Histone H3.1 (red) and HIF-1α (green) peptide signals m/z 1032 and 1117 respectively. Histone H3.1 signal is highest within the inner necrotic region of the spheroid aggregate and HIF-1α signal is highest in the perinecrotic region. H+E scale bar = 500μm.

Trypsin digestion of spheroid aggregate samples produced peptide molecular images for each treatment group. For each treatment group an average spectrum was used for a database search of the peptide species within. The first 4 protein hits within the database search of the most abundant peaks in each treatment group were collected (Table 4.1). These should not be compared between groups as they are just the most abundant peaks in each sample. A larger response comparison experiment should be performed in future in order to establish clear, significant differences due to treatment.

0μM	0.8μM	4μM
SRRM3	CIT	FHAD1
SRSF8	CFAP58	SACS
SH3BP5	SEMA6A	CEP104
ZNF100	MTIF2	MTIF2

Table 4.1 MASCOT server derived protein identifications for three doxorubicin treatment groups (0, 0.8, 4μM). The identifications are for the four most abundant peptide peaks and no significance should be drawn for differences between drug responses in this case.

4.3.2 Peptide quantification

Further experiments were conducted towards quantification of peptides and proteins within the spheroid aggregates. Achieving protein quantification whilst maintaining spatial information will enable the accurate abundance determination of biopharmaceuticals and endogenous molecules.

4.3.2.1 Use of Q-TOF MSI for quantification of a 3-peptide mix

Initially, a three-peptide array was produced consisting of proteotypic peptides for Actin, HSP 70 and HSP 90 (Section 4.2.1). This array was covered with a homogenous layer of the corresponding labelled peptides and analysed using MALDI-MSI (Figure 4.3). Unlabelled peptide species signals were concentration dependant as expected. As the peptides were observed at low concentration levels and the signals were not seen to plateau, the assumption was made that during analysis none of the peptides were 'saturated' and that a linear relationship could be observed. The sprayed labelled standard signal was relatively homogenous throughout the sample, although some 'hot spots' of higher signal were present. Standard graphs were produced for each peptide H^+ peak as well as their Na^+ peak for both non- normalised data and internal standard normalised (Figure 4.4). Overall, the use of internal standard in this case lead to a poorer fitting regression. The best fit for the internal standard samples was dependent on the initial signal intensity of the peptide standard. For example, the HSP 70 proteotypic peak was the least abundant ($R^2=0.4717$), which showed a best fit value well below the chosen cut-off ($R^2=0.8$), and the Actin peak was the most abundant ($R^2= 0.8426$). Only the HSP 90 Na+ species had an observed improvement with internal standard normalisation ($R^2= 0.852$ to 0.885). This was

also the only case with an improved LOD (From 28.46 pmol/µg to 24.62 pmol/µg) and LOQ (From 86.24 pmol/µg to 74.60 pmol/µg) but the values were still lower than the H+ peak (LOD= 24.54 pmol/µg, LOQ= 74.36 pmol/µg) (Table 4.2). Overall, the LOD and LOQ values were at the higher end of the standard array (>14 pmol/µg). The initial array additionally had three additional spots of the labelled standard mix on the right side of the array to observe the difference in signal between the array and standard spotting on glass as well as to observe any non-specific signal and saturation (Figure 4.3). These spots can be seen in the labelled peptide images as areas of higher signal, demonstrating the matrix suppression effects on the standards. The Na+ species for actin and HSP 90 showed some non-specific, labelled peptide related signal in the spotted areas.
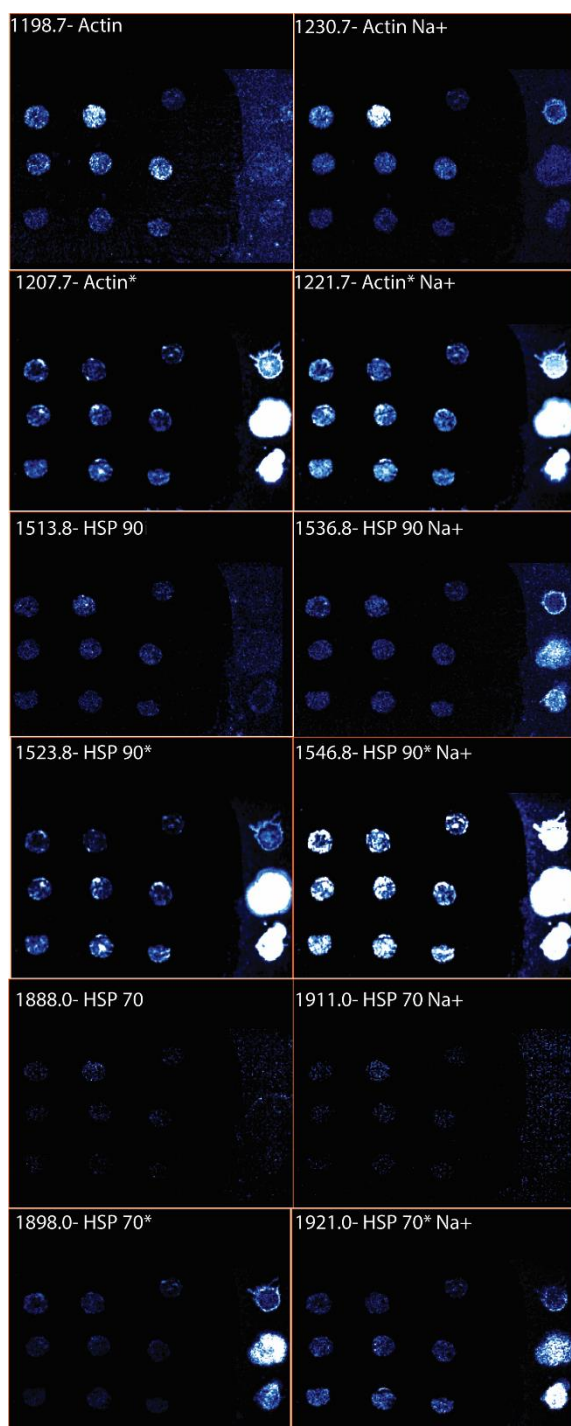
Figure 4.3 MSI of 3 peptide array of HSP-70, HSP-90 and actin peptide H+ and Na+ species as well as their labelled counterparts. A concentration dependent gradient can be observed for the embedded peptides with a consistent signal for the labelled peptides. Three spots on the right hand side of the images consist of the labelled peptide mix on the glass slide as control.
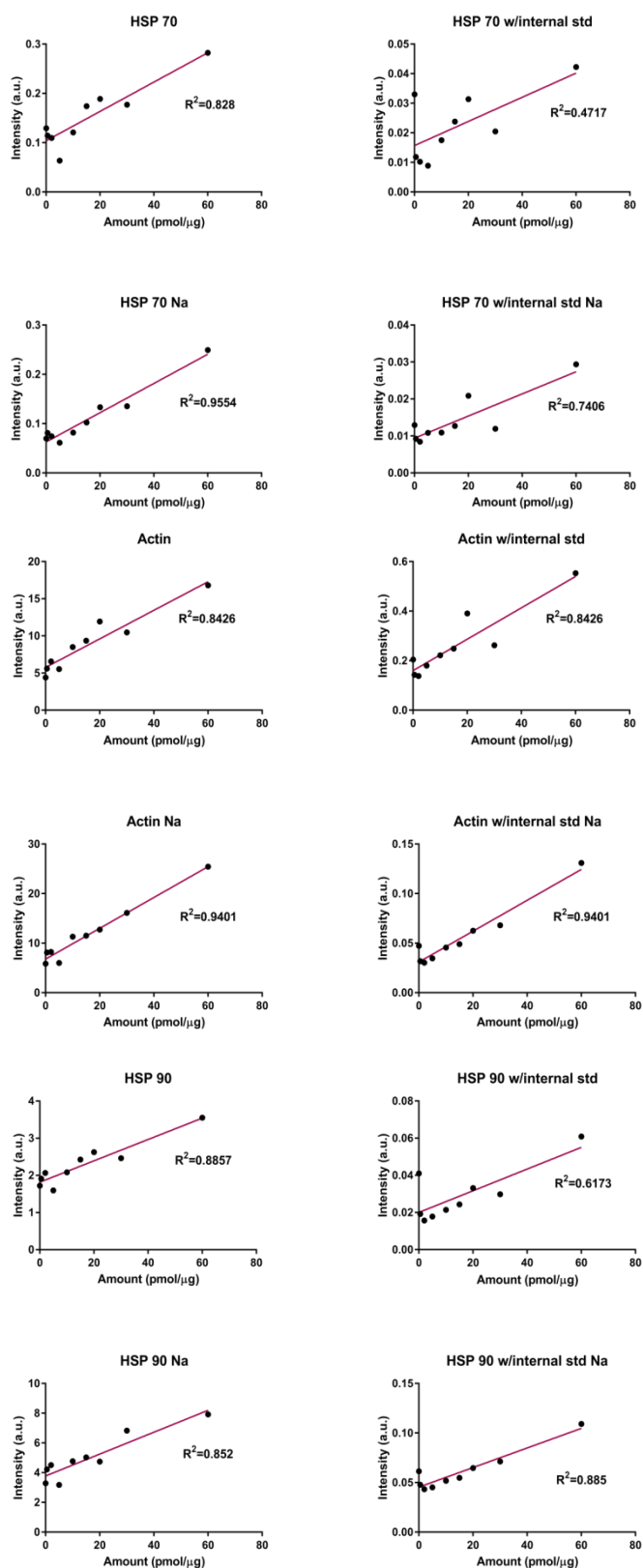
Figure 4.4 Three peptide mix (actin, HSP-90, HSP-70) standard graphs of pilot experiment. No normalisation results and label standard normalisation are shown.

Actin (pmol/µg)		Actin Na (pmol/µg)		Actin w/internal (pmol/µg)		Actin Na w/internal (pmol/µg)	
LOD	22.01	LOD	12.97	LOD	29.52	LOD	17.23
LOQ	66.69	LOQ	39.30	LOQ	89.46	LOQ	52.22
HSP 70 (pmol/µg)		HSP 70 Na (pmol/µg)		HSP 70 w/internal (pmol/µg)		HSP 70 Na w/internal (pmol/µg)	
LOD	31.13	LOD	14.76	LOD	72.27	LOD	40.42
LOQ	94.35	LOQ	44.72	LOQ	219.00	LOQ	122.48
HSP 90 (pmol/µg)		HSP 90 Na (pmol/µg)		HSP 90 w/internal (pmol/µg)		HSP 90 Na w/internal (pmol/µg)	
LOD	24.54	LOD	28.46	LOD	53.77	LOD	24.62
LOQ	74.36	LOQ	86.24	LOQ	162.93	LOQ	74.60

Table 4.2 Three peptide mix (actin, HSP-70, HSP-90) LOD and LOQ values for pilot experiment. No normalisation results and label standard normalisation are shown.

4.3.2.2 Use of FT-ICR-MSI for quantification of a 3 peptide mix array

The 3-peptide standard array was then analysed using FT-ICR-MSI in triplicate. The overall intensities for all three peptides were increased compared to the Q-TOF analysis along with the best fit values of the non-normalised data (average $R^2 = 0.8963$). Similarly to the previous analysis, the internal standard normalisation did not have a global improvement on the best fit values. For this experiment, the data was also normalised using root mean square (RMS) which did not have a significant overall increase in best fit. In the cases which arose with best fit values below the cut-off ($R^2 = 0.8$), a further investigation into the signal variation and a repeat experiment should be performed in order to identify the reason for the poor fit. If poor fit is consistent, then the peptide may be considered a poor candidate for quantification using this method as it would not meet the criteria.
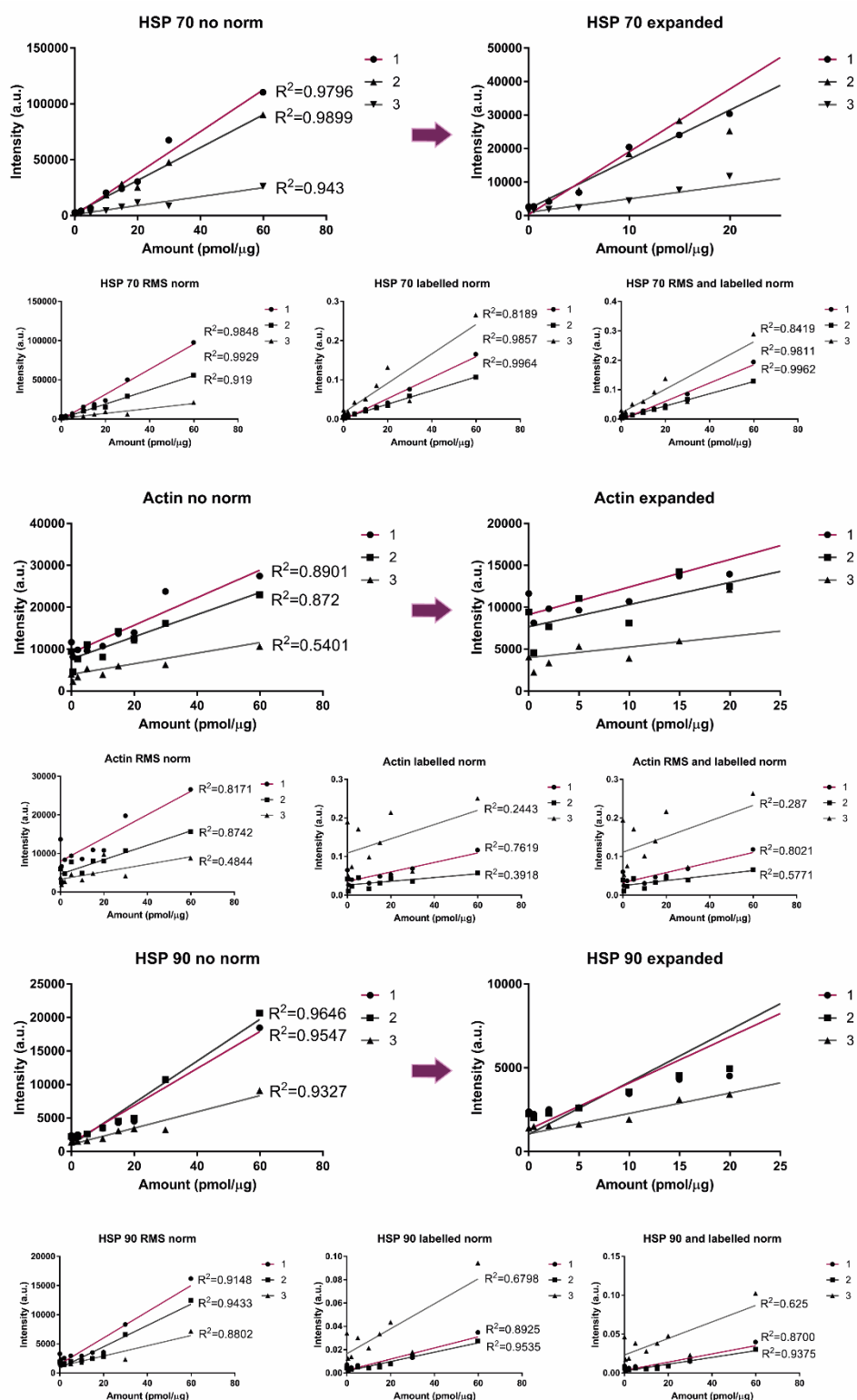
Figure 4.5 Three peptide mix (HSP70, actin, HSP90) standard graphs for 3 separate standard array FT-ICR-MSI experiments (labelled 1, 2, 3 in figure). Different types of normalisation - no normalisation, RMS, label and combined normalisation and an expanded view of the no normalisation lower concentration data is shown (n=3).

137

Actin (pmol/µg)		Actin RMS norm (pmol/µg)		Actin label norm (pmol/µg)		Actin RMS and label norm (pmol/µg)	
LOD	19.73	LOD	23.60	LOD	80.33	LOD	69.65
LOQ	59.78	LOQ	71.50	LOQ	243.42	LOQ	211.06

HSP 70 (pmol/µg)		HSP 70 RMS norm (pmol/µg)		HSP 70 label norm (pmol/µg)		HSP 70 RMS and label norm (pmol/µg)	
LOD	5.14	LOD	5.82	LOD	14.13	LOD	13.48
LOQ	15.57	LOQ	17.62	LOQ	42.83	LOQ	40.86

HSP 90 (pmol/µg)		HSP 90 RMS norm (pmol/µg)		HSP 90 label norm (pmol/µg)		HSP 90 RMS and label norm (pmol/µg)	
LOD	12.09	LOD	17.32	LOD	31.40	LOD	35.20
LOQ	36.62	LOQ	52.48	LOQ	95.16	LOQ	106.65

Table 4.3 Three peptide mix (actin, HSP-70, HSP-90) LOD and LOQ values for FT-ICR-MSI experiment. No normalisation, RMS normalised and label standard normalised results are shown.

4.3.2.3 Use of FT-ICR-MSI for quantification of a 120 peptide mix array

The 120-peptide standard array was analysed using FT-ICR-MSI in duplicate. Out of the 120 peptides present within the array, 25 were detected and all presented a concentration dependent trend (Figure 4.6 and Appendix chapter 4 figures 1-3). Due to the low concentration of the internal standard applied, internal standard normalisation was not successful. The best fit values for the majority of the proteotypic peptides were above an acceptable value ($R^2 > 0.8$).
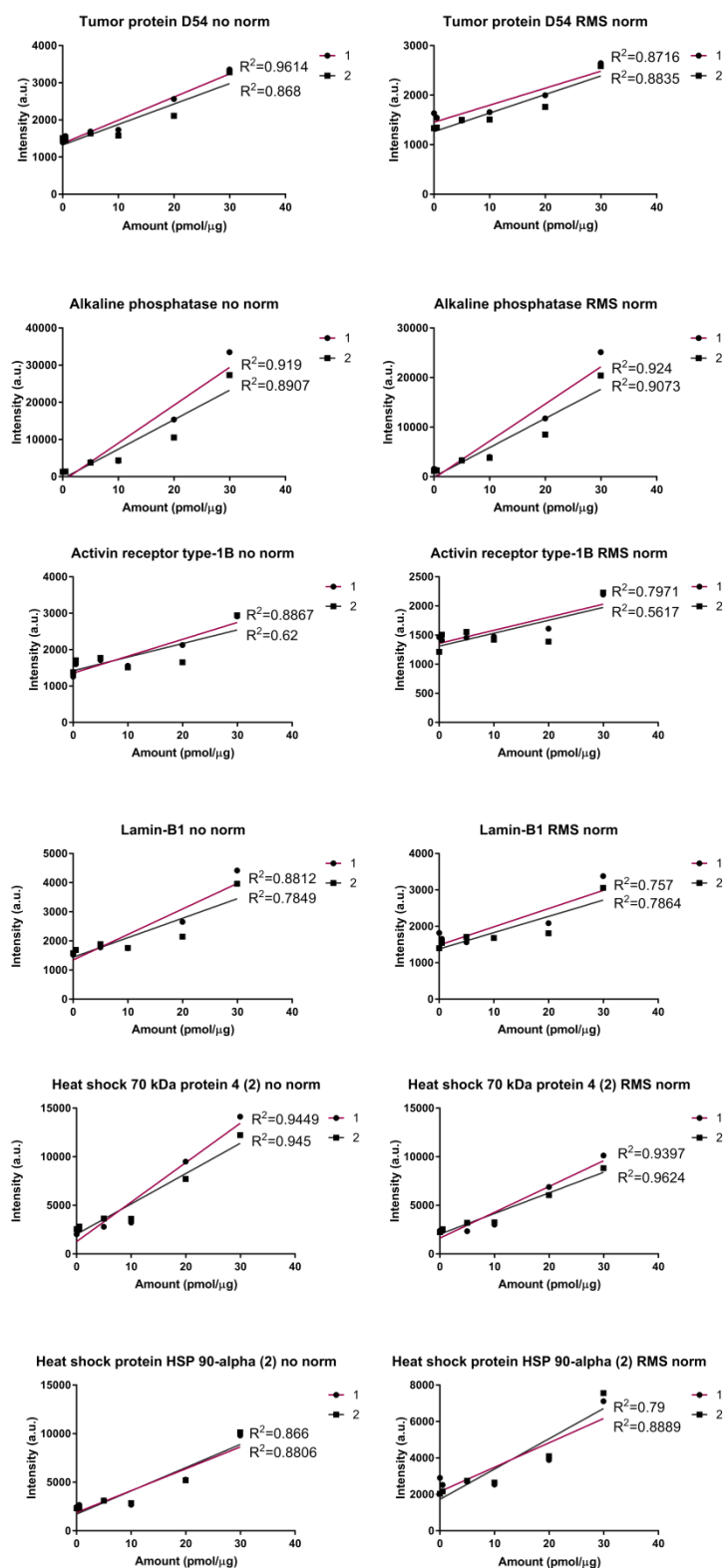
Figure 4.6 120 peptide mix standard graphs for 2 separate standard array FT-ICR-MSI experiments (labelled 1 and 2 in figure). No normalisation and RMS normalisation is shown (n=2).

Tumor protein D54 (pmol/µg)		**Tumor protein D54 RMS norm (pmol/µg)**	
LOD	12.07	LOD	15.36
LOQ	36.57	LOQ	46.55
Alkaline phosphatase (pmol/µg)		**Alkaline phosphatase RMS norm (pmol/µg)**	
LOD	13.93	LOD	13.12
LOQ	42.20	LOQ	39.76
Activin receptor type-1B (pmol/µg)		**Activin receptor type-1B RMS norm (pmol/µg)**	
LOD	23.38	LOD	28.79
LOQ	70.84	LOQ	87.26
Lamin-B1 (pmol/µg)		**Lamin-B1 RMS norm (pmol/µg)**	
LOD	18.88	LOD	22.69
LOQ	57.20	LOQ	68.75
Microtubule-associated protein 2 (pmol/µg)		**Microtubule-associated protein 2 RMS norm (pmol/µg)**	
LOD	16.92	LOD	23.71
LOQ	51.27	LOQ	71.85
Neuronal pentraxin-1 (pmol/µg)		**Neuronal pentraxin-1 RMS norm (pmol/µg)**	
LOD	20.09	LOD	23.68
LOQ	60.88	LOQ	71.77
Keratin, type I cytoskeletal 14 (pmol/µg)		**Keratin, type I cytoskeletal 14 RMS norm (pmol/µg)**	
LOD	27.97	LOD	54.51
LOQ	84.77	LOQ	165.19
Annexin A6 (pmol/µg)		**Annexin A6 RMS norm (pmol/µg)**	
LOD	17.20	LOD	16.92
LOQ	52.12	LOQ	51.27
Myosin regulatory light chain 2 (pmol/µg)		**Myosin regulatory light chain 2 RMS norm (pmol/µg)**	
LOD	29.00	LOD	53.92
LOQ	87.88	LOQ	163.40
Heat shock protein HSP 90-alpha (pmol/µg)		**Heat shock protein HSP 90-alpha RMS norm (pmol/µg)**	
LOD	24.41	LOD	42.16
LOQ	73.98	LOQ	127.77
Stress-70 protein, mitochondrial (pmol/µg)		**Stress-70 protein, mitochondrial RMS norm (pmol/µg)**	
LOD	12.10	LOD	16.40
LOQ	36.66	LOQ	49.70
Low-density lipoprotein receptor-related protein 2 (pmol/µg)		**Low-density lipoprotein receptor-related protein 2 RMS norm (pmol/µg)**	
LOD	12.57	LOD	12.21
LOQ	38.08	LOQ	36.99
Alpha-actinin-1 (pmol/µg)		**Alpha-actinin-1 RMS norm (pmol/µg)**	
LOD	16.33	LOD	16.37
LOQ	49.49	LOQ	49.62
Protein kinase C alpha type (pmol/µg)		**Protein kinase C alpha type RMS norm (pmol/µg)**	
LOD	14.43	LOD	13.81
LOQ	43.74	LOQ	41.86
Cell division control protein 42 homolog (pmol/µg)		**Cell division control protein 42 homolog RMS norm (pmol/µg)**	
LOD	14.50	LOD	13.54
LOQ	43.92	LOQ	41.04
Heat shock cognate 71 kDa protein (pmol/µg)		**Heat shock cognate 71 kDa protein RMS norm (pmol/µg)**	
LOD	15.31	LOD	14.69
LOQ	46.41	LOQ	44.50
Heat shock 70 kDa protein 4 (pmol/µg)		**Heat shock 70 kDa protein 4 RMS norm (pmol/µg)**	
LOD	22.45	LOD	25.55
LOQ	68.04	LOQ	77.41
Eukaryotic translation initiation factor 3 subunit H (pmol/µg)		**Eukaryotic translation initiation factor 3 subunit H RMS norm (pmol/µg)**	
LOD	24.18	LOD	30.24
LOQ	73.27	LOQ	91.63
Programmed cell death 6-interacting protein (pmol/µg)		**Programmed cell death 6-interacting protein RMS norm (pmol/µg)**	
LOD	15.21	LOD	14.88
LOQ	46.09	LOQ	45.08
Vascular endothelial growth factor receptor 2 (pmol/µg)		**Vascular endothelial growth factor receptor 2 RMS norm (pmol/µg)**	
LOD	17.12	LOD	20.65
LOQ	51.87	LOQ	62.59
F-actin-capping protein subunit beta (pmol/µg)		**F-actin-capping protein subunit beta RMS norm (pmol/µg)**	
LOD	28.51	LOD	37.32
LOQ	86.39	LOQ	113.10
Serine/threonine-protein kinase MRCK beta (pmol/µg)		**Serine/threonine-protein kinase MRCK beta RMS norm (pmol/µg)**	
LOD	18.13	LOD	22.00
LOQ	54.95	LOQ	66.65

Heat shock 70 kDa protein 4 (2) (pmol/µg)		Heat shock 70 kDa protein 4 (2) RMS norm (pmol/µg)	
LOD	10.34	LOD	9.68
LOQ	31.34	LOQ	29.33
Heat shock protein HSP 90-alpha (2) (pmol/µg)		Heat shock protein HSP 90-alpha (2) RMS norm (pmol/µg)	
LOD	16.66	LOD	18.46
LOQ	50.49	LOQ	55.94
Annexin A2 (pmol/µg)		Annexin A2 RMS norm (pmol/µg)	
LOD	12.64	LOD	12.19
LOQ	38.31	LOQ	36.94

Table 4.4 120 peptide mix LOD and LOQ values of FT-ICR-MSI experiment. A total of 25 proteotypic peptides were detected. No normalisation and RMS normalised results are shown.

4.4 Discussion

The aim of the chapter was to develop a method for the proteomic MSI of and quantification of proteins within spheroid aggregates of sarcoma. Several putative proteotypic peptides were identified in a concentration and location dependent manner. A novel method for protein quantification was further developed for use within the 3D model. The quantification method could potentially quantify as many as 25 proteotypic peptides within the sample in a single experiment. As this has not previously been reported for any amount of proteotypic peptides within an imaging experiment, it is a substantial amount which could be further increased with optimisation.

4.4.1 Assessment of osteosarcoma spheroid aggregate peptide composition using MALDI-MSI

A peptide species corresponding to histone H3.1 was located within the necrotic inner region of the spheroid aggregate. Histone H3.1 is a well-characterised core component of nucleosomes and is present at high levels in all cells within the model (Luger *et al.*, 1997). However, it is also well known that histone proteins are released during cell death and elevated levels are often observed in the serum of cancer patients, due to presence of necrotic regions, which contain both necrotic and apoptotic cells (Holdenrieder *et al.*, 2008). Release of the histone protein H3 from chromatin may increase the abundance of the corresponding peptide species as it may be more readily ionisable and has potential for use as a necrotic region marker within the model. Observation of a HIF-1α proteotypic peptide within the peri-necrotic region of the spheroid aggregate indicates the

presence of hypoxia within the model. HIF1α is rapidly degraded via the VHL-mediated ubiquitin protease pathway under normoxic conditions (Greijer & van der Wall, 2004). However, under hypoxic conditions the degradation of HIF1α is decreased which leads to an accumulation of the protein. The presence of a large hypoxic region could be a driver of the doxorubicin drug resistance observed in the 3D model compared to 2D. Previous work has found a large association between hypoxia in osteosarcoma cell line and cytotoxic drug resistance, however they found this effect to be independent of HIF-1α (Adamski *et al.*, 2013).

Of the other putative proteins identified within the spheroid aggregates a few have potential associations with osteosarcoma. For example, SEMA6A (Semaphorin 6A) is a member of the Semaphorin family, the members of which are identified as modifiers controlling tumour growth, angiogenesis and metastatic progression, and are abnormally expressed in several cancers (Rehman & Tamagnone, 2013). High levels of this protein were found in a study using the SAOS-2 cell line (Salah *et al.*, 2015). Sacsin molecular chaperone (SACS) was also putatively identified as abundant in the high treatment sample. SACS is a chaperone protein which is thought to regulate HSP70 and HSP90, which are families of proteins responsible for cellular stress responses and are overexpressed in most tumours (Ménade *et al.*, 2018; Murphy, 2013; Parfitt *et al.*, 2009). It could be a potential marker of the osteosarcoma drug response and should be confirmed using MS/MS and an additional method such as IHC.

The results derived from these preliminary experiments demonstrate the potential of using MSI on these treatments to extract useful information. There is further optimisation required in sample preparation and analysis in order to observe more proteotypic peptides and to enable tandem MS analysis for confirmation of species. The peptides discovered in the database search were based on the most abundant peaks within each sample and therefore cannot be classed as specific for that drug response. To completely reveal the proteomic drug response in this model several technical and biological repeats are required as well as a global multivariate comparison analysis of the data, as was performed in Chapter 3 with small molecules. The biological relevance of the protein species found during the untargeted imaging experiment should be further studied to discover proteomic markers of drug response.

4.4.2 Novel array method demonstrates quantification of up to 25 proteotypic peptides using MALDI-MSI

All imaged cell plug arrays produced concentration dependent standard graphs with a majority of acceptable best fit values. The acceptable best fit cut-off value (measured as R^2) was selected to be >0.8. This is lower than the typical cut-off value used of >0.95, which lowers the acceptable predictability power, however the margin of error for a proof-of-concept experiment is acceptable at the lower cut-off value. In future, with optimisation, this method may be able to achieve a higher predictive power and the R^2 value cut-off can be raised to >0.95. The internal standard normalisation was not successful in improving best fit. This may be because further optimisation is needed of the labelled peptide concentration and application (Mirzaei *et al.*, 2008). The way of applying a standard during an MSI experiment greatly alters it's signal and must be optimised and validated (Chumbley *et al.*, 2016). Out of 120 cancer related proteotypic peptides within the standard mix, 25 were identified by FT-ICR-MSI. The variability between separate experiments in the 120 peptide mix cases was lower than in the 3 peptide array experiments. This could be because the 120 peptide array peptides are only released once trypsinised and therefore are more stable throughout the sample preparation process in a folded protein form. As well as stability, incomplete trypsinisation could be a factor for variation, which should be considered in future experiments (Mirzaei *et al.*, 2008). As the quantification of proteotypic peptides has not been reported previously to be able to quantify 25 peptides in a single imaging experiment is a notable achievement. However, the method should be further optimised in the future in order to get a higher signal from the detected peptides and to increase the overall number of detected peptides. The 1000 peptide labelled standard which was sprayed on top of the sample may be supressing overall signal coming from the sample and therefore decreasing the number of detectable peptides. The largest number of ionisable proteotypic peptides within a single experiment should be determined in future experiments, as 120 peptides, combined with corresponding labelled peptide application, may lead to overall ion suppression and loss of detection capability. By optimising the peptide standard amount and concentrations the number of peptides detected will be increased. Additionally, a more in-depth study of the visualised peptides

should be performed in order to see if there were structural reasons as to why these were detected as opposed to others. In general, some structures will be more readily ionisable than others and concentrations may need to be adjust accordingly in future mixed peptide standard arrays.

In future experiments it may be useful to first normalise the peptide array determined concentration by the 0 pmol/µg control value. In some detected proteotypic peptide cases, such as F-actin-capping protein, subunit beta and Keratin type I cytoskeletal 14, the basal amount of peptide within the array is already quite high (>1000 a.u.) and in these cases accurate quantification of levels within a sample using the array would not be possible as the data would be skewed by the endogenous levels within the cells in the array. This may be an explanation of the poor best fit values these peptides are displaying. If the endogenous peptide concentration is already high, combining this with the standard will saturate the analysis. Checking the control values within the array can be used as a quality control step, however this issue may lead to an inability to quantify certain proteins in this manner. This is an issue that would also apply to on tissue spotting or mimetic tissue arrays of standards like the ones currently being used for MSI drug quantification (Groseclose & Castellino, 2013). However, in this case 2D cultured cells are used to produce the array and a 3D model is the sample to be quantified. The expression changes which occur due to cell culture method are expected to lead to an increase in the concentration of proteins of interest within the 3D culture model compared to the 2D cultured cells as the expression should be more similar to *in vivo*. This may aid the quantification process without having to alter the array and reduce its representability. This issue would however only occur when quantifying endogenous protein, rather than biopharmaceuticals, as these are not endogenously present within tissue or cell culture-based models. The technology developed could potentially be used with specifically selected proteotypic peptide arrays designed to assess levels of typical proteins of interest. The array model could also be expanded to quantification in other tissue types by changing the cell type within the array cores.

4.5 Concluding remarks

To conclude, a method for the proteomic MALDI-MS imaging of spheroid aggregates was developed. Several putative proteotypic peptides were identified in a concentration and location dependent manner and this method can be further optimised and used for a large-scale drug response comparison study. This method will require further optimisation to achieve a greater abundance of proteotypic peptides per sample and can be used to observe proteomic inter- and intra-spheroid aggregate differences. Additionally, a novel cell plug array method for protein QMSI was further developed for use within the 3D model. The quantification method identified 25 proteotypic peptides in a single imaging experiment and has the potential to include a higher number of peptides with further optimisation. This method, after further validation, could be used in the future for absolute quantification of proteotypic peptides within tissues and alternative models using MALDI-MSI.

Chapter 5: Optimisation of 3D liver cell culture and MS analysis

5.1 Introduction

5.1.1 The study of drug hepatoxicity

An integral part of the drug discovery process is the testing of drug toxicity. It is vital to determine the absorption, distribution, metabolism and excretion (ADME) properties of a drug of interest and to determine its potential adverse outcome pathways (AOPs) before moving onto clinical trials (Figure 1.3). In recent years, animal models have undergone a substantial amount of criticism in the field, due to their inability to accurately and consistently predict human response to drugs and disease (Greek & Menache, 2013). Due to the limits of animal based models, such as inter-species variability, low throughput and experimental cost, scientists have been looking at alternative models for use in the drug development workflow. Among other organs, the liver is crucial when toxicity is concerned, as it is responsible for the metabolism of drugs and toxins. In fact hepatoxicity, in particular acute liver toxicity often termed drug-induced liver injury (DILI), has been the most common cause of safety-related withdrawal and non-approval of drugs by the FDA (Chen *et al.*, 2011; Wysowski & Swartz, 2005; Temple, 2001). DILI has proven very difficult to predict with pre-clinical models and animal testing (Fontana *et al.*, 2014). Consequently, research has focused on the development of functional *3D in vitro* models for the testing of drug hepatotoxicity (Andersson, 2017; Godoy *et al.*, 2013). A cheap, simple way to predict DILI would be to use hepatoma cell lines, however several of these are known to have very little liver-specific metabolic function compared to human hepatocytes (Andersson *et al.*, 2012). 3D cell culture has been recently utilized as a way of improving hepatoma cell line liver-specific metabolic activity (Takahashi *et al.*, 2015).

Acetaminophen (APAP) is one of the most widely used drugs with a well characterised biotransformation process (McGill *et al.*, 2012). When consumed at a dose which exceeds recommended levels, patients experience acute liver toxicity due to the presence of a reactive intermediate metabolite, N-acetyl-p-benzoquinone imine (NAPQI), which depletes glutathione, an important antioxidant responsible for neutralising reactive molecules and modifies cellular proteins (McGill & Jaeschke, 2013). In the case of acetaminophen known altered

metabolic conditions can alter the hepatoxicity of the drug, therefore it is a useful drug to use for the validation of adverse outcome pathway analysis.

5.1.2 Adverse outcome pathway analysis

Whilst optimization of representative 3D cell cultures has advanced greatly there is still comparably little progress made with regard to analysis methods which can routinely be used in research and industry (End *et al.*, 2017; Rimann & Graf-Hausner, 2012). There are many mechanisms that are thought to cause DILI, for example formation of reactive metabolites, oxidative stress mitochondrial dysfunction or inhibition of bile salt excretion (Yuan & Kaplowitz, 2013). Ideally, an untargeted technique is required to elucidate these mechanisms. MSI, specifically Matrix-assisted laser desorption ionisation mass spectrometric imaging (MALDI-MSI) is an analytical technique with the ability to detect label-free analytes with limited *a priori* knowledge and perform *de novo* discoveries, which allows it to be used in untargeted studies of biological samples (Day & Palubeckaite, 2017; Aichler & Walch, 2015). Several studies using MSI have focused on the analysis of drug distribution and endogenous molecule analysis in treated tissue such as intestine, tumour and skin (Nilsson *et al.*, 2017; Giordano *et al.*, 2016; Mitchell *et al.*, 2015).

5.1.3 pNIPAM-Laponite hydrogel

In the following study, a 3D hydrogel-based model was developed. Hydrogels are 3D cross-linked, highly hydrated polymer networks (Tibbitt & Anseth, 2009). These scaffolds are well suited to 3D cell culture as they are highly porous, biocompatible structures. A previously reported synthetic composite poly-N-Isopropylacrylamide (pNIPAM)- Laponite® hydrogel was used for the experiments in this chapter (Figure 5.1) . The hydrogel design is based on the irreversible polymerisation of NIPAM using a thermal initiator, AIBN, which enables free radical polymerisation of pNIPAM chains anchored on Laponite® platelets (L-pNIPAM hydrogel), this forms a freely flowing solution when held above the lower critical solution temperature (LCST) of 32°C (Figure 5.1). Cells can be incorporated in the liquid L-pNIPAM hydrogel and due to the thermal transition of pNIPAM upon cooling below the LCST, the pNIPAM chains extend resulting in an entanglement of polymer chains and Laponite® platelets resulting

in a solidified hydrogel which is non reversible (Figure 5.1). This hydrogel has been shown to be biocompatible and suitable for differentiation of mesenchymal stem cells (MSCs) into nucleus pulposus (NP) and osteoblast-like cells for tissue engineering purposes (Thorpe *et al.*, 2016a; Thorpe *et al.*, 2016b). The pNIPAM-Laponite® hydrogel has additionally been used to produce a model of small intestinal epithelium using Caco-2 and HT29-MTX cells (Dosh *et al.*, 2017). The hydrogel is biocompatible, non-biodegradable and can be made very consistently and in large amounts if needed (Thorpe *et al.*, 2018).
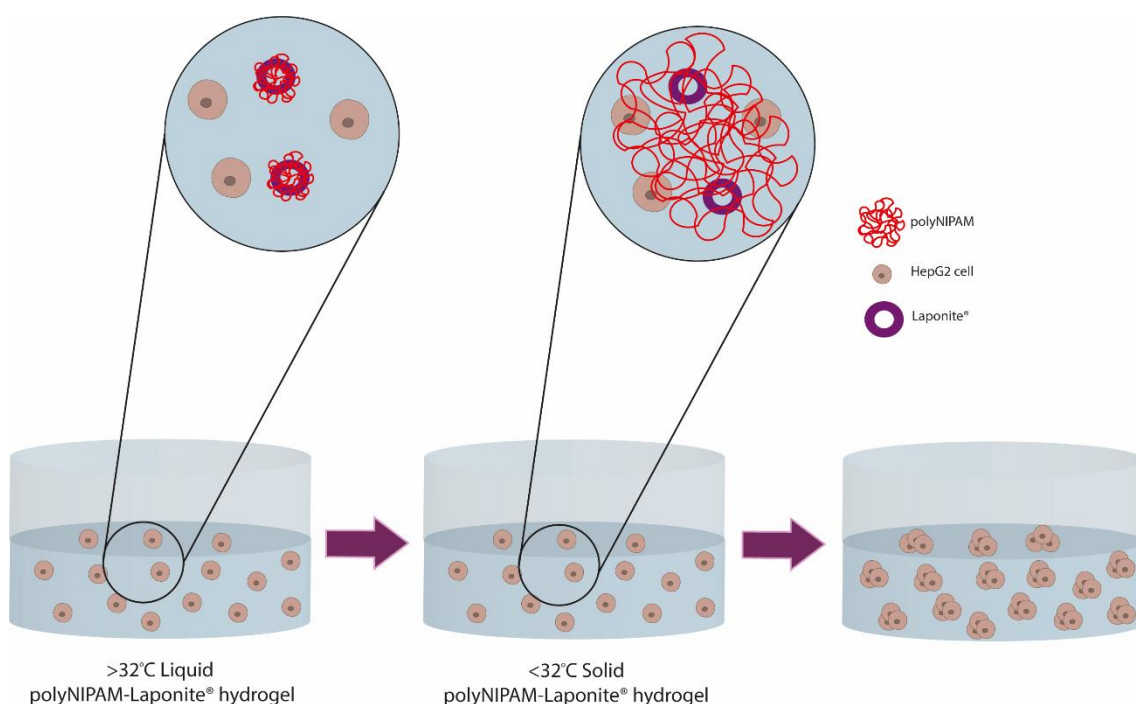
Figure 5.1 *pNIPAM-Laponite® hydrogel gelation. The temperature dependent gelation process of polyNIPAM and Laponite gels is shown where cells can be suspended within liquid hydrogel at >32°C and the gel can polymerise at room temperature with cells suspended inside and used for cell culture.*

The variant hydrogel used in this study polymerises irreversibly once below its lower critical solution temperature (LCST) of 32°C which means cells can be incorporated before or after gelation. An addition of 2% of hyaluronic acid (HA), producing a 0.4% HA/pNIPAM hydrogel, was investigated to determine if including this extracellular matrix component improved hepatic function. Incorporation of HA has been shown previously to maintain hepatic function in

cultures (Kim & Rajagopalan, 2010). The HepG2 hepatocellular carcinoma cell line was used in this model. Using a cell line is a good starting point in order to test whether the model would be suitable for culture of primary liver derived cells and have an effect on hepatocyte-like function of the cells. The HepG2 cell line is well established and simple to culture although its hepatocyte-like function is low in 2D cultures, thus this study determined if this 3D culture system could restore hepatocyte function. This model was tested for its potential to be developed for drug toxicity studies, the ability of the culture model to maintain viable, active cells over longer time periods (up to 4 weeks) was assessed. In order to characterise alterations in the hepatic phenotype during 3D culture, levels of albumin and alkaline phosphatase (ALP) were assessed. Albumin is a well known hepatic differentiation marker, shown to be expressed even at very early stages of differentiation (Cascio & Zaret, 1991). This makes it a very useful molecule for monitoring in different culture conditions, particularly because it is secreted by the cells. Alkaline phosphatase is present in many mammalian tissues and is especially abundant in hepatic tissue (Sharma *et al.*, 2014). It is a useful additional marker of hepatocyte differentiation and increases in ALP levels are associated with liver toxicity, and thus can be useful measure of potential toxicity.

5.1.4 Chapter Aims

The main aims of this chapter were to optimise the long-term culture of HepG2 cells within a pNIPAM or 0.4%HA/pNIPAM hydrogel, determine the hepatocyte activity change with culture method, and to assess whether the MSI methods developed previously can be used to analyse small molecules within these polymeric structures. The cells were cultured in hydrogel with and without HA and the cell activity over culture time was monitored. Hepatic differentiation was monitored in the cultures with the use of albumin ELISA and ALP IHC. The cultures were then treated with differing concentrations of the hepatotoxic drug acetaminophen (0-10mM) and imaged using MALDI-MS imaging, in order to determine whether mass spectrometry can be used for metabolomics and lipidomic analysis of the 3D constructs.

5.2 Materials and Methods

5.2.1 Preparation of the hydrogel

A synthetic composite hydrogel (L-pNIPAM), produced in-house by Essa Abdusalam, was either used as received or 2% HA was added to a final concentration of 0.4% HA (v/v) according to previously established protocols (Boyes *et al.*, 2012, 2013). Briefly, L-pNIPAM was prepared by vigorous stirring of 0.1g Laponite® (BYK Additives Ltd, Cheshire, UK) in 9ml water for 24h at RT. 0.009g of Azobisisobutyronitrile (AIBN) (Sigma, Poole UK), and 0.9g NIPAM (Sigma, Poole UK) were added to the suspension and stirred for 1h. After passing the suspension through a 5-8µm pore filter paper, polymerisation was initiated by heating to 80°C and the reagents were allowed to react for 24h without stirring in a covered glass vial. A solution of 2% (w/v) HA in H_2O (Sigma, Poole UK) was made by refrigerating HA in deionised water for 48 hours, with vigorous stirring every 8 hours. This was added (1:4 v/v, HA:hydrogel) to the pNIPAM hydrogel to make 0.4% HA/L-pNIPAM and sonicated to thoroughly mix. Both hydrogel solutions were kept at 60°C until use when they were cooled down to 38-39°C for cell suspension. Further cooling of the polymeric suspension below the LCST (32°C) resulted in rapid gelation into a solid hydrogel.

5.2.2 2D cell culture

HepG2 cells (hepatocellular carcinoma) were obtained from ATCC and cultured in DMEM supplemented with 10% FBS, 10 U/ml penicillin and 10 µg/mL streptomycin (Thermo Scientific, USA). The cell line was maintained in a humidified atmosphere containing 5% CO_2 at 37°C. The cells were cultured until they reached approximately 80% confluency before transfer to 3D culture. Once confluent, the cell lines were passaged by trypsinisation, subsequent centrifugation, resuspension in fresh medium and seeded in new flasks or used for 3D experiments. Once in culture, cells were used within a 15 passage window.

5.2.3 3D cell culture

The prepared hydrogels were cooled down to 38-39°C for use and cells were suspended in either L-pNIPAM or 0.04% HA/L-pNIPAM hydrogel. The gelation was induced by cooling below 32°C. To determine cell viability over time cells were seeded at 1, 2, 4 and 8 million cells/mL of hydrogel in 12-well plates, with 300µL of hydrogel in each well, and cultured for up to 21 days. Following which, assays were performed with a cell density of $2x10^6$/mL hydrogel. Further comparison was made between different seeding methods. HepG2 cells were seeded both on top of the hydrogel (layered) and suspended within the hydrogel. The benefits of dynamic culture were additionally considered as these were found to improve culture of other cell types within the hydrogel (Dosh *et al.*, 2017). Layered cultures were achieved by adding the cell suspension on top of the hydrogel after gelation. This suspension was left on top of the hydrogel for 30 minutes to enable cell attachment and media added. The dynamic cultured cells were cultured under static conditions for 24 hours prior to transfer to dynamic culture on an orbital shaker at 30 rpm. Acellular hydrogel controls were also produced for determination of hydrogel background signal and all samples were harvested in triplicate at each timepoint.

5.2.4 Cell activity/viability assay

To assess cell viability during prolonged culture a Resazurin assay was used. Resazurin (Sigma, Poole UK) stock was made at 3mg/mL in DMEM culture media. The stock was filter sterilised using a 0.2µm filter and stored in a light protected container. Resazurin (200µL of 0.3mg/mL) was added to each well and incubated for 1.5 hours at 37°C and protected from light. The fluorescence was recorded using a 530 nm excitation / 590 nm emission filter set using a CLARIOstar® plate reader (BMG LABTECH, Germany). After reading the plates, the cultures were washed twice with culture medium and cultured further until the last remaining time point. Resazurin has been shown to be relatively non-toxic with short incubation times and subsequent washes and therefore can be used for continuous studies (Riss *et al.*, 2004) which meant that the same cell population could be monitored over time.

5.2.5 Histological staining

After culture, samples were fast-frozen using liquid nitrogen and stored at -80ºC. Sample sections were cut using the Leica 1850 UV cryostat (Leica Biosystems, UK), set to -30ºC, at a 10µm thickness, thaw mounted on a positively charged X-tra® adhesive slide (Leica Biosystems, UK). Haematoxylin and Eosin staining was used to compare static, dynamic, suspended and layered cultures. The method used is described previously (Section 2.2.5.1) with the exception of an increased dehydration time of 10 minutes for each IMS wash before clearing and mounting the sections.

5.2.6 Cytospins of monolayer control cells

HepG2 cultured cells were centrifuged (2,000 rpm, 2mins) and suspended in PBS to a cell density of 1,000 cell/µl. Two hundred microliters of cell suspension was cytospun by centrifugation at 1,000 rpm for 5 mins (Shandon cytospin 3, Thermo Scientific, Loughborough, UK). Slides were then air-dried and stored at -80°C in air-tight containers until required for immunohistochemical investigation.

5.2.7 Immunohistochemistry

Sample sections were cut using the Leica 1850 UV cryostat (Leica Biosystems, UK), set to -30ºC, at a 10 µm thickness, thaw mounted on a positively charged X-tra® adhesive slide (Leica Biosystems, UK). Immunohistochemistry was performed to observe alkaline phosphatase levels, representing hepatic activity, within suspended static and dynamic hydrogel culture samples using an unlabelled anti-human ALP antibody (1:200, rabbit polyclonal) (Clone # ab108337 , Abcam, Cambridge, UK) and biotinylated goat anti-rabbit IgG (Clone # ab207995 , Abcam, Cambridge, UK). Cytospun HepG2 slides were used as a time zero control. Sample sections were fixed in acetone (-20ºC) for 5 minutes and immersed in Tris-Buffered Saline (TBS: 20mM Tris, 150mM NaCl, pH 7.5) for 5 minutes in triplicate. Endogenous peroxidases were blocked for 30 minutes by immersing slides into 3% w/v hydrogen peroxide (Sigma-Aldrich, Poole UK) in IMS. Sections were washed once in dH_2O and twice for 5 minutes in TBS. Sections were washed three times in TBS and placed in humidified slide boxes. Non-specific protein interactions were blocked and secondary antibody-host interactions were neutralised by the application of 200µL 1% BSA in 75% v/v TBS

and 25% v/v normal goat serum (Abcam, Cambridge, UK) and incubated for 2 hours at room temperature. Blocking solution was tapped off and excess wiped from around the tissues, before 200µL of anti-human ALP primary antibody (1:200 dilution) was then applied. Antibody dilutions were performed in 1% w/v BSA in TBS and sections incubated overnight at 4°C. Sections were washed three times in TBS before 200µL of goat anti-rabbit biotinylated secondary antibody (1:500 dilution) was applied for 30 minutes at room temperature. Antibody dilutions were performed in 1% w/v BSA in TBS. Sections were washed in TBS for 5 minutes in triplicate before 2 drops of horseradish peroxidase (HRP) streptavidin-biotin complex (Vector Laboratories, Peterborough, UK) was applied for 30 minutes at room temperature. Sections were washed three times in TBS for 5 minutes prior to application of 200µL 0.08% v/v hydrogen peroxide in 0.65mg/mL 3, 3 -diaminobenzidine tetrahydrochloride (DAB) (Sigma-Aldrich, Poole, UK) in TBS per section for 20 minutes. Sections were washed in dH$_2$O for 5 minutes prior to incubation in haematoxylin for 1 minute and blued under running tap water for 5 minutes. Sections were then immersed in 99% (v/v) IMS for 10 minutes followed by immersion in SubX for 5 minutes. Finally, sections were mounted using 2 drops of Pertex per slide and coverslips applied. A negative control in which rabbit IgG (Abcam, Cambridge, UK) replaced the primary antibody at an equal IgG concentration was previously tested on a hydrogel sample by Rasha Dosh in order to confirm absence of non specific binding (Dosh *et al.*, 2017).

5.2.7.1 Microscopy and Image capture

Sections were visualised on an Olympus BX60 microscope. Images were captured using a QImaging Micropublisher 5.0 RTV camera and Capture-Pro8 software. The IHC slides were assessed by visual assessment of five representative images from each sample and an intensity grade between 0-3 was assigned based on density of stain. Where grade 0 is no staining and grade 3 representing the most intense staining (Figure 5.2). Five representative images were graded by two independent graders (IP and CLM) and averaged.
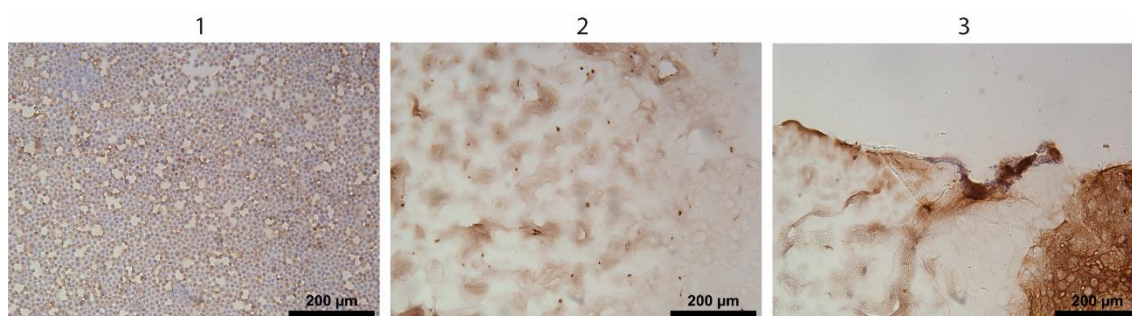
Figure 5.2 Example images of grade 1, 2 and 3 level ALP immunostaining intensity. Grade 0 would be given for no positive staining, however there were no samples marked at grade 0.

5.2.8 Albumin ELISA

During the 4 weeks of HepG2 cell culture within hydrogels, culture media was collected at 0, 2, 4, 7 and 14 days for both L-pNIPAM and 0.4% HA/L-pNIPAM cultures. The media was used in an enzyme linked immunosorbent assay (ELISA) for quantification of human albumin (Cat #ab179887, Abcam, Cambridge, UK) as per the manufacturer's instructions. Briefly, human albumin serially diluted standards of 200, 100, 50, 25, 12.5, 6.25, 3.125, 0 ng/mL were produced. To the wells of a 96 well plate, 50µL of standards and samples in triplicate along with 50µL blue conjugate and 50µL antibody was added. The plate was incubated at room temperature for 2 hours on an orbital shaker (500rpm). Following incubation, wells were washed 3 times with wash buffer. Excess wash buffer was tapped off and 200µL of p-Nitrophenyl Phosphate (pNpp) substrate solution was added to every well. Following incubation for 1 hour at room temperature without shaking, 50µL of stop solution was added to every well. The ELISA assay absorbance was read immediately using a CLARIOstar® plate reader (BMG LABTECH, Germany) at a wavelength of 450 nm. Wavelength correction was performed by subtraction of readings at 570 nm from those at 450 nm to correct for optical imperfections of the 96-well plate.

5.2.8.1 Data processing and statistical analysis

For ELISA data, a standard curve was generated by plotting the standard concentrations against the corresponding mean absorbance (at 450nm). A line of best fit was determined on GraphPad Prism v7 software (GraphPad Software, USA) by linear regression analysis. The unknown sample concentrations were

determined from the standard curve and combined over day measurements in order to calculate cumulative Albumin concentrations.

The ELISA data was identified as non-parametric by the Shapiro-Wilk test of normality. Therefore, the Kruskal-Wallis test was used to determine if there were any significant differences between the cultures and between time points. This analysis was combined with the Conover-Iman post-hoc test when a significant difference was observed between treatment groups. Statistical analysis was performed using StatsDirect software (StatsDirectLtd, UK).

5.2.9 Mass Spectrometric Imaging of HepG2 cells in hydrogel

5.2.9.1 Sample preparation

HepG2 L-pNIPAM samples were treated, in triplicate, with 0, 0.5, 2.5 mM acetaminophen for a total of 48 hours, replacing the drug media every 24 hours. At the end of the treatment the samples were fast-frozen and stored at -80°C. Sample sections were cut using the Leica 1850 UV cryostat (Leica Biosystems, UK), set to -30°C, at a 10 µm thickness, thaw mounted on a positively charged X-tra® adhesive slide (Leica Biosystems, UK). The samples were then stored at -80°C in an air tight container or used for MSI immediately.

5.2.9.2 Matrix deposition

All sections (10µm) were taken straight after cryosectioning or from -80°C storage and immediately placed in a vacuum desiccator for ~15 minutes prior to matrix application. X-tra® slide mounted sections were used for Synapt G2 analysis. Imaging was performed in positive mode, therefore the binary matrix α-CHCA: DHB (20/7) was prepared as a matrix solution (Section 3.2.4). The matrix was applied to the sample section using the SunCollect™ automated sprayer. Five layers of matrix were applied at 10µL/min (speed x: low 7, speed y: medium 1, Z position: 35).

5.2.9.3 Mass Spectrometric Imaging

Several images of the APAP treated HepG2 hydrogels were obtained using a Synapt G2 due to its high sensitivity and moderate resolving power (~10,000 in

sensitivity mode). Images of 60μm pixel size were acquired over an *m/z* range of 50-1,200 in positive mode. The ion mobility function was used in order to improve separation of peaks. Images generated using the Synapt G2 were processed using the Waters High Definition Imaging (HDI v 1.4) software package. The images were all TIC normalised.

5.3 Results

5.3.1 Characterisation of HepG2 3D model

The ability of the hydrogel to maintain cell viability over longer culture periods was assessed using the Resazurin cell viability assay. The cell viability of HepG2 cells in hydrogel was maintained for up to 21 days in culture with no significant changes at an initial seeding density of $2x10^6$ cells/mL (Figure 5.3). Other cell densities were tested, however these displayed a higher variance (Appendix chapter 5 figures 1-3). Overall, 0.4% v/v HA/L-pNIPAM culture viability, as determined by resazurin conversion, was significantly higher than that of L-pNIPAM cultures (p= 0.016) indicating either increased cell proliferation or viability due to the inclusion of HA in the culture. The 0.4% v/v HA/L-pNIPAM cultures displayed a higher overall cell viability, however showed a higher standard deviation which may be problematic for future standardisation.
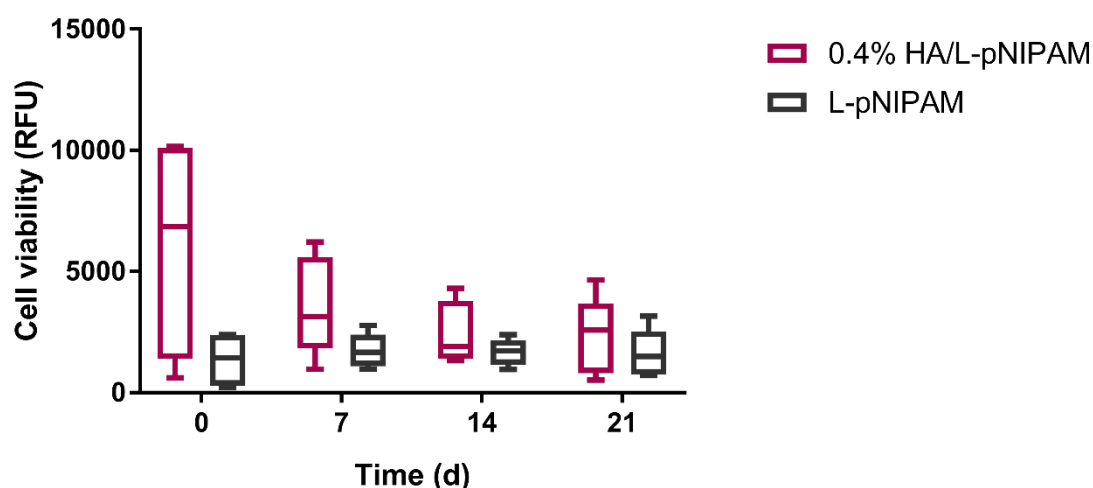
Figure 5.3 Cell viability of HepG2 cells cultured in a hydrogel scaffold. Two types of hydrogel were used; L-pNIPAM and 0.4% v/v HA/L-pNIPAM. The cells were seeded at a density of $2x10^6$ cells/mL (n=3).

An increase in cumulative albumin concentration was observed over 14 days in culture (Figure 5.4). A significant difference between the HA containing and pure hydrogel cultures was observed (p= 0.0001). This indicates that the cultures without the presence of HA in the gel either produced more albumin or it was more likely to be sequestered within these gels due to the presence of HA. The levels of albumin were significantly higher in the supernatant of both hydrogel compositions, when cells were included, compared to their acellular counterparts (p< 0.0001). The albumin concentration increased significantly between days 0-4 of culture in the 0.4% v/v HA/L-pNIPAM cultures (p= 0.0319) and in the L-pNIPAM cultures (p= 0.0021). After the 4 day point the albumin levels reached a plateau of 40ng/mL in HA hydrogel and 123ng/mL in HA free hydrogels.
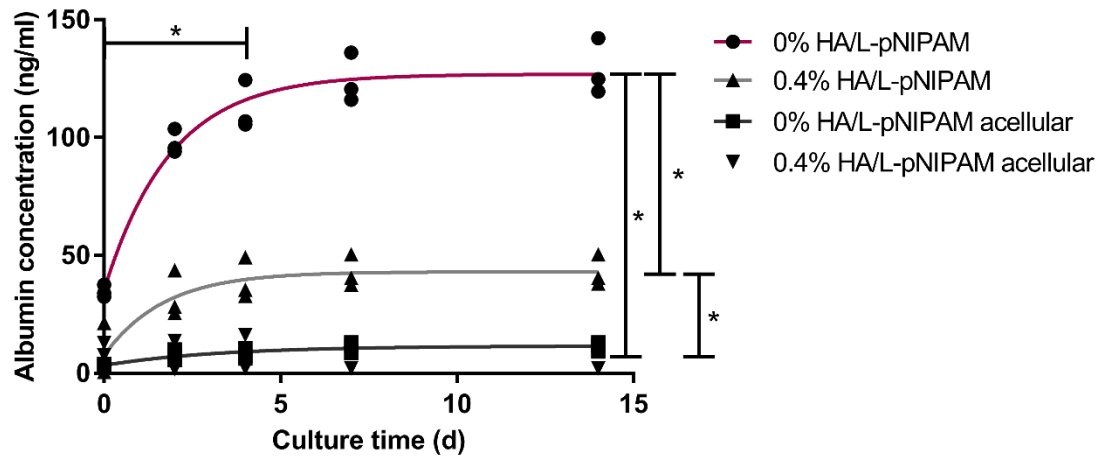
Figure 5.4 *Cumulative albumin concentration in the culture media of HepG2 hydrogel cultures (n=2).*

The ability of the cells to form larger structures and proliferate in different culture conditions within the hydrogel was assessed by H&E staining (Figure 5.5). Layered culture conditions, both static and dynamic, led to cell growth on top of the hydrogel without any migration into the gel. The cells continued to proliferate at a standard monolayer culture rate and, once at a certain size, cell masses visibly detached from the surface of the hydrogel into the media (data not shown). The suspended cultures began as single cell suspensions within the hydrogel which, over the period of 4 weeks, migrated towards each other primarily at the edge of the hydrogel to form solid masses within. Suspended static and dynamic cultures both formed solid masses at 4 weeks and were histologically identical.
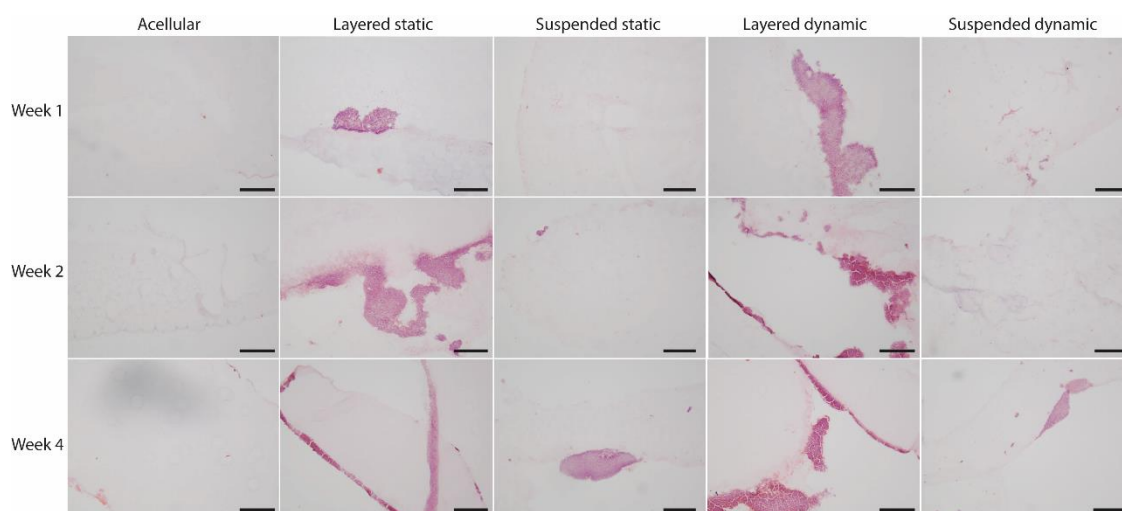
Figure 5.5 H&E staining of static and dynamic HepG2 cultures suspended within and layered on top of hydrogel. Cultures were kept up to 4 weeks. Scale bar = 200μm.

To evaluate hepatic activity Alkaline Phosphatase was monitored within the suspended static and dynamic cultures by IHC (Figure 5.6). Compared to the cytospin 2D control both static and dynamic cultures expressed a higher level of Alkaline Phosphatase indicating recovered hepatic function.
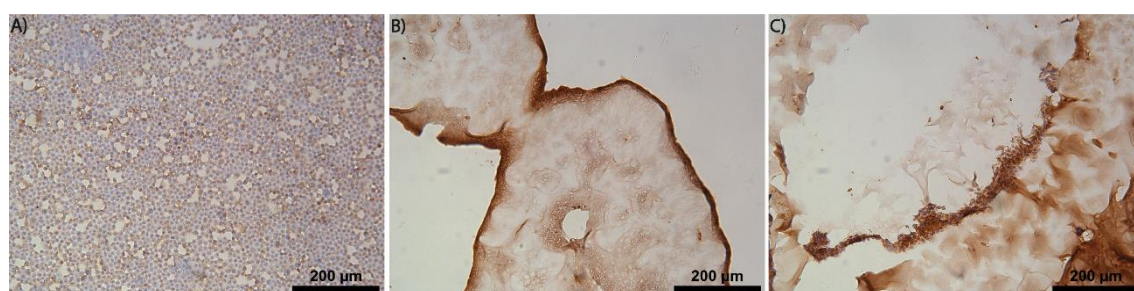
Figure 5.6 IHC of ALP in static 4 wk HepG2 cultures suspended within L-pNIPAM hydrogel. A) Cytospun HepG2 cell control, B) Static suspended HepG2 hydrogel culture C) Dynamic suspended HepG2 hydrogel culture. The image shows an increase in ALP expression in 3D cultures.
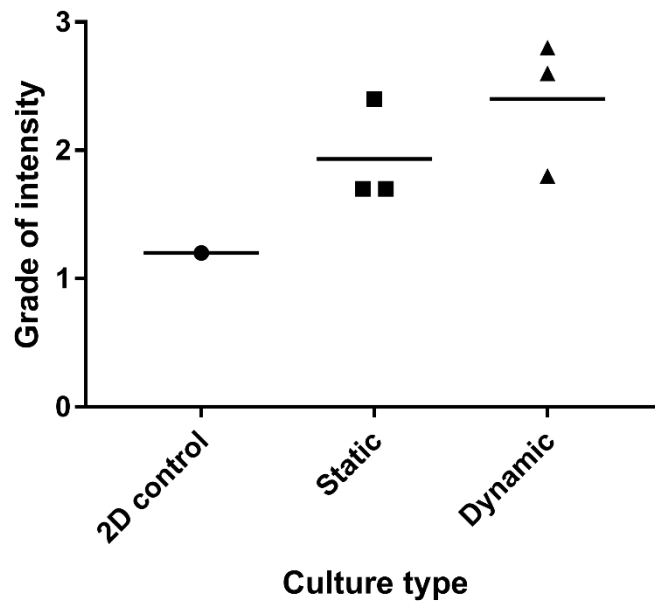
Figure 5.7 Grading intensity of ALP IHC between static and dynamic condition suspended 0% HA/L-pNIPAM hydrogel cultures compared to a control 2D cytospin. Grades are from 0-3 indicating no staining at 0 and very intense staining at 3. One biological repeat and 3 technical repeats were performed.

5.3.2 Mass spectrometry imaging of HepG2 model

Positive mode imaging of hydrogel HepG2 cultures revealed many cell related signals, such as *m/z* 184.0726 (phosphocholine) and ionic species *m/z* 723.4959, 754.5381, 782.5694 and 808.5851 putatively identified as phospholipid species PA and PC (Figure 5.8 and Appendix chapter 5 figures 4-13). The signal for phosphocholine was used as a cell location marker in order to correlate signals with cell mass locations. Signals of these ionic species were upregulated within the 0.5 and 2.5mM APAP treated samples compared to the untreated control indicating an altered lipid expression as a result of treatment.
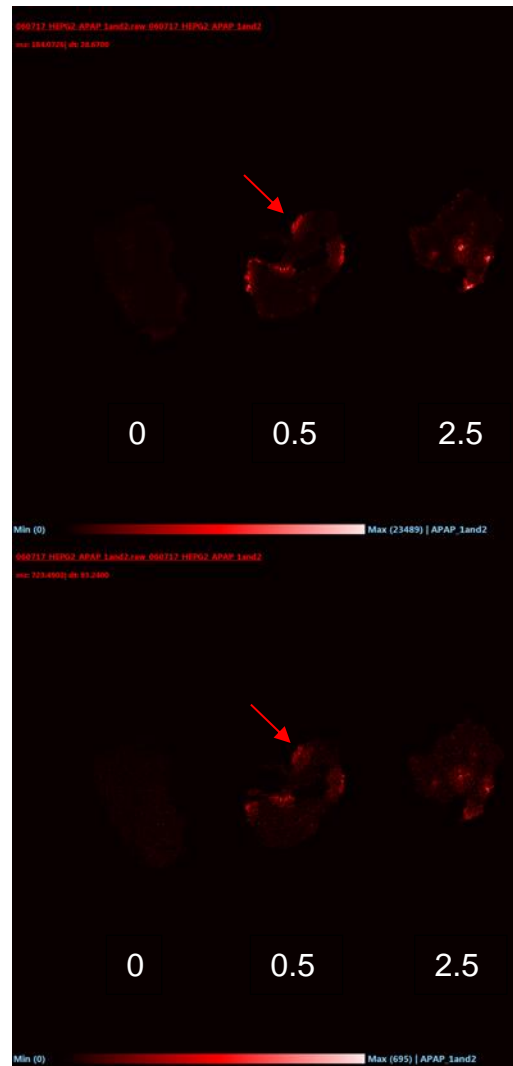
Figure 5.8 *MSI of untreated, 0.5 and 2.5mM APAP-treated HepG2 hydrogel cultures corresponding to ionic signals m/z 184.0726 (phosphocholine, top) m/z 723.4902 (bottom). The red arrows are pointing at the one of the cell locations within the gel marked by the increased signal.*

5.4 Discussion

In this chapter, an *in vitro* three-dimensional liver toxicity model has been developed using a nanocomposite hydrogel as a scaffold and its compatibility with the MSI technique MALDI-MSI was assessed. The HepG2 cell line retained its cell viability during growth in both 0.4% v/v HA/L-pNIPAM and pure hydrogel for up to 21 days and formed large cell masses after 4 weeks of culture. Hepatic differentiation of 0.4% v/v HA/L-pNIPAM cultures should be assessed further in the future, as addition of HA may either be beneficial or hinder differentiation inside the hydrogel construct. The method developed can be used to analyse small molecules and lipids to observe adverse outcome pathways related to DILI.

5.4.1 Characterisation of HepG2 hydrogel cultures

HepG2 3D culture hepatic function was assessed by quantifying the amount of albumin excreted into the cell media. Albumin is produced solely by hepatocytes and is subsequently used as a measure of hepatic function (Ebrahimkhani *et al.*, 2014). Albumin is responsible for the transport of insoluble endogenous e.g. bilirubin or fatty acids and exogenous e.g. drugs or nutrients substances. In fact, in albumin-drug binding causes increases in drug solubility but reduces toxicity and increases drug half-life, therefore is an important component of an *in vitro* toxicity model (Yamasaki *et al.*, 2013). Within the HepG2 hydrogel culture media, the Albumin concentration increases significantly within two days of culture in both L-pNIPAM and 0.4% v/v HA/L-pNIPAM sample sets, compared to acellular control samples at low background production levels. However, the release is decreased considerably after four days of culture in hydrogel. This could be due to increased or altered protein and glycan deposition during culture in hydrogel and subsequent increased sequestering of the albumin within the gel. Hepatocytes are responsible for production of several more extracellular proteins, namely clotting factors and α- and β-globulins, and protein glycosylation is a common post-translational modification, which could be restored in HepG2 3D cultures (Wiśniewski *et al.*, 2016). The ECM is known to sequester many biomolecules, principally growth factors, as part of its regulatory function (Tibbitt & Anseth, 2009) As the albumin is sequestered, it might no longer diffuse out of the hydrogel and into the media where it can be detected. This may also be an explanation for the lower signal observed in the HA hydrogels. A further

investigation of albumin levels inside the hydrogel is required in order to elucidate this further by proteomic MSI or IHC of sample sections.

The levels of alkaline phosphatase expressed within the hydrogel cultures compared to 2D cultures were increased. Levels of ALP are a sign of restored hepatic function and increases in the levels could be later monitored after treatment in order to confirm DILI occurrence (Hussaini & Farrington, 2007). Overall, the increased levels of albumin and ALP in the 3D cell cultures, which can be continually cultured for up to 4 weeks, indicate that the HepG2 cells have altered certain hepatocyte characteristics compared to 2D culture. Further indicators of increased activity could be studied, such as altered levels of P450 proteins as well as the altered sensitivity of the model to known therapeutics compared to the 2D equivalent.

Although 3D culture was shown to improve the HepG2 cell line hepatic function to an extent, higher functionality models have been developed in recent years (Otieno *et al.*, 2018). The production of a pre-clinical model which could capture liver processes such as inflammation, infection and oxidative stress as well as the genotype associated pre-disposition towards DILI is challenging (Mosedale & Watkins, 2017). In order to represent all these processes the model would have to contain a high amount of genetic variation, representative of the general patient pool, as well as contain stromal cell types in order to be inclusive of indirect effects associated with supporting cell types. Use of 3D cell culture has enabled longer culture of active primary hepatocytes. By growing hepatocytes in spheroid form, Bell and colleagues managed to create a co-culture compatible system which lasted for at least 5 weeks, which makes it suitable for long-term toxicological studies (Bell *et al.*, 2016). This model was shown to be much more representative of *in vivo* than the HepaRG cell line and stem cell derived hepatocytes (Bell *et al.*, 2017). Another recent study compared 2D sandwich cultures of primary human hepatocytes (PHHs) to 3D spheroid cultures of the same cells in order to observe differences in their phenotype maintenance (Bell *et al.*, 2018). They found that even in sandwich cultures there were certain aspects of hepatocyte dedifferentiation, which were not prevented and would lead to a lower capacity to detoxify reactive metabolic intermediates. In contrast, the 3D PHH spheroid cultures maintained high levels of ADME specific proteins and metabolic activity,

as demonstrated by their higher sensitivity to APAP and other drugs which lead to production of highly toxic intermediates by active CYP proteins (Bell *et al.*, 2018). Some groups have been working towards cell sources which are more widely available than limited primary human hepatocytes. A functional vascularized and human liver model was developed, based on the use of reprogrammed human induced pluripotent stem cells (iPSCs) (Takebe *et al.*, 2013). The model was able to rescue drug-induced lethal liver failure when transplanted, perform liver-specific functions, including human specific drug metabolism. The *in vitro* created iPSC liver buds resembled *in vivo* liver buds in their gene and protein expression (Takebe *et al.*, 2013). These functions would enable the retrieval of more accurate adverse outcome pathway data, though the model may need simplification for this application as opposed to tissue engineering. In order to improve 3D models of liver further, the combination of organoid technology and microfluidic models has been suggested. Both types of model have challenges, such as structural fidelity and environmental control, which could be overcome by combination/synergistic engineering (Takebe *et al.*, 2017).

5.4.2 MSI of HepG2 hydrogel cultures

The phosphocholine signal in the mass spectrometry images was used as a cell location marker. Phosphocholine is with a fragment of phosphatidylcholine, a major component of the cell membrane, therefore this was deemed suitable to detect cell locations in positive mode imaging (Jansen *et al.*, 2001). It may be particularly high within hepatocellular carcinoma cells as an increased expression of Choline Kinase α, which catalyses the conversion of choline to phosphocholine, was recently observed in tumour compared to normal tissues (Lin *et al.*, 2017). Several ionic species were observed specifically localised within the cell masses in the hydrogel. Several of those were upregulated in treated samples which may be an indication of phospholipidosis, which is characterised by an accumulation of phospholipids within drug-affected hepatocytes (Begriche *et al.*, 2011). To our knowledge this chapter presents the first instance of MSI of a liver toxicity model as well as the first instance of MSI of a 3D model based on a polymeric scaffold. Further identification and multivariate analysis would be required in order to elucidate significant small molecule and lipid differences between the different

treatment groups. The functional model could then be used for the study of unknown adverse outcome pathways in order to determine the molecular initiating events and toxicity pathways through the biochemical cell response to a drug.

5.5 Concluding remarks

Long-term culture of the HepG2 cell line was shown to improve the hepatic cell activity and increase the similarity of the cell line to *in vivo* in the elucidation of adverse outcome pathways. This synthetic polymer-based scaffold model was analysed using MSI for the first time in order to establish a method for evaluating AOPs. In the future, the technique can be useful in determining, in an untargeted fashion, the metabolomic changes occurring within 3D cell culture models. Additionally, proteomic MSI could be used to confirm differentiation and maintenance of the cell phenotype.

Chapter 6: Conclusions and future work

6.1 Conclusions and future work

6.1.1 3D model of osteosarcoma: Optimisation and MSI analysis

The most common application of 3D cell culture has been within the cancer field. Models such as this are particularly useful in cases of rare cancers where there is limited knowledge about origin, function and treatment options due to lack of affected people and therefore experience. In chapter 2, a 3D cell culture model of osteosarcoma was developed in order to better represent and study the disease. Because very little is known about osteosarcoma and access to patient samples is limited, even in designated hospitals, cell line derived 3D cell culture models are potentially a suitable alternative to study the disease.

The use of untargeted MSI was demonstrated in this chapter as a tool for the elucidation of unknown molecular disease mechanisms. Untargeted techniques, such as MSI, could aid in the discovery of potentially important pathways related to osteosarcoma formation, propagation and drug resistance, which can be achieved without prior knowledge, which for rare tumours such as osteosarcoma is currently lacking. The spheroid aggregate model designed in this chapter is a unique two-step culture model with the aim of producing a large mass which is representative of many of the tumour environments encountered but still maintaining some visible clonal differences, in order to better study the heterogeneity present within osteosarcoma. The spheroid aggregates are >500μm which produces a mass containing proliferating, apoptotic and necrotic regions due to diffusion distances within. These are representative of these cell states within an osteosarcoma tumour. Additionally, due to the heterogeneity observed within cell lines which is then expanded by culturing each of these cells into a colony, heterogeneity can be more easily studied. As the aggregates are made up of individual clonal spheroids they are uniquely capable of representing tumour heterogeneity whilst still maintaining larger regions of clonality which are easier to analyse and interpret than single cell heterogenous regions. Potentially a clonal spheroid within the spheroid aggregate may have a completely different reaction to a pharmaceutical than another clone within the same mass, which will

be easier to observe in a large clonal population than a single cell due to an increase in signal and area of regions of interest. This model is presently exclusive in these capabilities as all other 3D cell culture tumour models entail either MCTS or clonal spheroid methods.

This thesis additionally contains the first report of MSI of a mesenchymal tumour cell model. The clonal differences within a spheroid aggregate could be observed using MSI of endogenous metabolites and could be used in the future to determine different interactions within a single tumour due to heterogeneity. Observation of intra-aggregate differences would provide information on endogenous molecular heterogeneity and specific clonal behaviour. Intra-aggregate analysis could be taken further using a mass spectrometer capable of high spatial resolution imaging. Using higher spatial resolution would provide a clearer molecular map of the spheroid aggregate model and would better pinpoint certain active pathways within the proliferative, apoptotic or necrotic regions. In future, the model developed in this thesis has the potential for co-culture. As the method used involves two separate culture stages a second cell type could be introduced at the second stage, which would then be integrated into the aggregate mass. This may be potentially useful as a study of angiogenesis by the addition of an endothelial cell population, such as HUVECs, as an improved model, as was recently reported (Chaddad *et al.*, 2017). For future studies it would be useful to characterise the model further by studying potential mineralisation and altered expression of osteogenic markers such as SATB2, alkaline phosphatase and osteocalcin as well as expression of type I collagen (Evola *et al.*, 2017; Machado *et al.*, 2016).

6.1.2 3D model of osteosarcoma: Therapeutic treatment analysis

Chapter 3 focuses on use of the osteosarcoma model developed in chapter 2 for improved analysis of osteosarcoma drug response. The treatment options for osteosarcoma are lacking due to lack of research and tumour aggressiveness. 3D cell culture models, like the one developed in chapter 2, could demonstrate a more representative tumour response to chemotherapeutics, leading to less false positive results moving onto further stages of drug development and making the process more cost and time efficient. The higher time efficiency would potentially lead to more successful drug candidates in a shorter time period. The difference

in drug responses was demonstrated in chapter 3 where the SAOS-2 cell line proved to be completely resistant to doxorubicin in 3D cell culture when treated with a 4-fold higher doxorubicin concentration than the IC_{50} observed in the 2D cell culture. This may largely be due to the difference in cell proliferation and lack of penetration into the mass, however expression changes may also be contributing to resistance. Doxorubicin resistance is common in high-grade osteosarcoma patients mainly due to ABC transporter mediated drug efflux, therefore it may be interesting in the future to check for its increased expression (Hattinger *et al.*, 2017). For the first time, potential molecular biomarkers of drug response were determined by PCA-DA of MSI data obtained from a large treated spheroid aggregate cohort. The significantly differing species were calculated using two separate statistical methods and 10 highly differing species were detected using both tests, which may be indicative of the strong significance of these ionic species in drug response. Disease relevant putative assignments were given to some of the ionic species however additional analysis is required in order to confirm the identities of these molecules of interest by MS/MS. This had proved difficult due to the spheroid aggregate small size, which impeded MS/MS analysis, and spectral complexity, which made molecular identification more difficult. Instrumentation capable of smaller raster sizes and higher mass resolution may aid in solving these complications. Once identified, further study of the role these molecules play in drug resistance can be established.

6.1.3 3D model of osteosarcoma: Proteotypic peptide detection by MSI

Proteins are important targets when studying a rare disease, such as osteosarcoma. In oncology, the use of biomarkers is for therapeutic monitoring, potential prediction of severity and relapse (prognostic), and for earlier stage cancer detection so bone-targeted treatment can be started at an earlier stage (diagnostic). All the mentioned types of biomarker have been explored for osteosarcoma (Evola *et al.*, 2017). Despite the number of possible markers found, only the marker SATB2 is commonly used as a diagnostic marker of osteosarcoma tissue in the clinic, due to its high percentage positivity in OS compared to other markers (Machado *et al.*, 2016). Currently, this biomarker is being used as an additional diagnostic step in disputable cases after the main

diagnostic strategy involving identification of malignant osteoid matrix formation and use of clinical and radiological data. The untargeted proteomic analysis of a 3D osteosarcoma model may provide useful information in the form of biomarkers and drugable targets therefore focus was also directed towards novel peptide imaging within the osteosarcoma model. Chapter 4 demonstrated the adaptation of the analysis for proteotypic peptides within the osteosarcoma model developed in chapter 2. The analysis of tryptic peptide species was achieved within the spheroid aggregate. In future, the sample preparation requires further optimisation in order to observe a larger number of proteotypic species within the model. This would be improved with a 3D cell culture specific, optimised digestion step and optimisation of the instrumentation available. Once the analysis is fully optimised, a full cohort of treatment groups should be run, similarly to chapter 3, in order to identify significantly differing species.

6.1.4 3D model of osteosarcoma: QMSI

The quantification of peptides and proteins using MSI is currently under development, as it would prove very useful primarily in the biopharmaceutical and cancer biology fields. Quantification of multiple peptides/proteins within a single experiment has been heavily developed using other mass spectrometry-based methods, primarily LC-MS. However, these methods do not preserve topological information within the sample. The ability to accurately quantify a peptide/protein within a specific location of a tissue or a 3D cell culture model would increase the amount of information about a biopharmaceutical or biomarker of interest and improve knowledge of disease or treatment. In chapter 4, a method was developed for more accurate MSI quantification of up to 25 proteotypic peptides within a single mass spectrometry imaging experiment, which, to our knowledge, has never before been demonstrated. A cell plug construct was created, containing multiple peptide standards mixed with intact osteosarcoma cells in order to better represent proteotypic peptide signatures within an osteosarcoma culture sample. In future, this quantification method will be used to quantify proteotypic species within the 3D osteosarcoma culture model. Its applicability to osteosarcoma tissue will additionally be tested. The values should be confirmed using an accepted quantitative method such as LC-MS, western blot, ELISA or IHC. Of the four validation methods mentioned only IHC would maintain spatial

information of the molecule of interest. A suitable example of where this would be useful can be found in chapter 5 where accumulated albumin concentration in the cell medium plateaued at day 4 of culture using an ELISA method. In this case the method used may not have detected albumin which could be sequestered inside the scaffold. Additionally, three of the methods are antibody detection based and therefore higher-cost and lower throughput than MS-based methods. LC-MS is a MS-based validated method for protein quantification, which benefits from multiplex capabilities, however requires homogenisation of the sample. If QMSI was validated for the purpose of multiple protein quantification within one experiment it would quickly become the method of choice due to its multiplex capabilities and efficiency. This thesis describes the first steps taken towards the creation and validation of peptide QMSI methods.

6.1.5 3D model of liver: Adaptability of methods to a different 3D model

The pharmaceutical industry has struggled with high failure rates for drugs and low productivity within their R&D sector for many years (Smietana *et al.*, 2015). Another common application of 3D cell culture is its use in toxicity testing of promising pharmaceuticals in order to reduce risk of failure at later stages of testing. The use of hepatic and cardiac 3D cell culture models in toxicity testing was recognised in AstraZeneca's revised strategy as part of improving safety assessment by identifying early preclinical safety signals (Morgan *et al.*, 2018). In this setting the 3D cell culture and MSI methods developed would have a potential to save a significant amount of costs within the drug discovery field. This may be particularly important as analyses show that the majority of ongoing projects are pursuing novel mechanism therapeutics, which haven't had high success rates in the past compared to rigorously validated mechanisms (Shih *et al.*, 2017). Mass spectrometry would be a suitable tool for the definition of AOPs for pharmaceuticals of interest to acquire knowledge of the mechanisms involved. The aim of Chapter 5 was to demonstrate the applicability of the protocols developed in the previous chapters to a completely different 3D cell culture model, testing the robustness of the methods. The liver model was developed using a synthetic scaffold, in which the cell population was cultured long term. Complications may sometimes arise with the analysis of polymeric scaffolds. For

example, the pNIPAM based scaffold used in this chapter is auto-fluorescent at certain wavelengths, thus interfering with any fluorescent imaging techniques. Additionally, some synthetically derived polymeric scaffolds would impede certain metabolite, lipid or protein extraction protocols as they are hard to break down and extract from and, if broken down, may present with polymer contamination. In chapter 5 the MSI of small molecules within HepG2 cells within a synthetic hydrogel was demonstrated. Additionally, in order to analyse small molecules in their original state the sample preparation must be as fast and simple as possible. The method developed is the first of its kind, capable of detecting small molecule species within the synthetic scaffold. The sample preparation protocol developed for MSI of the samples was minimal in terms of interference and time period of sample collection. There was no sample interference to the analysis observed, therefore this protocol would be potentially suitable for definition of AOPs within the drug discovery workflow. Additionally, this protocol could be applied in future to analysis of other polymeric hydrogel samples. Further testing of the model would be required with an improved cell source consisting of an even higher functional activity, such as primary hepatocytes. MSI analysis could also be used for protein and glycan investigation of the cultures. This would be particularly useful in the confirmation of hepatocyte differentiation as hepatocytes are responsible for production of ECM components and display restored protein glycosylation (Wiśniewski *et al.*, 2016).

6.2 Closing Remarks

Further development of MSI is required to improve suitability to the alternative models available, so that the combined approach can successfully provide the information required in disease characterisation and treatment. The work within this thesis represents considerable method development towards this cause. Within this thesis, MSI has been shown to be capable of providing spatio-molecular information in tumour spheroids, and *in vitro* liver constructs. Due to a considerable interest and scientific effort there are many more designed alternative disease models available which would benefit from the information MSI could provide and the methods developed in this thesis have the robust potential to apply to many more types of alternative model.

Published data strongly suggests that MSI will develop into a valuable tool for biomedical research and wider clinical applications. The technique will complement pre-existing biomedical techniques such as immunohistochemistry in both research and *in-vitro* diagnostics. The use of alternative disease models in combination with MSI within research and industry environments will produce workflows capable of higher capability, lower cost, higher throughput and improved ethical impact. The use of these models in combination with suitable methodology will contribute towards the replacement and reduction of the use of animals in research and industry.

References

Acland, M., Mittal, P., Lokman, N. A., Klingler-Hoffmann, M., Oehler, M. K. & Hoffmann, P. (2018). Mass Spectrometry Analyses of Multicellular Tumor Spheroids. *PROTEOMICS - Clinical Applications*, 12(3), 1700124.

Adamski, J., Price, A., Dive, C. & Makin, G. (2013). Hypoxia–Induced Cytotoxic Drug Resistance in Osteosarcoma Is Independent of HIF-1Alpha (D. Heymann, Ed.). *PLoS ONE*, 8(6), e65304.

Addie, R. D., Balluff, B., Bovée, J. V. M. G., Morreau, H. & McDonnell, L. A. (2015). Current State and Future Challenges of Mass Spectrometry Imaging for Clinical Research. *Analytical Chemistry*, 87(13), 6426–6433.

Aichler, M. & Walch, A. (2015). MALDI Imaging Mass Spectrometry: Current Frontiers and Perspectives in Pathology Research and Practice. *Laboratory investigation; a journal of technical methods and pathology*, 95(4), 422–31.

Akeda, K., Nishimura, A., Satonaka, H., Shintani, K., Kusuzaki, K., Matsumine, A., Kasai, Y., Masuda, K. & Uchida, A. (2009). Three-Dimensional Alginate Spheroid Culture System of Murine Osteosarcoma. *Oncology Reports*, 22(5), 997–1003.

Albers, E. (2009). Metabolic Characteristics and Importance of the Universal Methionine Salvage Pathway Recycling Methionine from 5′-Methylthioadenosine. *IUBMB Life*, 61(12), 1132–1142.

Alizadeh, A. A. A., Aranda, V., Bardelli, A., Blanpain, C., Bock, C., Borowski, C., *et al.* (2015). Toward Understanding and Exploiting Tumor Heterogeneity. *Nat Med*, 21(8), 846–853.

Andersson, T. B. (2017). Evolution of Novel 3D Culture Systems for Studies of Human Liver Function and Assessments of the Hepatotoxicity of Drugs and Drug Candidates. *Basic & Clinical Pharmacology & Toxicology*, 121(4), 234–238.

Andersson, T. B., Kanebratt, K. P. & Kenna, J. G. (2012). The HepaRG Cell Line: A Unique *in Vitro* Tool for Understanding Drug Metabolism and Toxicology

in Human. *Expert Opinion on Drug Metabolism & Toxicology*, 8(7), 909–920.

Anderton, C. R., Chu, R. K., Tolić, N., Creissen, A. & Paša-Tolić, L. (2016). Utilizing a Robotic Sprayer for High Lateral and Mass Resolution MALDI FT-ICR MSI of Microbial Cultures. *Journal of The American Society for Mass Spectrometry*, 27(3), 556–559.

Angel, P. M., Spraggins, J. M., Baldwin, H. S. & Caprioli, R. (2012). Enhanced Sensitivity for High Spatial Resolution Lipid Analysis by Negative Ion Mode Matrix Assisted Laser Desorption Ionization Imaging Mass Spectrometry. *Analytical chemistry*, 84(3), 1557–64.

Annabi, N., Tamayol, A., Uquillas, J. A., Akbari, M., Bertassoni, L. E., Cha, C., *et al.* (2014). 25th Anniversary Article: Rational Design and Applications of Hydrogels in Regenerative Medicine. *Advanced materials (Deerfield Beach, Fla.)*, 26(1), 85–123.

Anthérieu, S., Chesné, C., Li, R., Guguen-Guillouzo, C. & Guillouzo, A. (2012). Optimization of the HepaRG Cell Model for Drug Metabolism and Toxicity Studies. *Toxicology in Vitro*, 26(8), 1278–1285.

Arai, K., Sakamoto, R., Kubota, D. & Kondo, T. (2013). Proteomic Approach toward Molecular Backgrounds of Drug Resistance of Osteosarcoma Cells in Spheroid Culture System. *PROTEOMICS*, 13(15), 2351–2360.

Arrowsmith, J. (2011). Phase III and Submission Failures: 2007–2010. *Nature Reviews Drug Discovery*, 10(2), 87–87.

Augst, A. D., Kong, H. J. & Mooney, D. J. (2006). Alginate Hydrogels as Biomaterials. *Macromolecular bioscience*, 6(8), 623–633.

Aurich, M., Hofmann, G. O., Best, N. & Rolauffs, B. (2018). Induced Redifferentiation of Human Chondrocytes from Articular Cartilage Lesion in Alginate Bead Culture After Monolayer Dedifferentiation: An Alternative Cell Source for Cell-Based Therapies? *Tissue Engineering Part A*, 24(3–4), 275–286.

Azam, F., Mehta, S. & Harris, A. L. (2010). Mechanisms of Resistance to

Antiangiogenesis Therapy. *European journal of cancer (Oxford, England : 1990)*, 46(8), 1323–32.

Bäcker, A., Erhardt, O., Wietbrock, L., Schel, N., Göppert, B., Dirschka, M., *et al.* (2017). Silk Scaffolds Connected with Different Naturally Occurring Biomaterials for Prostate Cancer Cell Cultivation in 3D (K. Breslauer, Ed.). *Biopolymers*, 107(2), 70–79.

Baek, N., Seo, O. W., Kim, M., Hulme, J. & An, S. S. A. (2016). Monitoring the Effects of Doxorubicin on 3D-Spheroid Tumor Cells in Real-Time. *OncoTargets and therapy*, 9, 7207–7218.

Baker, B. M. & Chen, C. S. (2012). Deconstructing the Third Dimension – How 3D Culture Microenvironments Alter Cellular Cues. *Journal of Cell Science*, 125(13), 3015–3024.

Baker, T. C., Han, J. & Borchers, C. H. (2017). Recent Advancements in Matrix-Assisted Laser Desorption/Ionization Mass Spectrometry Imaging. *Current Opinion in Biotechnology*, 43, 62–69.

Balluff, B., Hanselmann, M. & Heeren, R. M. A. (2017). Mass Spectrometry Imaging for the Investigation of Intratumor Heterogeneity, in: *Advances in cancer research*, (pp. 201–230).

Baluya, D., Cortes, A., Nishiofuku, H., Avritscher, R. & Cressman, E. (2017). Technical Challenges of Mass Spectrometry Imaging of Doxorubicin Localization in Rat Liver Treated with Drug-Eluting Beads, in: 65th ASMS Conference on Mass Spectrometry and Allied Topics.

Barnes, C. A., Brison, J., Robinson, M., Graham, D. J., Castner, D. G. & Ratner, B. D. (2012). Identifying Individual Cell Types in Heterogeneous Cultures Using Secondary Ion Mass Spectrometry Imaging with C_{60} Etching and Multivariate Analysis. *Analytical Chemistry*, 84(2), 893–900.

Baronzio, G. F., Gramaglia, A., Baronzio, A. & Freitas, I. (2008). Influence of Tumor Microenvironment on Thermoresponse, in: *Hyperthermia in Cancer Treatment: A Primer*, (pp. 67–91). Boston, MA.

Barré, F. P. Y., Flinders, B., Garcia, J. P., Jansen, I., Huizing, L. R. S., Porta, T., Creemers, L. B., Heeren, R. M. A. & Cillero-Pastor, B. (2016). Derivatization Strategies for the Detection of Triamcinolone Acetonide in Cartilage by Using Matrix-Assisted Laser Desorption/Ionization Mass Spectrometry Imaging. *Analytical Chemistry*, 88(24), 12051–12059.

Bateman, N. W. & Conrads, T. P. (2018). Recent Advances and Opportunities in Proteomic Analyses of Tumour Heterogeneity. *The Journal of Pathology*, 244(5), 628–637.

Beasley, E., Francese, S. & Bassindale, T. (2016). Detection and Mapping of Cannabinoids in Single Hair Samples through Rapid Derivatization and Matrix-Assisted Laser Desorption Ionization Mass Spectrometry. *Analytical Chemistry*, 88(20), 10328–10334.

Beaumont, K. A., Anfosso, A., Ahmed, F., Weninger, W. & Haass, N. K. (2015). Imaging- and Flow Cytometry-Based Analysis of Cell Position and the Cell Cycle in 3D Melanoma Spheroids. *Journal of visualized experiments : JoVE*, (106), e53486.

Begriche, K., Massart, J., Robin, M.-A., Borgne-Sanchez, A. & Fromenty, B. (2011). Drug-Induced Toxicity on Mitochondria and Lipid Metabolism: Mechanistic Diversity and Deleterious Consequences for the Liver. *Journal of Hepatology*, 54(4), 773–794.

Bell, C. C., Dankers, A. C. A., Lauschke, V. M., Sison-Young, R., Jenkins, R., Rowe, C., *et al.* (2018). Comparison of Hepatic 2D Sandwich Cultures and 3D Spheroids for Long-Term Toxicity Applications: A Multicenter Study. *Toxicological Sciences*, 162(2), 655–666.

Bell, C. C., Hendriks, D. F. G., Moro, S. M. L., Ellis, E., Walsh, J., Renblom, A., *et al.* (2016). Characterization of Primary Human Hepatocyte Spheroids as a Model System for Drug-Induced Liver Injury, Liver Function and Disease. *Scientific Reports*, 6(1), 25187.

Bell, C. C., Lauschke, V. M., Vorrink, S. U., Palmgren, H., Duffin, R., Andersson, T. B. & Ingelman-Sundberg, M. (2017). Transcriptional, Functional, and

Mechanistic Comparisons of Stem Cell-Derived Hepatocytes, HepaRG Cells, and Three-Dimensional Human Hepatocyte Spheroids as Predictive In Vitro Systems for Drug-Induced Liver Injury. *Drug metabolism and disposition: the biological fate of chemicals*, 45(4), 419–429.

Beynon, R. J., Doherty, M. K., Pratt, J. M. & Gaskell, S. J. (2005). Multiplexed Absolute Quantification in Proteomics Using Artificial QCAT Proteins of Concatenated Signature Peptides. *Nature Methods*, 2(8), 587–589.

Birgersdotter, A., Sandberg, R. & Ernberg, I. (2005). Gene Expression Perturbation in Vitro—A Growing Case for Three-Dimensional (3D) Culture Systems. *Seminars in Cancer Biology*, 15(5), 405–412.

Bonnel, D., Legouffe, R., Eriksson, A. H., Mortensen, R. W., Pamelard, F., Stauber, J. & Nielsen, K. T. (2018). MALDI Imaging Facilitates New Topical Drug Development Process by Determining Quantitative Skin Distribution Profiles. *Analytical and Bioanalytical Chemistry*, 410(11), 2815–2828.

Borisy, A. A., Elliott, P. J., Hurst, N. W., Lee, M. S., Lehar, J., Price, E. R., *et al.* (2003). Systematic Discovery of Multicomponent Therapeutics. *Proceedings of the National Academy of Sciences of the United States of America*, 100(13), 7977–82.

Botter, S. M., Neri, D. & Fuchs, B. (2014). Recent Advances in Osteosarcoma. *Current Opinion in Pharmacology*, 16(1), 15–23.

Boyes, V. L., Sammon, C., Lemaitre, C. & Breen, C. (2012). Composite The Synthesis and Development of Novel, Easily Processable Poly (n-Isopropylacrylamide) -Based Hydrogels.

Boyes, V. L., Sammon, C., Lemaitre, C., Breen, C., Le maitre, C. & Breen, C. (2013). Composite Hydrogel-Clay Particles.

Breslin, S. & O'Driscoll, L. (2016). The Relevance of Using 3D Cell Cultures, in Addition to 2D Monolayer Cultures, When Evaluating Breast Cancer Drug Sensitivity and Resistance. *Oncotarget*, 7(29), 45745–45756.

Broniowska, K. A., Diers, A. R. & Hogg, N. (2013). S-Nitrosoglutathione.

Biochimica et Biophysica Acta - General Subjects, 1830(5), 3173–3181.

Broutier, L., Andersson-Rolf, A., Hindley, C. J., Boj, S. F., Clevers, H., Koo, B.-K. & Huch, M. (2016). Culture and Establishment of Self-Renewing Human and Mouse Adult Liver and Pancreas 3D Organoids and Their Genetic Manipulation. *Nature Protocols*, 11(9), 1724–1743.

Bruheim, S., Bruland, O. S., Breistol, K., Maelandsmo, G. M. & Fodstad, O. (2004). Human Osteosarcoma Xenografts and Their Sensitivity to Chemotherapy. *Pathology oncology research : POR*, 10(3), 133–41.

Caliari, S. R. & Burdick, J. A. (2016). A Practical Guide to Hydrogels for Cell Culture. *Nature Methods*, 13(5), 405–414.

Caprioli, R. M., Farmer, T. B. & Gile, J. (1997). Molecular Imaging of Biological Samples: Localization of Peptides and Proteins Using MALDI-TOF MS. *Analytical Chemistry*, 69(23), 4751–4760.

Carpentier, A., Nimgaonkar, I., Chu, V., Xia, Y., Hu, Z. & Liang, T. J. (2016). Hepatic Differentiation of Human Pluripotent Stem Cells in Miniaturized Format Suitable for High-Throughput Screen. *Stem Cell Research*, 16(3), 640–650.

Cascio, S. & Zaret, K. S. (1991). Hepatocyte Differentiation Initiates during Endodermal-Mesenchymal Interactions Prior to Liver Formation. *Development (Cambridge, England)*, 113(1), 217–25.

Cavo, M., Caria, M., Pulsoni, I., Beltrame, F., Fato, M. & Scaglione, S. (2018). A New Cell-Laden 3D Alginate-Matrigel Hydrogel Resembles Human Breast Cancer Cell Malignant Morphology, Spread and Invasion Capability Observed "in Vivo". *Scientific Reports*, 8(1), 5333.

Chaddad, H., Kuchler-Bopp, S., Fuhrmann, G., Gegout, H., Ubeaud-Sequier, G., Schwinté, P., Bornert, F., Benkirane-Jessel, N. & Idoux-Gillet, Y. (2017). Combining 2D Angiogenesis and 3D Osteosarcoma Microtissues to Improve Vascularization. *Experimental Cell Research*, 360(2), 138–145.

Chan, G. & Mooney, D. J. (2013). Ca(2+) Released from Calcium Alginate Gels

Can Promote Inflammatory Responses in Vitro and in Vivo. *Acta biomaterialia*, 9(12), 10.1016/j.actbio.2013.08.002.

Chen, C.-D., Wang, C.-L., Yu, C.-J., Chien, K.-Y., Chen, Y.-T., Chen, M.-C., Chang, Y.-S., Wu, C.-C. & Yu, J.-S. (2014). Targeted Proteomics Pipeline Reveals Potential Biomarkers for the Diagnosis of Metastatic Lung Cancer in Pleural Effusion. *Journal of Proteome Research*, 13(6), 2818–2829.

Chen, M., Vijay, V., Shi, Q., Liu, Z., Fang, H. & Tong, W. (2011). FDA-Approved Drug Labeling for the Study of Drug-Induced Liver Injury. *Drug Discovery Today*, 16(15–16), 697–703.

Chumbley, C. W., Reyzer, M. L., Allen, J. L., Marriner, G. A., Via, L. E., Barry, C. E. & Caprioli, R. M. (2016). Absolute Quantitative MALDI Imaging Mass Spectrometry: A Case of Rifampicin in Liver Tissues. *Analytical chemistry*, 88(4), 2392–8.

Cipriano, M., Freyer, N., Knöspel, F., Oliveira, N. G., Barcia, R., Cruz, P. E., *et al.* (2017). Self-Assembled 3D Spheroids and Hollow-Fibre Bioreactors Improve MSC-Derived Hepatocyte-like Cell Maturation in Vitro. *Archives of Toxicology*, 91(4), 1815–1832.

Clevers, H. (2016). Modeling Development and Disease with Organoids. *Cell*, 165(7), 1586–1597.

Close, D. A., Camarco, D. P., Shan, F., Kochanek, S. J. & Johnston, P. A. (2018). The Generation of Three-Dimensional Head and Neck Cancer Models for Drug Discovery in 384-Well Ultra-Low Attachment Microplates, in: (pp. 355–369). Humana Press, New York, NY.

Cole, L. M., Mahmoud, K., Haywood-Small, S., Tozer, G. M., Smith, D. P. & Clench, M. R. (2013). Recombinant ' IMS TAG' Proteins - A New Method for Validating Bottom-up Matrix-Assisted Laser Desorption/Ionisation Ion Mobility Separation Mass Spectrometry Imaging. *Rapid communications in mass spectrometry : RCM*, 27(21), 2355–2362.

Cornett, D. S., Reyzer, M. L., Chaurand, P. & Caprioli, R. M. (2007). MALDI Imaging Mass Spectrometry: Molecular Snapshots of Biochemical Systems.

Nature Methods, 4(10), 828–833.

Costa, E. C., Gaspar, V. M., Coutinho, P. & Correia, I. J. (2014). Optimization of Liquid Overlay Technique to Formulate Heterogenic 3D Co-Cultures Models. *Biotechnology and bioengineering*, 111(8), 1672–85.

Costa, E. C., Moreira, A. F., de Melo-Diogo, D., Gaspar, V. M., Carvalho, M. P. & Correia, I. J. (2016). 3D Tumor Spheroids: An Overview on the Tools and Techniques Used for Their Analysis. *Biotechnology Advances*, 34(8), 1427–1441.

Dagg, B., Eustace, D. L. S., Han, X., Money, S. & Heyderman, E. (1992). Cytoblock Preparations for Examination of Cervical and Other Cells. *Journal of Clinical Pathology*, 45(12), 1122–1123.

Daublain, P., Feng, K.-I., Altman, M. D., Martin, I., Mukherjee, S., Nofsinger, R., *et al.* (2017). Analyzing the Potential Root Causes of Variability of Pharmacokinetics in Preclinical Species. *Molecular Pharmaceutics*, 14(5), 1634–1645.

David, B. P., Dubrovskyi, O., Speltz, T. E., Wolff, J. J., Frasor, J., Sanchez, L. M. & Moore, T. W. (2018). Using Tumor Explants for Imaging Mass Spectrometry Visualization of Unlabeled Peptides and Small Molecules. *ACS Medicinal Chemistry Letters*, 9(7), 768–772.

Day, R. E. & Palubeckaite, I. (2017). The Future in Disease Models for Mass Spectrometry Imaging, Ethical Issues, and the Way Forward, in: *Methods in Molecular Biology*, (pp. 191–201).

Derendorf, H. & Meibohm, B. (1999). Modeling of Pharmacokinetic/Pharmacodynamic (PK/PD) Relationships: Concepts and Perspectives. *Pharmaceutical Research*, 16(2), 176–185.

Diekjürgen, D. & Grainger, D. W. (2017). Polysaccharide Matrices Used in 3D in Vitro Cell Culture Systems. *Biomaterials*, 141, 96–115.

Dilillo, M., Ait-Belkacem, R., Esteve, C., Pellegrini, D., Nicolardi, S., Costa, M., *et al.* (2017). Ultra-High Mass Resolution MALDI Imaging Mass Spectrometry

of Proteins and Metabolites in a Mouse Model of Glioblastoma. *Scientific Reports*, 7(1), 603.

Dilillo, M., Pellegrini, D., Ait-Belkacem, R., de Graaf, E. L., Caleo, M. & McDonnell, L. A. (2017). Mass Spectrometry Imaging, Laser Capture Microdissection, and LC-MS/MS of the Same Tissue Section. *Journal of Proteome Research*, 16(8), 2993–3001.

Doerr, A. (2018). Mass Spectrometry Imaging Takes Off. *Nature Methods*, 15(1), 32.

Dosh, R. H., Essa, A., Jordan-Mahy, N., Sammon, C. & Le Maitre, C. L. (2017). Use of Hydrogel Scaffolds to Develop an in Vitro 3D Culture Model of Human Intestinal Epithelium. *Acta Biomaterialia*, 62, 128–143.

Drake, R. R., Powers, T. W., Jones, E. E., Bruner, E., Mehta, A. S. & Angel, P. M. (2017). MALDI Mass Spectrometry Imaging of N-Linked Glycans in Cancer Tissues. *Advances in Cancer Research*, 134, 85–116.

Dueñas, M. E., Carlucci, L. & Lee, Y. J. (2016). Matrix Recrystallization for MALDI-MS Imaging of Maize Lipids at High-Spatial Resolution. *Journal of The American Society for Mass Spectrometry*, 27(9), 1575–1578.

Dueñas, M. E., Essner, J. J. & Lee, Y. J. (2017). 3D MALDI Mass Spectrometry Imaging of a Single Cell: Spatial Mapping of Lipids in the Embryonic Development of Zebrafish. *Scientific Reports*, 7(1), 14946.

van Duinen, V., van den Heuvel, A., Trietsch, S. J., Lanz, H. L., van Gils, J. M., van Zonneveld, A. J., Vulto, P. & Hankemeier, T. (2017). 96 Perfusable Blood Vessels to Study Vascular Permeability in Vitro. *Scientific Reports*, 7(1), 18071.

Duong, H. H. P. & Yung, L.-Y. L. (2013). Synergistic Co-Delivery of Doxorubicin and Paclitaxel Using Multi-Functional Micelles for Cancer Treatment. *International Journal of Pharmaceutics*, 454(1), 486–495.

Dutta, D., Heo, I. & Clevers, H. (2017). Disease Modeling in Stem Cell-Derived 3D Organoid Systems. *Trends in Molecular Medicine*, 23(5), 393–410.

Duval, K., Grover, H., Han, L.-H., Mou, Y., Pegoraro, A. F., Fredberg, J. & Chen, Z. (2017). Modeling Physiological Events in 2D vs. 3D Cell Culture. *Physiology*, 32(4), 266–277.

Eary, J. F., O'Sullivan, F., O'Sullivan, J. & Conrad, E. U. (2008). Spatial Heterogeneity in Sarcoma 18F-FDG Uptake as a Predictor of Patient Outcome. *Journal of nuclear medicine : official publication, Society of Nuclear Medicine*, 49(12), 1973–9.

Ebrahimkhani, M. R., Neiman, J. A. S., Raredon, M. S. B., Hughes, D. J. & Griffith, L. G. (2014). Bioreactor Technologies to Support Liver Function in Vitro. *Advanced drug delivery reviews*, 69–70, 132–57.

Egger, D., Fischer, M., Clementi, A., Ribitsch, V., Hansmann, J., Kasper, C., *et al.* (2017). Development and Characterization of a Parallelizable Perfusion Bioreactor for 3D Cell Culture. *Bioengineering*, 4(4), 51.

Eikel, D., Vavrek, M., Smith, S., Bason, C., Yeh, S., Korfmacher, W. A. & Henion, J. D. (2011). Liquid Extraction Surface Analysis Mass Spectrometry (LESA-MS) as a Novel Profiling Tool for Drug Distribution and Metabolism Analysis: The Terfenadine Example. *Rapid Communications in Mass Spectrometry*, 25(23), 3587–3596.

Elbadawy, M., Usui, T., Yamawaki, H. & Sasaki, K. (2018). Development of an Experimental Model for Analyzing Drug Resistance in Colorectal Cancer. *Cancers*, 10(6), 164.

Emura, M. & Aufderheide, M. (2016). Challenge for 3D Culture Technology: Application in Carcinogenesis Studies with Human Airway Epithelial Cells. *Experimental and Toxicologic Pathology*, 68(5), 255–261.

End, P., Gerbes, A. L., Benesic, A., Andrade, R. J., Aithal, G. P., Kullak-Ublick, G. A. & Merz, M. (2017). Drug-Induced Liver Injury: Recent Advances in Diagnosis and Risk Assessment. *Gut*, 66(6), 1154–1164.

Engert, F., Kovac, M., Baumhoer, D., Nathrath, M. & Fulda, S. (2017). Osteosarcoma Cells with Genetic Signatures of BRCAness Are Susceptible to the PARP Inhibitor Talazoparib Alone or in Combination with

Chemotherapeutics. *Oncotarget*, 8(30), 48794–48806.

Evola, F. R., Costarella, L., Pavone, V., Caff, G., Cannavò, L., Sessa, A., Avondo, S. & Sessa, G. (2017). Biomarkers of Osteosarcoma, Chondrosarcoma, and Ewing Sarcoma. *Frontiers in Pharmacology*, 08, 150.

Eyre, R., Feltbower, R. G., Mubwandarikwa, E., Jenkinson, H. C., Parkes, S., Birch, J. M., *et al.* (2009). Incidence and Survival of Childhood Bone Cancer in Northern England and the West Midlands, 1981-2002. *British journal of cancer*, 100(1), 188–93.

Fanelli, M., Hattinger, C. M., Vella, S., Tavanti, E., Michelacci, F., Gudeman, B., Barnett, D., Picci, P. & Serra, M. (2016). Targeting ABCB1 and ABCC1 with Their Specific Inhibitor CBT-1® Can Overcome Drug Resistance in Osteosarcoma. *Current cancer drug targets*, 16(3), 261–74.

Feist, P. E., Sidoli, S., Liu, X., Schroll, M. M., Rahmy, S., Fujiwara, R., Garcia, B. A. & Hummon, A. B. (2017). Multicellular Tumor Spheroids Combined with Mass Spectrometric Histone Analysis To Evaluate Epigenetic Drugs. *Analytical Chemistry*, 89(5), 2773–2781.

Feist, P. E., Sun, L., Liu, X., Dovichi, N. J. & Hummon, A. B. (2015). Bottom-up Proteomic Analysis of Single HCT 116 Colon Carcinoma Multicellular Spheroids. *Rapid Communications in Mass Spectrometry*, 29(7), 654–658.

Feng, H., Ou, B., Zhao, J., Yin, S., Lu, A., Oechsle, E. & Thasler, W. E. (2017). Homogeneous Pancreatic Cancer Spheroids Mimic Growth Pattern of Circulating Tumor Cell Clusters and Macrometastases: Displaying Heterogeneity and Crater-like Structure on Inner Layer. *Journal of Cancer Research and Clinical Oncology*, 143(9), 1771–1786.

Fennema, E., Rivron, N., Rouwkema, J., van Blitterswijk, C. & de Boer, J. (2013). Spheroid Culture as a Tool for Creating 3D Complex Tissues. *Trends in biotechnology*, 31(2), 108–15.

Ferrari, S. & Serra, M. (2015). An Update on Chemotherapy for Osteosarcoma. *Expert Opinion on Pharmacotherapy*, 16(18), 2727–2736.

Fletcher, C. D. M., Unni, K. K. & Mertens, F. (2013). *IARC Press* (C. D. M. Fletcher, J. A. Bridge, P. C. W. Hogendoorn, and F. Mertens, Eds.). IARC Press.

Florczyk, S. J., Kievit, F. M., Wang, K., Erickson, A. E., Ellenbogen, R. G. & Zhang, M. (2016). 3D Porous Chitosan-Alginate Scaffolds Promote Proliferation and Enrichment of Cancer Stem-like Cells. *Journal of Materials Chemistry B*, 4(38), 6326–6334.

Fontana, R. J., Hayashi, P. H., Gu, J., Reddy, K. R., Barnhart, H., Watkins, P. B., *et al.* (2014). Idiosyncratic Drug-Induced Liver Injury Is Associated with Substantial Morbidity and Mortality within 6 Months from Onset. *Gastroenterology*, 147(1), 96–108.e4.

Forkert, P. G. (1999). In Vivo Formation and Localization of 1,1-Dichloroethylene Epoxide in Murine Liver: Identification of Its Glutathione Conjugate 2-S-Glutathionyl Acetate. *The Journal of pharmacology and experimental therapeutics*, 290(3), 1299–306.

Francese, S. & Clench, M. R. (2010). MALDI Mass Spectrometry Imaging, a New Frontier in Biostructural Techniques: Applications in Biomedicine, in: *Mass Spectrometry for Microbial Proteomics*, (pp. 91–116). Chichester, UK: John Wiley & Sons, Ltd.

Friedrich, J., Seidel, C., Ebner, R. & Kunz-Schughart, L. A. (2009). Spheroid-Based Drug Screen: Considerations and Practical Approach. *Nature Protocols*, 4(3), 309–324.

Gago-Fuentes, R., Carpintero-Fernandez, P., Goldring, M. B., Brink, P. R., Mayan, M. D. & Blanco, F. J. (2014). Biochemical Evidence for Gap Junctions and Cx43 Expression in Immortalized Human Chondrocyte Cell Line: A Potential Model in the Study of Cell Communication in Human Chondrocytes. *Osteoarthritis and Cartilage*, 22(4), 586–590.

Galateanu, B., Hudita, A., Negrei, C., Ion, R.-M., Costache, M., Stan, M., *et al.* (2016). Impact of Multicellular Tumor Spheroids as an in Vivo- like Tumor Model on Anticancer Drug Response. *International journal of oncology*, 48(6),

2295–302.

Gao, S., Shen, J., Hornicek, F. & Duan, Z. (2017). Three-Dimensional (3D) Culture in Sarcoma Research and the Clinical Significance. *Biofabrication*, 9(3), 032003.

Garofalo, C., Capristo, M., Manara, M. C., Mancarella, C., Landuzzi, L., Belfiore, A., Lollini, P.-L., Picci, P. & Scotlandi, K. (2013). Metformin as an Adjuvant Drug against Pediatric Sarcomas: Hypoxia Limits Therapeutic Effects of the Drug. *PloS one*, 8(12), e83832.

Gaston, B. M. (2003). S-Nitrosylation Signaling in Cell Biology. *Molecular Interventions*, 3(5), 253–263.

Gatta, G., Capocaccia, R., Botta, L., Mallone, S., De Angelis, R., Ardanaz, E., *et al.* (2017). Burden and Centralised Treatment in Europe of Rare Tumours: Results of RARECAREnet-a Population-Based Study. *The Lancet Oncology*, 18(8), 1022–1039.

Gatta, G., Van Der Zwan, J. M., Casali, P. G., Siesling, S., Dei Tos, A. P., Kunkler, I., *et al.* (2011). Rare Cancers Are Not so Rare: The Rare Cancer Burden in Europe. *European Journal of Cancer*, 47(17), 2493–2511.

Gebhard, C., Miller, I., Hummel, K., Neschi née Ondrovics, M., Schlosser, S. & Walter, I. (2018). Comparative Proteome Analysis of Monolayer and Spheroid Culture of Canine Osteosarcoma Cells. *Journal of Proteomics*, 177, 124–136.

Gemperline, E., Rawson, S. & Li, L. (2014). Optimization and Comparison of Multiple MALDI Matrix Application Methods for Small Molecule Mass Spectrometric Imaging. *Anal. Chem*, 86, 15.

Gencoglu, M. F., Barney, L. E., Hall, C. L., Brooks, E. A., Schwartz, A. D., Corbett, D. C., Stevens, K. R. & Peyton, S. R. (2018). Comparative Study of Multicellular Tumor Spheroid Formation Methods and Implications for Drug Screening. *ACS biomaterials science & engineering*, 4(2), 410–420.

Gentile, P., Ferreira, A. M., Callaghan, J. T., Miller, C. A., Atkinson, J., Freeman,

C. & Hatton, P. V. (2017). Multilayer Nanoscale Encapsulation of Biofunctional Peptides to Enhance Bone Tissue Regeneration In Vivo. *Advanced Healthcare Materials*, 6(8), 1601182.

Gillette, B. M., Jensen, J. A., Tang, B., Yang, G. J., Bazargan-Lari, A., Zhong, M. & Sia, S. K. (2008). In Situ Collagen Assembly for Integrating Microfabricated Three-Dimensional Cell-Seeded Matrices. *Nature materials*, 7(8), 636–40.

Giordano, S., Morosi, L., Veglianese, P., Licandro, S. A., Frapolli, R., Zucchetti, M., *et al.* (2016). 3D Mass Spectrometry Imaging Reveals a Very Heterogeneous Drug Distribution in Tumors. *Scientific reports*, 6, 37027.

Goddard, E. T., Hill, R. C., Barrett, A., Betts, C., Guo, Q., Maller, O., Borges, V. F., Hansen, K. C. & Schedin, P. (2016). Quantitative Extracellular Matrix Proteomics to Study Mammary and Liver Tissue Microenvironments. *The international journal of biochemistry & cell biology*, 81(Pt A), 223–232.

Godoy, P., Hewitt, N. J., Albrecht, U., Andersen, M. E., Ansari, N., Bhattacharya, S., *et al.* (2013). Recent Advances in 2D and 3D in Vitro Systems Using Primary Hepatocytes, Alternative Hepatocyte Sources and Non-Parenchymal Liver Cells and Their Use in Investigating Mechanisms of Hepatotoxicity, Cell Signaling and ADME. *Archives of Toxicology*, 87(8), 1315–1530.

Gottesman, M. M., Fojo, T. & Bates, S. E. (2002). Multidrug Resistance in Cancer: Role of ATP-Dependent Transporters. *Nature Reviews Cancer*, 2(1), 48–58.

Graf, B. W. & Boppart, S. A. (2010). Imaging and Analysis of Three-Dimensional Cell Culture Models. *Methods in molecular biology (Clifton, N.J.)*, 591, 211–27.

Greek, R. & Menache, A. (2013). Systematic Reviews of Animal Models: Methodology versus Epistemology. *International Journal of Medical Sciences*, 10(3), 206–221.

Greijer, A. E. & van der Wall, E. (2004). The Role of Hypoxia Inducible Factor 1 (HIF-1) in Hypoxia Induced Apoptosis. *Journal of clinical pathology*, 57(10), 1009–14.

Groseclose, M. R. & Castellino, S. (2013). A Mimetic Tissue Model for the Quantification of Drug Distributions by MALDI Imaging Mass Spectrometry. *Analytical Chemistry*, 85(21), 10099–10106.

Growney Kalaf, E. A., Flores, R., Bledsoe, J. G. & Sell, S. A. (2016). Characterization of Slow-Gelling Alginate Hydrogels for Intervertebral Disc Tissue-Engineering Applications. *Materials science & engineering. C, Materials for biological applications*, 63, 198–210.

Hait, W. N. (2010). Anticancer Drug Development: The Grand Challenges. *Nature reviews. Drug discovery*, 9(4), 253–254.

Hanahan, D. & Weinberg, R. A. (2011). Hallmarks of Cancer: The next Generation. *Cell*, 144(5), 646–74.

Harrelson, J. P., Henne, K. R., Alonso, D. O. V & Nelson, S. D. (2007). A Comparison of Substrate Dynamics in Human CYP2E1 and CYP2A6. *Biochemical and biophysical research communications*, 352(4), 843–9.

Harrison, R. K. (2016). Phase II and Phase III Failures: 2013-2015. *Nature Reviews Drug Discovery*, 15(12), 817–818.

Hattinger, C. M., Fanelli, M., Tavanti, E., Vella, S., Riganti, C., Picci, P. & Serra, M. (2017). Doxorubicin-Resistant Osteosarcoma: Novel Therapeutic Approaches in Sight? *Future Oncology*, 13(8), 673–677.

Hattinger, C. M., Pasello, M., Ferrari, S., Picci, P. & Serra, M. (2010). Emerging Drugs for High-Grade Osteosarcoma. *Expert opinion on emerging drugs*, 15(4), 615–634.

Hay, M., Thomas, D. W., Craighead, J. L., Economides, C. & Rosenthal, J. (2014). Clinical Development Success Rates for Investigational Drugs. *Nature biotechnology*, 32(1), 40–51.

Heyer, J., Kwong, L. N., Lowe, S. W. & Chin, L. (2010). Non-Germline Genetically Engineered Mouse Models for Translational Cancer Research. *Nature Reviews Cancer*, 10(7), 470–480.

Heymann, M.-F., Brown, H. K. & Heymann, D. (2016). Drugs in Early Clinical

Development for the Treatment of Osteosarcoma. *Expert Opinion on Investigational Drugs*, 25(11), 1265–1280.

Hiemstra, P. S., Grootaers, G., van der Does, A. M., Krul, C. A. M. & Kooter, I. M. (2018). Human Lung Epithelial Cell Cultures for Analysis of Inhaled Toxicants: Lessons Learned and Future Directions. *Toxicology in Vitro*, 47, 137–146.

Hilton, G., Barosova, H., Petri-Fink, A., Rothen-Rutishauser, B. & Bereman, M. (2019). Leveraging Proteomics to Compare Submerged versus Air-Liquid Interface Carbon Nanotube Exposure to a 3D Lung Cell Model. *Toxicology in Vitro*, 54, 58–66.

Himes, R. H. (1991). Interactions of the Catharanthus (Vinca) Alkaloids with Tubulin and Microtubules. *Pharmacology & therapeutics*, 51(2), 257–267.

Hiraide, T., Ikegami, K., Sakaguchi, T., Morita, Y., Hayasaka, T., Masaki, N., *et al.* (2016). Accumulation of Arachidonic Acid-Containing Phosphatidylinositol at the Outer Edge of Colorectal Cancer. *Scientific Reports*, 6(1), 29935.

Ho, W. Y., Yeap, S. K., Ho, C. L., Rahim, R. A. & Alitheen, N. B. (2012). Development of Multicellular Tumor Spheroid (MCTS) Culture from Breast Cancer Cell and a High Throughput Screening Method Using the MTT Assay. *PLoS ONE*, 7(9), e44640.

Hoffmann, E. de. & Stroobant, V. (2007). *Mass Spectrometry: Principles and Applications, 3rd Ed*. Wiley.

Holdenrieder, S., Nagel, D., Schalhorn, A., Heinemann, V., Wilkowski, R., von Pawel, J., *et al.* (2008). Clinical Relevance of Circulating Nucleosomes in Cancer. *Annals of the New York Academy of Sciences*, 1137(1), 180–189.

Holst, S., Heijs, B., De Haan, N., Van Zeijl, R. J. M., Briaire-De Bruijn, I. H., Van Pelt, G. W., *et al.* (2016). Linkage-Specific in Situ Sialic Acid Derivatization for N-Glycan Mass Spectrometry Imaging of Formalin-Fixed Paraffin-Embedded Tissues. *Analytical Chemistry*, 88(11), 5904–5913.

Hongisto, V., Jernström, S., Fey, V., Mpindi, J.-P., Kleivi Sahlberg, K., Kallioniemi, O. & Perälä, M. (2013). High-Throughput 3D Screening Reveals Differences in Drug Sensitivities between Culture Models of JIMT1 Breast Cancer Cells. *PLoS ONE*, 8(10), e77232.

Hoogerwerf, W. A., Hawkins, A. L., Perlman, E. J. & Griffin, C. A. (1994). Chromosome Analysis of Nine Osteosarcomas. *Genes, chromosomes & cancer*, 9(2), 88–92.

Horvath, P., Aulner, N., Bickle, M., Davies, A. M., Nery, E. Del, Ebner, D., *et al.* (2016). Screening out Irrelevant Cell-Based Models of Disease. *Nature Reviews Drug Discovery*, 15(11), 751–769.

Horwitz, S. B. (1994). Taxol (Paclitaxel): Mechanisms of Action. *Annals of oncology : official journal of the European Society for Medical Oncology*, 5 Suppl 6, S3-6.

Hussaini, S. H. & Farrington, E. A. (2007). Idiosyncratic Drug-Induced Liver Injury: An Overview. *Expert Opinion on Drug Safety*, 6(6), 673–684.

Hutchinson, L. & Kirk, R. (2011). High Drug Attrition Rates--Where Are We Going Wrong? *Nature reviews. Clinical oncology*, 8(4), 189–90.

Ibarrola-Villava, M., Cervantes, A. & Bardelli, A. (2018). Preclinical Models for Precision Oncology. *Biochimica et Biophysica Acta (BBA) - Reviews on Cancer*, 1870(2), 239–246.

Jansen, S. M., Groener, J. E., Bax, W., Suter, A., Saftig, P., Somerharju, P. & Poorthuis, B. J. (2001). Biosynthesis of Phosphatidylcholine from a Phosphocholine Precursor Pool Derived from the Late Endosomal/Lysosomal Degradation of Sphingomyelin. *The Journal of biological chemistry*, 276(22), 18722–7.

Jazirehi, A. R. & Bonavida, B. (2004). Resveratrol Modifies the Expression of Apoptotic Regulatory Proteins and Sensitizes Non-Hodgkin's Lymphoma and Multiple Myeloma Cell Lines to Paclitaxel-Induced Apoptosis. *Molecular cancer therapeutics*, 3(1), 71–84.

Jung, P., Sato, T., Merlos-Suárez, A., Barriga, F. M., Iglesias, M., Rossell, D., *et al.* (2011). Isolation and in Vitro Expansion of Human Colonic Stem Cells. *Nature Medicine*, 17(10), 1225–1227.

Kaplowitz, N. (2005). Idiosyncratic Drug Hepatotoxicity. *Nature reviews. Drug discovery*, 4(6), 489–99.

Kappler, B., Anic, P., Becker, M., Bader, A., Klose, K., Klein, O., *et al.* (2016). The Cytoprotective Capacity of Processed Human Cardiac Extracellular Matrix. *Journal of Materials Science: Materials in Medicine*, 27(7), 120.

Katt, M. E., Placone, A. L., Wong, A. D., Xu, Z. S. & Searson, P. C. (2016). In Vitro Tumor Models: Advantages, Disadvantages, Variables, and Selecting the Right Platform. *Frontiers in Bioengineering and Biotechnology*, 4, 12.

Kezutyte, T., Desbenoit, N., Brunelle, A. & Briedis, V. (2013). Studying the Penetration of Fatty Acids into Human Skin by Ex Vivo TOF-SIMS Imaging. *Biointerphases*, 8(1), 3.

Khetan, S., Guvendiren, M., Legant, W. R., Cohen, D. M., Chen, C. S. & Burdick, J. A. (2013). Degradation-Mediated Cellular Traction Directs Stem Cell Fate in Covalently Crosslinked Three-Dimensional Hydrogels. *Nature materials*, 12(5), 458–65.

Khurshid, M., Mulet-Sierra, A., Adesida, A. & Sen, A. (2018). Osteoarthritic Human Chondrocytes Proliferate in 3D Co-Culture with Mesenchymal Stem Cells in Suspension Bioreactors. *Journal of Tissue Engineering and Regenerative Medicine*, 12(3), e1418–e1432.

Kim, B. S., Lee, J.-S., Gao, G. & Cho, D.-W. (2017). Direct 3D Cell-Printing of Human Skin with Functional Transwell System. *Biofabrication*, 9(2), 025034.

Kim, Y. & Rajagopalan, P. (2010). 3D Hepatic Cultures Simultaneously Maintain Primary Hepatocyte and Liver Sinusoidal Endothelial Cell Phenotypes. *PloS one*, 5(11), e15456.

Kleinman, H. K., McGarvey, M. L., Hassell, J. R., Star, V. L., Cannon, F. B., Laurie, G. W. & Martin, G. R. (1986). Basement Membrane Complexes with

Biological Activity. *Biochemistry*, 25(2), 312–8.

Knowlton, S., Yenilmez, B. & Tasoglu, S. (2016). Towards Single-Step Biofabrication of Organs on a Chip via 3D Printing. *Trends in Biotechnology*, 34(9), 685–688.

Kong, C. & Hansen, M. F. (2009). Biomarkers in Osteosarcoma. *Expert Opinion on Medical Diagnostics*, 3(1), 13–23.

Kotze, H. L., Armitage, E. G., Fletcher, J. S., Henderson, A., Williams, K. J., Lockyer, N. P. & Vickerman, J. C. (2013). ToF-SIMS as a Tool for Metabolic Profiling Small Biomolecules in Cancer Systems. *Surface and Interface Analysis*, 45(1), 277–281.

Kovac, M., Blattmann, C., Ribi, S., Smida, J., Mueller, N. S., Engert, F., *et al.* (2015). Exome Sequencing of Osteosarcoma Reveals Mutation Signatures Reminiscent of BRCA Deficiency. *Nature Communications*, 6(1), 8940.

Kuhn, D. A., Hartmann, R., Fytianos, K., Petri-Fink, A., Rothen-Rutishauser, B. & Parak, W. J. (2015). Cellular Uptake and Cell-to-Cell Transfer of Polyelectrolyte Microcapsules within a Triple Co-Culture System Representing Parts of the Respiratory Tract. *Science and Technology of Advanced Materials*, 16(3), 034608.

LaBonia, G. J., Lockwood, S. Y., Heller, A. A., Spence, D. M. & Hummon, A. B. (2016). Drug Penetration and Metabolism in 3D Cell Cultures Treated in a 3D Printed Fluidic Device: Assessment of Irinotecan via MALDI Imaging Mass Spectrometry. *Proteomics*, 16(11–12), 1814–21.

Laštovičková, M., Chmelik, J. & Bobalova, J. (2009). The Combination of Simple MALDI Matrices for the Improvement of Intact Glycoproteins and Glycans Analysis. *International Journal of Mass Spectrometry*, 281(1–2), 82–88.

Laugesen, S. & Roepstorff, P. (2003). Combination of Two Matrices Results in Improved Performance of MALDI MS for Peptide Mass Mapping and Protein Analysis. *Journal of the American Society for Mass Spectrometry*, 14(9), 992–1002.

Lawrence, J., Cameron, D. & Argyle, D. (2015). Species Differences in Tumour Responses to Cancer Chemotherapy. *Philosophical Transactions of the Royal Society B: Biological Sciences*, 370(1673), 20140233.

Leclerc, E., Hamon, J., Claude, I., Jellali, R., Naudot, M. & Bois, F. (2015). Investigation of Acetaminophen Toxicity in HepG2/C3a Microscale Cultures Using a System Biology Model of Glutathione Depletion. *Cell biology and toxicology*, 31(3), 173–85.

Ledford, H. (2011). Translational Research: 4 Ways to Fix the Clinical Trial. *Nature*, 477(7366), 526–528.

Lee, J. M., Mhawech-Fauceglia, P., Lee, N., Parsanian, L. C., Lin, Y. G., Gayther, S. A. & Lawrenson, K. (2013). A Three-Dimensional Microenvironment Alters Protein Expression and Chemosensitivity of Epithelial Ovarian Cancer Cells in Vitro. *Laboratory investigation; a journal of technical methods and pathology*, 93(5), 528–42.

Lee, V., Singh, G., Trasatti, J. P., Bjornsson, C., Xu, X., Tran, T. N., Yoo, S.-S., Dai, G. & Karande, P. (2014). Design and Fabrication of Human Skin by Three-Dimensional Bioprinting. *Tissue engineering. Part C, Methods*, 20(6), 473–84.

Leung, B. M., Lesher-Perez, S. C., Matsuoka, T., Moraes, C. & Takayama, S. (2015). Media Additives to Promote Spheroid Circularity and Compactness in Hanging Drop Platform. *Biomaterials science*, 3(2), 336–344.

Lewis, E. E. L., Barrett, M. R. T., Freeman-Parry, L., Bojar, R. A. & Clench, M. R. (2018). Examination of the Skin Barrier Repair/Wound Healing Process Using a Living Skin Equivalent Model and Matrix-Assisted Laser Desorption-Ionization-Mass Spectrometry Imaging. *International Journal of Cosmetic Science*, 40(2), 148–156.

Lhuissier, E., Bazille, C., Aury-Landas, J., Girard, N., Pontin, J., Boittin, M., Boumediene, K. & Baugé, C. (2017). Identification of an Easy to Use 3D Culture Model to Investigate Invasion and Anticancer Drug Response in Chondrosarcomas. *BMC Cancer*, 17(1), 490.

Li, H. & Hummon, A. B. (2011). Imaging Mass Spectrometry of Three-Dimensional Cell Culture Systems. *Analytical Chemistry*, 83(22), 8794–8801.

Li, W., Zhang, H., Assaraf, Y. G., Zhao, K., Xu, X., Xie, J., Yang, D.-H. & Chen, Z.-S. (2016). Overcoming ABC Transporter-Mediated Multidrug Resistance: Molecular Mechanisms and Novel Therapeutic Drug Strategies. *Drug Resistance Updates*, 27, 14–29.

Liebler, D. C., Meredith, M. J. & Guengerich, F. P. (1985). Formation of Glutathione Conjugates by Reactive Metabolites of Vinylidene Chloride in Microsomes and Isolated Hepatocytes. *Cancer research*, 45(1), 186–93.

Lim, F. & Sun, A. M. (1980). Microencapsulated Islets as Bioartificial Endocrine Pancreas. *Science (New York, N.Y.)*, 210(4472), 908–910.

Lin, L.-E., Su, P.-R., Wu, H.-Y. & Hsu, C.-C. (2018). A Simple Sonication Improves Protein Signal in Matrix-Assisted Laser Desorption Ionization Imaging. *Journal of The American Society for Mass Spectrometry*, 29(4), 796–799.

Lin, X.-M., Hu, L., Gu, J., Wang, R.-Y., Li, L., Tang, J., *et al.* (2017). Choline Kinase α Mediates Interactions Between the Epidermal Growth Factor Receptor and Mechanistic Target of Rapamycin Complex 2 in Hepatocellular Carcinoma Cells to Promote Drug Resistance and Xenograft Tumor Progression. *Gastroenterology*, 152(5), 1187–1202.

Liston, D. R. & Davis, M. (2017). Clinically Relevant Concentrations of Anticancer Drugs: A Guide for Nonclinical Studies. *Clinical Cancer Research*, 23(14), 3489–3498.

Liu, W., Xu, J., Li, T., Zhao, L., Ma, C., Shen, S. & Wang, J. (2015). Monitoring Tumor Response to Anticancer Drugs Using Stable Three-Dimensional Culture in a Recyclable Microfluidic Platform. *Analytical Chemistry*, 87(19), 9752–9760.

Liu, X., Flinders, C., Mumenthaler, S. M. & Hummon, A. B. (2018). MALDI Mass Spectrometry Imaging for Evaluation of Therapeutics in Colorectal Tumor Organoids. *Journal of The American Society for Mass Spectrometry*, 29(3),

516–526.

Lorvellec, M., Scottoni, F., Crowley, C., Fiadeiro, R., Maghsoudlou, P., Pellegata, A. F., *et al.* (2017). Mouse Decellularised Liver Scaffold Improves Human Embryonic and Induced Pluripotent Stem Cells Differentiation into Hepatocyte-like Cells (G. D. Almeida-Porada, Ed.). *PLOS ONE*, 12(12), e0189586.

Lou, S., Balluff, B., de Graaff, M. A., Cleven, A. H. G., Briaire - de Bruijn, I., Bovée, J. V. M. G. & McDonnell, L. A. (2016). High-Grade Sarcoma Diagnosis and Prognosis: Biomarker Discovery by Mass Spectrometry Imaging. *PROTEOMICS*, 16(11–12), 1802–1813.

Lu, L., Hu, Z., Xu, X., Lv, D. & Lu, H. (2017). Three- dimensional Cell Culture: A Powerful Tool in Tumor Research and Drug Discovery (Review). *Oncology Letters*, 14(6), 6999–7010.

Luger, K., Mäder, A. W., Richmond, R. K., Sargent, D. F. & Richmond, T. J. (1997). Crystal Structure of the Nucleosome Core Particle at 2.8 Å Resolution. *Nature*, 389(6648), 251–260.

Lukowski, J. K., Weaver, E. M. & Hummon, A. B. (2017). Analyzing Liposomal Drug Delivery Systems in Three-Dimensional Cell Culture Models Using MALDI Imaging Mass Spectrometry. *Analytical Chemistry*, 89(16), 8453–8458.

Ly, A., Buck, A., Balluff, B., Sun, N., Gorzolka, K., Feuchtinger, A., *et al.* (2016). High-Mass-Resolution MALDI Mass Spectrometry Imaging of Metabolites from Formalin-Fixed Paraffin-Embedded Tissue. *Nature Protocols*, 11(8), 1428–1443.

Machado, I., Navarro, S., Picci, P. & Llombart-Bosch, A. (2016). The Utility of SATB2 Immunohistochemical Expression in Distinguishing between Osteosarcomas and Their Malignant Bone Tumor Mimickers, Such as Ewing Sarcomas and Chondrosarcomas. *Pathology - Research and Practice*, 212(9), 811–816.

Magin, C. M., Alge, D. L. & Anseth, K. S. (2016). Bio-Inspired 3D

Microenvironments: A New Dimension in Tissue Engineering. *Biomedical Materials*, 11(2), 022001.

Manning, L. S., Berger, J. D., O'Donoghue, H. L., Sheridan, G. N., Claringbold, P. G. & Turner, J. H. (1992). A Model of Multiple Myeloma: Culture of 5T33 Murine Myeloma Cells and Evaluation of Tumorigenicity in the C57BL/KaLwRij Mouse. *British journal of cancer*, 66(6), 1088–93.

Martin, J. W., Squire, J. A. & Zielenska, M. (2012). The Genetics of Osteosarcoma. *Sarcoma*, 2012, 1–11.

Mazzucchelli, S., Ravelli, A., Gigli, F., Minoli, M., Corsi, F., Ciuffreda, P. & Ottria, R. (2017). LC-MS/MS Method Development for Quantification of Doxorubicin and Its Metabolite 13-Hydroxy Doxorubicin in Mice Biological Matrices: Application to a Pharmaco-Delivery Study. *Biomedical Chromatography*, 31(4), e3863.

McDonnell, L. A., Angel, P. M., Lou, S. & Drake, R. R. (2017). Mass Spectrometry Imaging in Cancer Research: Future Perspectives. *Advances in Cancer Research*, 134, 283–290.

McGill, M. R. & Jaeschke, H. (2013). Metabolism and Disposition of Acetaminophen: Recent Advances in Relation to Hepatotoxicity and Diagnosis. *Pharmaceutical Research*, 30(9), 2174–2187.

McGill, M. R., Sharpe, M. R., Williams, C. D., Taha, M., Curry, S. C. & Jaeschke, H. (2012). The Mechanism Underlying Acetaminophen-Induced Hepatotoxicity in Humans and Mice Involves Mitochondrial Damage and Nuclear DNA Fragmentation. *The Journal of clinical investigation*, 122(4), 1574–83.

McMillan, K. S., Boyd, M. & Zagnoni, M. (2016). Transitioning from Multi-Phase to Single-Phase Microfluidics for Long-Term Culture and Treatment of Multicellular Spheroids. *Lab on a chip*, 16(18), 3548–57.

Mehling, M. & Tay, S. (2014). Microfluidic Cell Culture. *Current opinion in biotechnology*, 25, 95–102.

Meijer, T. G., Naipal, K. A., Jager, A. & van Gent, D. C. (2017). Ex Vivo Tumor Culture Systems for Functional Drug Testing and Therapy Response Prediction. *Future Science OA*, 3(2), FSO190.

Ménade, M., Kozlov, G., Trempe, J.-F., Pande, H., Shenker, S., Wickremasinghe, S., *et al.* (2018). Structures of Ubiquitin-like (Ubl) and Hsp90-like Domains of Sacsin Provide Insight into Pathological Mutations. *The Journal of biological chemistry*, 293(33), 12832–12842.

Mirzaei, H., McBee, J. K., Watts, J. & Aebersold, R. (2008). Comparative Evaluation of Current Peptide Production Platforms Used in Absolute Quantification in Proteomics. *Molecular & Cellular Proteomics*, 7(4), 813–823.

Mitchell, C. A., Long, H., Donaldson, M., Francese, S. & Clench, M. R. (2015). Lipid Changes within the Epidermis of Living Skin Equivalents Observed across a Time-Course by MALDI-MS Imaging and Profiling. *Lipids in Health and Disease*, 14(1), 84.

Modulevsky, D. J., Cuerrier, C. M. & Pelling, A. E. (2016). Biocompatibility of Subcutaneously Implanted Plant-Derived Cellulose Biomaterials. *PLoS ONE*, 11(6), e0157894.

Moffat, K. L., Goon, K., Moutos, F. T., Estes, B. T., Oswald, S. J., Zhao, X. & Guilak, F. (2018). Composite Cellularized Structures Created from an Interpenetrating Polymer Network Hydrogel Reinforced by a 3D Woven Scaffold. *Macromolecular Bioscience*, 1800140.

Mohan, P. & Rapoport, N. (2010). Doxorubicin as a Molecular Nanotheranostic Agent: Effect of Doxorubicin Encapsulation in Micelles or Nanoemulsions on the Ultrasound-Mediated Intracellular Delivery and Nuclear Trafficking. *Molecular Pharmaceutics*, 7(6), 1959–1973.

Molina-Ortiz, D., Camacho-Carranza, R., González-Zamora, J. F., Shalkow-Kalincovstein, J., Cárdenas-Cardós, R., Ností-Palacios, R. & Vences-Mejía, A. (2014). Differential Expression of Cytochrome P450 Enzymes in Normal and Tumor Tissues from Childhood Rhabdomyosarcoma (A. W. Lo, Ed.).

PLoS ONE, 9(4), e93261.

Moraleja, I., Mena, M. L., Lázaro, A., Neumann, B., Tejedor, A., Jakubowski, N., Gómez-Gómez, M. M. & Esteban-Fernández, D. (2018). An Approach for Quantification of Platinum Distribution in Tissues by LA-ICP-MS Imaging Using Isotope Dilution Analysis. *Talanta*, 178, 166–171.

Morgan, P., Brown, D. G., Lennard, S., Anderton, M. J., Barrett, J. C., Eriksson, U., *et al.* (2018). Impact of a Five-Dimensional Framework on R&D Productivity at AstraZeneca. *Nature Reviews Drug Discovery*, 17(3), 167–181.

Mosedale, M. & Watkins, P. (2017). Drug-Induced Liver Injury: Advances in Mechanistic Understanding That Will Inform Risk Management. *Clinical Pharmacology & Therapeutics*, 101(4), 469–480.

Moser, A. R., Luongo, C., Gould, K. A., McNeley, M. K., Shoemaker, A. R. & Dove, W. F. (1995). ApcMin: A Mouse Model for Intestinal and Mammary Tumorigenesis. *European journal of cancer*, 31A(7–8), 1061–4.

Murphy, M. E. (2013). The HSP70 Family and Cancer. *Carcinogenesis*, 34(6), 1181–8.

Nagelkerke, A., Bussink, J., Sweep, F. C. G. J. & Span, P. N. (2013). Generation of Multicellular Tumor Spheroids of Breast Cancer Cells: How to Go Three-Dimensional. *Analytical biochemistry*, 437(1), 17–9.

Nath, S. & Devi, G. R. (2016). Three-Dimensional Culture Systems in Cancer Research: Focus on Tumor Spheroid Model. *Pharmacology & Therapeutics*, 163, 94–108.

Nelson, K. A., Daniels, G. J., Fournie, J. W. & Hemmer, M. J. (2013). Optimization of Whole-Body Zebrafish Sectioning Methods for Mass Spectrometry Imaging. *Journal of biomolecular techniques : JBT*, 24(3), 119–27.

Nelson, L. J., Morgan, K., Treskes, P., Samuel, K., Henderson, C. J., LeBled, C., *et al.* (2017). Human Hepatic HepaRG Cells Maintain an Organotypic Phenotype with High Intrinsic CYP450 Activity/Metabolism and Significantly

Outperform Standard HepG2/C3A Cells for Pharmaceutical and Therapeutic Applications. *Basic & Clinical Pharmacology & Toxicology*, 120(1), 30–37.

Nguyen, D. G., Funk, J., Robbins, J. B., Crogan-Grundy, C., Presnell, S. C., Singer, T. & Roth, A. B. (2016). Bioprinted 3D Primary Liver Tissues Allow Assessment of Organ-Level Response to Clinical Drug Induced Toxicity In Vitro (L. A. van Grunsven, Ed.). *PLOS ONE*, 11(7), e0158674.

Niehaus, M. & Soltwisch, J. (2018). New Insights into Mechanisms of Material Ejection in MALDI Mass Spectrometry for a Wide Range of Spot Sizes. *Scientific Reports*, 8(1), 7755.

Niehoff, A.-C., Grünebaum, J., Moosmann, A., Mulac, D., Söbbing, J., Niehaus, R., *et al.* (2016). Quantitative Bioimaging of Platinum Group Elements in Tumor Spheroids. *Analytica Chimica Acta*, 938, 106–113.

Niehoff, A.-C., Moosmann, A., Söbbing, J., Wiehe, A., Mulac, D., Wehe, C. A., *et al.* (2014). A Palladium Label to Monitor Nanoparticle-Assisted Drug Delivery of a Photosensitizer into Tumor Spheroids by Elemental Bioimaging. *Metallomics : integrated biometal science*, 6(1), 77–81.

Nilsson, A., Peric, A., Strimfors, M., Goodwin, R. J. A., Hayes, M. A., Andrén, P. E. & Hilgendorf, C. (2017). Mass Spectrometry Imaging Proves Differential Absorption Profiles of Well-Characterised Permeability Markers along the Crypt-Villus Axis. *Scientific Reports*, 7(1), 6352.

Nunes, A. S., Barros, A. S., Costa, E. C., Moreira, A. F. & Correia, I. J. (2019). 3D Tumor Spheroids as in Vitro Models to Mimic in Vivo Human Solid Tumors Resistance to Therapeutic Drugs. *Biotechnology and Bioengineering*, 116(1), 206–226.

Van oosterwijk, J. G., Herpers, B., Meijer, D., Briaire-de bruijn, I. H., Cleton-jansen, A. M., Gelderblom, H., Van de water, B. & Bée, J. V. M. G. (2012). Restoration of Chemosensitivity for Doxorubicin and Cisplatin in Chondrosarcoma in Vitro: BCL-2 Family Members Cause Chemoresistance. *Annals of Oncology*, 23(6), 1617–1626.

Ortega-Prieto, A. M., Skelton, J. K., Wai, S. N., Large, E., Lussignol, M., Vizcay-

Barrena, G., *et al.* (2018). 3D Microfluidic Liver Cultures as a Physiological Preclinical Tool for Hepatitis B Virus Infection. *Nature Communications*, 9(1), 682.

Otieno, M. A., Gan, J. & Proctor, W. (2018). Status and Future of 3D Cell Culture in Toxicity Testing, in: (pp. 249–261). Humana Press, New York, NY.

Pampaloni, F., Reynaud, E. G. & Stelzer, E. H. K. (2007). The Third Dimension Bridges the Gap between Cell Culture and Live Tissue. *Nature reviews. Molecular cell biology*, 8(10), 839–45.

Parfitt, D. A., Michael, G. J., Vermeulen, E. G. M., Prodromou, N. V., Webb, T. R., Gallo, J.-M., *et al.* (2009). The Ataxia Protein Sacsin Is a Functional Co-Chaperone That Protects against Polyglutamine-Expanded Ataxin-1. *Human Molecular Genetics*, 18(9), 1556–1565.

Pasello, M., Michelacci, F., Scionti, I., Hattinger, C. M., Zuntini, M., Caccuri, A. M., Scotlandi, K., Picci, P. & Serra, M. (2008). Overcoming Glutathione S-Transferase P1-Related Cisplatin Resistance in Osteosarcoma. *Cancer Research*, 68(16), 6661–6668.

Passarelli, M. K., Newman, C. F., Marshall, P. S., West, A., Gilmore, I. S., Bunch, J., Alexander, M. R. & Dollery, C. T. (2015). Single-Cell Analysis: Visualizing Pharmaceutical and Metabolite Uptake in Cells with Label-Free 3D Mass Spectrometry Imaging. *Analytical Chemistry*, 87(13), 6696–6702.

Patel, E. (2017). Fresh Frozen Versus Formalin-Fixed Paraffin Embedded for Mass Spectrometry Imaging, in: (pp. 7–14). Humana Press, New York, NY.

Pereira, P. M. R., Berisha, N., Bhupathiraju, N. V. S. D. K., Fernandes, R., Tomé, J. P. C. & Drain, C. M. (2017). Cancer Cell Spheroids Are a Better Screen for the Photodynamic Efficiency of Glycosylated Photosensitizers. *PloS one*, 12(5), e0177737.

Pickup, M. W., Mouw, J. K. & Weaver, V. M. (2014). The Extracellular Matrix Modulates the Hallmarks of Cancer. *EMBO reports*, 15(12), 1243–1253.

Pietrowska, M., Gawin, M., Polanska, J. & Widlak, P. (2016). Tissue Fixed with

Formalin and Processed without Paraffin Embedding Is Suitable for Imaging of Both Peptides and Lipids by MALDI-IMS. *Proteomics*, 16(11–12), 1670–1677.

Piga, I., Heijs, B., Nicolardi, S., Giusti, L., Marselli, L., Marchetti, P., Mazzoni, M. R., Lucacchini, A. & McDonnell, L. A. (2019). Ultra-High Resolution MALDI-FTICR-MSI Analysis of Intact Proteins in Mouse and Human Pancreas Tissue. *International Journal of Mass Spectrometry*, 437, 10–16.

Pinheiro, J. & Bates, D. (2011). Linear and Nonlinear Mixed Effects Models (Nlme). *Package of the R software for statistical computing on the CRAN repository.*

Poh, A. (2016). Novartis Compiles Mouse Avatar 'Encyclopedia'. *Cancer discovery*, 6(1), 5–6.

Pradelli, L. A., Villa, E., Zunino, B., Marchetti, S. & Ricci, J.-E. (2014). Glucose Metabolism Is Inhibited by Caspases upon the Induction of Apoptosis. *Cell Death & Disease*, 5(9), e1406–e1406.

Prideaux, B., ElNaggar, M. S., Zimmerman, M., Wiseman, J. M., Li, X. & Dartois, V. (2015). Mass Spectrometry Imaging of Levofloxacin Distribution in TB-Infected Pulmonary Lesions by MALDI-MSI and Continuous Liquid Microjunction Surface Sampling. *International Journal of Mass Spectrometry*, 377, 699–708.

Qi, L., Knapton, E. K., Zhang, X., Zhang, T., Gu, C. & Zhao, Y. (2017). Pre-Culture Sudan Black B Treatment Suppresses Autofluorescence Signals Emitted from Polymer Tissue Scaffolds. *Scientific Reports*, 7(1), 8361.

R Core Team. (2017). R: A Language and Environment for Statistical Computing. *R Foundation for Statistical Computing*, 2(09/18/2009), ISBN 3-900051-07-0.

Ramaiahgari, S. C., den Braver, M. W., Herpers, B., Terpstra, V., Commandeur, J. N. M., van de Water, B. & Price, L. S. (2014). A 3D in Vitro Model of Differentiated HepG2 Cell Spheroids with Improved Liver-like Properties for Repeated Dose High-Throughput Toxicity Studies. *Archives of Toxicology*,

88(5), 1083–95.

Rangarajan, A. & Weinberg, R. A. (2003). Comparative Biology of Mouse versus Human Cells: Modelling Human Cancer in Mice. *Nature Reviews Cancer*, 3(12), 952–959.

Rankin, E. B. & Giaccia, A. J. (2016). Hypoxic Control of Metastasis. *Science*, 352(6282), 175–180.

Ravi, M., Paramesh, V., Kaviya, S. R., Anuradha, E. & Solomon, F. D. P. (2015). 3D Cell Culture Systems: Advantages and Applications. *Journal of Cellular Physiology*, 230(1), 16–26.

Ravi, M., Ramesh, A. & Pattabhi, A. (2017). Contributions of 3D Cell Cultures for Cancer Research. *Journal of Cellular Physiology*, 232(10), 2679–2697.

Rebelo, S. P., Costa, R., Estrada, M., Shevchenko, V., Brito, C. & Alves, P. M. (2014). HepaRG Microencapsulated Spheroids in DMSO-Free Culture: Novel Culturing Approaches for Enhanced Xenobiotic and Biosynthetic Metabolism. *Archives of Toxicology*, 89(8), 1347–58.

Rehman, M. & Tamagnone, L. (2013). Semaphorins in Cancer: Biological Mechanisms and Therapeutic Approaches. *Seminars in Cell & Developmental Biology*, 24(3), 179–189.

Rimann, M. & Graf-Hausner, U. (2012). Synthetic 3D Multicellular Systems for Drug Development. *Current opinion in biotechnology*, 23(5), 803–9.

Rimann, M., Laternser, S., Gvozdenovic, A., Muff, R., Fuchs, B., Kelm, J. M. & Graf-Hausner, U. (2014). An in Vitro Osteosarcoma 3D Microtissue Model for Drug Development. *Journal of biotechnology*, 189, 129–35.

Riss, T. L., Moravec, R. A., Niles, A. L., Duellman, S., Benink, H. A., Worzella, T. J. & Minor, L. (2004). *Eli Lilly & Company and the National Center for Advancing Translational Sciences*. Eli Lilly & Company and the National Center for Advancing Translational Sciences.

Robinson, K. N., Steven, R. T. & Bunch, J. (2018). Matrix Optical Absorption in UV-MALDI MS. *Journal of The American Society for Mass Spectrometry*,

29(3), 501–511.

Rodenhizer, D., Cojocari, D., Wouters, B. G. & McGuigan, A. P. (2016). Development of TRACER: Tissue Roll for Analysis of Cellular Environment and Response. *Biofabrication*, 8(4), 045008.

Rodenhizer, D., Gaude, E., Cojocari, D., Mahadevan, R., Frezza, C., Wouters, B. G. & McGuigan, A. P. (2015). A Three-Dimensional Engineered Tumour for Spatial Snapshot Analysis of Cell Metabolism and Phenotype in Hypoxic Gradients. *Nature Materials*, 15(2), 227–234.

Rodrigues, T., Kundu, B., Silva-Correia, J., Kundu, S. C., Oliveira, J. M., Reis, R. L. & Correlo, V. M. (2018). Emerging Tumor Spheroids Technologies for 3D in Vitro Cancer Modeling. *Pharmacology and Therapeutics*, 184, 201–211.

Roerink, S. F., Sasaki, N., Lee-Six, H., Young, M. D., Alexandrov, L. B., Behjati, S., *et al.* (2018). Intra-Tumour Diversification in Colorectal Cancer at the Single-Cell Level. *Nature*, 556(7702), 457–462.

Romero, I., Garrido, C., Algarra, I., Chamorro, V., Collado, A., Garrido, F. & Garcia-Lora, A. M. (2018). MHC Intratumoral Heterogeneity May Predict Cancer Progression and Response to Immunotherapy. *Frontiers in Immunology*, 9(JAN), 102.

Roncuzzi, L., Pancotti, F. & Baldini, N. (2014). Involvement of HIF-1alpha Activation in the Doxorubicin Resistance of Human Osteosarcoma Cells. *Oncology reports*, 32(1), 389–394.

Rowinsky, E. (2003). The Vinca Alkaloids (D. Kufe, R. Pollock, R. Weichselbaum, and et al., Eds.). *Holland-Frei Cancer Medicine*.

Russell WMS, B. K. (1992). The Principles of Humane Experimental Technique. *UFAW, London*, (October 1959), Available from: http://altweb. jhsph.edu/.

Russo, C., Lewis, E. E. L., Flint, L. & Clench, M. R. (2018). Mass Spectrometry Imaging of 3D Tissue Models. *Proteomics*, 18(14), 1700462.

Rye, I., Helland, Å., Sætersdal, A., Naume, B., Almendro, V., Polyak, K., Børessen-Dale, A.-L. & Russnes, H. (2012). Abstract P3-05-04: Intra-Tumor

Heterogeneity as a Predictor of Therapy Response in HER2 Positive Breast Cancer. *Cancer Research*, 72(24 Supplement), P3-05-04-P3-05–04.

Sachs, N., de Ligt, J., Kopper, O., Gogola, E., Bounova, G., Weeber, F., *et al.* (2018). A Living Biobank of Breast Cancer Organoids Captures Disease Heterogeneity. *Cell*, 172(1–2), 373–386.e10.

Sagawa, K., Li, F., Liese, R. & Sutton, S. C. (2009). Fed and Fasted Gastric PH and Gastric Residence Time in Conscious Beagle Dogs. *Journal of Pharmaceutical Sciences*, 98(7), 2494–2500.

Salah, Z., Arafeh, R., Maximov, V., Galasso, M., Khawaled, S., Abou-Sharieha, S., *et al.* (2015). MiR-27a and MiR-27a* Contribute to Metastatic Properties of Osteosarcoma Cells. *Oncotarget*, 6(7), 4920–35.

Saldin, L. T., Cramer, M. C., Velankar, S. S., White, L. J. & Badylak, S. F. (2017). Extracellular Matrix Hydrogels from Decellularized Tissues: Structure and Function. *Acta Biomaterialia*, 49, 1–15.

Sarkar, D. (2008). Scatter Plots and Extensions, in: *Lattice*, (pp. 67–90). New York, NY: Springer New York.

Sarkar, U., Ravindra, K. C., Large, E., Young, C. L., Rivera-Burgos, D., Yu, J., *et al.* (2017). Integrated Assessment of Diclofenac Biotransformation, Pharmacokinetics, and Omics-Based Toxicity in a Three-Dimensional Human Liver-Immunocompetent Coculture System. *Drug metabolism and disposition: the biological fate of chemicals*, 45(7), 855–866.

Sart, S., Tomasi, R. F.-X., Amselem, G. & Baroud, C. N. (2017). Multiscale Cytometry and Regulation of 3D Cell Cultures on a Chip. *Nature Communications*, 8(1), 469.

Sawicki, L. A., Choe, L. H., Wiley, K. L., Lee, K. H. & Kloxin, A. M. (2018). Isolation and Identification of Proteins Secreted by Cells Cultured within Synthetic Hydrogel-Based Matrices. *ACS biomaterials science & engineering*, 4(3), 836–845.

Schmid, J., Schwarz, S., Meier-Staude, R., Sudhop, S., Clausen-Schaumann, H.,

Schieker, M. & Huber, R. (2018). A Perfusion Bioreactor System for Cell Seeding and Oxygen-Controlled Cultivation of Three-Dimensional Cell Cultures. *Tissue engineering. Part C, Methods*, 24(10), 585–595.

Schultz, M. J., Holdbrooks, A. T., Chakraborty, A., Grizzle, W. E., Landen, C. N., Buchsbaum, D. J., *et al.* (2016). The Tumor-Associated Glycosyltransferase ST6Gal-I Regulates Stem Cell Transcription Factors and Confers a Cancer Stem Cell Phenotype. *Cancer Research*, 76(13), 3978–3988.

Schulz, S., Becker, M., Groseclose, M. R., Schadt, S. & Hopf, C. (2019). Advanced MALDI Mass Spectrometry Imaging in Pharmaceutical Research and Drug Development. *Current Opinion in Biotechnology*, 55, 51–59.

Senkowski, W., Jarvius, M., Rubin, J., Lengqvist, J., Gustafsson, M. G., Nygren, P., Kultima, K., Larsson, R. & Fryknäs, M. (2016). Large-Scale Gene Expression Profiling Platform for Identification of Context-Dependent Drug Responses in Multicellular Tumor Spheroids. *Cell chemical biology*, 23(11), 1428–1438.

Seo, J., Shin, J.-Y., Leijten, J., Jeon, O., Camci-Unal, G., Dikina, A. D., *et al.* (2018). High-Throughput Approaches for Screening and Analysis of Cell Behaviors. *Biomaterials*, 153, 85–101.

Sgodda, M., Dai, Z., Zweigerdt, R., Sharma, A. D., Ott, M. & Cantz, T. (2017). A Scalable Approach for the Generation of Human Pluripotent Stem Cell-Derived Hepatic Organoids with Sensitive Hepatotoxicity Features. *Stem Cells and Development*, 26(20), 1490–1504.

Shamir, E. R. & Ewald, A. J. (2014). Three-Dimensional Organotypic Culture: Experimental Models of Mammalian Biology and Disease. *Nature Reviews Molecular Cell Biology*, 15(10), 647–664.

Sharma, N. S., Nagrath, D. & Yarmush, M. L. (2010). Adipocyte-Derived Basement Membrane Extract with Biological Activity: Applications in Hepatocyte Functional Augmentation in Vitro. *FASEB journal : official publication of the Federation of American Societies for Experimental Biology*, 24(7), 2364–74.

Sharma, U., Pal, D. & Prasad, R. (2014). Alkaline Phosphatase: An Overview. *Indian journal of clinical biochemistry : IJCB*, 29(3), 269–78.

Shieh, H. F., Graham, C. D., Brazzo, J. A., Zurakowski, D. & Fauza, D. O. (2017). Comparisons of Human Amniotic Mesenchymal Stem Cell Viability in FDA-Approved Collagen-Based Scaffolds: Implications for Engineered Diaphragmatic Replacement. *Journal of Pediatric Surgery*, 52(6), 1010–1013.

Shih, H.-P., Zhang, X. & Aronov, A. M. (2017). Drug Discovery Effectiveness from the Standpoint of Therapeutic Mechanisms and Indications. *Nature Reviews Drug Discovery*, 17(1), 19–33.

Shin, H.-S., Hong, H. J., Koh, W.-G. & Lim, J.-Y. (2018). Organotypic 3D Culture in Nanoscaffold Microwells Supports Salivary Gland Stem-Cell-Based Organization. *ACS biomaterials science & engineering*, 4(12), 4311–4320.

Shri, M., Agrawal, H., Rani, P., Singh, D. & Onteru, S. K. (2017). Hanging Drop, A Best Three-Dimensional (3D) Culture Method for Primary Buffalo and Sheep Hepatocytes. *Scientific Reports*, 7(1), 1203.

Sitarski, A. M., Fairfield, H., Falank, C. & Reagan, M. R. (2018). 3D Tissue Engineered in Vitro Models of Cancer in Bone. *ACS Biomaterials Science & Engineering*, 4(2), 324–336.

Smietana, K., Ekstrom, L., Jeffery, B. & Møller, M. (2015). Improving R and D Productivity. *Nature Reviews Drug Discovery*, 14(7), 455–456.

Sokol, E. S., Miller, D. H., Breggia, A., Spencer, K. C., Arendt, L. M. & Gupta, P. B. (2016). Growth of Human Breast Tissues from Patient Cells in 3D Hydrogel Scaffolds. *Breast Cancer Research*, 18(1), 19.

Soltwisch, J., Kettling, H., Vens-Cappell, S., Wiegelmann, M., Müthing, J. & Dreisewerd, K. (2015). Mass Spectrometry Imaging with Laser-Induced Postionization. *Science (New York, N.Y.)*, 348(6231), 211–5.

Spengler, B. (1994). Ion Imaging and Confocal Microscopy with a New Scanning UV- Laser Microprobe, in: 42nd Annual Conference on Mass Spectrometry

and Allied Topics, Chicago, Illinois.

Spraggins, J. M., Rizzo, D. G., Moore, J. L., Noto, M. J., Skaar, E. P. & Caprioli, R. M. (2016). Next-Generation Technologies for Spatial Proteomics: Integrating Ultra-High Speed MALDI-TOF and High Mass Resolution MALDI FTICR Imaging Mass Spectrometry for Protein Analysis. *PROTEOMICS*, 16(11–12), 1678–1689.

Stadler, M., Dolznig, H., Pudelko, K., Unger, C., Kenner, L., Kramer, N., *et al.* (2016). Comparison of Cancer Cells in 2D vs 3D Culture Reveals Differences in AKT-MTOR-S6K Signaling and Drug Response. *Journal of cell science*, 130(1), 203–218.

Stock, K., Estrada, M. F., Vidic, S., Gjerde, K., Rudisch, A., Santo, V. E., *et al.* (2016). Capturing Tumor Complexity in Vitro: Comparative Analysis of 2D and 3D Tumor Models for Drug Discovery. *Scientific Reports*, 6(1), 28951.

Straubinger, R. (1996). Biopharmaceutics of Paclitaxel (Taxol): Formulation, Activity and Pharmacokinetics, in: *Taxol: Science and Applications*, (pp. 237–254).

Strohalm, M., Kavan, D., Novák, P., Volný, M. & Havlíček, V. (2010). MMass 3: A Cross-Platform Software Environment for Precise Analysis of Mass Spectrometric Data. *Analytical Chemistry*, 82(11), 4648–4651.

Sultan, F. & Ganaie, B. A. (2018). Comparative Oncology: Integrating Human and Veterinary Medicine. *Open veterinary journal*, 8(1), 25–34.

Sun, N., Fernandez, I. E., Wei, M., Wu, Y., Aichler, M., Eickelberg, O. & Walch, A. (2016). Pharmacokinetic and Pharmacometabolomic Study of Pirfenidone in Normal Mouse Tissues Using High Mass Resolution MALDI-FTICR-Mass Spectrometry Imaging. *Histochemistry and Cell Biology*, 145(2), 201–211.

Tacar, O., Sriamornsak, P. & Dass, C. R. (2013). Doxorubicin: An Update on Anticancer Molecular Action, Toxicity and Novel Drug Delivery Systems. *Journal of Pharmacy and Pharmacology*, 65(2), 157–170.

Takahashi, Y., Hori, Y., Yamamoto, T., Urashima, T., Ohara, Y. & Tanaka, H.

(2015). Three-Dimensional (3D) Spheroid Cultures Improve the Metabolic Gene Expression Profiles of HepaRG Cells. *Bioscience Reports*, 35(3), e00208.

Takebe, T., Sekine, K., Enomura, M., Koike, H., Kimura, M., Ogaeri, T., *et al.* (2013). Vascularized and Functional Human Liver from an IPSC-Derived Organ Bud Transplant. *Nature*, 499(7459), 481–484.

Takebe, T., Zhang, B. & Radisic, M. (2017). Cell Stem Cell Forum Synergistic Engineering: Organoids Meet Organs-on-a-Chip Organoid Technology and Organ-on-A. *Stem Cell*, 21, 297–300.

Tang, M., Chen, W., Liu, J., Weir, M. D., Cheng, L. & Xu, H. H. K. (2013). Human Induced Pluripotent Stem Cell-Derived Mesenchymal Stem Cell Seeding on Calcium Phosphate Scaffold for Bone Regeneration. *Tissue Engineering Part A*, 20(7–8), 1295–1305.

Tapias, L. F., Gilpin, S. E., Ren, X., Wei, L., Fuchs, B. C., Tanabe, K. K., Lanuti, M. & Ott, H. C. (2015). Assessment of Proliferation and Cytotoxicity in a Biomimetic Three-Dimensional Model of Lung Cancer. *The Annals of thoracic surgery*, 100(2), 414–21.

Teicher, B. A. (2012). Searching for Molecular Targets in Sarcoma. *Biochemical Pharmacology*, 84(1), 1–10.

Temple, R. (2001). Drug-Induced Liver Injury Impacts on the Food and Drug Administration (FDA), in: *Drug-Induced Liver Injury: A National and Global Problem. FDA, PhaRMA, AALSD Conference 12-13 February*. Center for Drug Evaluation and Research.

The ESMO/European Sarcoma Network Working Group. (2015). Bone Sarcomas: ESMO Clinical Practice Guidelines. *Annals of Oncology*, 26(suppl_5), v174–v177.

Thomsen, A. R., Aldrian, C., Bronsert, P., Thomann, Y., Nanko, N., Melin, N., *et al.* (2018). A Deep Conical Agarose Microwell Array for Adhesion Independent Three-Dimensional Cell Culture and Dynamic Volume Measurement. *Lab on a Chip*, 18(1), 179–189.

Thorpe, A. A., Boyes, V. L., Sammon, C. & Le Maitre, C. L. (2016). Thermally Triggered Injectable Hydrogel, Which Induces Mesenchymal Stem Cell Differentiation to Nucleus Pulposus Cells: Potential for Regeneration of the Intervertebral Disc. *Acta Biomaterialia*, 36, 99–111.

Thorpe, A. A., Freeman, C., Farthing, P., Hatton, P., Brook, I., Sammon, C. & Le Maitre, C. (2016). Osteogenic Differentiation of Human Mesenchymal Stem Cells in Hydroxyapatite Loaded Thermally Triggered, Injectable Hydrogel Scaffolds to Promote Repair and Regeneration of Bone Defects. *Frontiers in Bioengineering and Biotechnology*, 4, 2–3.

Thorpe, A., Freeman, C., Farthing, P., Callaghan, J., Hatton, P. V., Brook, I. M., Sammon, C. & Le Maitre, C. L. (2018). In Vivo Safety and Efficacy Testing of a Thermally Triggered Injectable Hydrogel Scaffold for Bone Regeneration and Augmentation in a Rat Model. *Oncotarget*, 9(26), 18277–18295.

Tian, H., Sparvero, L. J., Blenkinsopp, P., Amoscato, A. A., Watkins, S. C., Bayır, H., Kagan, V. E. & Winograd, N. (2019). Secondary-Ion Mass Spectrometry Images Cardiolipins and Phosphatidylethanolamines at the Subcellular Level. *Angewandte Chemie*, 131(10), 3188–3193.

Tibbitt, M. W. & Anseth, K. S. (2009). Hydrogels as Extracellular Matrix Mimics for 3D Cell Culture. *Biotechnology and bioengineering*, 103(4), 655–63.

Tillner, J., Wu, V., Jones, E. A., Pringle, S. D., Karancsi, T., Dannhorn, A., Veselkov, K., McKenzie, J. S. & Takats, Z. (2017). Faster, More Reproducible DESI-MS for Biological Tissue Imaging. *Journal of The American Society for Mass Spectrometry*, 28(10), 2090–2098.

Tixier, F., Le Rest, C. C., Hatt, M., Albarghach, N., Pradier, O., Metges, J.-P., Corcos, L. & Visvikis, D. (2011). Intratumor Heterogeneity Characterized by Textural Features on Baseline 18F-FDG PET Images Predicts Response to Concomitant Radiochemotherapy in Esophageal Cancer. *Journal of Nuclear Medicine*, 52(3), 369–378.

Trietsch, S. J., Naumovska, E., Kurek, D., Setyawati, M. C., Vormann, M. K., Wilschut, K. J., *et al.* (2017). Membrane-Free Culture and Real-Time Barrier

Integrity Assessment of Perfused Intestinal Epithelium Tubes. *Nature Communications*, 8(1), 262.

Trim, P. J., Djidja, M.-C., Atkinson, S. J., Oakes, K., Cole, L. M., Anderson, D. M. G., Hart, P. J., Francese, S. & Clench, M. R. (2010). Introduction of a 20 KHz Nd:YVO4 Laser into a Hybrid Quadrupole Time-of-Flight Mass Spectrometer for MALDI-MS Imaging. *Analytical and Bioanalytical Chemistry*, 397(8), 3409–3419.

Tung, Y.-C., Lee, C.-H., Patra, B., Peng, C.-C. & Liao, W.-H. (2016). Drug Testing and Flow Cytometry Analysis on a Large Number of Uniform Sized Tumor Spheroids Using a Microfluidic Device. *Scientific Reports*, 6(1), 21061.

Uzarski, J. S., DiVito, M. D., Wertheim, J. A. & Miller, W. M. (2017). Essential Design Considerations for the Resazurin Reduction Assay to Noninvasively Quantify Cell Expansion within Perfused Extracellular Matrix Scaffolds. *Biomaterials*, 129, 163–175.

Vanbellingen, Q. P., Elie, N., Eller, M. J., Della-Negra, S., Touboul, D. & Brunelle, A. (2015). Time-of-Flight Secondary Ion Mass Spectrometry Imaging of Biological Samples with Delayed Extraction for High Mass and High Spatial Resolutions. *Rapid Communications in Mass Spectrometry*, 29(13), 1187–1195.

Venkatesan, J., Bhatnagar, I., Manivasagan, P., Kang, K.-H. & Kim, S.-K. (2015). Alginate Composites for Bone Tissue Engineering: A Review. *International journal of biological macromolecules*, 72, 269–281.

Verjans, E.-T., Doijen, J., Luyten, W., Landuyt, B. & Schoofs, L. (2018). Three-Dimensional Cell Culture Models for Anticancer Drug Screening: Worth the Effort? *Journal of Cellular Physiology*, 233(4), 2993–3003.

Vermeulen, L., Todaro, M., de Sousa Mello, F., Sprick, M. R., Kemper, K., Perez Alea, M., Richel, D. J., Stassi, G. & Medema, J. P. (2008). Single-Cell Cloning of Colon Cancer Stem Cells Reveals a Multi-Lineage Differentiation Capacity. *Proceedings of the National Academy of Sciences of the United States of America*, 105(36), 13427–32.

Vukicevic, S., Kleinman, H. K., Luyten, F. P., Roberts, A. B., Roche, N. S. & Reddi, A. H. (1992). Identification of Multiple Active Growth Factors in Basement Membrane Matrigel Suggests Caution in Interpretation of Cellular Activity Related to Extracellular Matrix Components. *Experimental Cell Research*, 202(1), 1–8.

Wan, X., Ball, S., Willenbrock, F., Yeh, S., Vlahov, N., Koennig, D., *et al.* (2017). Perfused Three-Dimensional Organotypic Culture of Human Cancer Cells for Therapeutic Evaluation. *Scientific Reports*, 7(1), 9408.

Wang, Y., Mirza, S., Wu, S., Zeng, J., Shi, W., Band, H., Band, V. & Duan, B. (2018). 3D Hydrogel Breast Cancer Models for Studying the Effects of Hypoxia on Epithelial to Mesenchymal Transition. *Oncotarget*, 9(63), 32191–32203.

Van De Wetering, M., Francies, H. E. & Garnett, M. J. (2015). Prospective Derivation of a Living Organoid Biobank of Colorectal Cancer Patients. *Cell*, 161, 933–945.

Wiśniewski, J. R., Vildhede, A., Norén, A. & Artursson, P. (2016). In-Depth Quantitative Analysis and Comparison of the Human Hepatocyte and Hepatoma Cell Line HepG2 Proteomes. *Journal of Proteomics*, 136, 234–247.

Wysowski, D. K. & Swartz, L. (2005). Adverse Drug Event Surveillance and Drug Withdrawals in the United States, 1969-2002. *Archives of Internal Medicine*, 165(12), 1363.

Yamasaki, K., Chuang, V. T. G., Maruyama, T. & Otagiri, M. (2013). Albumin-Drug Interaction and Its Clinical Implication. *Biochimica et biophysica acta*, 1830(12), 5435–43.

Yang, L. & Lin, P. C. (2017). Mechanisms That Drive Inflammatory Tumor Microenvironment, Tumor Heterogeneity, and Metastatic Progression. *Seminars in Cancer Biology*.

Yang, X., Yang, P., Shen, J., Osaka, E., Choy, E., Cote, G., *et al.* (2014). Prevention of Multidrug Resistance (MDR) in Osteosarcoma by NSC23925.

British Journal of Cancer, 110(12), 2896–2904.

Yi, T., Huang, S., Liu, G., Li, T., Kang, Y., Luo, Y. & Wu, J. (2018). Bioreactor Synergy with 3D Scaffolds: New Era for Stem Cells Culture. *ACS Applied Bio Materials*, 1(2), 193–209.

Young, M., Rodenhizer, D., Dean, T., D'Arcangelo, E., Xu, B., Ailles, L. & McGuigan, A. P. (2018). A TRACER 3D Co-Culture Tumour Model for Head and Neck Cancer. *Biomaterials*, 164, 54–69.

Yuan, L. & Kaplowitz, N. (2013). Mechanisms of Drug-Induced Liver Injury. *Clinics in Liver Disease*, 17(4), 507–518.

Zanoni, M., Piccinini, F., Arienti, C., Zamagni, A., Santi, S., Polico, R., Bevilacqua, A. & Tesei, A. (2016). 3D Tumor Spheroid Models for in Vitro Therapeutic Screening: A Systematic Approach to Enhance the Biological Relevance of Data Obtained. *Scientific Reports*, 6(1), 19103.

Zavalin, A., Yang, J., Haase, A., Holle, A. & Caprioli, R. (2014). Implementation of a Gaussian Beam Laser and Aspheric Optics for High Spatial Resolution MALDI Imaging MS. *Journal of the American Society for Mass Spectrometry*, 25(6), 1079–82.

Zavalin, A., Yang, J., Hayden, K., Vestal, M. & Caprioli, R. M. (2015). Tissue Protein Imaging at 1 Mm Laser Spot Diameter for High Spatial Resolution and High Imaging Speed Using Transmission Geometry MALDI TOF MS. *Analytical and Bioanalytical Chemistry*, 407(8), 2337–2342.

Zeilinger, K., Freyer, N., Damm, G., Seehofer, D. & Knöspel, F. (2016). Cell Sources for *in Vitro* Human Liver Cell Culture Models. *Experimental Biology and Medicine*, 241(15), 1684–1698.

Zhang, Y., Yang, J., Zhao, N., Wang, C., Kamar, S., Zhou, Y., *et al.* (2018). Progress in the Chemotherapeutic Treatment of Osteosarcoma. *Oncology letters*, 16(5), 6228–6237.

Zheng, D., Wu, W., Dong, N., Jiang, X., Xu, J., Zhan, X., Zhang, Z. & Hu, Z. (2017). Mxd1 Mediates Hypoxia-Induced Cisplatin Resistance in

Osteosarcoma Cells by Repression of the PTEN Tumor Suppressor Gene. *Molecular Carcinogenesis*, 56(10), 2234–2244.

Zhong, C., Liu, J., Zhang, Y., Luo, J. & Zheng, J. (2017). MicroRNA-139 Inhibits the Proliferation and Migration of Osteosarcoma Cells via Targeting Forkhead-Box P2. *Life Sciences*, 191, 68–73.

Zink, K. E., Dean, M., Burdette, J. E. & Sanchez, L. M. (2018). Imaging Mass Spectrometry Reveals Crosstalk between the Fallopian Tube and the Ovary That Drives Primary Metastasis of Ovarian Cancer. *ACS central science*, 4(10), 1360–1370.

Zou, X.-Y., Ding, D., Zhan, N., Liu, X.-M., Pan, C. & Xia, Y.-M. (2015). Glyoxalase I Is Differentially Expressed in Cutaneous Neoplasms and Contributes to the Progression of Squamous Cell Carcinoma. *The Journal of investigative dermatology*, 135(2), 589–598.

Zscheppang, K., Berg, J., Hedtrich, S., Verheyen, L., Wagner, D. E., Suttorp, N., Hippenstiel, S. & Hocke, A. C. (2018). Human Pulmonary 3D Models For Translational Research. *Biotechnology Journal*, 13(1), 1700341.

Word count (main body of text): 39,531 words

Appendices
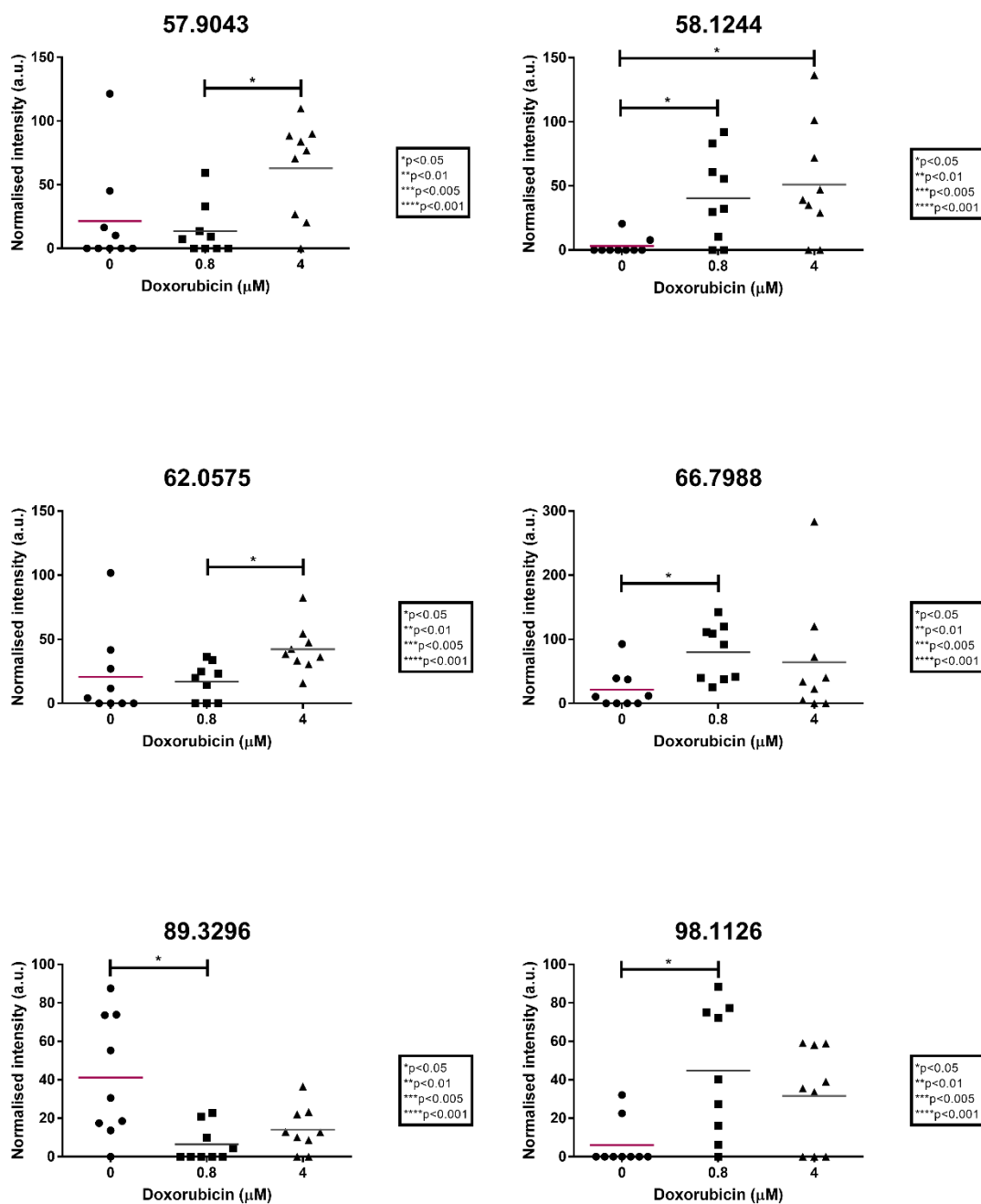
Appendix chapter 3 figure 1 Ionic species significantly varying between doxorubicin treated spheroid aggregates. The data was extracted from PCA-DA analysis, tested using the Kruskal-Wallis test of significance or using ANOVA.
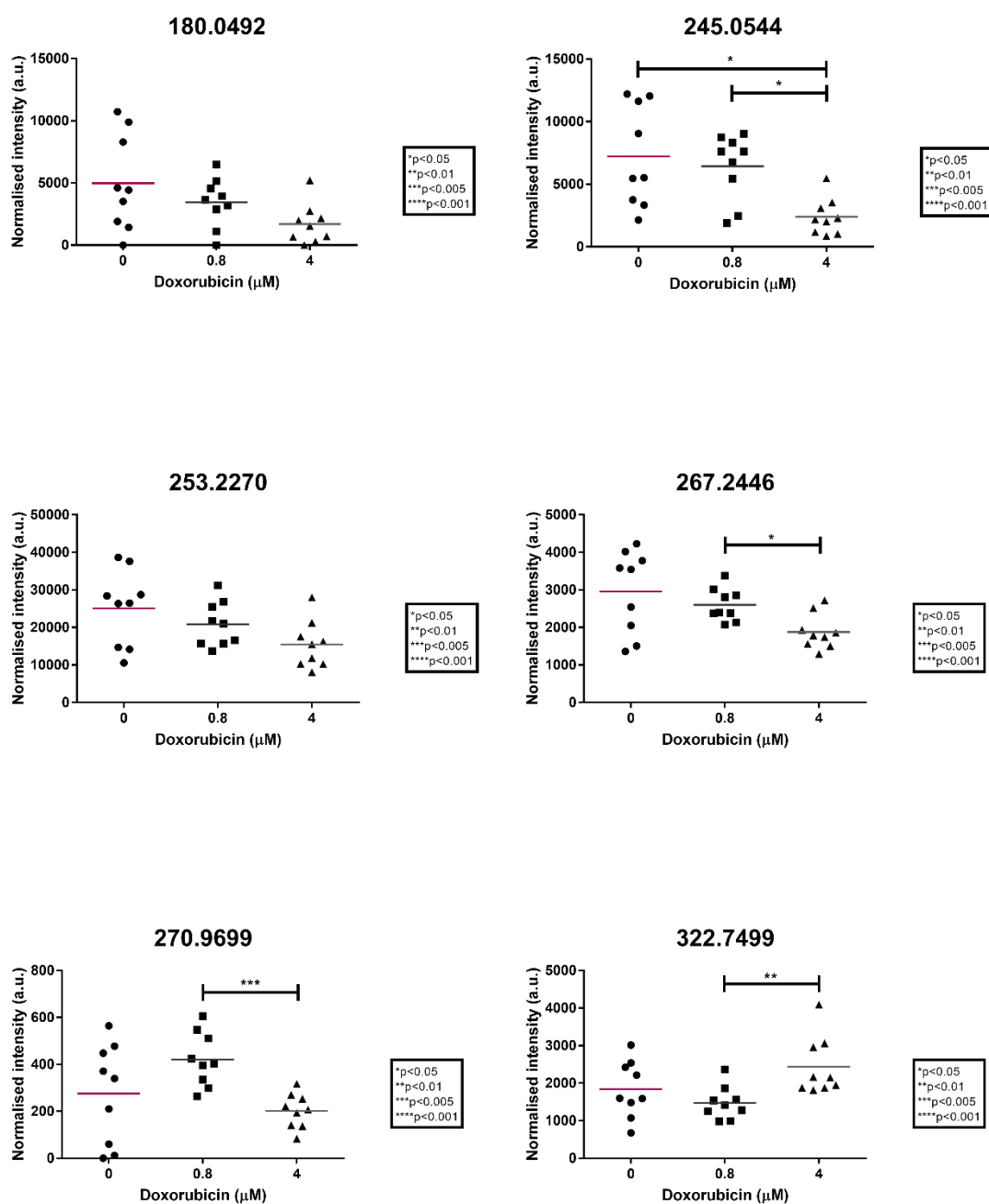
Appendix chapter 3 figure 2 Ionic species significantly varying between doxorubicin treated spheroid aggregates. The data was extracted from PCA-DA analysis, tested using the Kruskal-Wallis test of significance or using ANOVA.
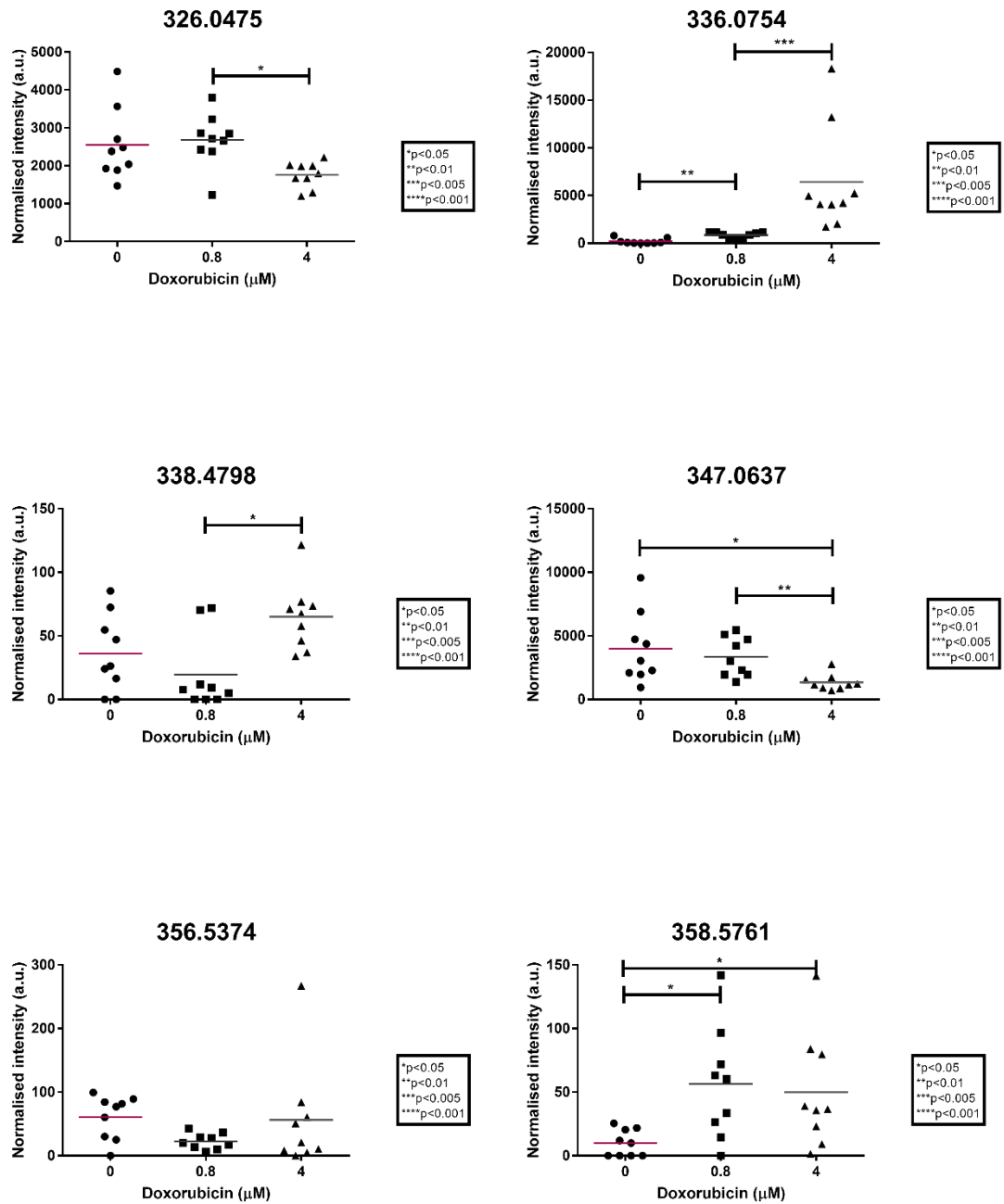
Appendix chapter 3 figure 3 Ionic species significantly varying between doxorubicin treated spheroid aggregates. The data was extracted from PCA-DA analysis, tested using the Kruskal-Wallis test of significance or using ANOVA.
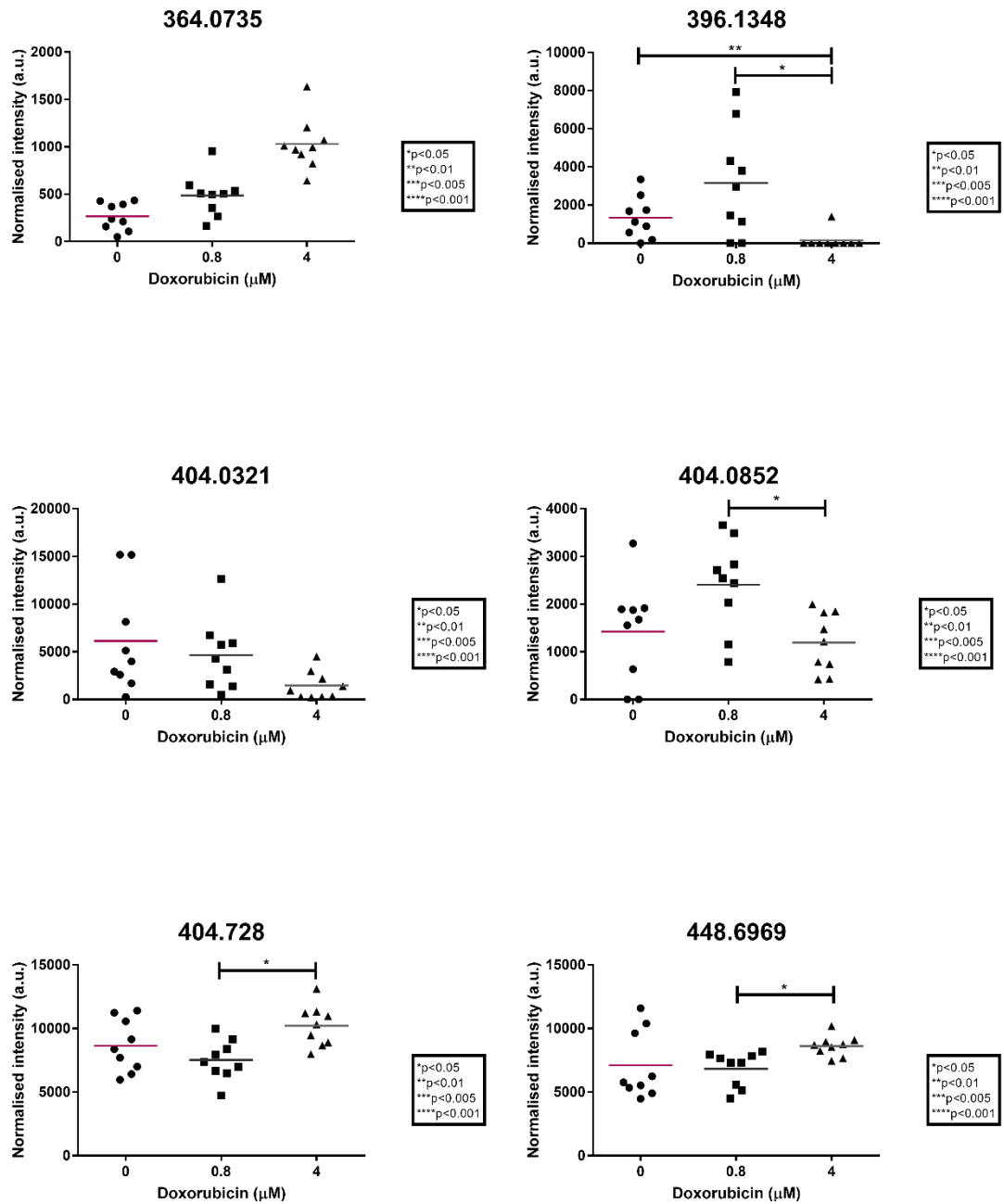
Appendix chapter 3 figure 4 Ionic species significantly varying between doxorubicin treated spheroid aggregates. The data was extracted from PCA-DA analysis, tested using the Kruskal-Wallis test of significance or using ANOVA.
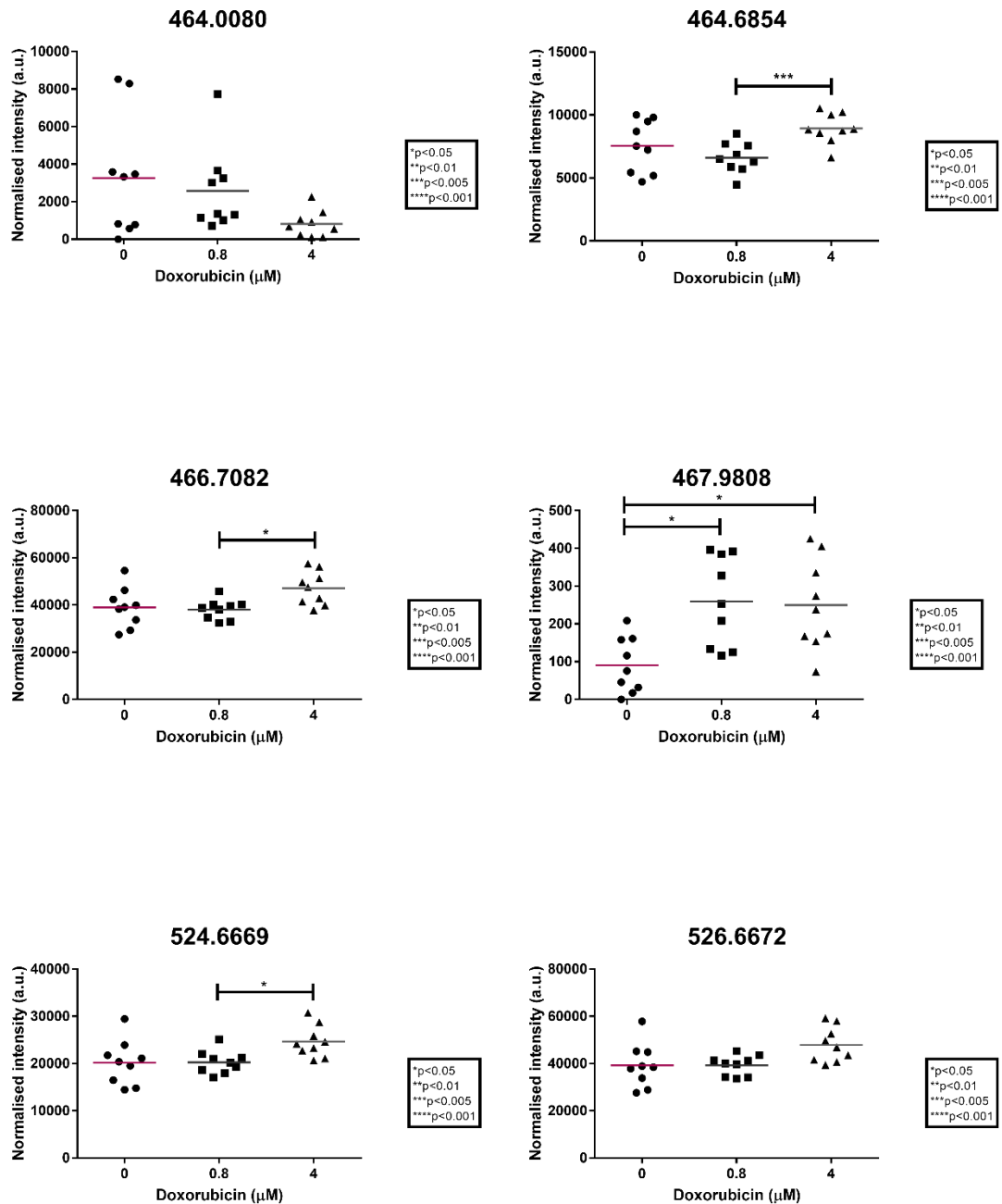
Appendix chapter 3 figure 5 Ionic species significantly varying between doxorubicin treated spheroid aggregates. The data was extracted from PCA-DA analysis, tested using the Kruskal-Wallis test of significance or using ANOVA.
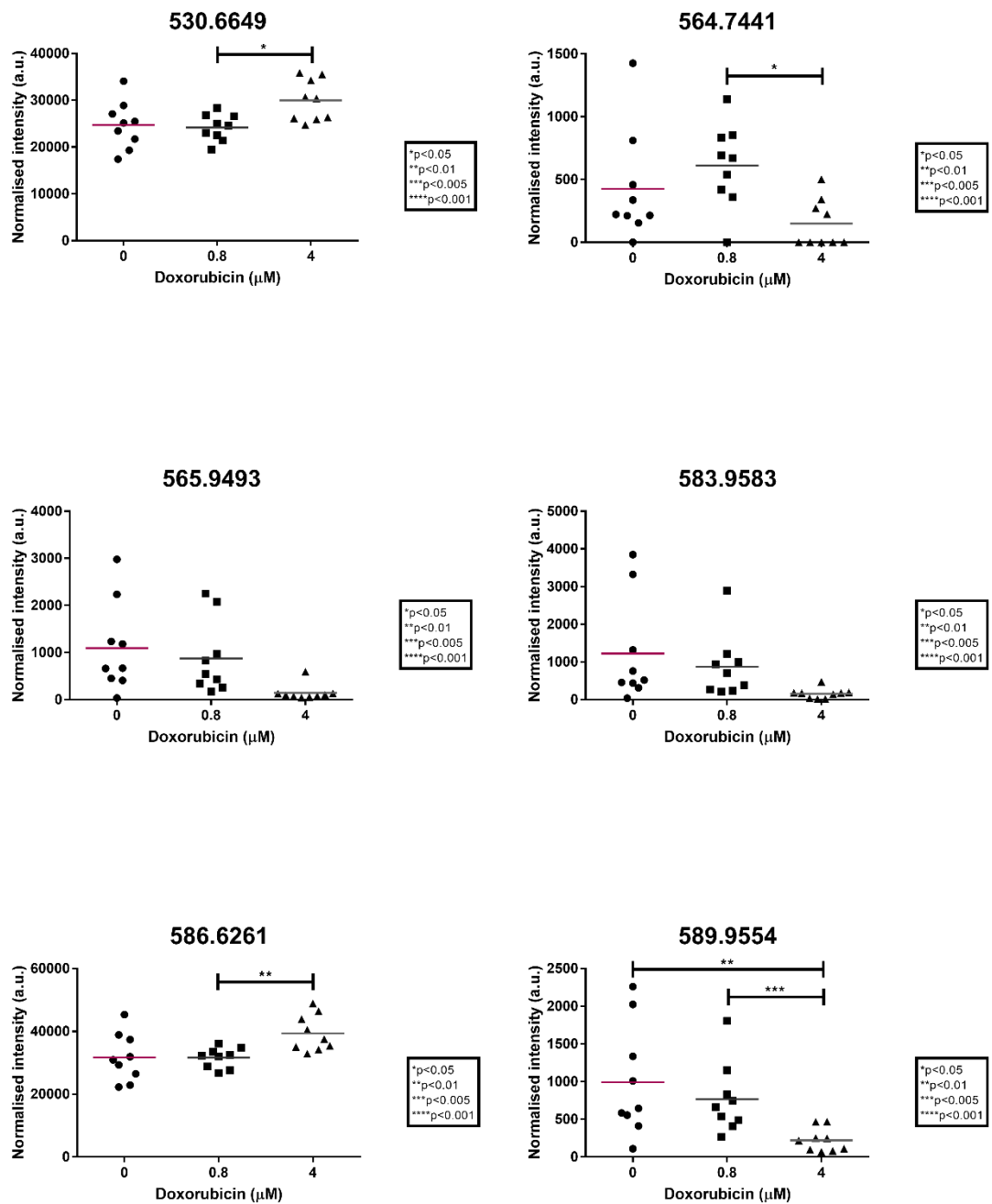
Appendix chapter 3 figure 6 Ionic species significantly varying between doxorubicin treated spheroid aggregates. The data was extracted from PCA-DA analysis, tested using the Kruskal-Wallis test of significance or using ANOVA.
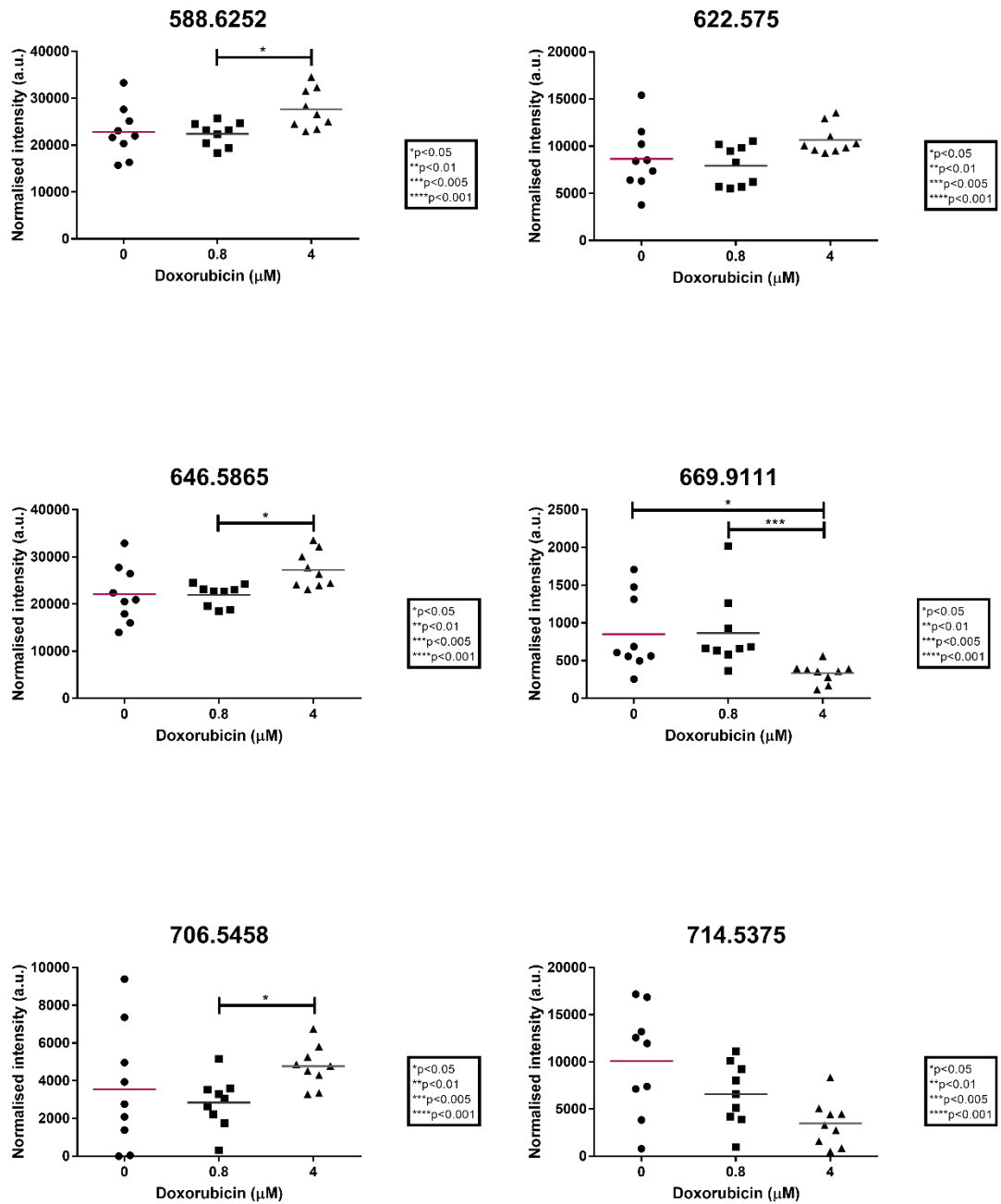
Appendix chapter 3 figure 7 Ionic species significantly varying between doxorubicin treated spheroid aggregates. The data was extracted from PCA-DA analysis, tested using the Kruskal-Wallis test of significance or using ANOVA.
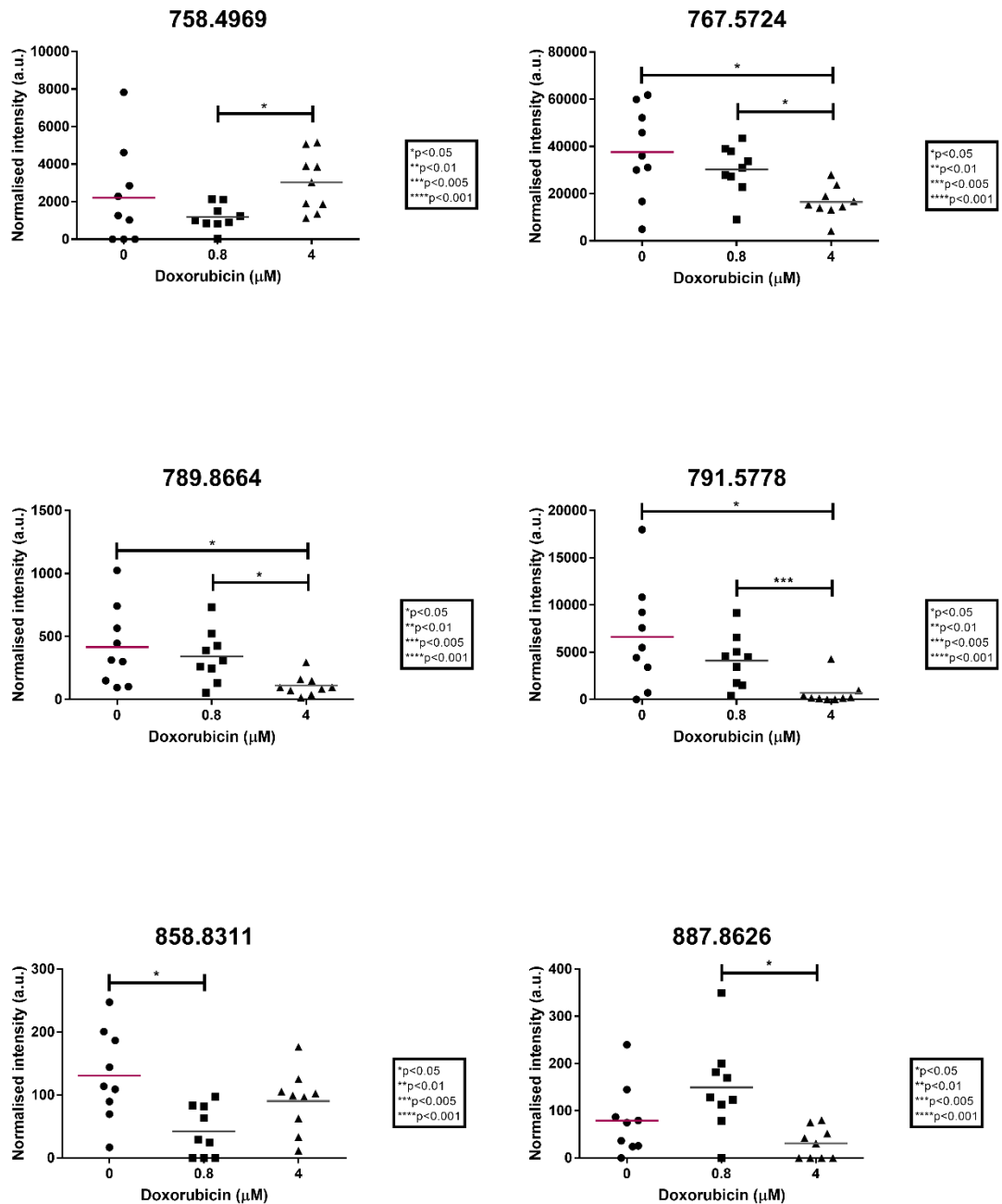
Appendix chapter 3 figure 8 Ionic species significantly varying between doxorubicin treated spheroid aggregates. The data was extracted from PCA-DA analysis, tested using the Kruskal-Wallis test of significance or using ANOVA.
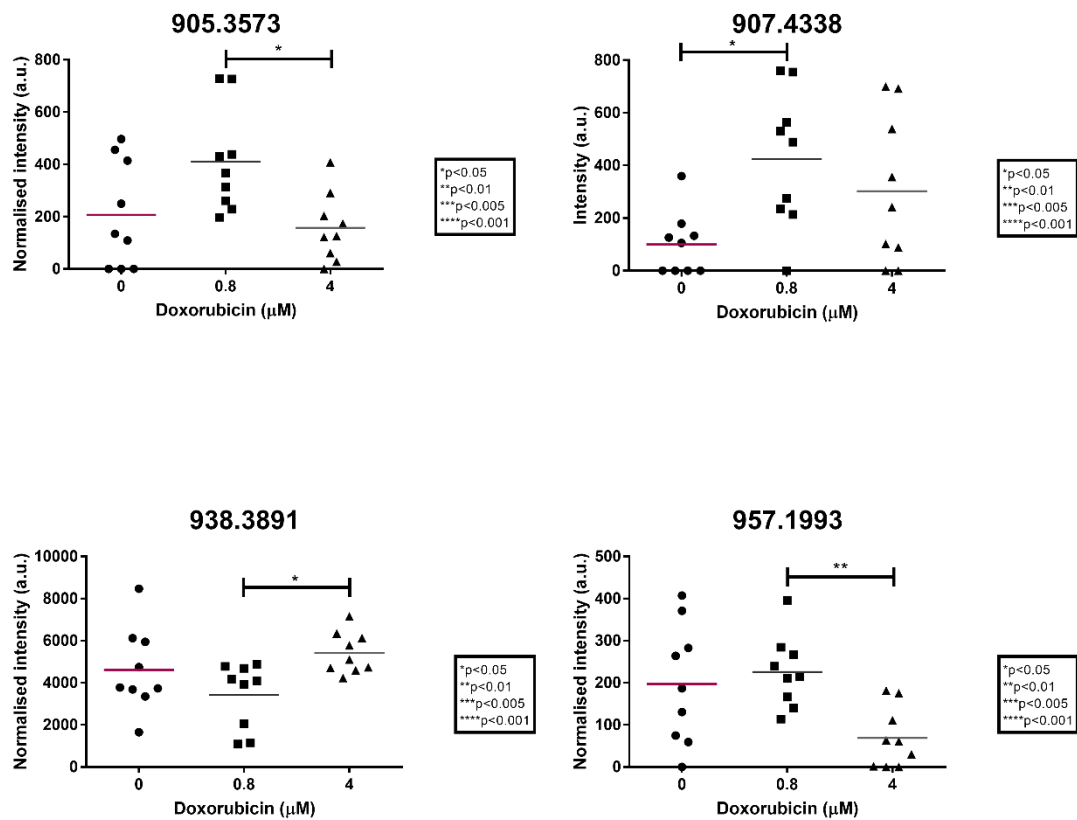
Appendix chapter 3 figure 9 Ionic species significantly varying between doxorubicin treated spheroid aggregates. The data was extracted from PCA-DA analysis, tested using the Kruskal-Wallis test of significance or using ANOVA.
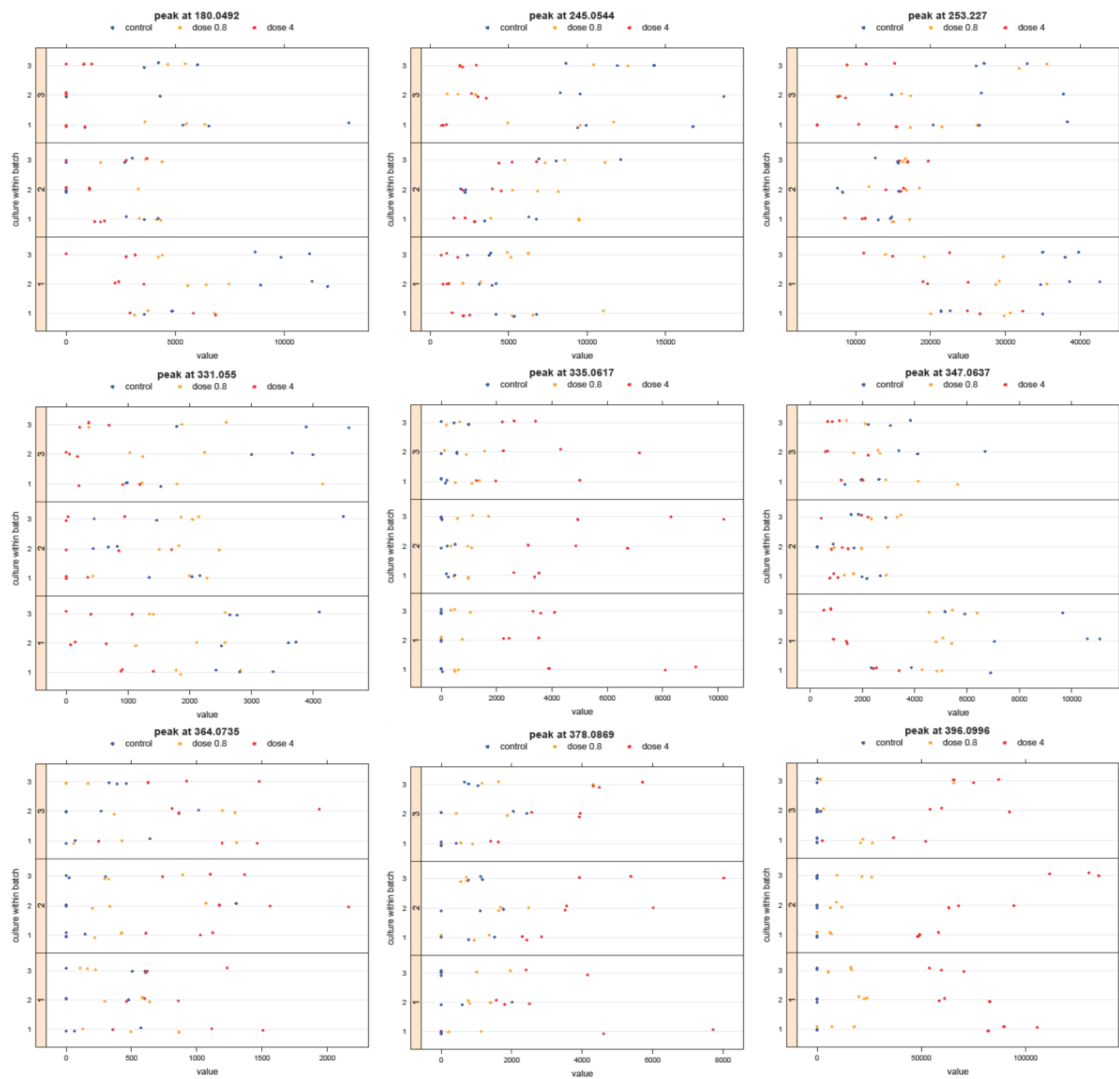
Appendix chapter 3 figure 10 Nine of 18 significantly differing species discovered using PCA-DA and defined using a linear mixed effects model. The graphs show the variability due to random and fixed effects.

Appendix chapter 3 figure 11 Nine of 18 significantly differing species discovered using PCA-DA and defined using a linear mixed effects model (2). The graphs show the variability due to random and fixed effects.

	p-values			
m/z	0.8 to 4	0.8 to 0	4 to 0.8	4 to 0
180.492	0.0052	0.0133	0.0052	<0.00001
245.544	<0.00001	0.3334	<0.00001	<0.00001
253.227	0.0044	0.0266	0.0044	<0.00001
331.055	<0.00001	0.0202	<0.00001	<0.00001
335.0617	<0.00001	0.0991	<0.00001	<0.00001
347.0637	<0.00001	0.145	<0.00001	<0.00001
364.0735	<0.00001	0.0405	<0.00001	<0.00001
378.0869	<0.00001	0.2896	<0.00001	<0.00001
396.0996	<0.00001	0.0038	<0.00001	<0.00001
404.0321	0.0001	0.0579	0.0001	<0.00001
414.1022	<0.00001	0.1723	<0.00001	<0.00001
464.008	0.0001	0.1217	0.0001	<0.00001
565.9493	0.0001	0.2042	0.0001	<0.00001
583.9583	0.0008	0.0871	0.0008	<0.00001
589.9554	0.0001	0.0786	0.0001	<0.00001
714.5375	0.0037	0.0011	0.0037	<0.00001
765.5488	0.0001	0.0004	0.0001	<0.00001
791.5778	0.0008	0.0117	0.0008	<0.00001

Appendix chapter 3 table 1 18 significantly differing species discovered using PCA-DA and defined using a linear mixed effects model. P-values for each comparison are given next to each peak.
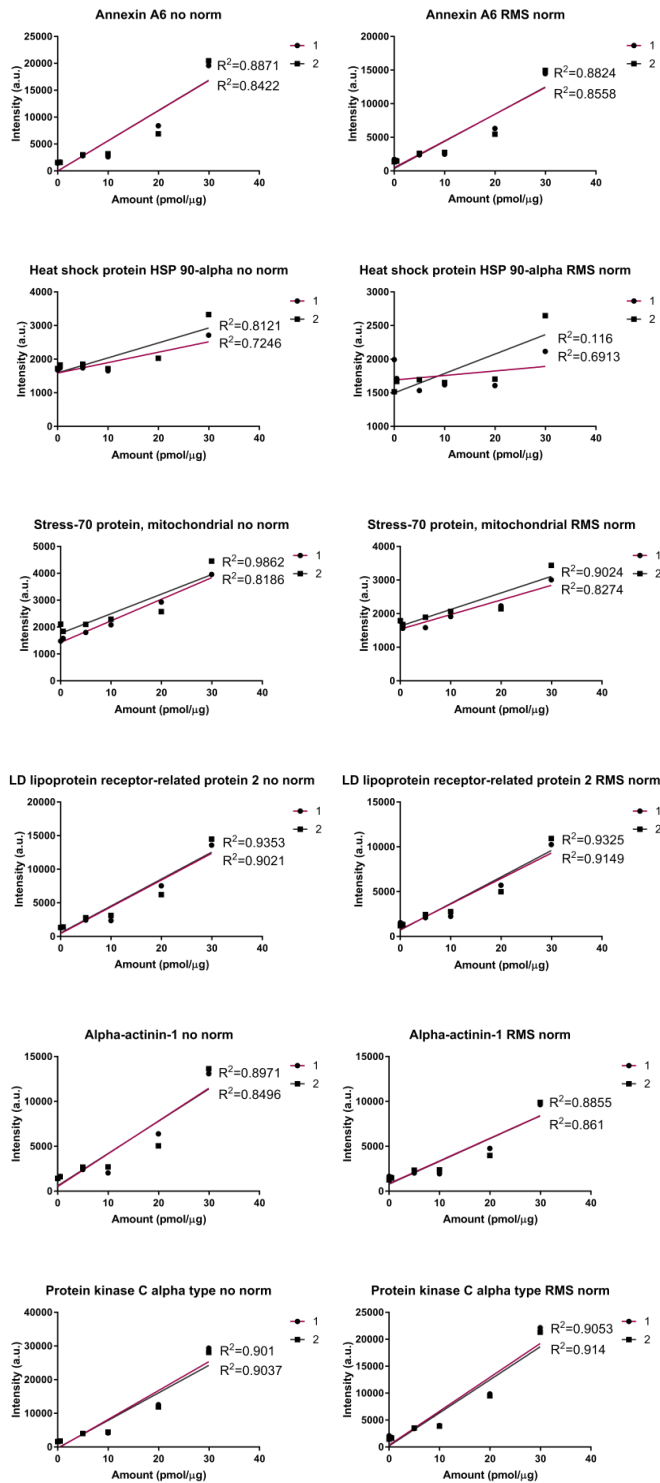
Appendix chapter 4 figure 1 120 peptide mix standard graphs for 2 separate standard array experiments. No normalisation and RMS normalisation is shown.
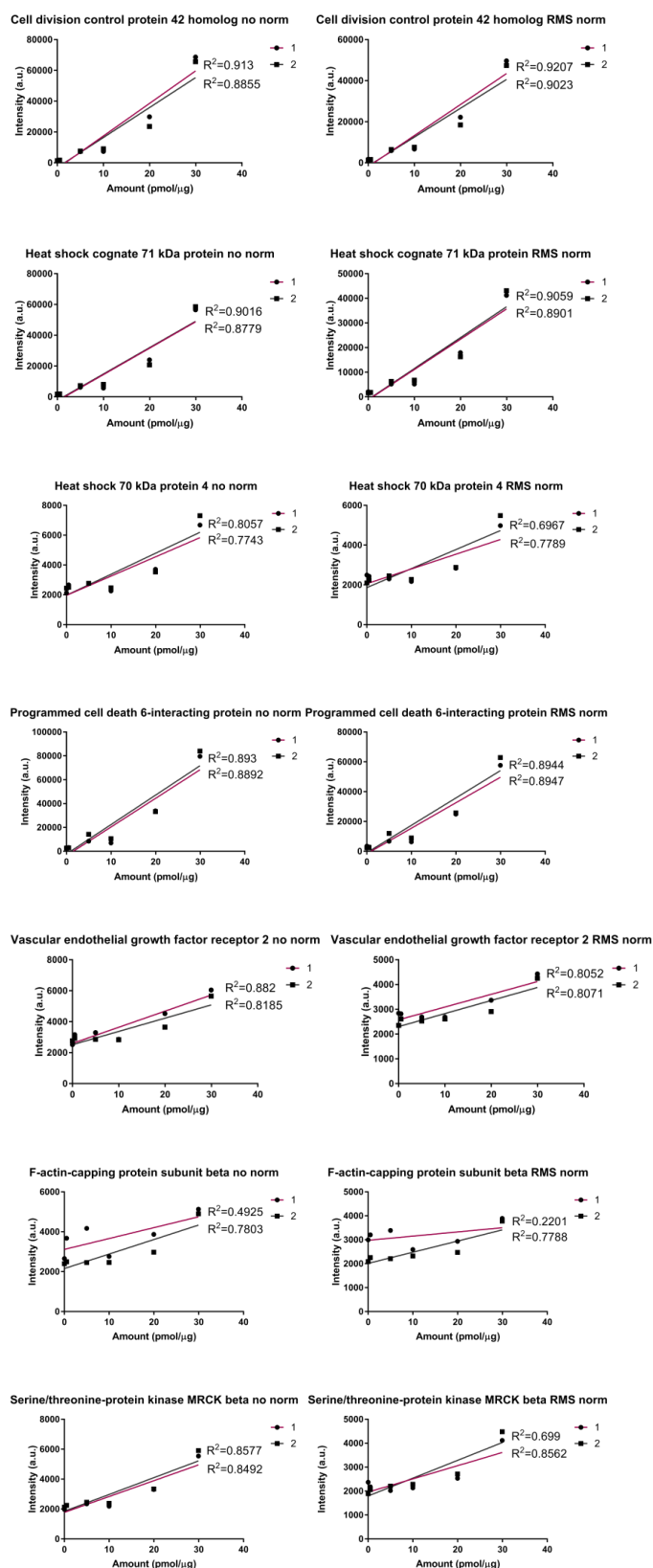
Appendix chapter 4 figure 2 120 peptide mix standard graphs for 2 separate standard array experiments (2). No normalisation and RMS normalisation is shown.
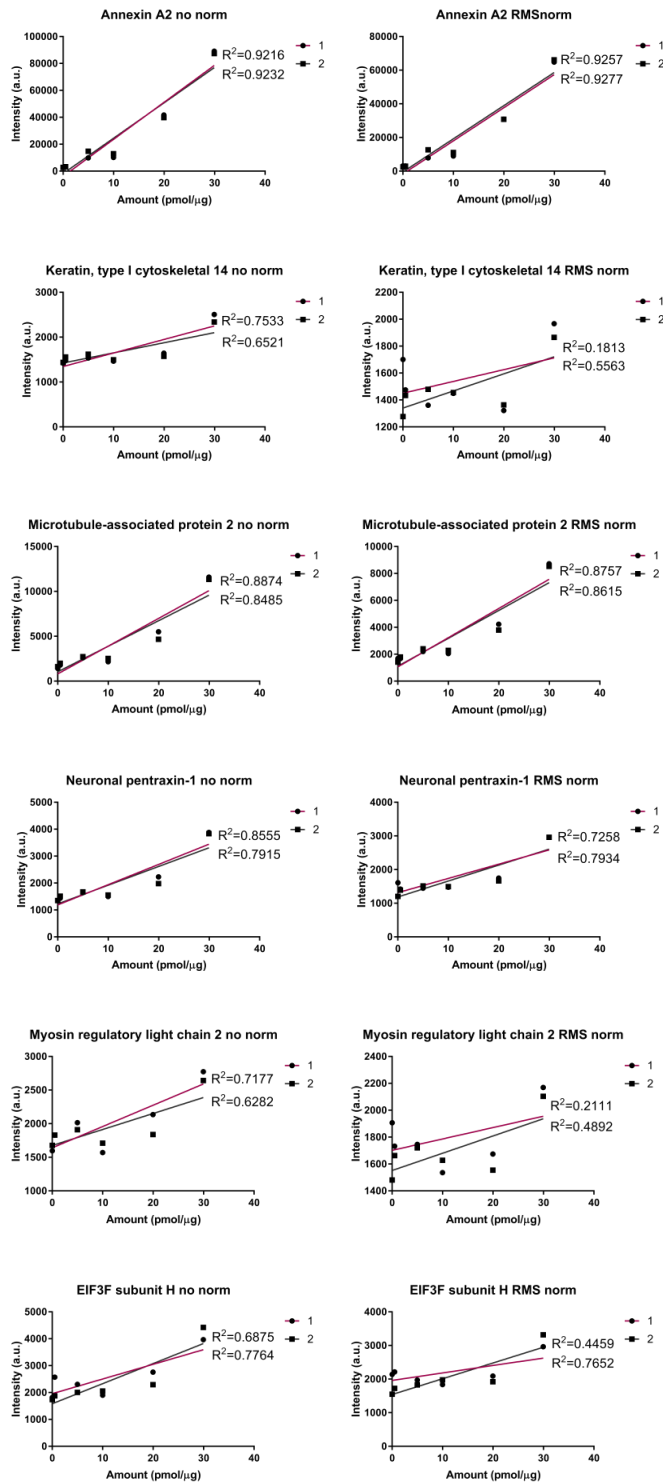
Appendix chapter 4 figure 3 120 peptide mix standard graphs for 2 separate standard array experiments (3). No normalisation and RMS normalisation is shown.

Peptide Sequence	C-term	MW (average)	Description (Human)
GVGASGSFR	R	836.89234	Histone H1.0
VGENADSQIK	K	1060.11602	Histone H1.0
TFEDIPLEEPEVK	K	1545.68532	Vascular endothelial growth factor receptor 2
GAFGQVIEADAFGIDK	K	1637.78728	Vascular endothelial growth factor receptor 2
DITSDTSGDFR	R	1213.20834	Annexin A1
GPAGPQGPR	R	835.90758	Collagen alpha-1(I) chain
SIAFPSIGSGR	R	1091.21772	Core histone macro-H2A.1
ADHGEPIGR	R	950.99498	Heat shock protein HSP 90-beta
ISSSSFSR	R	869.91896	Keratin, type II cytoskeletal 8
WSLLQQQK	K	1030.1777	Keratin, type II cytoskeletal 8
LINQPLPDLK	K	1150.36774	Microtubule-associated protein 2
TDAPLNIR	R	899.00324	Heat shock protein 75 kDa, mitochondrial
NPDDITNEEYGEFYK	K	1833.85798	Heat shock protein HSP 90-alpha
ALLFIPR	R	829.04082	Heat shock protein HSP 90-beta
LLDEEEATDNDLR	R	1532.56244	Programmed cell death 6-interacting protein
AQLLQPTLEINPR	R	1492.71872	Heat shock protein 75 kDa, mitochondrial
GVVGLPGQR	R	882.01908	Collagen alpha-1(I) chain
VAQLEAQZQEPZK	K	1560.7513	Fibrinogen gamma chain
LALASLGYEK	K	1064.23214	Programmed cell death 6-interacting protein
DYETATLSEIK	K	1269.35442	Alpha-actinin-1
LAILGIHNEVSK	K	1293.5116	Alpha-actinin-1
VEVLAGDLR	R	971.10896	Contactin-2
DNZZILDER	R	1194.2961	Fibrinogen gamma chain
DQVANSAFVER	R	1235.30328	Heat shock protein HSP 90-alpha
EFSITDVVPYPISLR	R	1735.97334	Heat shock 70 kDa protein 4
VGLQVVAVK	K	912.12788	60 kDa heat shock protein, mitochondrial
AGGIETIANEYSDR	R	1495.54712	Heat shock 70 kDa protein 4
SQIHDIVLVGGSTR	R	1481.65302	Heat shock cognate 71 kDa protein
VEEEIVTLR	R	1087.22418	Tumor protein D54
FVVQNVSAQK	K	1119.27088	Heat shock protein 105 kDa
GGSASVWSER	R	1035.06834	Aldehyde dehydrogenase family 16 member A1
YQGLZPPVPR	R	1186.38322	Angiotensin-converting enzyme
IGPLGLSPK	K	881.07078	60S ribosomal protein L12
HELLSLASSNHLGK	K	1505.67442	Eukaryotic translation initiation factor 3 subunit H
ILYLTPEQEK	K	1233.40998	Eukaryotic peptide chain release factor subunit 1
YLEESNFVHR	R	1293.38396	Tyrosine-protein kinase SYK
LFPDVLFPADSEHNK	K	1728.89788	Mitogen-activated protein kinase 8
SNFGYNIPLK	K	1152.29904	Proteasome subunit alpha type-3
LTTFQALQHPWVTGK	K	1726.97142	Calcium/calmodulin-dependent protein kinase type IV
FQFPSHVTDVSEEAK	K	1720.83282	Serine/threonine-protein kinase MRCK beta
LSVEIWDWDR	R	1318.43318	Protein kinase C alpha type
FLEEFITPIVK	K	1335.58628	DNA topoisomerase 2-alpha
TLEVEIEPGVR	R	1241.39068	DnaJ homolog subfamily B member 11

230

Peptide	AA	Mass	Protein
GTEELYAIK	K	1023.13716	Protein kinase C alpha type
GFFLLVEGGR	R	1094.26296	Alkaline phosphatase, tissue-nonspecific isozyme
DGIVLGADTR	R	1016.10652	Proteasome subunit beta type-7
AEDGSVIDYELIDQDAR	R	1908.9694	Annexin A2
LEVEANNAFDQYR	R	1568.64244	F-actin-capping protein subunit beta
ITNSLTVLZSEK	K	1364.56474	Eukaryotic translation initiation factor 3 subunit J
AASAHAIGTVK	K	1025.15964	cAMP-dependent protein kinase type II-beta regulatory subunit
EAFTVIDQNR	R	1192.27854	Myosin regulatory light chain 2, skeletal muscle isoform
SVGIVTTTR	R	933.06098	Alkaline phosphatase, tissue-nonspecific isozyme
ISVYYNEATGGK	K	1301.40112	Tubulin beta chain
TIVLQEIIGK	K	1113.34758	Activin receptor type-1B
LGGEVSZLVAGTK	K	1290.4862	Electron transfer flavoprotein subunit alpha, mitochondrial
QVLGLGVNGK	K	984.15078	MAP kinase-activated protein kinase 3
SAAQAAAQTNSNAAGK	K	1460.50638	Plasminogen activator inhibitor 1 RNA-binding protein
DAFVAIVQSVK	K	1176.36196	Annexin A6
TVLVSEGIVTPR	R	1270.47496	Low-density lipoprotein receptor-related protein 2
ELWFSDDPNVTK	K	1450.5478	Apoptosis-inducing factor 1, mitochondrial
IPVGPETLGR	R	1038.19816	ATP synthase subunit beta, mitochondrial
LADDLYR	R	864.9422	Attractin
GPFPQELVR	R	1042.1884	Cadherin-2
FGFLQEFSK	K	1102.2386	Contactin-2
STTPDITGYR	R	1110.1747	Fibronectin
LWDLTTGTTTR	R	1264.38426	Guanine nucleotide-binding protein subunit beta-2-like 1
NLPLPPPPPPR	R	1194.42514	Heterogeneous nuclear ribonucleoprotein K
ALELDSNLYR	R	1193.30636	Myosin-9
LLTSGYLQR	R	1050.20886	Ubiquitin thioesterase OTUB1
TPENFPZK	K	992.1065	Plasminogen
ETLPAEQDLTTK	K	1345.45214	Proteasome subunit alpha type-1
DLPVSEQQER	R	1200.25594	26S proteasome non-ATPase regulatory subunit 13
NSLTFPDDNDISK	K	1465.51784	Rho-associated protein kinase 1
ITQSEFDR	R	995.04424	Endophilin-B1
LHLDYIGPZK	K	1215.42114	SPARC
ALDLDSSZK	K	1008.10436	Stress-induced-phosphoprotein 1
ALASQLQDSLK	K	1173.31672	Vinculin
AENYWWR	R	1024.08854	Activated CDC42 kinase 1
LSDPANWLK	K	1043.17316	Cadherin-2
FSVSPVVR	R	890.03778	Elongation factor 2
VQQTVQDLFGR	R	1290.42484	Stress-70 protein, mitochondrial
LLEYTPTAR	R	1063.20432	Glycogen synthase kinase-3 beta
ALLSAPWYLNR	R	1303.50796	Beta-hexosaminidase subunit alpha
DAEEWFFTK	K	1172.24232	Keratin, type I cytoskeletal 14
ITQYLDAGGIPR	R	1303.46336	Calcium/calmodulin-dependent protein kinase type II subunit alpha
ALTSELANAR	R	1045.14774	Moesin
LENLEQYSR	R	1151.22662	Neuronal pentraxin-1
ILEFFGLK	K	966.1735	Protein disulfide-isomerase
VYLSEZK	K	898.03502	Plasminogen
LPLVTPHTQZR	R	1321.54814	26S protease regulatory subunit 4
DYLHYIR	R	979.08944	40S ribosomal protein S11
FGISSVPTK	K	935.0751	SAP domain-containing ribonucleoprotein
VSTEVDAR	R	875.92354	Transaldolase

GYAPESVLER	R	1120.21258	tRNA pseudouridine synthase A, mitochondrial
LLQTLPQLR	R	1081.30902	E3 ubiquitin-protein ligase UBR4
DPLADLNIK	K	998.131	Clathrin coat assembly protein AP180
YVEZSALTQK	K	1198.34602	Cell division control protein 42 homolog
LVFSNVNLK	K	1033.2214	DNA damage-binding protein 1
LQSQLLSIEK	K	1158.34514	Dynamin-1
SADZSVEEEPWK	K	1436.49976	Excitatory amino acid transporter 2
ELEASEELDTIZPK	K	1633.77228	Glutaredoxin-3
DAGQISGLNVLR	R	1242.38204	Stress-70 protein, mitochondrial
EPGZGZZSVZAR	R	1412.5959	Insulin-like growth factor-binding protein 2
ENIWDGVTTK	K	1162.24926	Protein kinase C beta type
EVZQLLPFLVR	R	1373.66246	Neurochondrin
DQLVLGR	R	799.91524	Platelet-derived growth factor receptor beta
LAYINPDLALEEK	K	1488.68036	Stress-induced-phosphoprotein 1
IIALDGDTK	K	945.06838	Transketolase
DTQLQQIVDK	K	1187.30024	Calcineurin subunit B type 1
NSQGEEVAQR	R	1117.12758	Lamin-B1
ELIFQETAR	R	1106.22906	Mitogen-activated protein kinase 3
TIVLQESIGK	K	1087.26724	TGF-beta receptor type-1
QENGASVILR	R	1086.19966	Elongation factor 1-delta
ISZTIANR	R	934.07218	Fibronectin
TPFLLVGTQIDLR	R	1472.72732	Cell division control protein 42 homolog
LLGYVATLK	K	977.1979	Cold shock domain-containing protein E1
ALFAISZLVR	R	1149.40612	Hsp70-binding protein 1
GEFTIETEGK	K	1110.1714	Glycine--tRNA ligase
DNPGVVTZLDEAR	R	1445.55464	Ubiquitin-like modifier-activating enzyme 1
IEAAZFATIK	K	1123.32248	Isocitrate dehydrogenase [NAD] subunit alpha, mitochondrial

Appendix chapter 4 table 1 *120 peptide standards.*

Sequence	Sequence (mod)	Monoisot. Mass	Description
GGSASVWSER	GGSASVWSEX	1044.48638	Aldehyde dehydrogenase family 16 member A1
YQGLCPPVPR	YQGLZPPVPX	1195.60472	Angiotensin-converting enzyme
IGYSSPQTLADQSSK	IGYSSPQTLADQSSB	1588.78241	Long-chain-fatty-acid--CoA ligase 3
IGYSSPLTLSDQSSK	IGYSSPLTLSDQSSB	1589.80281	Long-chain-fatty-acid--CoA ligase 4
ALQSNHFELSLR	ALQSNHFELSLX	1423.74472	Agrin
HSFFSGVNWQDVYDK	HSFFSGVNWQDVYDB	1835.83583	RAC-gamma serine/threonine-protein kinase
INPDHIGFYR	INPDHIGFYX	1240.62281	Glutamyl aminopeptidase
LTFDEYR	LTFDEYX	952.45296	Annexin A3
NAGFTPQER	NAGFTPQEX	1028.49147	DNA-(apurinic or apyrimidinic site) lyase
STYPPSGPTYR	STYPPSGPTYX	1234.58577	Acid ceramidase
IADFGWSVHAPSLR	IADFGWSVHAPSLX	1564.80255	Aurora kinase B
LSDSYSNTLPVR	LSDSYSNTLPVX	1360.68621	Brain-specific angiogenesis inhibitor 1-associated protein 2
FGFPAFSGISR	FGFPAFSGISX	1194.60609	Biliverdin reductase A
SNAQGIDLNR	SNAQGIDLNX	1096.55005	Carboxypeptidase E
DNEDFQESNR	DNEDFQESNX	1262.50389	Ceruloplasmin
ELQDLALQGAK	ELQDLALQGAB	1192.65428	Chromogranin-A
AALSSFQK	AALSSFQB	858.46906	COP9 signalosome complex subunit 2
ISNYGWDQSDK	ISNYGWDQSDB	1319.58734	Calcyclin-binding protein
DLTPEHLPLLR	DLTPEHLPLLX	1312.73783	m7GpppX diphosphatase
EFTAQNLGK	EFTAQNLGB	1014.52255	Eukaryotic translation initiation factor 3 subunit H
DDFTEFGK	DDFTEFGB	965.42216	Eukaryotic translation initiation factor 3 subunit J
IDIPSFDWPIAPFPR	IDIPSFDWPIAPFPX	1779.92232	4-aminobutyrate aminotransferase, mitochondrial
YIQHTYR	YIQHTYX	989.49584	Rho GDP-dissociation inhibitor 1
NQQIFLR	NQQIFLX	927.51657	Growth factor receptor-bound protein 2
GVGASGSFR	GVGASGSFX	846.42232	Histone H1.0
FGLFTPGSR	FGLFTPGSX	990.51622	Coproporphyrinogen-III oxidase, mitochondrial
HSGPNSADSANDGFVR	HSGPNSADSANDGFVX	1639.72141	Heterogeneous nuclear ribonucleoprotein F
LGDGLFLQCCR	LGDGLFLQZZX	1347.63028	Isocitrate dehydrogenase [NAD] subunit gamma, mitochondrial
TEAESWYQTK	TEAESWYQTB	1249.57063	Keratin, type II cytoskeletal 5
YEELQQTAGR	YEELQQTAGX	1203.57593	Keratin, type II cytoskeletal 5
HLSSGDLLR	HLSSGDLLX	1006.5435	GTP:AMP phosphotransferase AK3, mitochondrial
TSLPWQGLK	TSLPWQGLB	1036.57967	Casein kinase I isoform alpha
LQEFNAR	LQEFNAX	886.45363	Calcium/calmodulin-dependent protein kinase type IV
GFCLPPHCSR	GFZLPPHZSX	1239.55164	Creatine kinase B-type
SGYFDER	SGYFDEX	882.37471	Creatine kinase U-type, mitochondrial
LGSGPDGEPTIR	LGSGPDGEPTIX	1207.60721	Protein kinase C gamma type
ASSSLGLQDFDLLR	ASSSLGLQDFDLLX	1530.79172	Protein kinase C iota type
ISQGLGLQDFDLIR	ISQGLGLQDFDLIX	1583.85465	Protein kinase C zeta type
TEEGPTLSYGR	TEEGPTLSYGX	1218.57559	Matrin-3
TDFGIFR	TDFGIFX	864.43691	Methylcrotonoyl-CoA carboxylase beta chain, mitochondrial
HIGYDDSSK	HIGYDDSSB	1028.46543	S-adenosylmethionine synthase isoform type-2
LPLPEPWR	LPLPEPWX	1016.56825	UPF0160 protein MYG1, mitochondrial
ELLPEIR	ELLPEIX	878.51007	Nuclear autoantigenic sperm protein
LVEPGSPAEK	LVEPGSPAEB	1033.5535	Na(+)/H(+) exchange regulatory cofactor NHE-RF1
VDNDENEHQLSLR	VDNDENEHQLSLX	1577.73092	Nucleophosmin
LTLEDSGTYECR	LTLEDSGTYEZX	1452.64302	Neuroplastin

VAQLPLSLK	VAQLPLSLB	975.6208	Neuronal pentraxin receptor
LLLPLFR	LLLPLFX	880.57736	N-terminal Xaa-Pro-Lys N-methyltransferase 1
DFSLEQLR	DFSLEQLX	1016.51662	Membrane-associated progesterone receptor component 2
ELCGTPGYLAPEILK	ELZGTPGYLAPEILB	1667.86836	Phosphorylase b kinase gamma catalytic chain, liver/testis isoform
FGIDDQDFQNSLTR	FGIDDQDFQNSLTX	1664.76697	Phosphatidylinositol 5-phosphate 4-kinase type-2 alpha
SAPLPNDSQAR	SAPLPNDSQAX	1164.57626	Phosphatidylinositol 5-phosphate 4-kinase type-2 alpha
LFTNFHR	LFTNFHX	943.49035	Phosphatidylinositol transfer protein alpha isoform
CPLQDFLR	ZPLQDFLX	1057.52541	Lysosomal acid phosphatase
FPLGPCPR	FPLGPZPX	952.48281	Lysosomal acid phosphatase
ELSELSLLSLYGIHK	ELSELSLLSLYGIHB	1708.94906	Prostatic acid phosphatase
APLDIPIPDPPPK	APLDIPIPDPPPB	1376.77946	Proteasome activator complex subunit 2
SLEPDTFQGLER	SLEPDTFQGLEX	1400.68111	Reticulon-4 receptor-like 2
IGPLGLSPK	IGPLGLSPB	888.55238	60S ribosomal protein L12
YSLDPENPTK	YSLDPENPTB	1170.56481	60S ribosomal protein L17
LLADQAEAR	LLADQAEAX	995.52751	60S ribosomal protein L19
LSYNTASNK	LSYNTASNB	1004.50183	60S ribosomal protein L34
LDELYGTWR	LDELYGTWX	1161.56938	60S ribosomal protein L4
ANPFGGASHAK	ANPFGGASHAB	1063.52902	40S ribosomal protein S23
SLQAQLQR	SLQAQLQX	952.53295	Phosphatidylinositide phosphatase SAC1
NFSDNQLQEGK	NFSDNQLQEGB	1286.59824	Transgelin-2
VGEFSGANK	VGEFSGANB	915.45413	Thioredoxin
SCHTGLGR	SZHTGLGX	896.4162	Serotransferrin
LPDGTSLTQTFR	LPDGTSLTQTFX	1344.69129	UBX domain-containing protein 1
AFHPFIAGPYNR	AFHPFIAGPYNX	1398.7072	Vigilin
ASLYPCPETPQER	ASLYPZPETPQEX	1556.71685	V-type proton ATPase 116 kDa subunit a isoform 1
AGQAVDDFIEK	AGQAVDDFIEB	1199.59134	6-phosphogluconate dehydrogenase, decarboxylating
LCFFYNK	LZFFYNB	998.47752	Afamin
ALANSLACQGK	ALANSLAZQGB	1139.58483	Fructose-bisphosphate aldolase A
SEIDLLDIR	SEIDLLDIX	1082.58469	Annexin A3
NHLLHVFDEYK	NHLLHVFDEYB	1421.71828	Annexin A4
VAPPGLTQIPQIQK	VAPPGLTQIPQIQB	1496.88059	Sodium/potassium-transporting ATPase subunit beta-1
HEQNIDCGGGYVK	HEQNIDZGGGYVB	1483.66051	Calreticulin
EETPGTEWEK	EETPGTEWEB	1212.53898	Clathrin light chain B
VTEQEWR	VTEQEWX	956.45911	Clathrin light chain B
VAHQLQALR	VAHQLQALX	1044.60677	Chromogranin-A
DFLPLYFGWFLTK	DFLPLYFGWFLTB	1653.86862	2',3'-cyclic-nucleotide 3'-phosphodiesterase
YNTPGFSGCLSGVR	YNTPGFSGZLSGVX	1523.70662	Contactin-associated protein 1
LFTAESLIGLK	LFTAESLIGLB	1198.70525	Coatomer subunit delta
VTQVDGNSPVR	VTQVDGNSPVX	1180.60756	Coatomer subunit delta
FIPCSPFSDYVYK	FIPZSPFSDYVYB	1629.76285	Dihydropyrimidinase-related protein 3
SAADLISQAR	SAADLISQAX	1040.54898	Dihydropyrimidinase-related protein 3
VTNLSEDTR	VTNLSEDTX	1043.51227	Eukaryotic translation initiation factor 3 subunit G
HELLSLASSNHLGK	HELLSLASSNHLGB	1512.81397	Eukaryotic translation initiation factor 3 subunit H
ILYLTPEQEK	ILYLTPEQEB	1240.67944	Eukaryotic peptide chain release factor subunit 1
VGENADSQIK	VGENADSQIB	1067.53384	Histone H1.0
GQLEQITGK	GQLEQITGB	980.5382	Heterochromatin protein 1-binding protein 3
NVTLNPDPNEIK	NVTLNPDPNEIB	1360.70778	Isopentenyl-diphosphate Delta-isomerase 1
EVSFDVELPK	EVSFDVELPB	1169.60593	Inter-alpha-trypsin inhibitor heavy chain H3
IGLIQGNR	IGLIQGNX	879.51656	6-phosphofructokinase, muscle type
TVGIDDLTGEPLIQR	TVGIDDLTGEPLIQX	1635.87069	GTP:AMP phosphotransferase AK3, mitochondrial

ILQGGVGIPHIR	ILQGGVGIPHIX	1268.75923	Casein kinase I isoform alpha
YLEESNFVHR	YLEESNFVHX	1302.62321	Tyrosine-protein kinase SYK
YHEEFEK	YHEEFEB	988.43815	LIM and SH3 domain protein 1
SADTLWGIQK	SADTLWGIQB	1125.59096	L-lactate dehydrogenase A chain
LTTVPTQAFEYLSK	LTTVPTQAFEYLSB	1604.85411	Leucine-rich repeat-containing protein 4B
VLNHPNIVK	VLNHPNIVB	1040.6222	Serine/threonine-protein kinase MARK2
NSIASCADEQPHIGNYR	NSIASZADEQPHIGNYX	1940.86743	MAP/microtubule affinity-regulating kinase 3
DLGSELVR	DLGSELVX	897.4795	Hepatocyte growth factor receptor
FVIGGPQGDAGLTGR	FVIGGPQGDAGLTGX	1453.75526	S-adenosylmethionine synthase isoform type-2
LFPDVLFPADSEHNK	LFPDVLFPADSEHNB	1735.86605	Mitogen-activated protein kinase 8
HAFFEGLNWENIR	HAFFEGLNWENIX	1641.79272	Serine/threonine-protein kinase MRCK beta
EGLEETLR	EGLEETLX	955.48498	Neurofilament light polypeptide
FACHSASLTVR	FAZHSASLTVX	1257.61635	Non-POU domain-containing octamer-binding protein
TGTSCALDCGAGIGR	TGTSZALDZGAGIGX	1504.66376	N-terminal Xaa-Pro-Lys N-methyltransferase 1
VEGGTPLFTLR	VEGGTPLFTLX	1198.65852	Dihydrolipoyllysine-residue succinyltransferase component of 2-oxoglutarate dehydrogenase complex, mitochondrial
IQDLIDDK	IQDLIDDB	966.51131	Pachytene checkpoint protein 2 homolog
GFLLWYSGR	GFLLWYSGX	1107.57407	Procollagen C-endopeptidase enhancer 1
ALLPILQWHK	ALLPILQWHB	1225.74264	[Pyruvate dehydrogenase [acetyl-transferring]]-phosphatase 1, mitochondrial
SGGASHSELIHNLR	SGGASHSELIHNLX	1486.75159	Protein-L-isoaspartate(D-aspartate) O-methyltransferase
SNFGYNIPLK	SNFGYNIPLB	1159.6117	Proteasome subunit alpha type-3
DGSSGGVIR	DGSSGGVIX	856.4278	Proteasome subunit beta type-6
LFLQNNLIR	LFLQNNLIX	1139.66904	Reticulon-4 receptor-like 2
IDIDPEETVK	IDIDPEETVB	1165.59576	UV excision repair protein RAD23 homolog B
VELCSFSGYK	VELZSFSGYB	1196.5627	60S ribosomal protein L24
VFQFLNAK	VFQFLNAB	973.54764	60S ribosomal protein L24
NCSSFLIK	NZSSFLIB	975.4939	60S ribosomal protein L28
YNGLIHR	YNGLIHX	881.4747	60S ribosomal protein L28
TGSQGQCTQVR	TGSQGQZTQVX	1230.56506	40S ribosomal protein S28
DVTCDVHYENYR	DVTZDVHYENYX	1579.66007	Septin-5
IYEFPETDDEEENK	IYEFPETDDEEENB	1764.74573	Septin-7
TPPSEEDSAEAER	TPPSEEDSAEAEX	1426.60873	Small glutamine-rich tetratricopeptide repeat-containing protein alpha
VADISGDTQK	VADISGDTQB	1040.52294	Staphylococcal nuclease domain-containing protein 1
SIEQSIEQEEGLNR	SIEQSIEQEEGLNX	1640.7881	Syntaxin-1A
IADGYEQAAR	IADGYEQAAX	1102.52824	T-complex protein 1 subunit epsilon
LNWLSVDFNNWK	LNWLSVDFNNWB	1542.77105	Prostaglandin E synthase 3
VLDASWYSPGTR	VLDASWYSPGTX	1360.66507	Thiosulfate sulfurtransferase
DEFPLLTTK	DEFPLLTTB	1070.57391	Thymidylate synthase
TFEDIPLEEPEVK	TFEDIPLEEPEVB	1552.77517	Vascular endothelial growth factor receptor 2
DLLNHAFFQEETGVR	DLLNHAFFQEETGVX	1784.87209	Serine/threonine-protein kinase WNK1
EVYLSGSFNNWSK	EVYLSGSFNNWSB	1537.72925	5'-AMP-activated protein kinase subunit beta-1
LTLLAQQK	LTLLAQQB	921.57386	Long-chain-fatty-acid--CoA ligase 4
EGYSGVGLLSR	EGYSGVGLLSX	1146.59084	DNA-(apurinic or apyrimidinic site) lyase
YNPNVLPVQCTGK	YNPNVLPVQZTGB	1496.75369	Sodium/potassium-transporting ATPase subunit beta-1
ATLWYVPLSLK	ATLWYVPLSLB	1297.75254	Cytosolic acyl coenzyme A thioester hydrolase
IIQLIEGK	IIQLIEGB	920.5786	3'(2'),5'-bisphosphate nucleotidase 1
AEEDEILNR	AEEDEILNX	1097.52282	Calnexin
CVNTTLQIK	ZVNTTLQIB	1083.58378	Adenylyl cyclase-associated protein 1
YPLYVLK	YPLYVLB	902.53568	Carboxypeptidase B2
FTQISPVWLQLK	FTQISPVWLQLB	1466.83767	Chitinase domain-containing protein 1

HVVFYPTLK	HVVFYPTLB	1110.6317	Chitinase domain-containing protein 1
AVLFCLSEDK	AVLFZLSEDB	1188.59399	Cofilin-1
HELQANCYEEVK	HELQANZYEEVB	1526.69148	Cofilin-1
HGVFLVR	HGVFLVX	836.48961	Adapter molecule crk
SINSILDYISTSK	SINSILDYISTSB	1447.76497	COP9 signalosome complex subunit 2
NVLCSACSGQGGK	NVLZSAZSGQGGB	1344.60056	DnaJ homolog subfamily A member 2
ELAEQLGLSTGEK	ELAEQLGLSTGEB	1381.718	Eukaryotic translation initiation factor 3 subunit G
NVLVSSNDCVK	NVLVSSNDZVB	1241.61653	Focal adhesion kinase 1
LLLAGYDDFNCNVWDALK	LLLAGYDDFNZNVWDALB	2134.02844	Guanine nucleotide-binding protein G(I)/G(S)/G(T) subunit beta-1
SIQEIQELDK	SIQEIQELDB	1209.63322	Rho GDP-dissociation inhibitor 1
VAPSAVLGPNVSIGK	VAPSAVLGPNVSIGB	1415.82273	Mannose-1-phosphate guanyltransferase alpha
HDGAFLIR	HDGAFLIX	937.5009	Growth factor receptor-bound protein 2
TFDEIASGFR	TFDEIASGFX	1151.54864	Solute carrier family 2, facilitated glucose transporter member 1
VICAEEPYICK	VIZAEEPYIZB	1388.65594	GMP synthase [glutamine-hydrolyzing]
GLPWSCSADEVQR	GLPWSZSADEVQX	1513.68588	Heterogeneous nuclear ribonucleoprotein H
VDPEIQNVK	VDPEIQNVB	1048.56441	Keratin, type II cytoskeletal 2 epidermal
SEIDNVK	SEIDNVB	811.41669	Keratin, type II cytoskeletal 1
LTTFQALQHPWVTGK	LTTFQALQHPWVTGB	1733.93442	Calcium/calmodulin-dependent protein kinase type IV
VLTPELYAELR	VLTPELYAELX	1312.7266	Creatine kinase B-type
FEACNYPLELYER	FEAZNYPLELYEX	1712.77436	Protein kinase C gamma type
YAVTDDYQLSK	YAVTDDYQLSB	1309.62814	MAP kinase-activated protein kinase 3
LETLGIGQR	LETLGIGQX	995.5639	Methionine adenosyltransferase 2 subunit beta
FQFPSHVTDVSEEAK	FQFPSHVTDVSEEAB	1727.82459	Serine/threonine-protein kinase MRCK beta
DQGTYEDYVEGLR	DQGTYEDYVEGLX	1553.68732	Myosin light polypeptide 6
YAVLYQPLFDK	YAVLYQPLFDB	1363.72672	Nucleosome assembly protein 1-like 1
VGWIFTDLVSEDTR	VGWIFTDLVSEDTX	1646.81793	Nuclear protein localization protein 4 homolog
GPSSVEDIK	GPSSVEDIB	938.48001	Nucleophosmin
EFSPFGTITSAK	EFSPFGTITSAB	1291.65395	Polyadenylate-binding protein 1
GYGFVHFETQEAAER	GYGFVHFETQEAAEX	1749.79859	Polyadenylate-binding protein 1
DGLILTSR	DGLILTSX	883.50024	Protein DJ-1
FYGPAGPYGIFAGR	FYGPAGPYGIFAGX	1481.73307	Membrane-associated progesterone receptor component 2
IITEGASILR	IITEGASILX	1081.63706	Serine/threonine-protein phosphatase 2B catalytic subunit alpha isoform
GVNTFSPEGR	GVNTFSPEGX	1072.51768	Proteasome subunit alpha type-5
TTTGSYIANR	TTTGSYIANX	1092.54391	Proteasome subunit beta type-6
YSSPANLYVR	YSSPANLYVX	1178.59594	Receptor-type tyrosine-protein phosphatase S
TFAYTNHTVLPEALER	TFAYTNHTVLPEALEX	1870.94526	Glycogen phosphorylase, liver form
EILGTAQSVGCNVDGR	EILGTAQSVGZNVDGX	1684.80778	60S ribosomal protein L12
STESLQANVQR	STESLQANVQX	1241.62395	60S ribosomal protein L13
TIGISVDPR	TIGISVDPX	966.53735	60S ribosomal protein L13
NQSFCPTVNLDK	NQSFZPTVNLDB	1429.67511	60S ribosomal protein L27a
DETEFYLGK	DETEFYLGB	1108.51679	60S ribosomal protein L35a
AGNFYVPAEPK	AGNFYVPAEPB	1199.6066	60S ribosomal protein L7
IVEPYIAWGYPNLK	IVEPYIAWGYPNLB	1669.8959	60S ribosomal protein L7
HFYWYLTNEGIQYLR	HFYWYLTNEGIQYLX	2011.98199	40S ribosomal protein S10
TVQVEQSK	TVQVEQSB	925.49601	Septin-7
HSAILASPNPDEK	HSAILASPNPDEB	1385.70302	Syntaxin-1A
AVFDETYPDPVR	AVFDETYPDPVX	1417.67529	Alanine--tRNA ligase, cytoplasmic
ALYESEENCEVDPIK	ALYESEENZEVDPIB	1802.81237	Ras/Rap GTPase-activating protein SynGAP
ALTVPELTQQVFDAK	ALTVPELTQQVFDAB	1666.90211	Tubulin beta chain

SEALGVGDVK	SEALGVGDVB	981.5222	Testin
SPQELLCGASLISDR	SPQELLZGASLISDX	1654.82237	Prothrombin
YGFYTHVFR	YGFYTHVFX	1198.57989	Prothrombin
TVSVLNGGFR	TVSVLNGGFX	1058.5748	Thiosulfate sulfurtransferase
TATPQQAQEVHEK	TATPQQAQEVHEB	1473.73031	Triosephosphate isomerase
DQYELLCLDNTR	DQYELLZLDNTX	1548.71177	Serotransferrin
LYVELHR	LYVELHX	938.52131	UBX domain-containing protein 1
DLNPDVNVFQR	DLNPDVNVFQX	1325.66032	V-type proton ATPase 116 kDa subunit a isoform 1
FYDSWESTVK	FYDSWESTVB	1268.58046	Serine/threonine-protein kinase WNK1
LLWTLESLVTGR	LLWTLESLVTGX	1396.79535	Aldehyde dehydrogenase family 16 member A1
GIVNEQFLLQR	GIVNEQFLLQX	1325.73309	Very long-chain specific acyl-CoA dehydrogenase, mitochondrial
IAFLPFGYLVDQWR	IAFLPFGYLVDQWX	1733.91685	Angiotensin-converting enzyme
VGAPLVCCEIK	VGAPLVZZEIB	1252.63989	Long-chain-fatty-acid--CoA ligase 3
AAYFGIYDTAK	AAYFGIYDTAB	1226.60627	ADP/ATP translocase 2
FLVNLVK	FLVNLVB	839.53601	Afamin
GILAADESTGSIAK	GILAADESTGSIAB	1339.70743	Fructose-bisphosphate aldolase A
TQDVFTVIR	TQDVFTVIX	1087.59012	Glutamyl aminopeptidase
SEIDLLNIR	SEIDLLNIX	1081.60068	Annexin A6
ANACNSVIK	ANAZNSVIB	983.49496	Sarcoplasmic/endoplasmic reticulum calcium ATPase 2
LVASAYSIAQK	LVASAYSIAQB	1157.65356	3'(2'),5'-bisphosphate nucleotidase 1
YSFTIELR	YSFTIELX	1037.54211	Carboxypeptidase B2
LTASAPGYLAITK	LTASAPGYLAITB	1312.74818	Carboxypeptidase E
DLYSGLIGPLIVCR	DLYSGLIGPLIVZX	1584.85729	Ceruloplasmin
WDYLTQVEK	WDYLTQVEB	1188.59063	Calcyclin-binding protein
LLLQLEATK	LLLQLEATB	1035.64193	Dynactin subunit 2
INCPVYITK	INZPVYITB	1114.59361	Dihydropyrimidinase-related protein 1
VAVFFGGLSIK	VAVFFGGLSIB	1144.67355	Spliceosome RNA helicase DDX39B
EAALGAGFSDK	EAALGAGFSDB	1072.52801	Trifunctional enzyme subunit beta, mitochondrial
VNQIGSVTESLQACK	VNQIGSVTESLQAZB	1640.82831	Alpha-enolase
TAIQAAGYPDK	TAIQAAGYPDB	1141.58587	Beta-enolase
VNQIGSVTESIQACK	VNQIGSVTESIQAZB	1640.82831	Beta-enolase
AVLHVALR	AVLHVALX	887.55802	Glucose-6-phosphate isomerase
AVILIGGPQK	AVILIGGPQB	1002.63169	Mannose-1-phosphate guanyltransferase alpha
VTILELFR	VTILELFX	999.59922	Solute carrier family 2, facilitated glucose transporter member 1
GIVEECCFR	GIVEEZZFX	1178.50877	Insulin-like growth factor II
VLVVHDGFEGLAK	VLVVHDGFEGLAB	1390.76996	6-phosphofructokinase, muscle type
NPDSQYGELIEK	NPDSQYGELIEB	1399.67106	UMP-CMP kinase
LSVEIWDWDR	LSVEIWDWDX	1327.6436	Protein kinase C alpha type
EFIWGVFGK	EFIWGVFGB	1089.57384	Protein kinase C eta type
SVVYQETNGETR	SVVYQETNGETX	1391.65564	Phosphoribosyl pyrophosphate synthase-associated protein 1
HLEILQLSK	HLEILQLSB	1087.64808	Leucine-rich repeat-containing protein 4B
ITPENLPQILLQLK	ITPENLPQILLQLB	1626.97997	Matrin-3
DLIGFGLQVAK	DLIGFGLQVAB	1167.67428	Hepatocyte growth factor receptor
VCGSNLLSICK	VZGSNLLSIZB	1257.63007	Myelin proteolipid protein
FFLCQVAGDAK	FFLZQVAGDAB	1262.62087	Neural cell adhesion molecule 1
FIVLSNNYLQIR	FIVLSNNYLQIX	1488.83281	Neural cell adhesion molecule 1
IDVAFVDR	IDVAFVDX	943.50023	Pachytene checkpoint protein 2 homolog
FNVYCFR	FNVYZFX	1014.46209	Brevican core protein
GVVFLYR	GVVFLYX	862.49403	Brevican core protein
LTAEQALQHPFFER	LTAEQALQHPFFEX	1695.8608	Phosphorylase b kinase gamma catalytic chain, liver/testis isoform

237

LEESVALR	LEESVALX	925.5108	Serine/threonine-protein phosphatase 2B catalytic subunit alpha isoform
FVTLVFR	FVTLVFX	890.52533	Prostatic acid phosphatase
AVENSSTAIGIR	AVENSSTAIGIX	1226.64942	Proteasome subunit alpha type-3
ANINIEK	ANINIEB	808.45341	Ras-related protein Rab-10
DTLYEAVR	DTLYEAVX	975.49007	60S ribosomal protein L10a
IEGVYAR	IEGVYAX	816.43691	60S ribosomal protein L35a
FCIWTESAFR	FZIWTESAFX	1325.6102	60S ribosomal protein L4
DYLHLPPEIVPATLR	DYLHLPPEIVPATLX	1742.95944	40S ribosomal protein S10
LGEWVGLCK	LGEWVGLZB	1068.55173	40S ribosomal protein S12
VVGCSCVVVK	VVGZSZVVVB	1113.57657	40S ribosomal protein S12
IVVNLTGR	IVVNLTGX	880.53696	40S ribosomal protein S15a
NAWADNANACAK	NAWADNANAZAB	1312.57097	Phosphatidylinositide phosphatase SAC1
FLEEFITPIVK	FLEEFITPIVB	1342.76276	DNA topoisomerase 2-alpha
TLAVSGLGVVGR	TLAVSGLGVVGX	1137.6745	DNA topoisomerase 2-alpha
ITAFVVER	ITAFVVEX	943.53662	Very long-chain specific acyl-CoA dehydrogenase, mitochondrial
HDAVTDTIDIAPNQR	HDAVTDTIDIAPNQX	1674.82006	Activin receptor type-1B
AYGTGFVGCLR	AYGTGFVGZLX	1209.58398	Agrin
ANILYAWAR	ANILYAWAX	1086.58497	Peptidyl-glycine alpha-amidating monooxygenase
NNLVIFHR	NNLVIFHX	1021.56966	Peptidyl-glycine alpha-amidating monooxygenase
WYVVQTNYDR	WYVVQTNYDX	1352.63887	Acid ceramidase
IYLILEYAPR	IYLILEYAPX	1259.71531	Aurora kinase B
NLFIQVDYFPLTEQK	NLFIQVDYFPLTEQB	1861.97053	Contactin-associated protein 1
LLHEVQELTTEVEK	LLHEVQELTTEVEB	1674.89194	Dynactin subunit 2
AYALAFAER	AYALAFAEX	1020.52678	Peroxisomal multifunctional enzyme type 2
TLEVEIEPGVR	TLEVEIEPGVX	1250.67456	DnaJ homolog subfamily B member 11
NCPHIVVGTPGR	NZPHIVVGTPGX	1315.66944	Spliceosome RNA helicase DDX39B
LAAAFAVSR	LAAAFAVSX	914.5213	Trifunctional enzyme subunit beta, mitochondrial
VIGNGSFGVVYQAR	VIGNGSFGVVYQAX	1475.77601	Glycogen synthase kinase-3 alpha
GASGSFVVVQK	GASGSFVVVQB	1085.59604	Heterochromatin protein 1-binding protein 3
DIDILIVR	DIDILIVX	965.57848	Isocitrate dehydrogenase [NAD] subunit gamma, mitochondrial
AFSVFLFNTENK	AFSVFLFNTENB	1423.7227	Isopentenyl-diphosphate Delta-isomerase 1
GFSSGSAVVSGGSR	GFSSGSAVVSGGSX	1263.60828	Keratin, type II cytoskeletal 2 epidermal
GTEELYAIK	GTEELYAIB	1030.54261	Protein kinase C alpha type
IGEAVGLQPTR	IGEAVGLQPTX	1149.63812	Protein kinase C eta type
NVLLVTQHYAK	NVLLVTQHYAB	1292.73321	Tyrosine-protein kinase SYK
GFSVVADTPELQR	GFSVVADTPELQX	1427.72839	LIM and SH3 domain protein 1
VTLITENLGHPR	VTLITENLGHPX	1358.75455	Low-density lipoprotein receptor-related protein 2
AVLENNLGAAVLR	AVLENNLGAAVLX	1348.77019	Methionine adenosyltransferase 2 subunit beta
GLSATVTGGQK	GLSATVTGGQB	1025.55966	Myelin proteolipid protein
AGEVFIHK	AGEVFIHB	907.50068	Non-POU domain-containing octamer-binding protein
GIPEFWLTVFK	GIPEFWLTVFB	1343.73688	Nucleosome assembly protein 1-like 1
FVALENISCK	FVALENISZB	1187.60998	Nuclear protein localization protein 4 homolog
SDLYIGGVAK	SDLYIGGVAB	1029.55859	Neurexin-1
GLVVPVIR	GLVVPVIX	861.56752	Dihydrolipoyllysine-residue succinyltransferase component of 2-oxoglutarate dehydrogenase complex, mitochondrial
VTVAGLAGK	VTVAGLAGB	822.50543	Protein DJ-1
YGSVTVWR	YGSVTVWX	976.50058	Serine/threonine-protein phosphatase 4 catalytic subunit
GFFLLVEGGR	GFFLLVEGGX	1103.60027	Alkaline phosphatase, tissue-nonspecific isozyme
NILQLHDLTTGALLK	NILQLHDLTTGALLB	1656.96538	Prolyl endopeptidase
DTNGSQFFITTVK	DTNGSQFFITTVB	1464.734	Peptidyl-prolyl cis-trans isomerase B

VNLAELFK	VNLAELFB	940.5473	Peroxiredoxin-5, mitochondrial
FSNQETSVEIGESVR	FSNQETSVEIGESVX	1690.80375	Ribose-phosphate pyrophosphokinase 2
DGIVLGADTR	DGIVLGADTX	1025.53807	Proteasome subunit beta type-7
FHTITTSYYR	FHTITTSYYX	1297.63306	Ras-related protein Rab-10
ASVDELFAEIVR	ASVDELFAEIVX	1357.71167	Ras-related protein Rap-2b
LWTLVSEQTR	LWTLVSEQTX	1241.66435	60S ribosomal protein L27a
AFLIEEQK	AFLIEEQB	984.53713	60S ribosomal protein L34
FLDGIYVSEK	FLDGIYVSEB	1177.61102	60S ribosomal protein L9
LTNVAVVR	LTNVAVVX	880.53696	Ribosome maturation protein SBDS
GLLDVTCK	GLLDVTZB	912.48299	S-phase kinase-associated protein 1
SSHYDELLAAEAR	SSHYDELLAAEAX	1470.69782	Staphylococcal nuclease domain-containing protein 1
LVVVDFSATWCGPCK	LVVVDFSATWZGPZB	1745.83602	Thioredoxin
ASVITQVFHVPLEER	ASVITQVFHVPLEEX	1733.93396	Vigilin
TAFDEAIAELDTLNEESYK	TAFDEAIAELDTLNEESYB	2166.00954	14-3-3 protein beta/alpha
SIDDEVVEQR	SIDDEVVEQX	1198.5705	5'-AMP-activated protein kinase catalytic subunit alpha-2
AEDGSVIDYELIDQDAR	AEDGSVIDYELIDQDAX	1917.8831	Annexin A2
NSVSQISVLSGGK	NSVSQISVLSGGB	1282.69722	Actin-related protein 2/3 complex subunit 1B
LEVEANNAFDQYR	LEVEANNAFDQYX	1577.73494	F-actin-capping protein subunit beta
STLNEIYFGK	STLNEIYFGB	1178.60628	F-actin-capping protein subunit beta
AGQVFLEELGNHK	AGQVFLEELGNHB	1448.7503	2',3'-cyclic-nucleotide 3'-phosphodiesterase
VSHYIINSLPNR	VSHYIINSLPNX	1421.76546	Crk-like protein
ITNSLTVLCSEK	ITNSLTVLZSEB	1371.71591	Eukaryotic translation initiation factor 3 subunit J
FAEIVNTLDK	FAEIVNTLDB	1156.62192	Ephrin type-B receptor 1
AQLSTILEEEK	AQLSTILEEEB	1267.67508	Focal adhesion kinase 1
EAEILEVLR	EAEILEVLX	1080.60542	Coproporphyrinogen-III oxidase, mitochondrial
AHQLWLSVEALK	AHQLWLSVEALB	1401.78596	Mitochondrial inner membrane protein
VVSQYHELVVQAR	VVSQYHELVVQAX	1536.82878	Mitochondrial inner membrane protein
TNAENEFVTIK	TNAENEFVTIB	1272.64412	Keratin, type II cytoskeletal 1
AASAHAIGTVK	AASAHAIGTVB	1032.58072	cAMP-dependent protein kinase type II-beta regulatory subunit
GQDIFIIQTIPR	GQDIFIIQTIPX	1409.7906	Phosphoribosyl pyrophosphate synthase-associated protein 1
EAFTVIDQNR	EAFTVIDQNX	1201.59666	Myosin regulatory light chain 2, skeletal muscle isoform
GADPEDVITGAFK	GADPEDVITGAFB	1326.65466	Myosin regulatory light chain 2, skeletal muscle isoform
ALVEEALAQR	ALVEEALAQX	1108.61157	UPF0160 protein MYG1, mitochondrial
HVLVTLGEK	HVLVTLGEB	1002.59531	Myosin light polypeptide 6
ITTQITAGAR	ITTQITAGAX	1040.58537	Neurexin-1
GCITIIGGGDTATCCAK	GZITIIGGGDTATZZAB	1761.7939	Phosphoglycerate kinase 1
EILVEESNVQR	EILVEESNVQX	1324.6862	Serine/threonine-protein phosphatase 4 catalytic subunit
SVGIVTTTR	SVGIVTTTX	942.53736	Alkaline phosphatase, tissue-nonspecific isozyme
FGPYYTEPVIAGLDPK	FGPYYTEPVIAGLDPB	1773.90685	Proteasome subunit beta type-3
IEDGNDFGVAIQEK	IEDGNDFGVAIQEB	1541.74527	Proteasome activator complex subunit 2
SAINEVVTR	SAINEVVTX	997.54317	60S ribosomal protein L31
DFNHINVELSLLGK	DFNHINVELSLLGB	1605.86058	60S ribosomal protein L9
EGDVLTLLESER	EGDVLTLLESEX	1369.69642	40S ribosomal protein S28
DIATIVADK	DIATIVADB	952.53204	Ribosome maturation protein SBDS
AIELNPANAVYFCNR	AIELNPANAVYFZNX	1760.85434	Small glutamine-rich tetratricopeptide repeat-containing protein alpha
ISVYYNEATGGK	ISVYYNEATGGB	1308.64412	Tubulin beta chain
VVLAYEPVWAIGTGK	VVLAYEPVWAIGTGB	1609.89589	Triosephosphate isomerase
GSLTFEPLTLVPIQTK	GSLTFEPLTLVPIQTB	1750.99601	Xaa-Pro aminopeptidase 1
TIVLQEIIGK	TIVLQEIIGB	1120.69469	Activin receptor type-1B

EGDLITLLVPEAR	EGDLITLLVPEAX	1434.79573	Brain-specific angiogenesis inhibitor 1-associated protein 2
FGVVVVGVGR	FGVVVVGVGX	997.59479	Biliverdin reductase A
INSITVDNCK	INSITVDNZB	1170.57942	Adenylyl cyclase-associated protein 1
IGLVEALCGFQFTFK	IGLVEALZGFQFTFB	1736.90508	DnaJ homolog subfamily A member 2
LGGEVSCLVAGTK	LGGEVSZLVAGTB	1297.67911	Electron transfer flavoprotein subunit alpha, mitochondrial
SFLIWVNEEDHTR	SFLIWVNEEDHTX	1654.79787	Creatine kinase U-type, mitochondrial
LGIYTVLFER	LGIYTVLFEX	1219.68401	Mitochondrial 2-oxoglutarate/malate carrier protein
QVLGLGVNGK	QVLGLGVNGB	991.59056	MAP kinase-activated protein kinase 3
NIIGLLNVFTPQK	NIIGLLNVFTPQB	1463.85913	Mitogen-activated protein kinase 8
SGNVAELALK	SGNVAELALB	1008.56949	Nuclear autoantigenic sperm protein
IVTSEEVIIR	IVTSEEVIIX	1167.67384	Neuroplastin
SAAQAAAQTNSNAAGK	SAAQAAAQTNSNAAGB	1467.71572	Plasminogen activator inhibitor 1 RNA-binding protein
LNVEFALIHK	LNVEFALIHB	1190.69027	Ribose-phosphate pyrophosphokinase 2
SALTVQFVTGSFIEK	SALTVQFVTGSFIEB	1633.88065	Ras-related protein Rap-2b
HGYIGEFEIIDDHR	HGYIGEFEIIDDHX	1709.80367	40S ribosomal protein S15a
AALCHFIVDELNAK	AALZHFIVDELNAB	1607.82208	Beta-soluble NSF attachment protein
GAFGQVIEADAFGIDK	GAFGQVIEADAFGIDB	1644.82384	Vascular endothelial growth factor receptor 2
DFLAGGVAAAISK	DFLAGGVAAAISB	1226.675	ADP/ATP translocase 2
DAFVAIVQSVK	DAFVAIVQSVB	1183.6692	Annexin A6
DIVPGDIVEIAVGDK	DIVPGDIVEIAVGDB	1546.83334	Sarcoplasmic/endoplasmic reticulum calcium ATPase 2
GQTLVVQFTVK	GQTLVVQFTVB	1226.71141	Calreticulin
IDVVNNAGILR	IDVVNNAGILX	1291.74873	Peroxisomal multifunctional enzyme type 2
LSVLGAITSVQQR	LSVLGAITSVQQX	1380.79642	Eukaryotic peptide chain release factor subunit 1
ETEEILADVLK	ETEEILADVLB	1266.67982	Eukaryotic translation initiation factor 6
LWAYLTIEQLLEK	LWAYLTIEQLLEB	1626.91122	Inter-alpha-trypsin inhibitor heavy chain H3
TVLVSEGIVTPR	TVLVSEGIVTPX	1279.7375	Low-density lipoprotein receptor-related protein 2
LVEVNGENVEK	LVEVNGENVEB	1236.64411	Na(+)/H(+) exchange regulatory cofactor NHE-RF1
FIATLQYIVGR	FIATLQYIVGX	1289.73711	Prolyl endopeptidase
TGTTIAGVVYK	TGTTIAGVVYB	1116.62701	Proteasome subunit beta type-7
NPILWNVADVVIK	NPILWNVADVVIB	1487.85912	Dolichyl-diphosphooligosaccharide--protein glycosyltransferase subunit 2
TGQEVVFVAEPDNK	TGQEVVFVAEPDNB	1539.76601	Dolichyl-diphosphooligosaccharide--protein glycosyltransferase subunit 2
VANVSLLALYK	VANVSLLALYB	1197.72124	40S ribosomal protein S23
GVLEELLWFIK	GVLEELLWFIB	1353.77874	Thymidylate synthase
LQLLEPFDK	LQLLEPFDB	1109.62119	Aconitate hydratase, mitochondrial
TIPWLEDR	TIPWLEDX	1038.53735	Alpha-actinin-4
SASFNTDPYVR	SASFNTDPYVX	1265.59158	Protein argonaute-2
ELWFSDDPNVTK	ELWFSDDPNVTB	1457.69179	Apoptosis-inducing factor 1, mitochondrial
SATEQSGTGIR	SATEQSGTGIX	1115.54463	Apoptosis-inducing factor 1, mitochondrial
DITSDTSGDFR	DITSDTSGDFX	1222.53412	Annexin A1
TPAQFDADELR	TPAQFDADELX	1271.60213	Annexin A1
YGTDLSR	YGTDLSX	820.39545	Sodium/potassium-transporting ATPase subunit alpha-1
FDTDELNFPTEK	FDTDELNFPTEB	1462.67072	Sodium/potassium-transporting ATPase subunit alpha-2
SPDCTHDNPLETR	SPDZTHDNPLETX	1550.66588	Sodium/potassium-transporting ATPase subunit alpha-3
IDESSLTGESDQVR	IDESSLTGESDQVX	1544.71935	Plasma membrane calcium-transporting ATPase 2
IPVGPETLGR	IPVGPETLGX	1047.59519	ATP synthase subunit beta, mitochondrial
LADDLYR	LADDLYX	874.44239	Attractin
LTLTPWVGLR	LTLTPWVGLX	1164.68943	Attractin
FSDIQIR	FSDIQIX	887.47403	C-1-tetrahydrofolate synthase, cytoplasmic
GPFPQELVR	GPFPQELVX	1051.56898	Cadherin-2
NLDENGLDLLSK	NLDENGLDLLSB	1337.69179	Cyclin-dependent kinase 1

VVPPLDEDGR	VVPPLDEDGX	1105.56428	Cyclin-dependent kinase 2
DLLQNLLK	DLLQNLLB	963.58442	Cyclin-dependent kinase 5
IGNCPFSQR	IGNZPFSQX	1087.51083	Chloride intracellular channel protein 1
NSNPALNDNLEK	NSNPALNDNLEB	1335.651	Chloride intracellular channel protein 1
IGDWLQER	IGDWLQEX	1025.51695	Dual specificity protein kinase CLK3
FGFLQEFSK	FGFLQEFSB	1109.56368	Contactin-2
GPAGPQGPR	GPAGPQGPX	845.4383	Collagen alpha-1(I) chain
FNDILGR	FNDILGX	843.44781	Casein kinase II subunit alpha
ALQDLGLR	ALQDLGLX	894.51622	N(G),N(G)-dimethylarginine dimethylaminohydrolase 2
NLYAGDYYR	NLYAGDYYX	1143.52244	Epithelial discoidin domain-containing receptor 1
LNLSQVR	LNLSQVX	838.49002	ATP-dependent RNA helicase DDX1
TGHSLLHTLYGR	TGHSLLHTLYGX	1363.72359	Succinate dehydrogenase [ubiquinone] flavoprotein subunit, mitochondrial
ISLQWLR	ISLQWLX	924.54205	Dipeptidyl peptidase 4
ELLGQGLLLR	ELLGQGLLLX	1120.68434	Eukaryotic translation initiation factor 3 subunit C
SYSSGGEDGYVR	SYSSGGEDGYVX	1285.54502	Eukaryotic translation initiation factor 3 subunit I
FDTQYPYGEK	FDTQYPYGEB	1254.56481	Endoplasmic reticulum resident protein 29
SGYLSSER	SGYLSSEX	907.42748	Ezrin
FDASFFGVHPK	FDASFFGVHPB	1258.62258	Fatty acid synthase
LSPDAIPGK	LSPDAIPGB	904.51091	Fatty acid synthase
IPSNPSHR	IPSNPSHX	916.47543	EGF-containing fibulin-like extracellular matrix protein 1
LNCEDIDECR	LNZEDIDEZX	1332.53136	EGF-containing fibulin-like extracellular matrix protein 1
STTPDITGYR	STTPDITGYX	1119.54357	Fibronectin
ALELDSNNEK	ALELDSNNEB	1139.55497	Peptidyl-prolyl cis-trans isomerase FKBP4
LSFQEFLK	LSFQEFLB	1018.55787	Follistatin-related protein 1
GTPQQIDYAR	GTPQQIDYAX	1157.57045	Far upstream element-binding protein 1
QLLSFGNPR	QLLSFGNPX	1040.56424	Tyrosine-protein kinase Fyn
LWDLTTGTTTR	LWDLTTGTTTX	1273.65418	Guanine nucleotide-binding protein subunit beta-2-like 1
QLICDPSYIPDR	QLIZDPSYIPDX	1485.71612	Rab GDP dissociation inhibitor alpha
SIAFPSIGSGR	SIAFPSIGSGX	1100.58536	Core histone macro-H2A.1
NLPLPPPPPPR	NLPLPPPPPPX	1203.70032	Heterogeneous nuclear ribonucleoprotein K
ADHGEPIGR	ADHGEPIGX	960.46524	Heat shock protein HSP 90-beta
LDGNQDLIR	LDGNQDLIX	1052.54898	Isocitrate dehydrogenase [NADP], mitochondrial
DEQLESLFQR	DEQLESLFQX	1273.61779	Eukaryotic translation initiation factor 2 subunit 1
ISSSSFSR	ISSSSFSX	879.43257	Keratin, type II cytoskeletal 8
WSLLQQQK	WSLLQQQB	1037.57493	Keratin, type II cytoskeletal 8
ITADQALK	ITADQALB	866.49527	Calcium/calmodulin-dependent protein kinase type II subunit gamma
SFGNPFEGSR	SFGNPFEGSX	1106.50203	Calcium/calmodulin-dependent protein kinase kinase 2
CSLNPEWNETFR	ZSLNPEWNETFX	1561.68589	Protein kinase C beta type
ANSLEPEPWFFK	ANSLEPEPWFFB	1471.72269	Tyrosine-protein kinase Lck
IDSLSAQLSQLQK	IDSLSAQLSQLQB	1437.79185	Prelamin-A/C
LQQLPADFGR	LQQLPADFGX	1153.61191	Leucine-rich repeat-containing protein 59
GSFSLSVR	GSFSLSVX	861.45838	Tyrosine-protein kinase Lyn
IYLSSAR	IYLSSAX	818.45257	Mitogen-activated protein kinase kinase kinase 1
EIQGLFDELR	EIQGLFDELX	1228.6327	Mitogen-activated protein kinase kinase kinase 11
LINQPLPDLK	LINQPLPDLB	1157.68994	Microtubule-associated protein 2
TPLYDLR	TPLYDLX	886.47878	Protein MEMO1
YSYYDESQGEIYR	YSYYDESQGEIYX	1681.71355	Protein MEMO1
NYLQSLPSK	NYLQSLPSB	1056.56951	Mitogen-activated protein kinase 3
ALELDSNLYR	ALELDSNLYX	1202.61706	Myosin-9
LDCPFFGSPIPTLR	LDZPFFGSPIPTLX	1628.82599	Neurofascin

FQLTFPLR	FQLTFPLX	1030.58391	Neuronal pentraxin-1
ELTDEEAER	ELTDEEAEX	1100.4861	Nuclear migration protein nudC
LQELSAEER	LQELSAEEX	1083.54356	Obg-like ATPase 1
VPVPDER	VPVPDEX	820.43182	Obg-like ATPase 1
SSLNPILFR	SSLNPILFX	1055.60029	Dolichyl-diphosphooligosaccharide--protein glycosyltransferase 48 kDa subunit
LLTSGYLQR	LLTSGYLQX	1059.59521	Ubiquitin thioesterase OTUB1
GLECSTLYR	GLEZSTLYX	1107.52581	Phosphatidylinositol 3-kinase regulatory subunit alpha
YGVSGYPTLK	YGVSGYPTLB	1091.57425	Protein disulfide-isomerase A3
FDVSGYPTIK	FDVSGYPTIB	1133.58481	Protein disulfide-isomerase A4
GYFFLDER	GYFFLDEX	1055.49515	PDZ and LIM domain protein 4
SQVEPADYK	SQVEPADYB	1043.50148	Phosphatidylinositol transfer protein beta isoform
TPENFPCK	TPENFPZB	999.45751	Plasminogen
FEDENFHYK	FEDENFHYB	1235.53384	Peptidyl-prolyl cis-trans isomerase D
ADEGISFR	ADEGISFX	903.43255	Peroxiredoxin-1
CTDDFNGAQCK	ZTDDFNGAQZB	1322.51108	26S protease regulatory subunit 6A
ETLPAEQDLTTK	ETLPAEQDLTTB	1352.69146	Proteasome subunit alpha type-1
TQIPTQR	TQIPTQX	852.46929	Proteasome subunit alpha type-1
LSEGFSIHTR	LSEGFSIHTX	1155.59118	Proteasome subunit beta type-1
DLPVSEQQER	DLPVSEQQEX	1209.58649	26S proteasome non-ATPase regulatory subunit 13
APLDIPVPDPVK	APLDIPVPDPVB	1267.7267	Proteasome activator complex subunit 1
NQGDFSLSVR	NQGDFSLSVX	1131.5548	Tyrosine-protein phosphatase non-receptor type 6
ACGNFGIPCELR	AZGNFGIPZELX	1402.63609	Multifunctional protein ADE2
LTSEPQPQR	LTSEPQPQX	1064.54899	Ras-related protein Rab-14
LALDYGIK	LALDYGIB	899.52075	Ras-related protein Rab-8A
NTLQLHR	NTLQLHX	890.49617	60S ribosomal protein L15
ECADLWPR	EZADLWPX	1055.47337	60S ribosomal protein L23
HGSLGFLPR	HGSLGFLPX	992.5431	60S ribosomal protein L3
YYPTEDVPR	YYPTEDVPX	1148.53775	60S ribosomal protein L6
NFGIGQDIQPK	NFGIGQDIQPB	1223.63897	60S ribosomal protein L7a
DIIHDPGR	DIIHDPGX	931.47508	60S ribosomal protein L8
GGNFGFGDSR	GGNFGFGDSX	1022.44451	Heterogeneous nuclear ribonucleoproteins A2/B1
NIDNFLSR	NIDNFLSX	987.50131	Rho-associated protein kinase 1
NSLTFPDDNDISK	NSLTFPDDNDISB	1472.68744	Rho-associated protein kinase 1
GLSQSALPYR	GLSQSALPYX	1100.58537	40S ribosomal protein S13
TPGPGAQSALR	TPGPGAQSALX	1063.56496	40S ribosomal protein S14
IPDWFLNR	IPDWFLNX	1069.55842	40S ribosomal protein S18
TTDGYLLR	TTDGYLLX	947.49516	40S ribosomal protein S3a
LNEQSPTR	LNEQSPTX	953.48058	Vesicle-trafficking protein SEC22b
ITQSEFDR	ITQSEFDX	1004.48024	Endophilin-B1
LHLDYIGPCK	LHLDYIGPZB	1222.62596	SPARC
LGESQTLQQFSR	LGESQTLQQFSX	1402.70801	Spectrin alpha chain, non-erythrocytic 1
DLEDLFYK	DLEDLFYB	1049.51606	Serine/arginine-rich splicing factor 9
ASSGLLYPLER	ASSGLLYPLEX	1214.65344	FACT complex subunit SSRP1
ALDLDSSCK	ALDLDSSZB	1015.47355	Stress-induced-phosphoprotein 1
VPQDGDFDFLK	VPQDGDFDFLB	1287.62264	Serine/threonine-protein kinase 3
DALSDLALHFLNK	DALSDLALHFLNB	1463.78635	T-complex protein 1 subunit delta
TEDFGLDVPAFR	TEDFGLDVPAFX	1375.66472	Dual specificity testis-specific protein kinase 1
GNLQEYLTR	GNLQEYLTX	1102.56464	TGF-beta receptor type-2
EELLDHLEK	EELLDHLEB	1132.58553	Tropomodulin-1

VTQSDLYK	VTQSDLYB	960.50076	Tumor protein D54
TDAPLNIR	TDAPLNIX	908.49549	Heat shock protein 75 kDa, mitochondrial
ILGPAESDEFLAR	ILGPAESDEFLAX	1426.73313	E3 ubiquitin-protein ligase UBR4
GNLQNLER	GNLQNLEX	952.49656	V-type proton ATPase subunit C 1
ALASQLQDSLK	ALASQLQDSLB	1180.65429	Vinculin
ELALPGELTQSR	ELALPGELTQSX	1322.70693	Vacuolar protein sorting-associated protein 26A
HYTEHADGLCHK	HYTEHADGLZHB	1474.65028	Tyrosine-protein kinase Yes
LLLNPGNQR	LLLNPGNQX	1033.59079	Tyrosine-protein kinase Yes
HLIPAANTGESK	HLIPAANTGESB	1244.66043	14-3-3 protein epsilon
SVTEQGAELSNEER	SVTEQGAELSNEEX	1557.7146	14-3-3 protein zeta/delta
AENYWWR	AENYWWX	1033.46453	Activated CDC42 kinase 1
TLCVGPFPR	TLZVGPFPX	1055.54614	Activated CDC42 kinase 1
VQQLVPK	VQQLVPB	818.51053	Alpha-actinin-4
VLQPPSILYGGR	VLQPPSILYGGX	1308.74292	Protein argonaute-2
SDGSFIGYK	SDGSFIGYB	980.46945	RAC-beta serine/threonine-protein kinase
LDQGGAPLAGTNK	LDQGGAPLAGTNB	1248.65534	Fructose-bisphosphate aldolase B
LLSTDPVAAK	LLSTDPVAAB	1021.58989	AP-1 complex subunit beta-1
FLELLPK	FLELLPB	866.53567	AP-2 complex subunit beta
LGYLLFR	LGYLLFX	890.52533	Beta-adrenergic receptor kinase 1
NFPLTISER	NFPLTISEX	1085.57447	Beta-adrenergic receptor kinase 1
EFSIDVGYER	EFSIDVGYEX	1223.56977	Actin-related protein 3
YSYVCPDLVK	YSYVZPDLVB	1250.60965	Actin-related protein 3
ASHTAPQVLFSHR	ASHTAPQVLFSHX	1459.75595	Actin-related protein 2/3 complex subunit 2
VLSIGDGIAR	VLSIGDGIAX	1009.57954	ATP synthase subunit alpha, mitochondrial
LSDPANWLK	LSDPANWLB	1050.55893	Cadherin-2
IFDLIGLPPEDDWPR	IFDLIGLPPEDDWPX	1791.90706	Cyclin-dependent kinase 4
LEAFEHPNVVR	LEAFEHPNVVX	1319.68613	Cyclin-dependent kinase 4
APELLFGAR	APELLFGAX	982.54751	Cyclin-dependent kinase 7
LLVLDPAQR	LLVLDPAQX	1033.61593	Cyclin-dependent kinase 9
HSIEVPIPR	HSIEVPIPX	1056.59553	Contactin-1
ADQCYEDVR	ADQZYEDVX	1164.4745	Coronin-1A
NITLDDASAPR	NITLDDASAPX	1181.59157	Cold shock domain-containing protein E1
VSDFGLTK	VSDFGLTB	873.46872	Tyrosine-protein kinase CSK
ATTADGSSILDR	ATTADGSSILDX	1215.59705	COP9 signalosome complex subunit 4
AGAVNPTVK	AGAVNPTVB	863.4956	Dipeptidyl peptidase 4
SELDTIDSQHR	SELDTIDSQHX	1309.61377	Excitatory amino acid transporter 2
FSVSPVVR	FSVSPVVX	899.51041	Elongation factor 2
STLTDSLVCK	STLTDSLVZB	1130.57327	Elongation factor 2
LLLTPWVK	LLLTPWVB	976.62007	Eukaryotic translation initiation factor 3 subunit A
TLSFGSDLNYATR	TLSFGSDLNYATX	1453.70767	Eukaryotic translation initiation factor 3 subunit A
DAHNALLDIQSSGR	DAHNALLDIQSSGX	1505.74617	Eukaryotic translation initiation factor 3 subunit C
ESYPVFYLFR	ESYPVFYLFX	1329.66328	Endoplasmic reticulum resident protein 29
ALQLEEER	ALQLEEEX	996.51153	Ezrin
YIEDEDYYK	YIEDEDYYB	1244.53284	Protein-tyrosine kinase 2-beta
EVAAPDVGR	EVAAPDVGX	922.47474	Flotillin-2
IQVDYDGHCK	IQVDYDGHZB	1241.55901	Follistatin-related protein 1
DETNYGIPQR	DETNYGIPQX	1201.56028	Guanine nucleotide-binding protein subunit beta-2-like 1
YIETDPANR	YIETDPANX	1087.51735	Gelsolin
VQQTVQDLFGR	VQQTVQDLFGX	1299.68106	Stress-70 protein, mitochondrial
LLEYTPTAR	LLEYTPTAX	1072.57922	Glycogen synthase kinase-3 beta

243

ALLSAPWYLNR	ALLSAPWYLNX	1312.71671	Beta-hexosaminidase subunit alpha
GLETFSQLVWK	GLETFSQLVWB	1314.70632	Beta-hexosaminidase subunit alpha
DLTEYLSR	DLTEYLSX	1005.50064	Heterogeneous nuclear ribonucleoprotein D-like
VIGGDDLSTLTGK	VIGGDDLSTLTGB	1282.68597	Hypoxanthine-guanine phosphoribosyltransferase
NPDDITNEEYGEFYK	NPDDITNEEYGEFYB	1840.78827	Heat shock protein HSP 90-alpha
ALLFIPR	ALLFIPX	838.53041	Heat shock protein HSP 90-beta
INLIAPPR	INLIAPPX	902.55769	Eukaryotic translation initiation factor 2 subunit 1
LAAFGQLHK	LAAFGQLHB	991.56943	Interleukin enhancer-binding factor 3
LSVEAPPK	LSVEAPPB	847.48945	IST1 homolog
DAEEWFFTK	DAEEWFFTB	1179.53277	Keratin, type I cytoskeletal 14
VVSTHEQVLR	VVSTHEQVLX	1176.64903	Keratin, type I cytoskeletal 14
ITQYLDAGGIPR	ITQYLDAGGIPX	1312.70145	Calcium/calmodulin-dependent protein kinase type II subunit alpha
FTDEYQLFEELGK	FTDEYQLFEELGB	1625.77043	Calcium/calmodulin-dependent protein kinase type II subunit delta
SLSAPGNLLTK	SLSAPGNLLTB	1107.63791	Calcium/calmodulin-dependent protein kinase kinase 2
CAFSIPNNCSGAR	ZAFSIPNNZSGAX	1462.63208	Serine/threonine-protein kinase D2
DLNSHNCLVR	DLNSHNZLVX	1236.59087	LIM domain kinase 1
DNPLDPVLAK	DNPLDPVLAB	1088.5957	Leucine-rich repeat-containing protein 59
LSNVAPPCILR	LSNVAPPZILX	1248.68878	Microtubule-associated protein RP/EB family member 3
ALTSELANAR	ALTSELANAX	1054.56463	Moesin
IPEQILGK	IPEQILGB	904.5473	Dual specificity mitogen-activated protein kinase kinase 1
LENLEQYSR	LENLEQYSX	1160.57012	Neuronal pentraxin-1
LFADAEEEQR	LFADAEEEQX	1216.55993	Vesicle-fusing ATPase
SPNELVDDLFK	SPNELVDDLFB	1283.64886	NSFL1 cofactor p47
VNVPGSQAQLK	VNVPGSQAQLB	1147.64406	Nucleobindin-1
GFGFVDFNSEEDAK	GFGFVDFNSEEDAB	1568.68742	Nucleolin
LQLEIDQK	LQLEIDQB	993.5586	Nuclear migration protein nudC
IEQLSPFPFDLLLK	IEQLSPFPFDLLLB	1666.94251	2-oxoglutarate dehydrogenase, mitochondrial
FANPFPAAVR	FANPFPAAVX	1098.58496	Propionyl-CoA carboxylase beta chain, mitochondrial
LLDEEEATDNDLR	LLDEEEATDNDLX	1541.70844	Programmed cell death 6-interacting protein
ILEFFGLK	ILEFFGLB	973.57278	Protein disulfide-isomerase
EISLLPDNLLR	EISLLPDNLLX	1291.7375	[Pyruvate dehydrogenase (acetyl-transferring)] kinase isozyme 1, mitochondrial
LYAQYFQGDLK	LYAQYFQGDLB	1352.68559	[Pyruvate dehydrogenase (acetyl-transferring)] kinase isozyme 1, mitochondrial
QFLDFGSSNACEK	QFLDFGSSNAZEB	1509.66493	[Pyruvate dehydrogenase (acetyl-transferring)] kinase isozyme 2, mitochondrial
VDLGSEVYR	VDLGSEVYX	1046.52718	PDZ and LIM domain protein 4
HGESAWNLENR	HGESAWNLENX	1321.60387	Phosphoglycerate mutase 1
YGDLVDYLHR	YGDLVDYLHX	1259.61739	Platelet-derived growth factor receptor beta
VYLSECK	VYLSEZB	905.4408	Plasminogen
VFFDVDIGGER	VFFDVDIGGEX	1262.61704	Peptidyl-prolyl cis-trans isomerase D
YGNANAWR	YGNANAWX	960.44413	Serine/threonine-protein phosphatase 6 catalytic subunit
VSVADHSLHLSK	VSVADHSLHLSB	1299.70263	Peroxiredoxin-4
LPLVTPHTQCR	LPLVTPHTQZX	1330.7055	26S protease regulatory subunit 4
VDILDPALLR	VDILDPALLX	1133.66835	26S protease regulatory subunit 6A
VVGSEFVQK	VVGSEFVQB	999.54803	26S protease regulatory subunit 6B
SILYDER	SILYDEX	904.45296	Proteasome subunit alpha type-2
TTIFSPEGR	TTIFSPEGX	1016.51662	Proteasome subunit alpha type-4
FILNLPTFSVR	FILNLPTFSVX	1315.75276	Proteasome subunit beta type-2
DYLHYIR	DYLHYIX	988.50058	40S ribosomal protein S11
DVNQQEFVR	DVNQQEFVX	1143.5548	40S ribosomal protein S19

244

AELNEFLTR	AELNEFLTX	1101.56938	40S ribosomal protein S3
AQCPIVER	AQZPIVEX	981.49411	40S ribosomal protein S5
DIPGLTDTTVPR	DIPGLTDTTVPX	1293.68038	40S ribosomal protein S6
VETFSGVYK	VETFSGVYB	1036.53205	40S ribosomal protein S7
IEDFLER	IEDFLEX	930.4686	40S ribosomal protein S9
FGISSVPTK	FGISSVPTB	942.52657	SAP domain-containing ribonucleoprotein
FGLNVSSISR	FGLNVSSISX	1088.58537	SAP domain-containing ribonucleoprotein
LAADAGTFLSR	LAADAGTFLSX	1130.59592	Endophilin-B1
LGEGSYGSVFK	LGEGSYGSVFB	1150.57497	Serine/threonine-protein kinase 3
IYGISFPDPK	IYGISFPDPB	1143.60554	Threonine--tRNA ligase, cytoplasmic
VSTEVDAR	VSTEVDAX	885.44312	Transaldolase
ILFQETR	ILFQETX	915.50533	Serine/threonine-protein kinase TAO3
HIAEDADR	HIAEDADX	935.43361	Tropomyosin alpha-1 chain
AQLLQPTLEINPR	AQLLQPTLEINPX	1501.84918	Heat shock protein 75 kDa, mitochondrial
GYAPESVLER	GYAPESVLEX	1129.56429	tRNA pseudouridine synthase A, mitochondrial
IFINLPR	IFINLPX	881.53623	Thioredoxin-like protein 1
LLQTLPQLR	LLQTLPQLX	1090.67379	E3 ubiquitin-protein ligase UBR4
VDALLSAQPK	VDALLSAQPB	1048.60079	UDP-glucose:glycoprotein glucosyltransferase 1
IGDLGHVTR	IGDLGHVTX	976.53293	Wee1-like protein kinase
DICNDVLSLLEK	DIZNDVLSLLEB	1425.72646	14-3-3 protein zeta/delta
EVFISGSFNNWSTK	EVFISGSFNNWSTB	1622.78201	5'-AMP-activated protein kinase subunit beta-2
LVVFDTSLQVK	LVVFDTSLQVB	1255.72672	5'-AMP-activated protein kinase subunit gamma-1
DLEDLQILIK	DLEDLQILIB	1206.69508	Aconitate hydratase, mitochondrial
DPLADLNIK	DPLADLNIB	1005.55859	Clathrin coat assembly protein AP180
ECHLNADTVSSK	EZHLNADTVSSB	1367.62307	AP-2 complex subunit beta
ELYLFDVLR	ELYLFDVLX	1176.64181	Asparagine synthetase [glutamine-hydrolyzing]
WINATDPSAR	WINATDPSAX	1139.55988	Asparagine synthetase [glutamine-hydrolyzing]
IVEIPFNSTNK	IVEIPFNSTNB	1268.68559	Sodium/potassium-transporting ATPase subunit alpha-1
GGQDNIPVLK	GGQDNIPVLB	1047.58039	Sodium/potassium-transporting ATPase subunit alpha-3
LDIDPETITWQR	LDIDPETITWQX	1495.75461	C-1-tetrahydrofolate synthase, cytoplasmic
VWSVASTVR	VWSVASTVX	1013.55334	Cell adhesion molecule 4
YVECSALTQK	YVEZSALTQB	1205.58417	Cell division control protein 42 homolog
VVPGYGHAVLR	VVPGYGHAVLX	1176.66427	Citrate synthase, mitochondrial
YLTNAYSR	YLTNAYSX	996.49042	Chloride intracellular channel protein 4
GVVGLPGQR	GVVGLPGQX	891.51655	Collagen alpha-1(I) chain
LPYSVVR	LPYSVVX	842.48895	Complement C3
DAGPLLISLK	DAGPLLISLB	1033.62627	Coronin-1A
LLYPPETGLFLVR	LLYPPETGLFLVX	1526.87359	Tyrosine-protein kinase CSK
VIDCLYTCK	VIDZLYTZB	1178.55551	Calsyntenin-1
LVFSNVNLK	LVFSNVNLB	1040.61097	DNA damage-binding protein 1
IIPGGAAAQDGR	IIPGGAAAQDGX	1134.60206	Disks large homolog 4
SLLQALNEVK	SLLQALNEVB	1121.65356	Cytoplasmic dynein 1 heavy chain 1
LQSQLLSIEK	LQSQLLSIEB	1165.67978	Dynamin-1
SADCSVEEEPWK	SADZSVEEEPWB	1443.60674	Excitatory amino acid transporter 2
LVPVGYGIR	LVPVGYGIX	982.5839	Elongation factor 1-delta
VLVPATDR	VLVPATDX	879.50532	Eukaryotic translation initiation factor 3 subunit E
NILVASPECVK	NILVASPEZVB	1236.66274	Protein-tyrosine kinase 2-beta
VAQLEAQCQEPCK	VAQLEAQZQEPZB	1567.7214	Fibrinogen gamma chain
IAQITGPPDR	IAQITGPPDX	1076.58536	Far upstream element-binding protein 1
IINDLLQSLR	IINDLLQSLX	1193.70073	Far upstream element-binding protein 2

EVEPALELLEPIDQK	EVEPALELLEPIDQB	1729.92289	Rab GDP dissociation inhibitor alpha
ELEASEELDTICPK	ELEASEELDTIZPB	1640.76944	Glutaredoxin-3
YEISSVPTFLFFK	YEISSVPTFLFFB	1584.83191	Glutaredoxin-3
DAGQISGLNVLR	DAGQISGLNVLX	1251.68105	Stress-70 protein, mitochondrial
IILDLISESPIK	IILDLISESPIB	1347.81044	Heterogeneous nuclear ribonucleoprotein K
FESPEVAER	FESPEVAEX	1072.50644	Heterogeneous nuclear ribonucleoprotein M
FFADLLDYIK	FFADLLDYIB	1251.66305	Hypoxanthine-guanine phosphoribosyltransferase
EPGCGCCSVCAR	EPGZGZZSVZAX	1421.51837	Insulin-like growth factor-binding protein 2
GECWCVNPNTGK	GEZWZVNPNTGB	1428.60056	Insulin-like growth factor-binding protein 2
DIFQEIYDK	DIFQEIYDB	1177.57464	Isocitrate dehydrogenase [NADP] cytoplasmic
SEITELR	SEITELX	856.45296	Keratin, type I cytoskeletal 10
YLHDLGIVHR	YLHDLGIVHX	1231.67009	Calcium/calmodulin-dependent protein kinase type 1
VLAGQEYAAK	VLAGQEYAAB	1056.56949	Calcium/calmodulin-dependent protein kinase type II subunit alpha
IPTGQEYAAK	IPTGQEYAAB	1084.56441	Calcium/calmodulin-dependent protein kinase type II subunit delta
ENIWDGVTTK	ENIWDGVTTB	1169.58079	Protein kinase C beta type
CITLFQNNTTNR	ZITLFQNNTTNX	1490.71754	Serine/threonine-protein kinase D2
DILADVNHPFVVK	DILADVNHPFVVB	1473.80708	Ribosomal protein S6 kinase alpha-1
AANEVSSADVK	AANEVSSADVB	1097.5444	Limbic system-associated membrane protein
ITVQASPGLDR	ITVQASPGLDX	1165.63304	Mitogen-activated protein kinase kinase kinase 11
LIGTAVPQR	LIGTAVPQX	963.57407	Microtubule-associated protein RP/EB family member 3
LVGTPGAELLK	LVGTPGAELLB	1104.66338	Mitogen-activated protein kinase 14
EALLQASR	EALLQASX	896.49549	Moesin
EVCQLLPFLVR	EVZQLLPFLVX	1382.76194	Neurochondrin
SGQQIVGPPR	SGQQIVGPPX	1047.57005	NSFL1 cofactor p47
LSQETEALGR	LSQETEALGX	1112.57011	Nucleobindin-1
AYPFYWAWLPQAK	AYPFYWAWLPQAB	1647.83291	Phosphatidylinositol 4-kinase type 2-alpha
DTADGTFLVR	DTADGTFLVX	1103.54864	Phosphatidylinositol 3-kinase regulatory subunit alpha
GFVDDIIQPSSTR	GFVDDIIQPSSTX	1443.72331	Propionyl-CoA carboxylase beta chain, mitochondrial
VNLSAAQTLR	VNLSAAQTLX	1081.61192	Programmed cell death protein 10
LALASLGYEK	LALASLGYEB	1071.60554	Programmed cell death 6-interacting protein
GSFSEQGINEFLR	GSFSEQGINEFLX	1492.71856	Protein disulfide-isomerase A6
DQLVLGR	DQLVLGX	809.46346	Platelet-derived growth factor receptor beta
IGDFGLATK	IGDFGLATB	928.51091	Serine/threonine-protein kinase PLK1
TIAQDYGVLK	TIAQDYGVLB	1114.61136	Peroxiredoxin-1
LVQAFQYTDK	LVQAFQYTDB	1219.63283	Peroxiredoxin-4
AVANQTSATFLR	AVANQTSATFLX	1287.68106	26S protease regulatory subunit 4
EVVETPLLHPER	EVVETPLLHPEX	1427.76477	26S protease regulatory subunit 7
AVAHHTDCTFIR	AVAHHTDZTFIX	1436.68582	26S protease regulatory subunit 8
LLDSSTVTHLFK	LLDSSTVTHLFB	1367.754	Proteasome subunit alpha type-6
GPGLYYVDSEGNR	GPGLYYVDSEGNX	1435.66071	Proteasome subunit beta type-5
IVVLLQR	IVVLLQX	849.56753	Proteasome activator complex subunit 1
IIEVSGQK	IIEVSGQB	880.51092	Ras-related protein Rab-14
YDGIILPGK	YDGIILPGB	982.55786	60S ribosomal protein L11
FWYFVSQLK	FWYFVSQLB	1224.64227	60S ribosomal protein L18a
LDHYAIIK	LDHYAIIB	979.5582	60S ribosomal protein L23a
YCQVIR	YZQVIX	847.42498	60S ribosomal protein L3
YEITEQR	YEITEQX	947.45878	60S ribosomal protein L6
VPPAINQFTQALDR	VPPAINQFTQALDX	1578.83934	60S ribosomal protein L7a
AVDFAER	AVDFAEX	816.40052	60S ribosomal protein L8
TILPAAAQDVYYR	TILPAAAQDVYYX	1489.78043	Dolichyl-diphosphooligosaccharide--protein glycosyltransferase subunit 1

246

LILIESR	LILIESX	852.53081	40S ribosomal protein S13
TLLVADPR	TLLVADPX	893.52097	40S ribosomal protein S16
VLNTNIDGR	VLNTNIDGX	1010.53842	40S ribosomal protein S18
VLQALEGLK	VLQALEGLB	977.60006	40S ribosomal protein S19
VCADLIR	VZADLIX	855.45118	40S ribosomal protein S20
AALQELLSK	AALQELLSB	979.57933	40S ribosomal protein S25
LITEDVQGK	LITEDVQGB	1009.55351	40S ribosomal protein S3a
GSSNSYAIK	GSSNSYAIB	933.46471	40S ribosomal protein S5
LIEVDDER	LIEVDDEX	997.49554	40S ribosomal protein S6
LDYILGLK	LDYILGLB	941.5677	40S ribosomal protein S9
AVLLAGPPGTGK	AVLLAGPPGTGB	1087.64806	RuvB-like 1
GEALSALDSK	GEALSALDSB	997.51712	Vesicle-trafficking protein SEC22b
TQIQSVEPYTK	TQIQSVEPYTB	1300.67543	Signal transducer and activator of transcription 3
VVENLQDDFDFNYK	VVENLQDDFDFNYB	1752.80861	Signal transducer and activator of transcription 3
LAYINPDLALEEK	LAYINPDLALEEB	1495.80133	Stress-induced-phosphoprotein 1
GEEILSGAQR	GEEILSGAQX	1068.54389	Aspartate--tRNA ligase, cytoplasmic
TVYSVFGFSFK	TVYSVFGFSFB	1288.65831	Threonine--tRNA ligase, cytoplasmic
LASAAYPDPSK	LASAAYPDPSB	1126.57497	Tyrosine--tRNA ligase, cytoplasmic
ADVQSIIGLQR	ADVQSIIGLQX	1208.67524	Transcription intermediary factor 1-beta
IIALDGDTK	IIALDGDTB	952.53204	Transketolase
EVFGTFGIPFLLR	EVFGTFGIPFLLX	1504.83172	Ubiquitin carboxyl-terminal hydrolase 7
FLFVDADQIVR	FLFVDADQIVX	1331.71128	UDP-glucose:glycoprotein glucosyltransferase 1
LDGFILTER	LDGFILTEX	1072.57921	Serine/threonine-protein kinase ULK3
AVAGNISDPGLQK	AVAGNISDPGLQB	1276.68664	Vinculin
HSVLLSASR	HSVLLSASX	978.54859	Wee1-like protein kinase
AVGHPFVIQLGR	AVGHPFVIQLGX	1302.74358	Exportin-1
LICCDILDVLDK	LIZZDILDVLDB	1483.75056	14-3-3 protein epsilon
WYFDVTEGK	WYFDVTEGB	1151.53786	Amyloid beta A4 protein
SIDDEITEAK	SIDDEITEAB	1127.54373	5'-AMP-activated protein kinase catalytic subunit alpha-1
DYETATLSEIK	DYETATLSEIB	1276.6278	Alpha-actinin-1
LAILGIHNEVSK	LAILGIHNEVSB	1300.75941	Alpha-actinin-1
GSWQGENVAVK	GSWQGENVAVB	1181.59202	Activin receptor type-1
AAVVTSPPPTTAPHK	AAVVTSPPPTTAPHB	1480.8129	Alpha-adducin
SLLAGLLK	SLLAGLLB	821.54657	RAC-beta serine/threonine-protein kinase
EPLVDVVDPK	EPLVDVVDPB	1117.61101	Protein arginine N-methyltransferase 1
LQSSNIFTVAK	LQSSNIFTVAB	1214.67503	AP-1 complex subunit beta-1
GQVYILGR	GQVYILGX	914.52131	Argininosuccinate synthase
IDIVENR	IDIVENX	867.46894	Argininosuccinate synthase
DTQLQQIVDK	DTQLQQIVDB	1194.63356	Calcineurin subunit B type 1
EFIEGVSQFSVK	EFIEGVSQFSVB	1376.70671	Calcineurin subunit B type 1
LGTLSALDILIK	LGTLSALDILIB	1263.78931	Cullin-associated NEDD8-dissociated protein 1
SVILEAFSSPSEEVK	SVILEAFSSPSEEVB	1628.83884	Cullin-associated NEDD8-dissociated protein 1
LNQDQLDAVSK	LNQDQLDAVSB	1237.63937	Caprin-1
SPEVLLGSAR	SPEVLLGSAX	1037.57446	Cyclin-dependent kinase 1
IGEGTYGTVFK	IGEGTYGTVFB	1178.60627	Cyclin-dependent kinase 5
LDFLGEGQFATVYK	LDFLGEGQFATVYB	1594.81223	Cyclin-dependent kinase 7
IGQGTFGEVFK	IGQGTFGEVFB	1189.62225	Cyclin-dependent kinase 9
WLLLTGISAQQNR	WLLLTGISAQQNX	1508.83387	Clathrin heavy chain 1
EVEIAYSDVAK	EVEIAYSDVAB	1230.62231	Chloride intracellular channel protein 4
VEVLAGDLR	VEVLAGDLX	980.55299	Contactin-2

247

NEQVEIR	NEQVEIX	896.45911	Complement C3
LTVTAYDCGK	LTVTAYDZGB	1134.54705	Calsyntenin-1
QSGESIDIITR	QSGESIDIITX	1227.63344	DNA damage-binding protein 1
HCILDVSANAVR	HZILDVSANAVX	1363.69057	Disks large homolog 4
EFLLIFR	EFLLIFX	946.55154	EF-hand domain-containing protein D2
LGDDIDLIVR	LGDDIDLIVX	1137.62688	Eukaryotic translation initiation factor 3 subunit D
LFIFETFCR	LFIFETFZX	1241.61422	Eukaryotic translation initiation factor 3 subunit E
EGDLLFTVAK	EGDLLFTVAB	1099.60045	Eukaryotic translation initiation factor 3 subunit I
LIINSLYK	LIINSLYB	970.59426	Endoplasmin
IHVLEAQDLIAK	IHVLEAQDLIAB	1356.78562	Extended synaptotagmin-1
GNFGEVYK	GNFGEVYB	920.44832	Tyrosine-protein kinase Fer
LIGVCTQR	LIGVZTQX	955.51485	Tyrosine-protein kinase Fer
DNCCILDER	DNZZILDEX	1203.48877	Fibrinogen gamma chain
GPATVEDLPSAFEEK	GPATVEDLPSAFEEB	1596.77623	PDZ domain-containing protein GIPC1
NPDELAEALDER	NPDELAEALDEX	1380.63963	PDZ domain-containing protein GIPC1
ITPSYVAFTPEGER	ITPSYVAFTPEGEX	1575.78082	78 kDa glucose-regulated protein
CVLIFGVPSR	ZVLIFGVPSX	1156.6302	Delta-aminolevulinic acid dehydratase
DYAFIHFDER	DYAFIHFDEX	1321.59665	Heterogeneous nuclear ribonucleoprotein Q
EQILEEFSK	EQILEEFSB	1129.57464	Heterogeneous nuclear ribonucleoprotein Q
DQVANSAFVER	DQVANSAFVEX	1244.60247	Heat shock protein HSP 90-alpha
SEGGFIWACK	SEGGFIWAZB	1161.53681	Isocitrate dehydrogenase [NADP] cytoplasmic
IIWQFIK	IIWQFIB	954.57821	Isocitrate dehydrogenase [NADP], mitochondrial
AAVENLPTFLVELSR	AAVENLPTFLVELSX	1667.91216	Importin subunit beta-1
YETELNLR	YETELNLX	1046.52719	Keratin, type I cytoskeletal 14
HNIQALLK	HNIQALLB	943.56944	cAMP-dependent protein kinase type I-alpha regulatory subunit
LIFQVLDAVK	LIFQVLDAVB	1152.69977	Calcium/calmodulin-dependent protein kinase type 1
FYFENLLAK	FYFENLLAB	1151.61063	Calcium/calmodulin-dependent protein kinase type II subunit beta
NSQGEEVAQR	NSQGEEVAQX	1126.52423	Lamin-B1
QLLAPGNSAGAFLIR	QLLAPGNSAGAFLIX	1536.86515	Tyrosine-protein kinase Lyn
GANLLIDSTGQR	GANLLIDSTGQX	1253.66032	Mitogen-activated protein kinase kinase kinase 1
DLATDLSLIEVK	DLATDLSLIEVB	1323.73767	Microtubule-associated protein 2
LTVEDLEK	LTVEDLEB	953.51606	Microtubule-associated protein RP/EB family member 1
ELIFQETAR	ELIFQETAX	1115.58503	Mitogen-activated protein kinase 3
ISELGAGNGGVVFK	ISELGAGNGGVVFB	1354.73358	Dual specificity mitogen-activated protein kinase kinase 1
ELDDATEANEGLSR	ELDDATEANEGLSX	1528.68804	Myosin-10
ATNDEIFSILK	ATNDEIFSILB	1257.6696	Nuclear cap-binding protein subunit 1
DYYECTGIYK	DYYEZTGIYB	1318.5631	Neprilysin
IPLITATPR	IPLITATPX	990.61012	Sialidase-1
GLSEDTTEETLK	GLSEDTTEETLB	1329.63909	Nucleolin
TLGDFAAEYAK	TLGDFAAEYAB	1192.58553	Poly [ADP-ribose] polymerase 1
ELLDTVNNVFK	ELLDTVNNVFB	1298.69615	Programmed cell death protein 10
IVQAEGEAEAAK	IVQAEGEAEAAB	1222.62845	Prohibitin-2
ALDEGDIALLK	ALDEGDIALLB	1164.64812	26S protease regulatory subunit 7
VEIATLTR	VEIATLTX	911.53154	Proteasome subunit alpha type-4
NGYELSPTAAANFTR	NGYELSPTAAANFTX	1620.77714	Proteasome subunit beta type-2
AIYQATYR	AIYQATYX	994.51115	Proteasome subunit beta type-5
LNILDTLSK	LNILDTLSB	1023.60555	26S proteasome non-ATPase regulatory subunit 2
NIEEHASADVEK	NIEEHASADVEB	1348.635	Ras-related protein Rab-8A
AEEILEK	AEEILEB	838.45273	60S ribosomal protein L11
LYDIDVAK	LYDIDVAB	943.51058	60S ribosomal protein L23a

248

|			
GCTATLGNFAK	GZTATLGNFAB	1146.55828	40S ribosomal protein S2
HVVFIAQR	HVVFIAQX	978.56384	40S ribosomal protein S7
LLVVTDPR	LLVVTDPX	921.55227	40S ribosomal protein SA
ILQDGGLQVVEK	ILQDGGLQVVEB	1305.73834	D-3-phosphoglycerate dehydrogenase
GVVEVTHDLQK	GVVEVTHDLQB	1231.66518	Serpin H1
LNEQASEEILK	LNEQASEEILB	1280.67033	Protein SET
VEVTEFEDIK	VEVTEFEDIB	1215.61141	Protein SET
LLLNAENPR	LLLNAENPX	1048.59045	Proto-oncogene tyrosine-protein kinase Src
AIVPILLDANVSTYDK	AIVPILLDANVSTYDB	1738.95962	Syntaxin-binding protein 1
EVLLDEDDDLWIALR	EVLLDEDDDLWIALX	1823.91802	Syntaxin-binding protein 1
GFVEIQTPK	GFVEIQTPB	1025.56368	Aspartate--tRNA ligase, cytoplasmic
IYLYLTK	IYLYLTB	920.54625	Glycine--tRNA ligase
IDVGEAEPR	IDVGEAEPX	994.49587	Tyrosine--tRNA ligase, cytoplasmic
VLIDLIQR	VLIDLIQX	978.61012	Serine/threonine-protein kinase TAO3
AVFVDLEPTVIDEIR	AVFVDLEPTVIDEIX	1724.92238	Tubulin alpha-4A chain
TSASIILR	TSASIILX	869.52098	T-complex protein 1 subunit alpha
VIDPATATSVDLR	VIDPATATSVDLX	1366.73314	T-complex protein 1 subunit delta
LDQLIYIPLPDEK	LDQLIYIPLPDEB	1563.86393	Transitional endoplasmic reticulum ATPase
IGAGFFSEVYK	IGAGFFSEVYB	1224.627	Dual specificity testis-specific protein kinase 1
TIVLQESIGK	TIVLQESIGB	1094.64266	TGF-beta receptor type-1
HENILQFLTAEER	HENILQFLTAEEX	1608.81352	TGF-beta receptor type-2
LVIIESDLER	LVIIESDLEX	1195.66875	Tropomyosin alpha-1 chain
NFPNAIEHTLQWAR	NFPNAIEHTLQWAX	1705.85639	Ubiquitin-like modifier-activating enzyme 1
LTLSALLDGK	LTLSALLDGB	1037.62119	Voltage-dependent anion-selective channel protein 1
VESLEQEAANER	VESLEQEAANEX	1383.65054	Amyloid beta A4 protein
EAYPEEAYIADLDAK	EAYPEEAYIADLDAB	1704.79736	ATP-citrate synthase
GVSCSEVTASSLIK	GVSZSEVTASSLIB	1444.73228	Beta-adducin
TIEEVVGR	TIEEVVGX	911.49515	Aldehyde dehydrogenase, mitochondrial
ALQASALAAWGGK	ALQASALAAWGGB	1250.68624	Fructose-bisphosphate aldolase B
DLSTVEALQNLK	DLSTVEALQNLB	1337.72818	Acidic leucine-rich nuclear phosphoprotein 32 family member E
ATNSSWVVVFK	ATNSSWVVVFB	1244.66446	Clathrin coat assembly protein AP180
GIVIATGDR	GIVIATGDX	910.51113	Sodium/potassium-transporting ATPase subunit alpha-2
HALIIYDDLSK	HALIIYDDLSB	1294.70123	ATP synthase subunit alpha, mitochondrial
TVLELQYVLDK	TVLELQYVLDB	1327.74785	Caprin-1
YEIVGNLGEGTFGK	YEIVGNLGEGTFGB	1490.74963	Dual specificity protein kinase CLK3
ATSVALTWSR	ATSVALTWSX	1100.58537	Contactin-1
LFLVQLQEK	LFLVQLQEB	1124.66848	Cleavage and polyadenylation specificity factor subunit 5
QENGASVILR	QENGASVILX	1095.59118	Elongation factor 1-delta
STFVLDEFK	STFVLDEFB	1092.55826	Elongation factor 1-gamma
WFLTCINQPQFR	WFLTZINQPQFX	1618.79538	Elongation factor 1-gamma
VQAINVSSR	VQAINVSSX	982.54351	EF-hand domain-containing protein D2
ISCTIANR	ISZTIANX	943.47847	Fibronectin
TQLAVCQQR	TQLAVZQQX	1112.5636	Peptidyl-prolyl cis-trans isomerase FKBP4
VQVQVVER	VQVQVVEX	965.55334	Flotillin-1
QTLPVIYVK	QTLPVIYVB	1067.64702	Glycogen synthase kinase-3 beta
INEILSNALK	INEILSNALB	1121.65356	Heterogeneous nuclear ribonucleoprotein M
EFSITDVVPYPISLR	EFSITDVVPYPISLX	1744.92748	Heat shock 70 kDa protein 4
VLGVLEVSR	VLGVLEVSX	980.58938	Integrin-linked kinase-associated serine/threonine phosphatase 2C
LENEIQTYR	LENEIQTYX	1174.58577	Keratin, type I cytoskeletal 10
QETVECLR	QETVEZLX	1043.49451	Calcium/calmodulin-dependent protein kinase type II subunit gamma

GSGTAEVELK	GSGTAEVELB	997.51712	Pyruvate kinase PKM
AANILVSDTLSCK	AANILVSDTLSZB	1398.7268	Tyrosine-protein kinase Lck
EAALSTALSEK	EAALSTALSEB	1126.5961	Prelamin-A/C
ALYETELADAR	ALYETELADAX	1260.62253	Lamin-B1
HENVIGLLDVFTPAR	HENVIGLLDVFTPAX	1689.90774	Mitogen-activated protein kinase 14
AAEDLFVNIR	AAEDLFVNIX	1156.61157	Nck-associated protein 1
GWNILTNSEK	GWNILTNSEB	1168.59678	NADH-ubiquinone oxidoreductase 75 kDa subunit, mitochondrial
LELSVLYK	LELSVLYB	971.57827	Ubiquitin thioesterase OTUB1
LVVLDYIIR	LVVLDYIIX	1112.68328	Phosphatidylinositol 4-kinase type 2-alpha
LAPEYEAAATR	LAPEYEAAATX	1200.6014	Protein disulfide-isomerase A3
TQEEIVAK	TQEEIVAB	924.50075	Protein disulfide-isomerase A4
TLSQFTDALVTIR	TLSQFTDALVTIX	1473.80665	[Pyruvate dehydrogenase (acetyl-transferring)] kinase isozyme 2, mitochondrial
DLQNVNITLR	DLQNVNITLX	1194.6596	Prohibitin
LLNDEDPVVVTK	LLNDEDPVVVTB	1348.73292	Junction plakoglobin
HINPVAASLIQK	HINPVAASLIQB	1297.75975	Serine/threonine-protein kinase PLK1
SPIAEAVFR	SPIAEAVFX	998.54243	Low molecular weight phosphotyrosine protein phosphatase
DVFISAAER	DVFISAAEX	1016.51661	Proteasome subunit beta type-1
VNAADIENR	VNAADIENX	1010.50203	Tyrosine-protein phosphatase non-receptor type 6
SLQSVAEER	SLQSVAEEX	1027.51735	60S ribosomal protein L15
LVILANNCPALR	LVILANNZPALX	1362.76809	60S ribosomal protein L30
VCTLAIIDPGDSDIIR	VZTLAIIDPGDSDIIX	1766.91117	60S ribosomal protein L30
EAIEGTYIDK	EAIEGTYIDB	1145.56955	40S ribosomal protein S11
ECLPLIIFLR	EZLPLIIFLX	1282.73466	40S ribosomal protein S4, X isoform
LTPEEEEILNK	LTPEEEEILNB	1321.68564	40S ribosomal protein S8
FAAATGATPIAGR	FAAATGATPIAGX	1212.64901	40S ribosomal protein SA
VPAINVNDSVTK	VPAINVNDSVTB	1263.6914	Adenosylhomocysteinase
STLINSLFLTDLYPER	STLINSLFLTDLYPEX	1890.99663	Septin-2
GGIVDEGALLR	GGIVDEGALLX	1108.61156	D-3-phosphoglycerate dehydrogenase
HLAGLGLTEAIDK	HLAGLGLTEAIDB	1344.74923	Serpin H1
QYDQEIENLEK	QYDQEIENLEB	1415.66598	STE20-like serine/threonine-protein kinase
NVLVTLYER	NVLVTLYEX	1115.62142	SPARC
EFLVAGGEDFK	EFLVAGGEDFB	1218.60117	Serine-threonine kinase receptor-associated protein
LAVEAVLR	LAVEAVLX	879.5417	T-complex protein 1 subunit beta
APGLGLVLER	APGLGLVLEX	1033.61592	tRNA pseudouridine synthase A, mitochondrial
VDVIFCDK	VDVIFZDB	1002.49355	Ubiquitin carboxyl-terminal hydrolase 7
LGSGTYATVYK	LGSGTYATVYB	1166.60628	Serine/threonine-protein kinase ULK3
VTQSNFAVGYK	VTQSNFAVGYB	1220.62808	Voltage-dependent anion-selective channel protein 1
FLNWIPLGYIFETK	FLNWIPLGYIFETB	1747.94285	Exportin-1
SDFEVFDALK	SDFEVFDALB	1177.57463	5'-AMP-activated protein kinase subunit beta-2
VGNLTVVGK	VGNLTVVGB	893.54255	Aspartate aminotransferase, cytoplasmic
VNLGVGAYR	VNLGVGAYX	957.52712	Aspartate aminotransferase, cytoplasmic
TIAIIAEGIPEALTR	TIAIIAEGIPEALTX	1576.90634	ATP-citrate synthase
DNTINLIHTFR	DNTINLIHTFX	1352.70761	Actin-related protein 2/3 complex subunit 2
TPFLLVGTQIDLR	TPFLLVGTQIDLX	1481.84811	Cell division control protein 42 homolog
LTGEVVALK	LTGEVVALB	936.57351	Cyclin-dependent kinase 2
VGLQVVAVK	VGLQVVAVB	919.59458	60 kDa heat shock protein, mitochondrial
LLGYVATLK	LLGYVATLB	984.6099	Cold shock domain-containing protein E1
GAEIVADTFR	GAEIVADTFX	1087.55372	N(G),N(G)-dimethylarginine dimethylaminohydrolase 2
YLATLNFVHR	YLATLNFVHX	1242.67485	Epithelial discoidin domain-containing receptor 1

|			
GVIALCIEDGSIHR	GVIALZIEDGSIHX	1548.79575	Succinate dehydrogenase [ubiquinone] flavoprotein subunit, mitochondrial
ALQGASQIIAEIR	ALQGASQIIAEIX	1378.78076	Dynamin-1-like protein
DTLQSELVGQLYK	DTLQSELVGQLYB	1500.79151	Dynamin-1-like protein
VNFLPEIITLSK	VNFLPEIITLSB	1380.81078	Cytoplasmic dynein 1 heavy chain 1
DITAALAAER	DITAALAAEX	1039.55372	Dynamin-1
TTLTAAITK	TTLTAAITB	926.55279	Elongation factor Tu, mitochondrial
NLFNVVDCK	NLFNVVDZB	1115.55247	Eukaryotic translation initiation factor 3 subunit B
GAVIATELK	GAVIATELB	908.54221	Eukaryotic translation initiation factor 3 subunit D
FAFQAEVNR	FAFQAEVNX	1090.5435	Endoplasmin
ALTLGALTLPLAR	ALTLGALTLPLAX	1318.82116	Extended synaptotagmin-1
DADIGVAEAER	DADIGVAEAEX	1154.54427	Flotillin-2
HSVGVVIGR	HSVGVVIGX	932.5431	Far upstream element-binding protein 2
GFCFITYTDEEPVK	GFZFITYTDEEPVB	1712.7847	Heterogeneous nuclear ribonucleoprotein D-like
ALFAISCLVR	ALFAISZLVX	1158.64585	Hsp70-binding protein 1
YLEAGAAGLR	YLEAGAAGLX	1029.54824	Hsp70-binding protein 1
AGGIETIANEYSDR	AGGIETIANEYSDX	1504.7033	Heat shock 70 kDa protein 4
SQIHDIVLVGGSTR	SQIHDIVLVGGSTX	1490.80804	Heat shock cognate 71 kDa protein
ASGVEGADVVK	ASGVEGADVVB	1038.54366	Hexokinase-1
IAEFAFEYAR	IAEFAFEYAX	1225.60067	Isocitrate dehydrogenase [NAD] subunit alpha, mitochondrial
ASSVIFGLK	ASSVIFGLB	928.5473	Integrin-linked kinase-associated serine/threonine phosphatase 2C
LAATNALLNSLEFTK	LAATNALLNSLEFTB	1612.89155	Importin subunit beta-1
LQSEVAELK	LQSEVAELB	1023.56916	IST1 homolog
LFENFLVDICR	LFENFLVDIZX	1434.72047	Inositol 1,4,5-trisphosphate receptor type 1
SENEEFVEVGR	SENEEFVEVGX	1303.59196	cAMP-dependent protein kinase type I-alpha regulatory subunit
NTGIICTIGPASR	NTGIIZTIGPASX	1368.70589	Pyruvate kinase PKM
GLTSVINQK	GLTSVINQB	966.55894	L-lactate dehydrogenase B chain
IVVVTAGVR	IVVVTAGVX	922.5839	L-lactate dehydrogenase B chain
LNFITEYIK	LNFITEYIB	1147.63685	LIM domain kinase 1
FQDNFEFVQWFK	FQDNFEFVQWFB	1641.77071	Microtubule-associated protein RP/EB family member 1
ATISALEAK	ATISALEAB	910.52148	Myosin-10
NLFLVIFQR	NLFLVIFQX	1158.67887	Nuclear cap-binding protein subunit 1
SATYVNTEGR	SATYVNTEGX	1106.52317	NADH-ubiquinone oxidoreductase 75 kDa subunit, mitochondrial
TEDIVAVQK	TEDIVAVQB	1009.55351	Neprilysin
GTLLAFAEAR	GTLLAFAEAX	1057.57954	Sialidase-1
AETYEGVYQCTAR	AETYEGVYQZTAX	1556.68047	Neuronal cell adhesion molecule
VLDDGELLVQQTK	VLDDGELLVQQTB	1464.7915	Vesicle-fusing ATPase
NTLLIAGLQAR	NTLLIAGLQAX	1178.70106	Dolichyl-diphosphooligosaccharide--protein glycosyltransferase 48 kDa subunit
EADDIVNWLK	EADDIVNWLB	1209.61208	Protein disulfide-isomerase
IEELQLIVNDK	IEELQLIVNDB	1320.73801	26S protease regulatory subunit 8
LYQVEYAFK	LYQVEYAFB	1167.60555	Proteasome subunit alpha type-6
SSDEAVILCK	SSDEAVILZB	1128.55761	26S proteasome non-ATPase regulatory subunit 13
LSLDGQNIYNACCTLR	LSLDGQNIYNAZZTLX	1906.89048	Polypyrimidine tract-binding protein 1
IDTIEIITDR	IDTIEIITDX	1197.64802	Heterogeneous nuclear ribonucleoproteins A2/B1
GTGIVSAPVPK	GTGIVSAPVPB	1032.60587	40S ribosomal protein S2
TPVEPEVAIHR	TPVEPEVAIHX	1256.67523	40S ribosomal protein S20
LNNLVLFDK	LNNLVLFDB	1082.62153	40S ribosomal protein S25
TEIILATR	TEIILATX	1038.63125	40S ribosomal protein S3
LSNIFVIGK	LSNIFVIGB	997.60515	40S ribosomal protein S4, X isoform
ADGYVLEGK	ADGYVLEGB	958.48509	40S ribosomal protein S8

VNIVPVIAK	VNIVPVIAB	959.62588	Septin-2
EAAIWELEER	EAAIWELEEX	1254.61196	STE20-like serine/threonine-protein kinase
ELPTAFDYVEFTR	ELPTAFDYVEFTX	1596.76992	Spectrin alpha chain, non-erythrocytic 1
EAGDVCYADVQK	EAGDVZYADVQB	1361.60126	Serine/arginine-rich splicing factor 9
FDEISFVNFAR	FDEISFVNFAX	1353.65925	FACT complex subunit SSRP1
GEFTIETEGK	GEFTIETEGB	1117.53825	Glycine--tRNA ligase
NGTCCIADLGLAVR	NGTZZIADLGLAVX	1528.73653	TGF-beta receptor type-1
AVELAANTK	AVELAANTB	923.51673	Transketolase
VEEEIVTLR	VEEEIVTLX	1096.60034	Tumor protein D54
DNPGVVTCLDEAR	DNPGVVTZLDEAX	1454.66989	Ubiquitin-like modifier-activating enzyme 1
YLAEVATGEK	YLAEVATGEB	1087.56407	14-3-3 protein gamma
QITLLECVGK	QITLLEZVGB	1167.64128	Activin receptor type-1
VNILGEVVEK	VNILGEVVEB	1106.64265	Beta-adducin
ATLYVTAIEDR	ATLYVTAIEDX	1260.65892	Protein arginine N-methyltransferase 1
ALGVLAQLIWSR	ALGVLAQLIWSX	1335.7902	Citrate synthase, mitochondrial
AQQVAVQEQEIAR	AQQVAVQEQEIAX	1478.77166	Flotillin-1
HVVPNEVVVQR	HVVPNEVVVQX	1284.71777	Gelsolin
ELEEIVQPIISK	ELEEIVQPIISB	1404.79552	78 kDa glucose-regulated protein
EFVEAVLELR	EFVEAVLELX	1213.65818	Core histone macro-H2A.1
LAEVALAYAK	LAEVALAYAB	1055.61062	Delta-aminolevulinic acid dehydratase
FVVQNVSAQK	FVVQNVSAQB	1126.6226	Heat shock protein 105 kDa
SVLDAAQIVGLNCLR	SVLDAAQIVGLNZLX	1637.87982	Heat shock protein 105 kDa
IEAACFATIK	IEAAZFATIB	1130.58851	Isocitrate dehydrogenase [NAD] subunit alpha, mitochondrial
LLVPTQYVGAIIGK	LLVPTQYVGAIIGB	1478.89517	Insulin-like growth factor 2 mRNA-binding protein 1
AYAALAALEK	AYAALAALEB	1027.57932	Interleukin enhancer-binding factor 3
AVLNPTNADILIETK	AVLNPTNADILIETB	1618.90211	Inositol 1,4,5-trisphosphate receptor type 1
VSHLLGINVTDFTR	VSHLLGINVTDFTX	1580.85499	Myosin-9
ILGAWLAEETSSLR	ILGAWLAEETSSLX	1554.8281	Neurochondrin
EVAGDTIIFR	EVAGDTIIFX	1129.60067	Neurofascin
ENIVIQCEAK	ENIVIQZEAB	1210.61071	Neuronal cell adhesion molecule
VFSATLGLVDIVK	VFSATLGLVDIVB	1368.81077	Poly [ADP-ribose] polymerase 1
TGEAIVDAALSALR	TGEAIVDAALSALX	1395.75968	Protein disulfide-isomerase A6
VTNEFVHINNLK	VTNEFVHINNLB	1434.77105	Serine/threonine-protein phosphatase 6 catalytic subunit
LLHVAVSDVNDDVR	LLHVAVSDVNDDVX	1560.81351	26S proteasome non-ATPase regulatory subunit 1
AVPLALALISVSNPR	AVPLALALISVSNPX	1529.91685	26S proteasome non-ATPase regulatory subunit 2
DIICQIAYAR	DIIZQIAYAX	1231.62585	60S ribosomal protein L5
ELGITALHIK	ELGITALHIB	1101.66372	40S ribosomal protein S14
LLEPVLLLGK	LLEPVLLLGB	1101.72525	40S ribosomal protein S16
VADIGLAAWGR	VADIGLAAWGX	1137.61698	Adenosylhomocysteinase
DVNAAIAAIK	DVNAAIAAIB	992.57457	Tubulin alpha-4A chain
AVAQALEVIPR	AVAQALEVIPX	1175.69015	T-complex protein 1 subunit gamma
VPITAVIAAK	VPITAVIAAB	989.63644	Tripeptidyl-peptidase 2
IDQYQGADAVGLEEK	IDQYQGADAVGLEEB	1642.79295	Thioredoxin-like protein 1
SLVQGELVTASK	SLVQGELVTASB	1238.69615	Alpha-adducin
TVEGVLIVHEHR	TVEGVLIVHEHX	1397.76544	Cleavage and polyadenylation specificity factor subunit 5
ELLIIGGVAAR	ELLIIGGVAAX	1120.68433	ATP-dependent RNA helicase DDX1
GTQGVVTNFEIFR	GTQGVVTNFEIFX	1476.76003	Eukaryotic translation initiation factor 3 subunit B
GAALITAVGVR	GAALITAVGVX	1036.62682	Hexokinase-1
GCDVVVIPAGVPR	GZDVVVIPAGVPX	1347.72079	Malate dehydrogenase, mitochondrial
IFGVTTLDIVR	IFGVTTLDIVX	1242.72112	Malate dehydrogenase, mitochondrial

|			
FGLEGCEVLIPALK	FGLEGZEVLIPALB	1552.84141	2-oxoglutarate dehydrogenase, mitochondrial
DLSHIGDAVVISCAK	DLSHIGDAVVISZAB	1591.81191	Proliferating cell nuclear antigen
LLLGAGAVAYGVR	LLLGAGAVAYGVX	1268.74799	Prohibitin-2
TVEIVHIDIADR	TVEIVHIDIADX	1389.74912	Phosphatidylinositol transfer protein beta isoform
SVLFVCLGNICR	SVLFVZLGNIZX	1446.73508	Low molecular weight phosphotyrosine protein phosphatase
AANGVVLATEK	AANGVVLATEB	1079.6066	Proteasome subunit alpha type-2
VSTAVLSITAK	VSTAVLSITAB	1096.65831	26S proteasome non-ATPase regulatory subunit 1
EIVLADVIDNDSWR	EIVLADVIDNDSWX	1653.82374	Multifunctional protein ADE2
DLTTAGAVTQCYR	DLTTAGAVTQZYX	1464.69064	60S ribosomal protein L18a
TALALAIAQELGSK	TALALAIAQELGSB	1392.80675	RuvB-like 1
SDVWSFGILLTELTTK	SDVWSFGILLTELTTB	1816.97019	Proto-oncogene tyrosine-protein kinase Src
AATAAADFTAK	AATAAADFTAB	1044.5331	Serine-threonine kinase receptor-associated protein
NLLLALVGEVGELAELFQ WK	NLLLALVGEVGELAELFQ WB	2249.25505	dCTP pyrophosphatase 1

Appendix chapter 4 table 2 *1000 labelled peptide standards.*
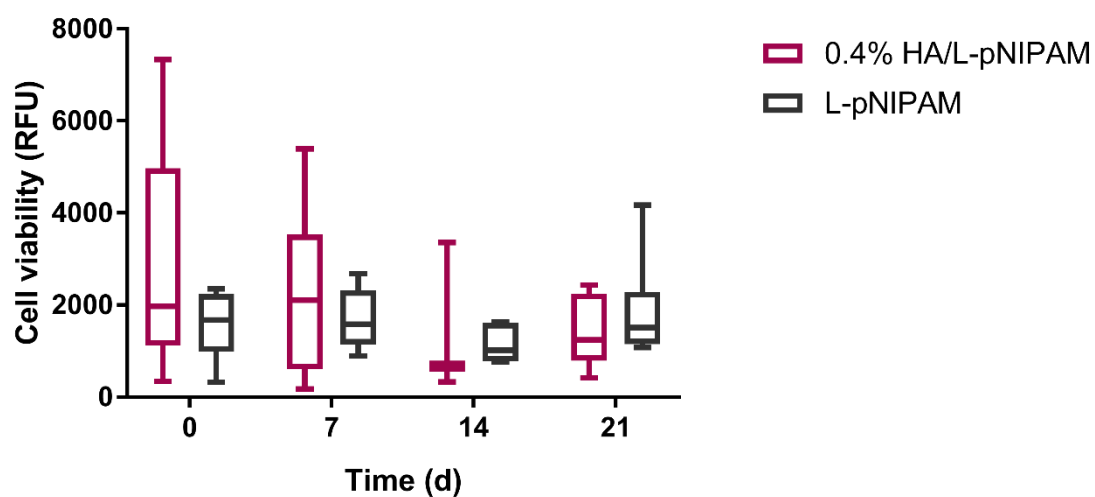
Appendix chapter 5 figure 1 *Cell viability of HepG2 cells in cultured in hydrogel (0/0.4% HA/L-pNIPAM) at cell seeding density 1x10^6 cell/mL.*
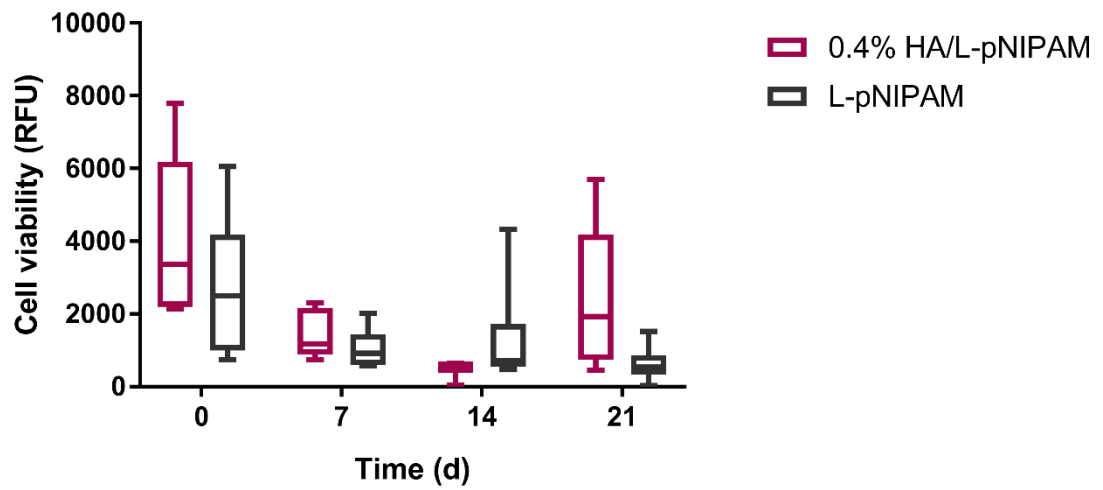
Appendix chapter 5 figure 2 *Cell viability of HepG2 cells in cultured in hydrogel (0/0.4% HA/L-pNIPAM) at cell seeding density 4×10^6 cell/mL.*
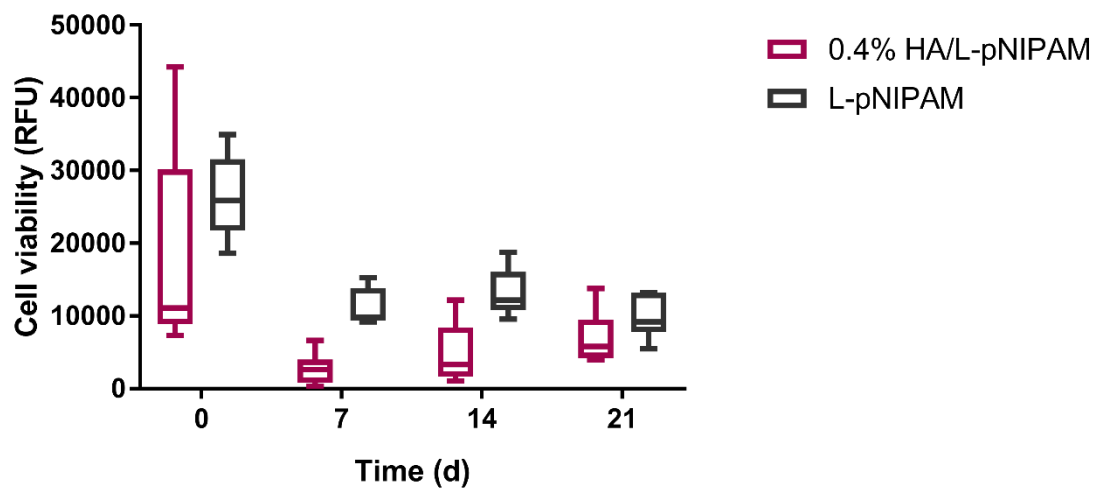
Appendix chapter 5 figure 3 *Cell viability of HepG2 cells in cultured in hydrogel (0/0.4% HA/L-pNIPAM) at cell seeding density 8×10^6 cell/mL.*
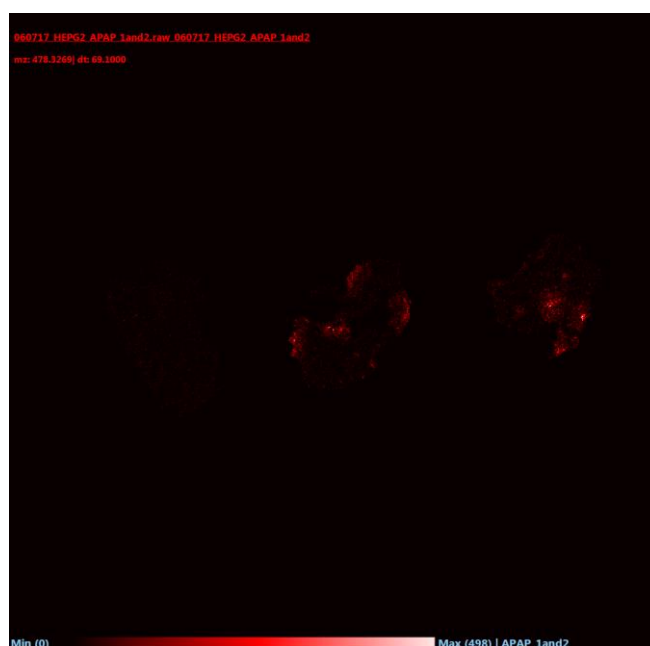
Appendix chapter 5 figure 4 *MSI of small molecule species (m/z=198.0881) present within the hydrogel at cell locations.*
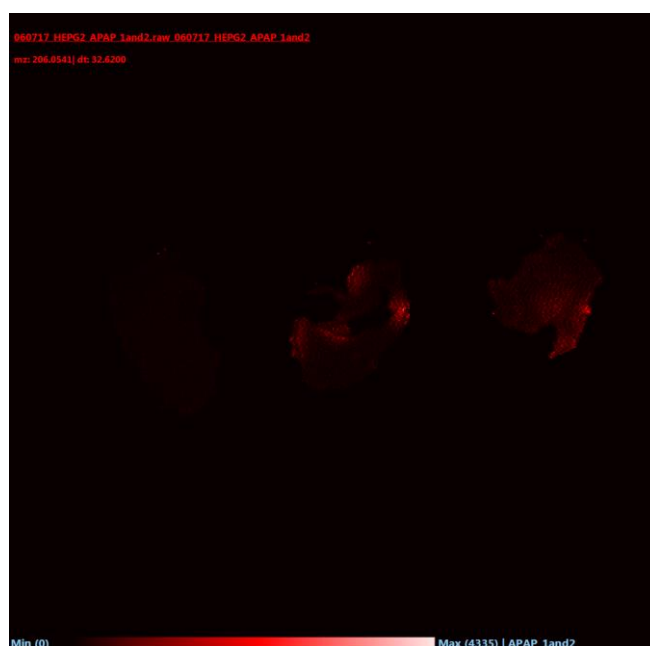
Appendix chapter 5 figure 5 *MSI of small molecule species (m/z=206.0541) present within the hydrogel at cell locations.*
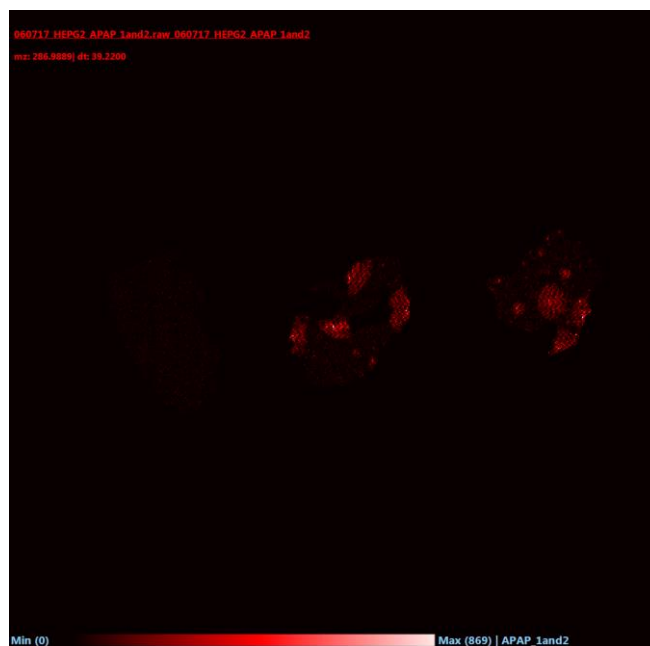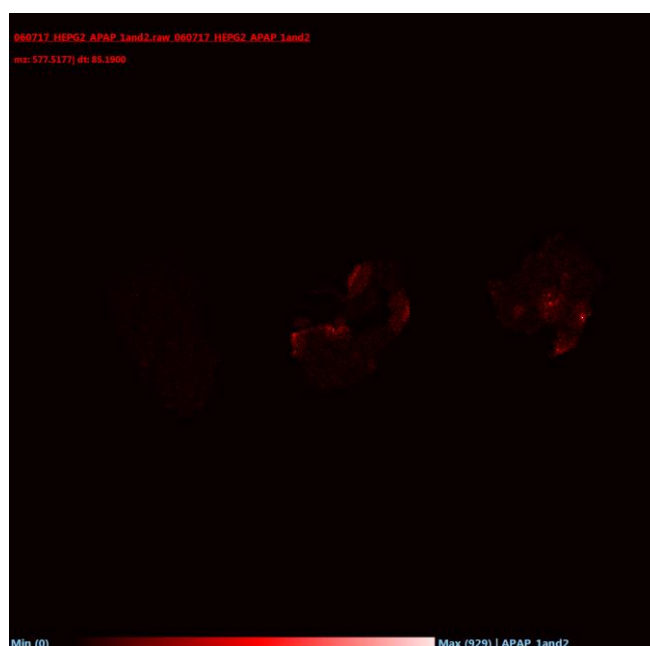
Appendix chapter 5 figure 6 *MSI of small molecule species (m/z=286.9889) present within the hydrogel at cell locations.*
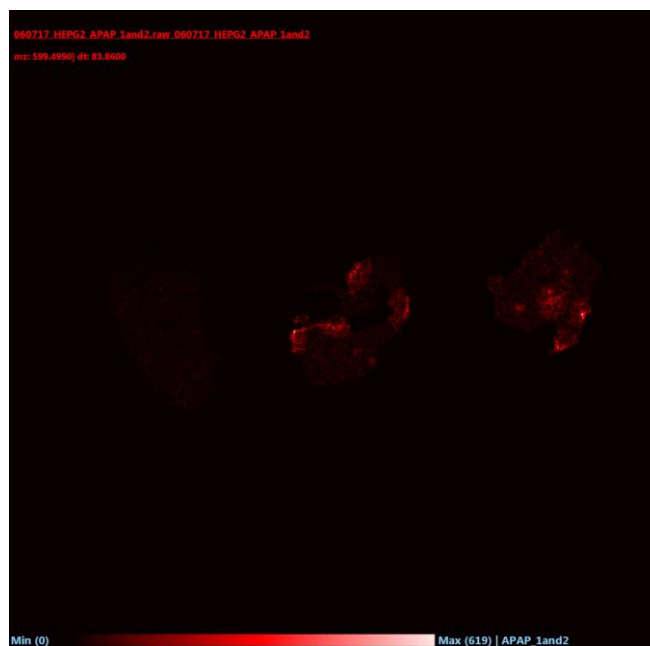

Appendix chapter 5 figure 7 *MSI of small molecule species (m/z=478.3269) present within the hydrogel at cell locations.*

Appendix chapter 5 figure 8 *MSI of small molecule species (m/z=549.4863) present within the hydrogel at cell locations.*
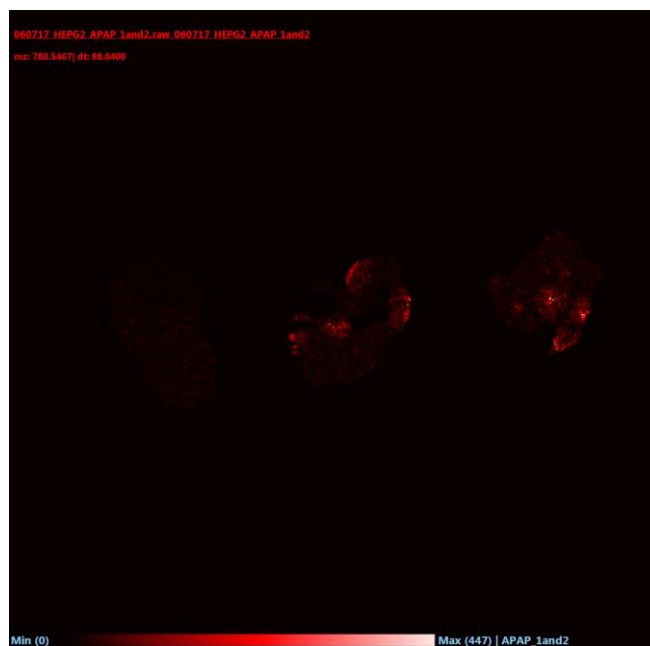

Appendix chapter 5 figure 9 *MSI of small molecule species (m/z=577.5177) present within the hydrogel at cell locations.*
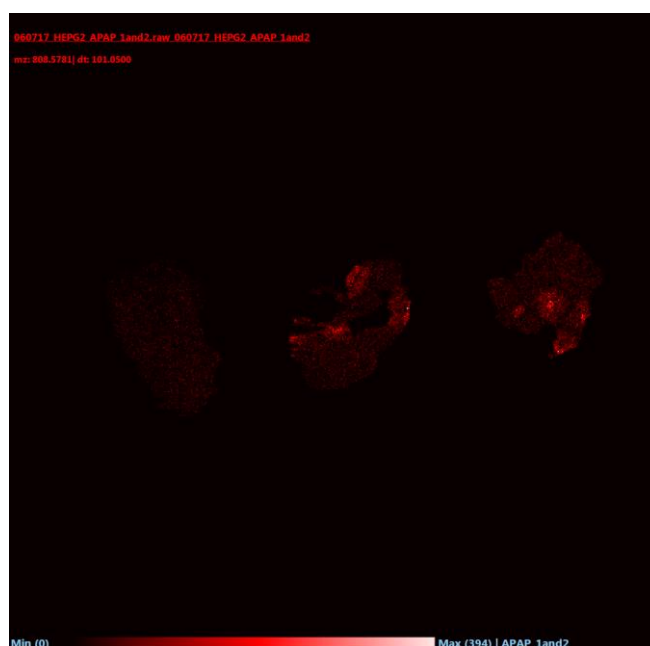
Appendix chapter 5 figure 10 *MSI of small molecule species (m/z=599.4990) present within the hydrogel at cell locations.*

Appendix chapter 5 figure 11 *MSI of small molecule species (m/z=754.5301) present within the hydrogel at cell locations.*

Appendix chapter 5 figure 12 *MSI of small molecule species (m/z=780.5467) present within the hydrogel at cell locations.*

Appendix chapter 5 figure 13 *MSI of small molecule species (m/z=808.5781) present within the hydrogel at cell locations.*

Publications

Day, R. E. and Palubeckaite, I. (2017) The Future in Disease Models for Mass Spectrometry Imaging, Ethical Issues, and the Way Forward. Methods in Molecular Biology 1618: 191-201. doi: 10.1007/978-1-4939-7051-3_16.

Oral presentations

BMSS annual conference 2015- Mass spectrometric analysis of a threedimensional hepatocarcinoma cell model to determine acetaminophen toxicity.

BMSS imaging symposium 2017- Mass spectrometry imaging method development for the analysis of a three-dimensional model of Osteosarcoma.

Ourcon V 2017- Mass spectrometry imaging method development for the analysis of a three-dimensional model of Osteosarcoma.

Poster presentations

ASMS 2015 annual conference- Mass spectrometric analysis of a three-dimensional hepatocarcinoma cell model to determine acetaminophen toxicity.

ASMS 2016 annual conference - Mass spectrometric imaging of a three-dimensional osteosarcoma model.

ASMS 2017 annual conference - Mass spectrometric imaging of a three-dimensional osteosarcoma model.

Ourcon III- Mass spectrometric analysis of a three-dimensional hepatocarcinoma cell model to determine acetaminophen toxicity.

Ourcon IV- Mass spectrometric analysis of endogenous small molecules in a three-dimensional cell culture model of osteosarcoma.

BMSS imaging symposium 2015- Mass spectrometric imaging of a three-dimensional osteosarcoma model

BMSS imaging symposium 2016- Mass spectrometric imaging of a three-dimensional osteosarcoma model

BMSS annual conference 2017- Mass spectrometric imaging of a three-dimensional osteosarcoma model

Laboratory visits

2 week visit to Leiden, The Netherlands Centre for Proteomics and Metabolomics

Workshops

COST Action BM1104 workshop 2015

External funding

BMSS £300

ASMS $200x2

Royal Society of Chemistry Analytical Division (£500)

The Biochemical Society (£550)

2015 Workshop in Vienna fully paid by COST Action BM1104.